AFRL-RQ-WP-TR-2014-0195

UNSTEADY AERODYNAMIC INTERACTION IN A CLOSELY COUPLED TURBINE CONSISTENT WITH CONTRA-ROTATION

Michael Kenneth Ooten, John P. Clark, Richard Anthony, and Andrew Lethander

Turbomachinery Branch
Turbine Engine Division

AUGUST 2014
Interim Report

AIR FORCE RESEARCH LABORATORY
AEROSPACE SYSTEMS DIRECTORATE
WRIGHT-PATTERSON AIR FORCE BASE, OH 45433-7541
AIR FORCE MATERIEL COMMAND
UNITED STATES AIR FORCE

NOTICE AND SIGNATURE PAGE

Using Government drawings, specifications, or other data included in this document for any purpose other than Government procurement does not in any way obligate the U.S. Government. The fact that the Government formulated or supplied the drawings, specifications, or other data does not license the holder or any other person or corporation; or convey any rights or permission to manufacture, use, or sell any patented invention that may relate to them.

This report was cleared for public release by the USAF 88th Air Base Wing (88 ABW) Public Affairs Office (PAO) and is available to the general public, including foreign nationals.

Copies may be obtained from the Defense Technical Information Center (DTIC) (http://www.dtic.mil).

AFRL-RQ-WP-TR-2014-0195 HAS BEEN REVIEWED AND IS APPROVED FOR PUBLICATION IN ACCORDANCE WITH ASSIGNED DISTRIBUTION STATEMENT.

*//Signature//

JOHN P. CLARK
Program Manager
Turbomachinery Branch
Turbine Engine Division

//Signature//

CHARLES W. STEVENS, Chief
Turbomachinery Branch
Turbine Engine Division

//Signature//

ROBERT D. HANCOCK, Principal Scientist
Turbine Engine Division
Aerospace Systems Directorate

This report is published in the interest of scientific and technical information exchange, and its publication does not constitute the Government's approval or disapproval of its ideas or findings.

*Disseminated copies will show "//Signature//" stamped or typed above the signature blocks.

REPORT DOCUMENTATION PAGE

Form Approved
OMB No. 0704-0188

1. REPORT DATE *(DD-MM-YY)*	2. REPORT TYPE	3. DATES COVERED *(From - To)*
August 2014	Interim	04 August 2012 – 04 August 2014

4. TITLE AND SUBTITLE
UNSTEADY AERODYNAMIC INTERACTION IN A CLOSELY COUPLED TURBINE CONSISTENT WITH CONTRA-ROTATION

5a. CONTRACT NUMBER
In-house

5b. GRANT NUMBER

5c. PROGRAM ELEMENT NUMBER
62203F

6. AUTHOR(S)
Michael Kenneth Ooten, John P. Clark, Richard Anthony, and Andrew Lethander

5d. PROJECT NUMBER
3066

5e. TASK NUMBER
N/A

5f. WORK UNIT NUMBER
Q0B2

7. PERFORMING ORGANIZATION NAME(S) AND ADDRESS(ES)
Turbomachinery Branch (AFRL/RQTT)
Turbine Engine Division
Air Force Research Laboratory, Aerospace Systems Directorate
Wright-Patterson Air Force Base, OH 45433-7541
Air Force Materiel Command, United States Air Force

8. PERFORMING ORGANIZATION REPORT NUMBER
AFRL-RQ-WP-TR-2014-0195

9. SPONSORING/MONITORING AGENCY NAME(S) AND ADDRESS(ES)
Air Force Research Laboratory
Aerospace Systems Directorate
Wright-Patterson Air Force Base, OH 45433-7541
Air Force Materiel Command
United States Air Force

10. SPONSORING/MONITORING AGENCY ACRONYM(S)
AFRL/RQTT

11. SPONSORING/MONITORING AGENCY REPORT NUMBER(S)
AFRL-RQ-WP-TR-2014-0195

12. DISTRIBUTION/AVAILABILITY STATEMENT
Approved for public release; distribution unlimited.

13. SUPPLEMENTARY NOTES
PA Case Number: 88ABW-2014-3137; Clearance Date: 30 Jun 2014.

14. ABSTRACT
A significant design concern for turbomachinery parts is forced vibrational response due to unsteady pressure fields. Shortened component lives, increased maintenance costs, and catastrophic engine failure can result due to unmitigated vibrational stresses. Geometry changes, increased airfoil count and wall thickness, and the inclusion of damping systems are a few of the current strategies employed by designers in order to move modal frequencies out of the engine running range or reduce the vibrational stresses on the airfoil. However, these techniques have a negative impact on performance, system weight, and/or life cycle cost. The focus of the study presented here was to investigate the reaction between the blade and downstream vane of the stage-and-a-half High Impact Technologies (HIT) Research Turbine via CFD analysis and experimental data. Code Leo—a Reynolds-Averaged Navier-Stokes (RANS) flow solver with the two-equation Wilcox 1998 k-ω turbulence model—was used as the numerical analysis tool for comparison for all of the experiments conducted, which includes two- and three-dimensional geometries and both time-averaged and time-accurate simulations. The rigorous blade and downstream vane interaction study was accomplished by first testing the midspan and quarter-tip two-dimensional geometries of the blade in a linear transonic cascade. The effects of varying the incidence angle and pressure ratio on the pressure distribution were captured both numerically and experimentally. This was used during the stage-and-one-half post-test analysis to confirm that the target corrected speed and pressure ratio were achieved. Then, in a full annulus facility, the first vane itself was tested in order to characterize the flow field exiting the vane that would be provided to the blade row during the rotating experiments. Finally, the full stage-and-a-half Research Turbine was tested in the full annulus cascade with a data resolution not seen in any studies to date. A rigorous convergence study was conducted that assessed the grid, iterative, periodic, temporal, and geometric convergences to sufficiently model the flow physics of the Research Turbine. The surface pressure traces and the Discrete Fourier Transforms thereof were compared to the numerical analysis. To track the trajectory of the shocks, time lags to maximum correlations coefficient were analyzed also.

15. SUBJECT TERMS
Vane blade interaction, CFD, experiment, turbomachinery, unsteady analysis, time-accurate simulations, reflected shocks, contra-rotation

16. SECURITY CLASSIFICATION OF:			17. LIMITATION OF ABSTRACT:	18. NUMBER OF PAGES	19a. NAME OF RESPONSIBLE PERSON (Monitor)
a. REPORT	b. ABSTRACT	c. THIS PAGE			John P. Clark
Unclassified	Unclassified	Unclassified	SAR	170	19b. TELEPHONE NUMBER *(Include Area Code)* N/A

TABLE OF CONTENTS

LIST OF FIGURES

LIST OF TABLES

LIST OF SYMBOLS

1B = First Blade
1V = First Vane
2V = Second Vane
α = Angle of attack
CCF = Cross-Correlation Coefficient
CFD = Computational Fluid Dynamic results DFT = Discrete Fourier Transform
f_A = Fuzzy set parameter of Discrete Fourier Transform amplitude
f_C = Total fuzzy set convergence
f_M = Fuzzy set parameter of the time-mean value
f_P = Fuzzy set parameter of power spectral density
f_S = Fuzzy set parameter of cross-correlation coefficient
f_ϕ = Fuzzy set parameter of Discrete Fourier Transform phase
HIT RT = High-Impact Technology Research Turbine
HPT1B = High Pressure Turbine First Blade ID = Inner Diameter
LPT = Low-Pressure Turbine M = Mach number
OD = Outer Diameter
P = Pressure
Re = Reynolds number
T = Temperature

Subscript

c = Cooling flow
in = At inlet
ex = At exit
s = Static
t = Total or stagnation
∞ = Free stream flow

To Amanda and Family

ACKNOWLEDGEMENTS

This thesis would not have been possible without the help of a number of people. First, my most sincere thanks to Dr. John P. Clark, whose expertise, mentorship, and friendship were invaluable throughout the effort of this research. Dr. Clark added immeasurable value to this work with his technical advice and direction, development of analysis tools, and review of this thesis.

I would also like to thank my faculty advisor, Dr. Aaron Altman at the University of Dayton, for his guidance while pursuing my graduate degree.

I would like to acknowledge the contributions of several of my coworkers that contributed to this research effort: Dr. Andy Lethander, Robert Wirrig, Aaron Brown and Natalia Posada for their technical support in obtaining experimental data from the transonic cascade; Dr. Richard Anthony, John Finnegan, Mike Kobelak, Kyle Kavanaugh, Rob Free, Dan Hill, and Mike Fisher for their technical support in obtaining experimental data from the Turbine Research Facility; Major Jamie J. Johnson and Captain Eric Lyall for their technical advice; additional computational support from Tom McCray and Mike List; administrative support from Emilee Brown. Support from others at the Air Force Research Laboratory is also greatly appreciated. I would also like to thank Mary Meyer for reviewing this thesis.

CHAPTER I
INTRODUCTION

Motivation

The forced vibrational response of turbomachinery components due to unsteady pressures is a significant design concern for engineers. Vibrational stresses can drastically shorten the lives of engine components or even cause a catastrophic engine failure. Designers have a shortlist of available options to prevent or combat the unsteady forces, and these include: moving resonant frequencies out of the operating or dwelling ranges through changes in geometry, increasing component counts to reduce the strength of the unsteadiness and also therefore altering the frequency of forcing, incorporating a damping system that diminishes the response amplitude of the component, and increasing wall thickness of components to reduce stress levels. Performance, system weight, and life-cycle cost can be negatively impacted by design changes made to the airfoils that compromise the original intent of the designer or by adding material and increasing part counts that add weight to the engine. As described in a following section, an objective of the turbomachinery community has been to develop the Computational Fluid Dynamics (CFD) tools necessary to predict the unsteadiness inherent in the turbine component with high fidelity. Designers would then have the ability to reduce confidently the forced vibrational responses on the rotating components through aerodynamic design.

The Air Force Research Laboratory (AFRL) Research Turbine, hereafter referred to as the Research Turbine, was designed by the Turbine Analysis Team, beginning from cycle requirements, to a meanline analysis, then to a two-dimensional steady analysis, and finally to a three-dimensional, time-accurate analysis [1]. The goal of the first build of the Research Turbine is to validate CFD tools for accurate predictions of the unsteady interaction in a contra-rotating turbine [2][3]. Subsequent experiments will incorporate aerodynamic design changes in an effort to reduce the unsteadiness inherent in the interactions between turbine components. Each build is one and one-half stages consisting of a highly loaded single stage high-pressure turbine (HP) and a downstream vane consistent with a low-pressure (LP) turbine. The Research Turbine is consistent with contra-rotation, wherein the high-pressure and low-pressure spools rotate in opposite directions. The turbines are intended for testing at the Turbine Research Facility at Wright-Patterson AFB.

Contra-rotating turbines have a high degree of periodic unsteadiness associated with shock interactions between the high-pressure blade and the low-pressure vane, and these can result in high-cycle fatigue failure. A snapshot of the unsteady flow field in the Research Turbine is shown in Figure 1. The colorization in the figure is static pressure; whereas the contours are calculated from the change in entropy through the turbine. Shocks from the blade travel downstream and reflect off of the LP vane back upstream to impact the blade on the suction side. The shocks interact with boundary layers and wakes throughout this process, so accurate predictions of unsteady interaction could require advanced viscous modeling capability.

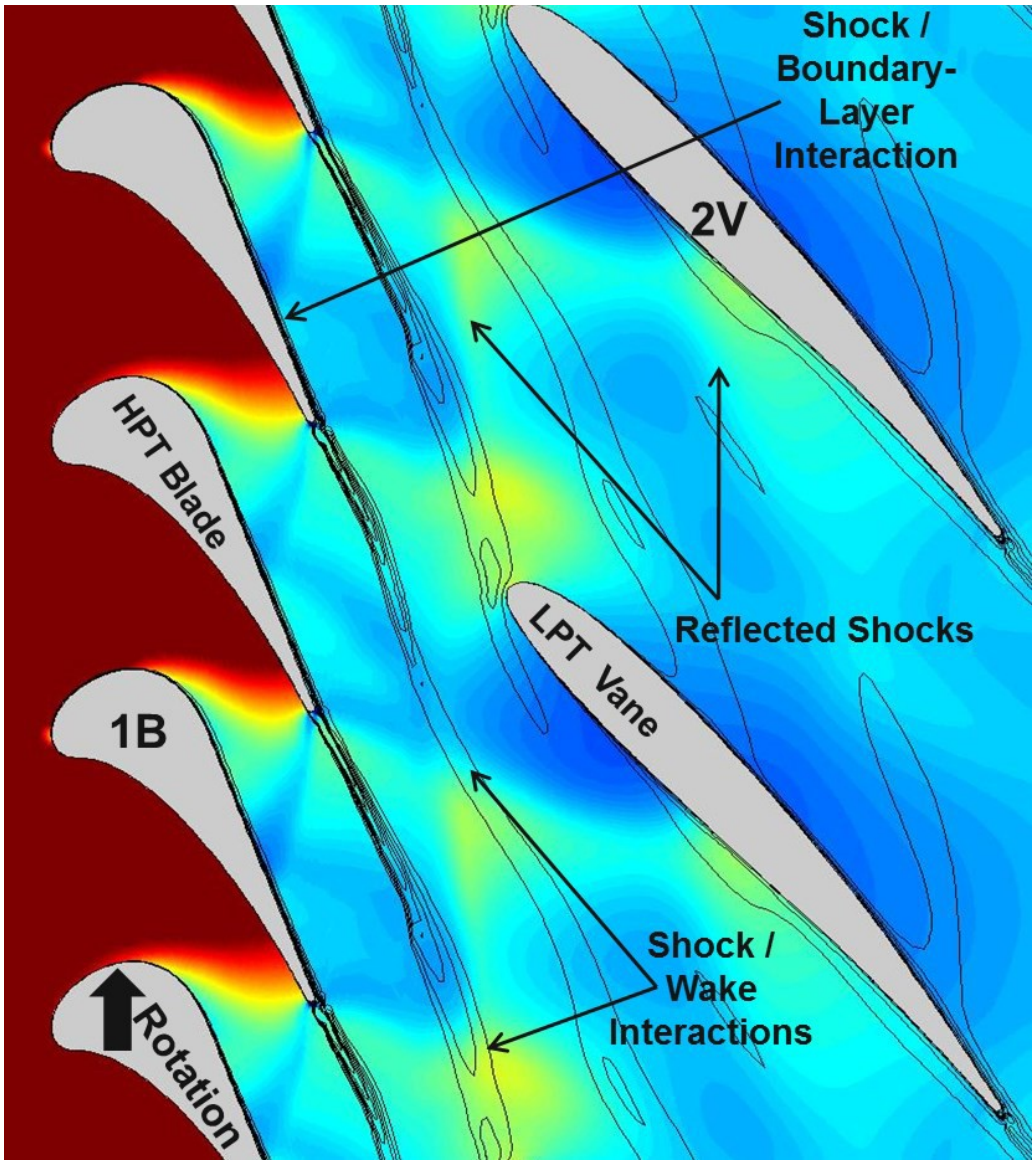

Figure 1: Unsteady Flow Field in Contra-Rotating Research Turbine

The purpose of this thesis is to investigate rigorously the unsteady interaction between the blade and downstream vane of the Research Turbine. Through both numerical and physical experiments, the overall goal is to improve the understanding of the flow physics in order to predict more accurately the forced response on the blade. The Research Turbine design details are given in Chapter II. In the subsequent chapters, the effort to build the experimental and numerical analysis fidelity leading up to the stage-and-a-half experiments is detailed. First, a two-dimensional, steady comparison between CFD analysis and experimental data of the midspan and quarter-tip radial sections of the Research Turbine blade will be shown in Chapter III. The effects varying the incidence angle and the pressure ratio of the blade on the pressure distribution were of particular interest. The effects would be used during the post-test analysis of the stage-and-one-half experiments to determine whether or not the targeted corrected speed and pressure ratio were achieved. The aerodynamic performance of the upstream vane that sets up the flow for the rotor is shown in Chapter IV, which will compare

the three-dimensional, steady CFD analysis and experimental data of the first-vane-only build in the TRF. Then, a concerted effort to determine the appropriate grid density and wheel sector in which to model the unsteady, stage-and-a-half Research Turbine is shown in Chapter V. Using the outcome from the previous chapter, Chapter VI will contain the comparison of the Research Turbine experimental data to unsteady, three-dimensional, stage-and-a-half CFD analysis. Finally, the conclusions and recommendations for future research will be presented in Chapter VII.

Signal Analysis Techniques

Several signal analysis techniques were used in this research. The objective of this section is to briefly describe each of the techniques used.

The most simplistic analysis technique used was unsteady envelopes. In this application, unsteady envelopes were used to bound the pressure fluctuations of the time-accurate numerical analysis. Therefore, the unsteady pressure envelopes represent a peak-to-peak pressure variation of the numerical analysis at each node, and this was used to compare to the experimental peak-to-peak data.

Ensemble averaging was used to analyze the experimental data from the rotating tests. All pressure measurements were phase-locked relative to the position of the blade at the top-dead-center. The ensemble average of the pressure was then taken from the phase-locked data [4][5].

The Discrete Fourier Transform (DFT) is a powerful signal processing tool used in a broad spectrum of applications [6]. In the present work, the discrete Fourier transform—and occasionally the more efficient fast Fourier transform—are used to determine the frequencies at which the unsteady pressures are particularly large. This is accomplished by plotting the DFT amplitudes of each frequency of the signal. Larger magnitudes indicate that more of the unsteadiness in the signal is due to that particular frequency. In addition, the variation of the DFT amplitudes and phase angles at frequencies of interest from one computational cycle to the next were used as a measure of periodic convergence.

The Power Spectral Density (PSD) was used to determine the percent magnitude of the unsteadiness at a given frequency relative to the sum of the magnitudes over the entire frequency range by invoking Parseval's Theorem. This usage of the PSD was in keeping with that of Clark and Grover [7]. Mathematically, the PSD at a given frequency is the product of the Fourier component at that frequency and its complex conjugate divided by the number of samples.

The cross-correlation coefficient (CCF) is a measure of the similarity between two signals [6]. The value of the cross-correlation of two signals varies depending on thelag from one signal to another. Both the maximum CCF and the lags to maximum CCF are used in this research. The maximum CCF is used to compare the pressure signals at various locations on the surface of the downstream vane. High correlation indicates that the unsteadiness measured on the airfoil is due to the same source, such as a reflected shock. The time difference between predicted and measured unsteady events can be inferred from the lag to maximum CCF. For this reason, lag values were used to track unsteady events, such as shock impingements, across airfoil surfaces.

Literature Review

Very early theoretical studies regarding airfoil interaction were performed in the 1950s by Kemp and Sears [8] [9]. Kemp and Sears applied a linearized potential flow solution to the vane-blade interaction problem. They concluded that the unsteady pressures could be as high as 18 percent of the steady-state pressure. This early theoretical work indicated a strong need to develop both the computational tools required to perform numerical simulations of these highly complex flow phenomena and improved experimental facilities that accurately replicate the unsteady turbine engine environment.

A relatively simple and low-cost, yet effective, method of investigating rotor- stator interaction experimentally was through the use of a wind tunnel with a stationary blade row and rotating rods. The rotating rods upstream of the stationary blade row simulate the effect of the blades passing through the wakes of the upstream vane. Among the work that was carried out in such experimental facilities was that of Ashworth et al. [10]. Ashworth et al. investigated the unsteady aerodynamic and heat transfer loads in their facility. They found that the data that they collected was periodic at the vane passing frequency. The unsteady nature of the aerodynamic forces and heat loads due to the simulated passing upstream vane wakes was clearly defined by the airfoil surface data. Then, the research of Ashworth, Guenette et al. [11] conducted a fully scaled transonic turbine experiment in which they investigated rotor heat flux measurements in a blowdown facility. Unlike the linear, stationary blade row cascades, a blowdown facility is a full-annulus apparatus which contains the actual upstream stator and the rotating blade row. The data of Guenette clearly indicated high levels of unsteadiness in the heat flux data as a result of the vane-blade interaction. Guenette compared the measurements at the appropriate spanwise location to that of the Ashworth et al. linear cascade with rotating rods [10]. The data from each rig compared well in many respects. However, there were some notable differences. Both authors agreed that there was value in a relatively simple, quick turnaround linear cascade facility. However, they also suggested that a rotating rig was necessary to capture truly the rotor-stator interaction that would be present in a turbine engine with a high degree of accuracy.

Dring et al. [12] also investigated rotor-stator interaction on a large-scale turbine. Dring studied the interaction at two different axial gaps between the vane and blade: 15 and 65 percent axial chord. Strong pressure fluctuations were present on the vane downstream of the throat and on the blade upstream of the throat. This indicated that the fluctuations on the vane and blade were due to the vane-blade interaction. This research confirmed that higher levels of unsteady pressures occurred at smaller axial gaps, for which unsteady pressures were measured as high as 80 percent of the relative dynamic pressure on the blade. Dunn and Haldeman [13] measured phase-resolved surface pressure measurements on the first stage of the Space Shuttle main engine fuel turbine.

The facility used in their experiment was a pressurized shock tube that generates a shock that raises the pressure and temperature to engine relevant values. The test duration was on the order of tens of milliseconds; however a great deal of engine representative data can be captured during such a short time interval. Dunn and Haldeman recorded surface pressures and heat fluxes at 10, 50, and 90 percent span. Ensemble averages of the measurements were conducted to produce the phase-resolved unsteady surface pressure experimental data and to show clearly the vane-blade interaction.

As more and more facilities became capable of measuring time-resolved pressure and heat flux data, it became increasingly apparent that in order to improve the durability of turbine airfoils, more sophisticated analytic tools would need to be developed and used throughout the design process. Previous numerical analysis techniques were shown to predict the average, steady-state flowfield reasonably well [14, 15, 16, 17]. However, the capability to model vane-blade interaction did not exist until relatively recently. Rai recognized the importance of accurate numerical analysis of rotor-stator interaction, and he was one of the first to make use of Navier-Stokes simulations to perform the analysis. Rai developed a Reynolds-Averaged Navier-Stokes (RANS) CFD code to compare two-dimensional [18] and three-dimensional simulations to experimental data [19]. He used patched and overlaid grid methods to model the geometry. In both the two- and three- dimensional cases, Rai simplified the geometry he used in the CFD analysis in order to reduce the computational burden. The most significant simplification was a reduction in the number of blades to match the vane count so that a one-to-one airfoil ratio could be used for the CFD simulation. As a result, the blade geometry was scaled up slightly. The unsteady amplitudes calculated by the CFD code compared very well to the experimental data for both the two- and three-dimensional cases, especially when considering the simplifications used in the model. Giles [20] also developed a CFD code in order to investigate vane-blade interaction. He used an inviscid, unsteady Euler numerical method on a highly loaded, transonic turbine. The approach of Giles included a conservative treatment of the computational cells at the rotor/stator grid boundary that made it suitable to handle shocks across the boundary. Analysis of the Giles geometry shows the reflected shock structures from the vane to the blade, and back upstream to the vane again in detail. Also, secondary reflected shocks appeared to interact with the companion blade in the rotor passage, which reflected back upon the suction side of the originating blade. Giles concluded that the unsteady interaction between the vane and blade produced a 40 percent variation of the lift on the blade and he determined that the unsteady surface pressures would cause blade vibration that would decrement airfoil durability and increase the aerodynamic losses.

Many others have contributed toward advancing the numerical tools to model accurately the unsteady interaction between the vane and blade. This includes the research of Dunn et al. [21] and Rao et al. [22], both of whom compare CFD predictions to data from short-duration shock tunnel facilities. Rao et al. used a two-dimensional RANS code with an O-H grid system to predict time-averaged and time-resolved surface pressure data in a transonic turbine. The numerical analysis performed by Rao et al. was shown to predict the unsteady pressure envelopes reasonably well. The CFD simulations predicted a high degree of unsteadiness caused by the vane-blade shock interaction, and the experimental data taken from the shock tunnel showed a similar result. An assessment of numerical models was reported by Sharma et al [23]. Sharma assessed predictive accuracy of the state-of-the-art of steady and unsteady CFD codes relative to experimental work. The report concluded that there was a real need to simulate the unsteady flowfield in a turbine engine within the design process. Steady simulations were not capturing all of the pertinent physics.

There has been a lot of recent work which focuses on incorporating the numerical analysis of vane-blade interaction into the design loop. Such efforts could greatly improve the durability of turbine engines and decrease engine weight. Clark et al [3] used modern numerical analysis in the design cycle to predict and reduce the magnitude of the unsteadiness on the

blade as a result of vane-blade interaction. The work explored two methods designed to reduce the unsteady magnitude via CFD: asymmetric vane spacing and modification to the vane geometry. The latter option was chosen for experimental evaluation due to the relative ease of manufacturing and testing. Experimental results confirmed that the design changes did reduce the unsteadiness observed on the blade, as predicted. Clark further investigates design strategies to mitigate unsteady forcing [3]. Clark and Grover [7] detail the design methodology used to reduce the unsteady magnitude on the blade, as well as stresses the importance of ensuring periodic convergence in order to assess accurately the unsteady flowfield. A fuzzy set convergence criteria was implemented in order to quantify periodic convergence of the unsteady flowfield prior to post-processing the numerical analysis to obtain resonant stresses. Additional work using fuzzy set analysis can be found in Klir et al. [24]. Also, Clark and Yuan [25] used fuzzy logic in a turbomachinery application.

Most of the research aimed at reducing the unsteady magnitudes seen on the blade has focused on a single-stage turbine only. However, modern transonic turbines that are contra-rotating experience a significant amount of unsteadiness driven by shocks reflecting off the downstream vane and returning upstream to the suction side of the blade. Davis et al. [26] have investigated the unsteady interaction of a stage-and-a-half turbine experimentally, including the effects of the downstream vane, and compared the results to CFD predictions. The steady-state results and the unsteady pressure envelopes of the numerical analysis agreed well with the experimental data. The focus of this research is to investigate the interaction between the blade and downstream vane via CFD analysis and experimental data with temporal and spatial data resolution not seen in any studies to date, which is made possible by an extremely well instrumented turbine tested at the Turbine Research Facility at AFRL.

CHAPTER II
RESEARCH TURBINE DESIGN

Design Tools

Over the past several years, a complete aerodynamic design, analysis, and optimization system for turbine airfoils was implemented at the Air Force Research Laboratory. The system, which is described fully in [1, 7, 16, 17 and 27], was created to allow the development of non-proprietary airfoil geometries of interest to the USAF. The system enables 2D and 3D design of turbine components using both traditional and design-optimization methods. It is also modular and thus amenable to modification as new analysis tools become available. While only two 2D profiles were tested in the linear cascade, this represented the constant-radius section from the midspan and quarter-tip of a rotating airfoil from a stage-and-one-half transonic turbine [2]. The blade of interest is representative of a single-stage high pressure turbine with a design pressure ratio of 3.75.

The blade profile was defined using the 2D components of the design and analysis system, which is built around an airfoil profile generator defined by Frank Huber at Florida Turbine Technologies [1]. The algorithm is similar to one described by Casey [28] in that it uses Bezier curves in conjunction with typical leading- and trailing-edge specifications (e.g. wedge angles, edge radii of curvature, gage areas, and uncovered turning) to define airfoil shapes using a small number of control points. This algorithm is coded in MATLAB, so modularity and user friendliness were achievable through the object-oriented programming and graphical user interfaces (GUIs) available in that software. Three sets of grid generators and flow solvers are accessible, depending primarily on the level of viscous modeling desired for the analysis. The grid generator and RANS solver described by Dorney and Davis [29] allows for algebraic turbulence modeling along with an ad hoc implementation of the transition models of Praisner and Clark [30]. Additionally, the Leo analysis code described by Ni et al. [27] and the MBFLO solver of Davis and Dannenhoffer [31] are also selectable. Both codes employ the 2-equation turbulence model of Wilcox [32], while the latter also allows for detached- eddy simulations. GUIs are employed to alter the specification of the airfoil shape as well as parameters used to define both the generation of the grid and the operation of the flow solvers.

Both GUI-driven iterations and design optimization studies using Sequential Quadratic Programming (SQP) [33] were conducted to derive the final blade shape. Objective functions were used both to reduce loss and to minimize the circumferential distribution in static pressure downstream of the airfoil [3]. The airfoil pressure distribution that resulted from this endeavor was characterized by a double shock system terminating on the suction side of the airfoil after crossing the channel from the pressure- side trailing edge. Figure 2 is a plot of airfoil loading for a range of exit relative Mach numbers. The blade is intended for testing over a range of Reynolds numbers, pressure ratios, and wheel speeds [2]. Accordingly, the behavior of the airfoil over a range of off- design conditions approaching limit loading was assessed via simulations and experiments in the transonic cascade facility. Limit loading occurs when the cross-passage shock travels between the trailing edges of adjacent blades, and this occurs at Mach 1.75, corresponding to a total-to-total pressure ratio near 5. It is clear that the airfoil behaves as intended over a very wide range of Mach numbers.

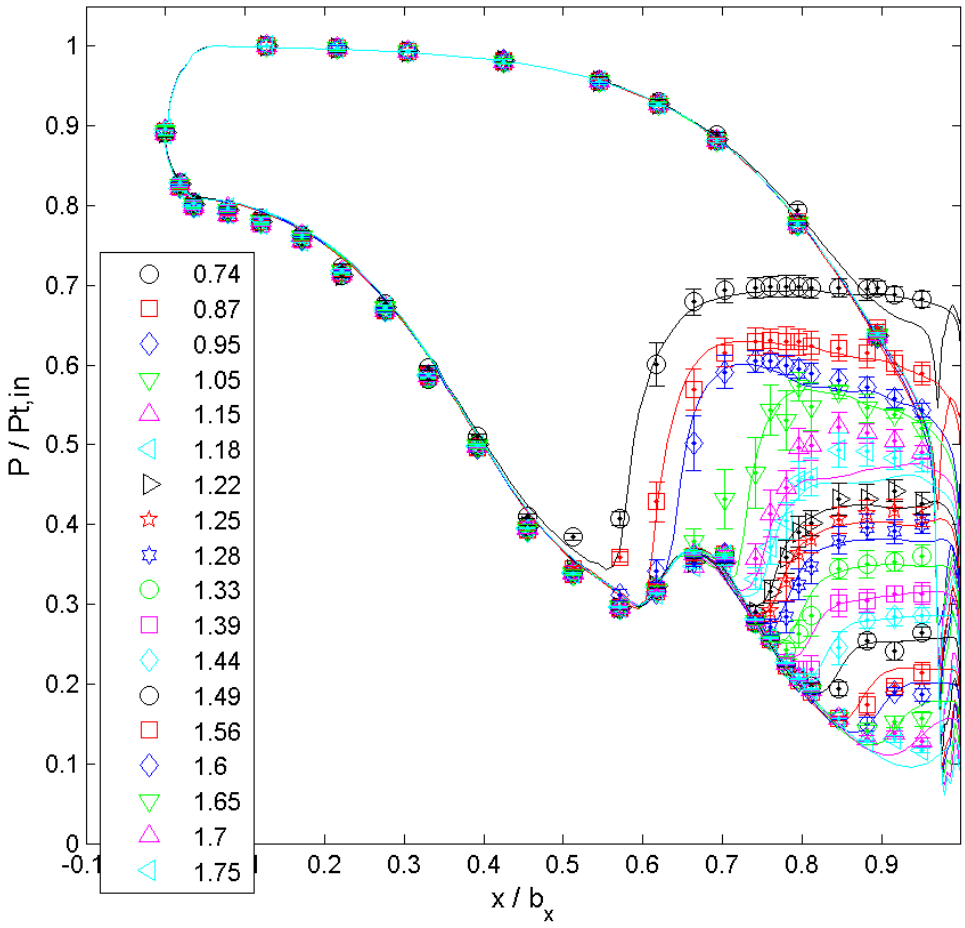

Figure 2: Airfoil loading calculation and experimental data for the midspan profile of a transonic research turbine blade row [2] in cascade over a range of exit Mach numbers

The AFRL HIT Research Turbine

At the most fundamental level, the Research Turbine at the Air Force Research Laboratory was designed as a research article to directly investigate and support numerous studies by the government and its partners in academia and industry. The flexible nature of the hardware and test schedule will also enable scientific inquiries that were not conceived at the time of the design and fabrication to be investigated using the turbine. The government designed and owned geometry adds the desirable ability to share relevant turbine research data with all interested US entities.

The first build of the Research Turbine—which is the build that is investigated in this thesis—is comprised of a single stage high pressure turbine and a downstream vane consistent with that of a contra-rotating low pressure turbine. It is heavily instrumented with pressure, thermocouple, and heat flux sensors to allow engineers substantial opportunity to gain an understanding of the complex, unsteady, three-dimensional flow field. While the unsteady pressure interaction of the blade and downstream vane is the major focus of this work, numerous heat transfer studies have been enabled by heat flux gages and thermocouples located on the airfoils [34]. The first build of the Research Turbine was designed starting from meanline analyses conducted with relevant military engine cycles. The meanline

provided the initial metal angles and flow parameters to begin the 2-D optimization. The two-dimensional constant-radius cuts at the root, midspan, and tip of each airfoil were designed using the tools described in the previous section. After the optimization, each airfoil shape was interpolated from the constant- radius cuts to generate three-dimensional geometries. The research turbine geometry was then analyzed using time-accurate 3-D CFD. This process is shown in Figure 3. The hardware illustrated in the figure was tested in Air Force facilities, which feeds the validation of the numerical tools used in the design.

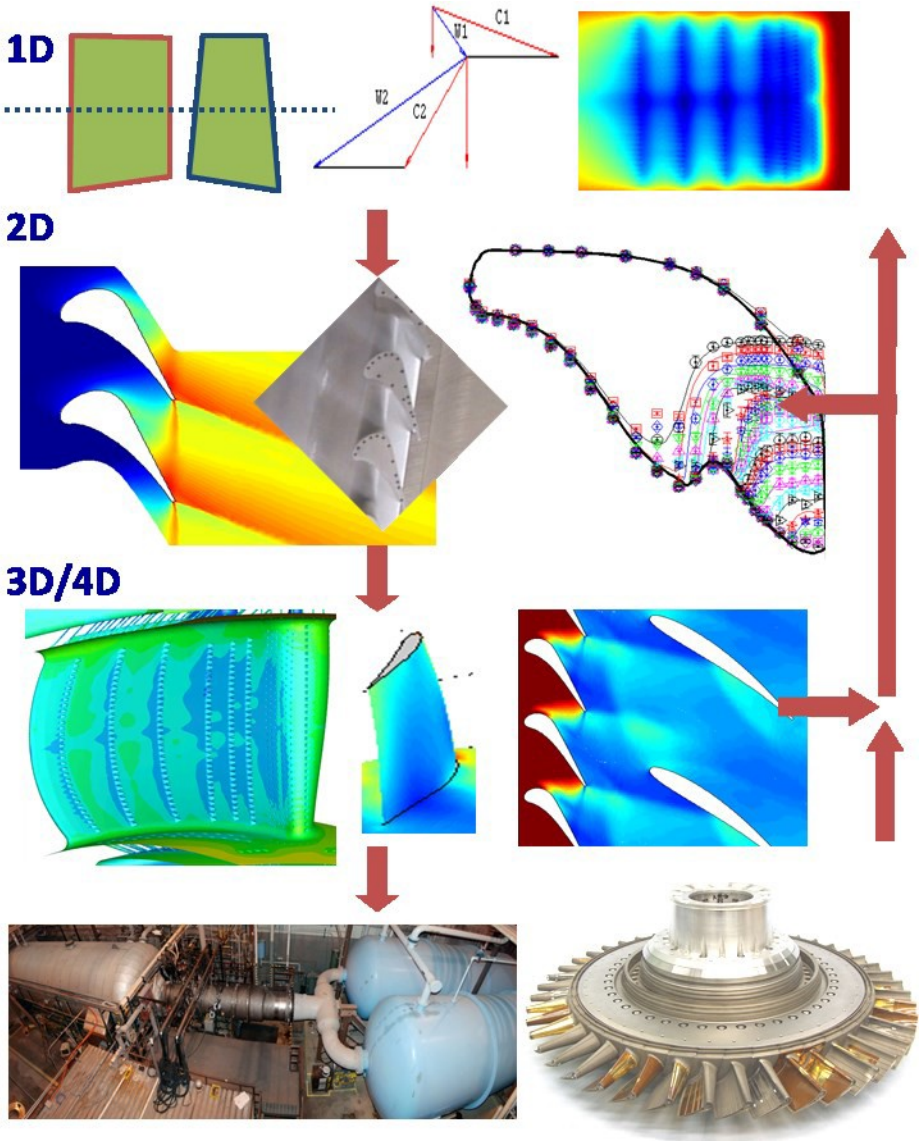

Figure 3: Turbine Design/Validation Flow Chart

As previously mentioned, the Research Turbine is heavily instrumented in order to capture the three-dimensional, unsteady aerothermal behavior of the flow field. The sensor locations on each airfoil were determined by using the design-point CFD analysis. Pressure sensor placement was driven by the desire to capture constant-radius loading profiles, areas of high and low unsteadiness, and the progression of unsteady pressure features across airfoil

surfaces. Pressure loading profiles at five constant-radius cuts on the first vane are shown in Figure 4. The red and black circles represent the sensor placement on the pressure and suction sides, respectively. It is important to note that only the sensor location is represented in this figure, not actual data. Dashed lines represent the predicted unsteady pressure distribution envelope. The loading on the first vane is fairly steady. Pressures become slightly unsteady on the suction side, particularly towards the root. The relatively well-behaved pressure profile and low unsteadiness on the vane pressure side afforded the engineers the opportunity to place more of the pressure sensors on the suction side. The vane suction side loading was slightly more interesting and had areas of greater unsteadiness. Also, the loading varied more in the span-wise direction on the suction side compared to the pressure side. Contours of unsteadiness magnitude at 5.84 kHz are shown in Figure 5. The frequency shown is the fundamental passing frequency of the downstream blade. The pressure and suction sides are depicted on the left and right, respectively. One can see in the figure the relatively high levels of unsteadiness on the suction side compared to the pressure side, especially at the root. For these reasons, it was more advantageous to place more pressure sensors on the suction side—and in additional constant-radius cuts—than the pressure side. The predicted performance, using 3-D analysis tools, allowed the sensors to be optimally arranged in order to capture the physics of interest to the researchers.

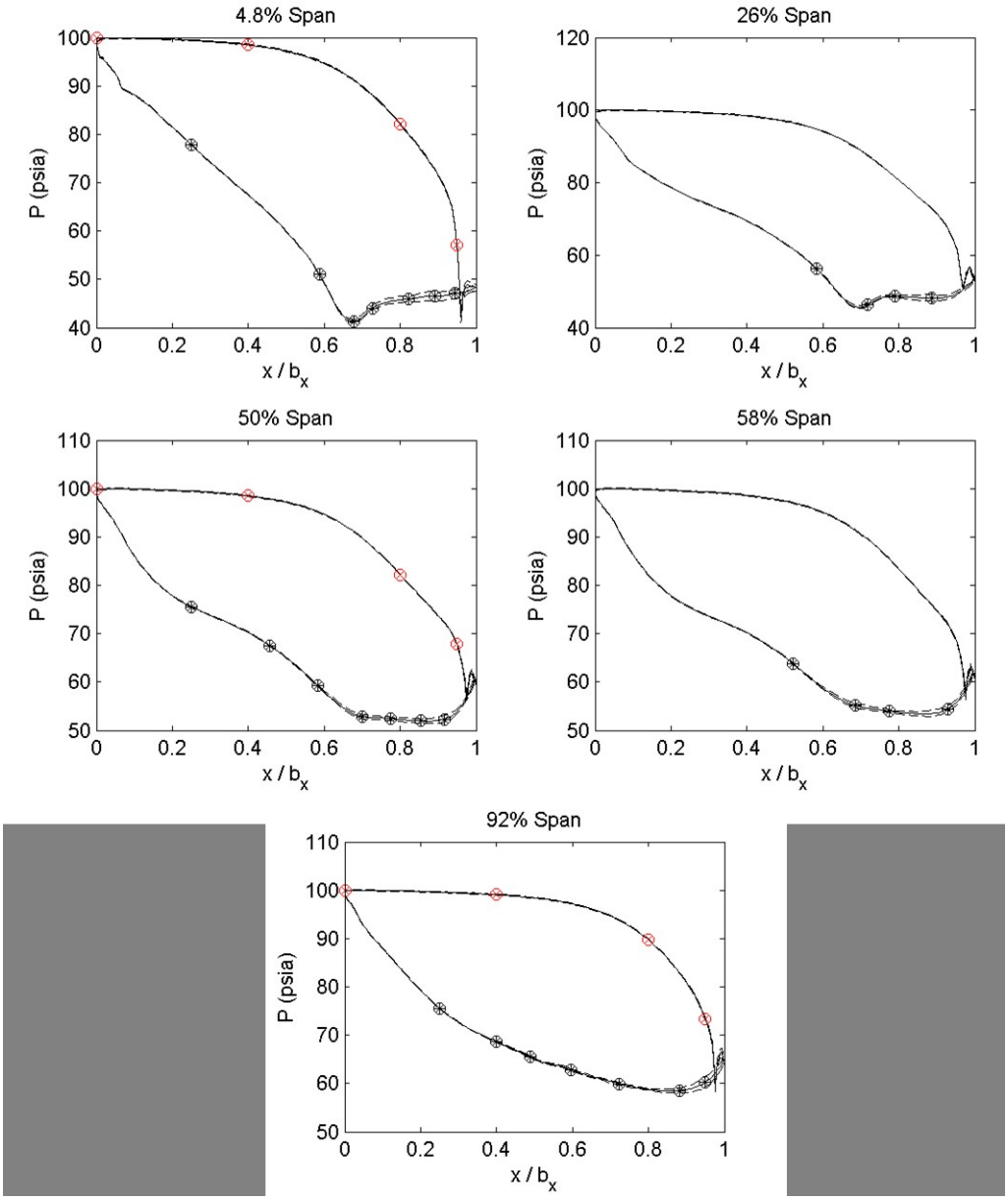

Figure 4: First Vane Pressure Distributions at Constant-Radius Cuts

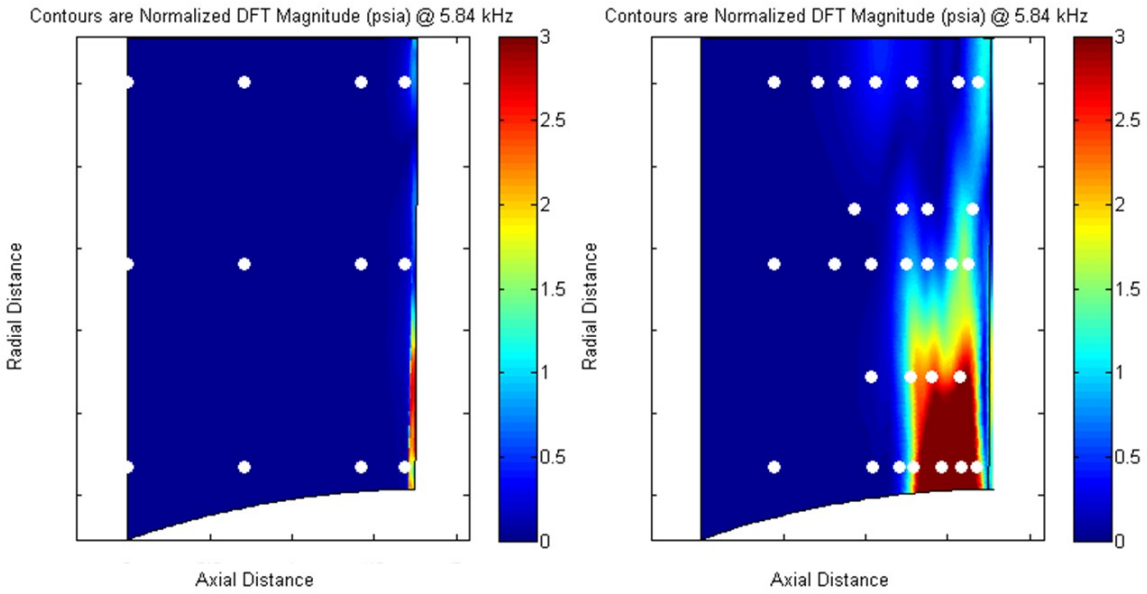

Figure 5: Normalized DFT Magnitude (psia) at 5.84 kHz for the 1V Pressure Side (left) and Suction Side (right)

A similar analysis was conducted to determine the appropriate placement of the pressure sensors on the blade. Pressure loading profiles at six constant-radius cuts on the first blade are shown in Figure 6. The red and black circles represent the sensor placement on the pressure and suction sides, respectively, and the dashed lines represent the unsteady pressure distribution envelope. As expected, the blade is predicted to experience higher levels of unsteadiness. The sensor placements on the pressure and suction sides at each of the constant-radius cuts were chosen in order to capture the loading profile shapes as best as possible. Areas of high unsteadiness were also emphasized. Contours of unsteadiness magnitude at 2.92 kHz and 5.84 kHz are shown in Figure 7 and Figure 8, respectively. The frequencies are the fundamental and first harmonic passing frequency of the up- and downstream vanes. From the figures, it is obvious that different frequencies are the source of unsteadiness on different areas of the blade. This topic will be discussed in greater detail in subsequent chapters. The purpose at this point is to illustrate the coverage of the pressure sensors. Also, the location of the shock on the suction side was heavily instrumented in order to capture the shock location as accurately as possible. The suction-side shock is most identifiable at 5.84 kHz. The shock is clearly defined by the stark difference in the magnitude contours near the trailing edge.

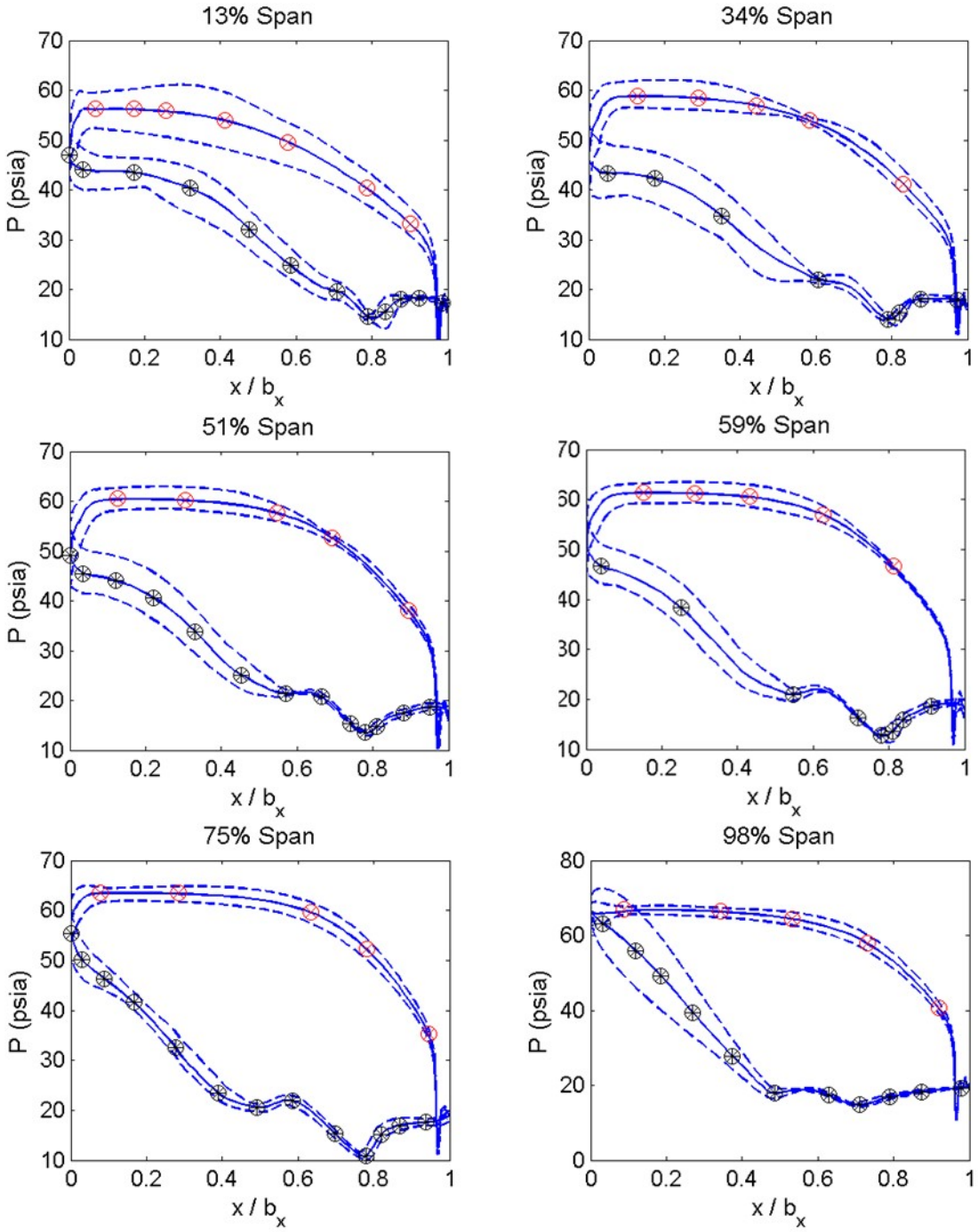

Figure 6: First Blade Pressure Distributions at Constant-Radius Cuts

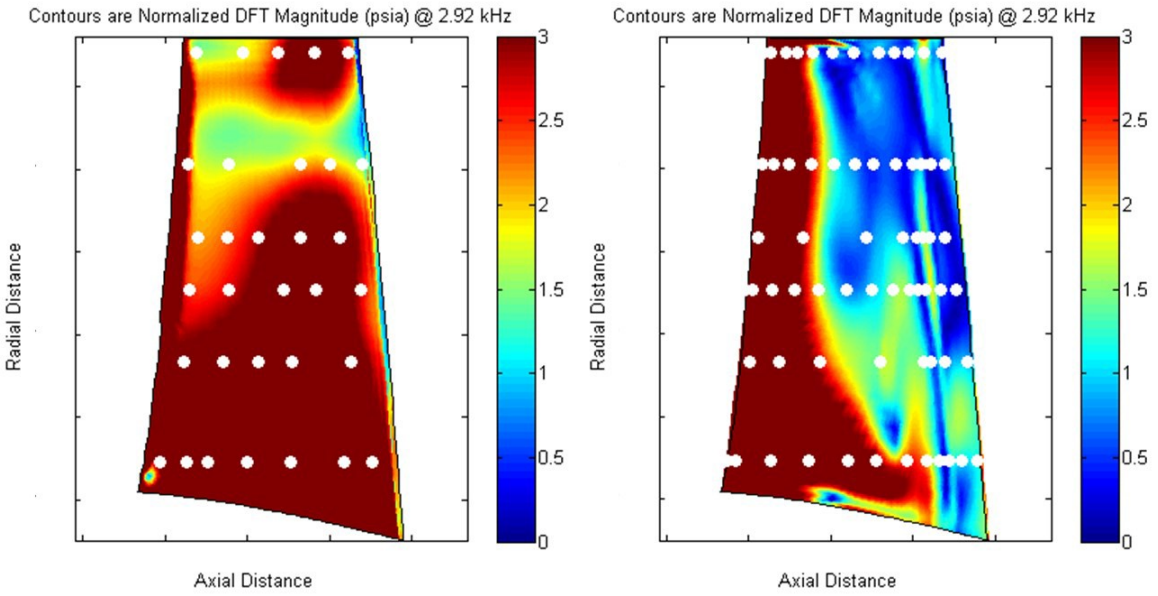

Figure 7: Normalized DFT Magnitude (psia) at 2.92 kHz for the 1B Pressure Side (left) and Suction Side (right)

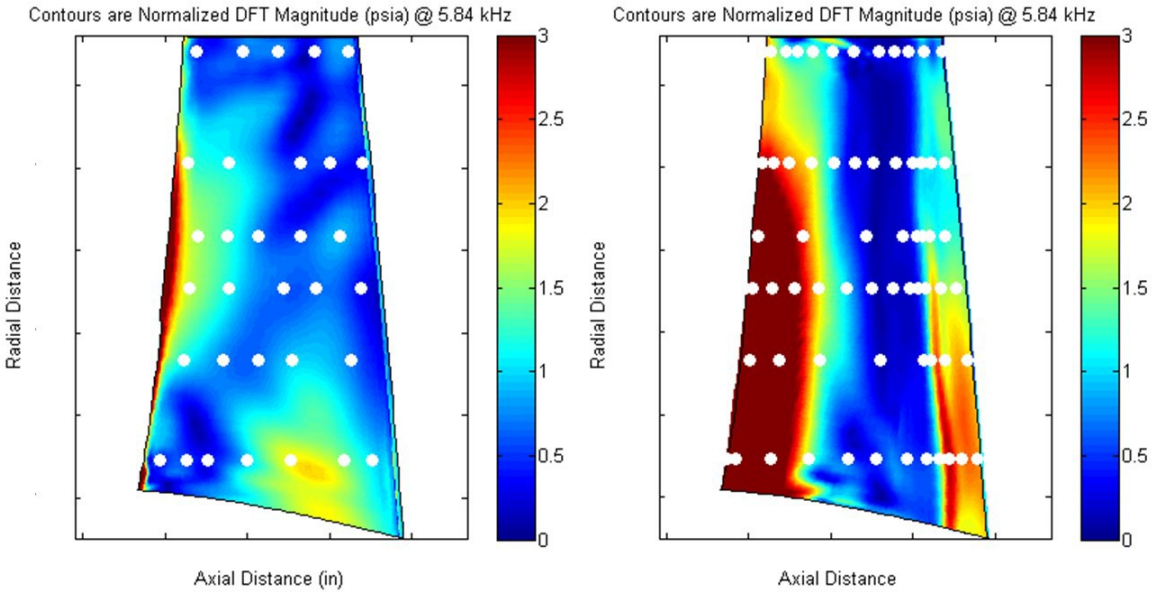

Figure 8: Normalized DFT Magnitude (psia) at 5.84 kHz for the 1B Pressure Side (left) and Suction Side (right)

The pressure sensor placement philosophy and analysis on the second vane mirrored that of the first vane and blade shown above. One minor difference, however, is that a cross-correlation analysis was also conducted on the downstream vane. Essentially, a cross-correlation analysis illustrates the number of time lags of delay that an unsteady signal is felt at each point on the vane in reference to another. The cross-correlation analysis is shown in Figure

9. Each contour represents a time bucket of approximately $8.83x10^{-4}$ milliseconds. The shapes of the contours indicate how the unsteadiness travels about the surface. This topic will be discussed in more detail in subsequent chapters. The important point here is that the sensors are sufficiently placed to capture the unsteady signal progression on the surface of the airfoil.

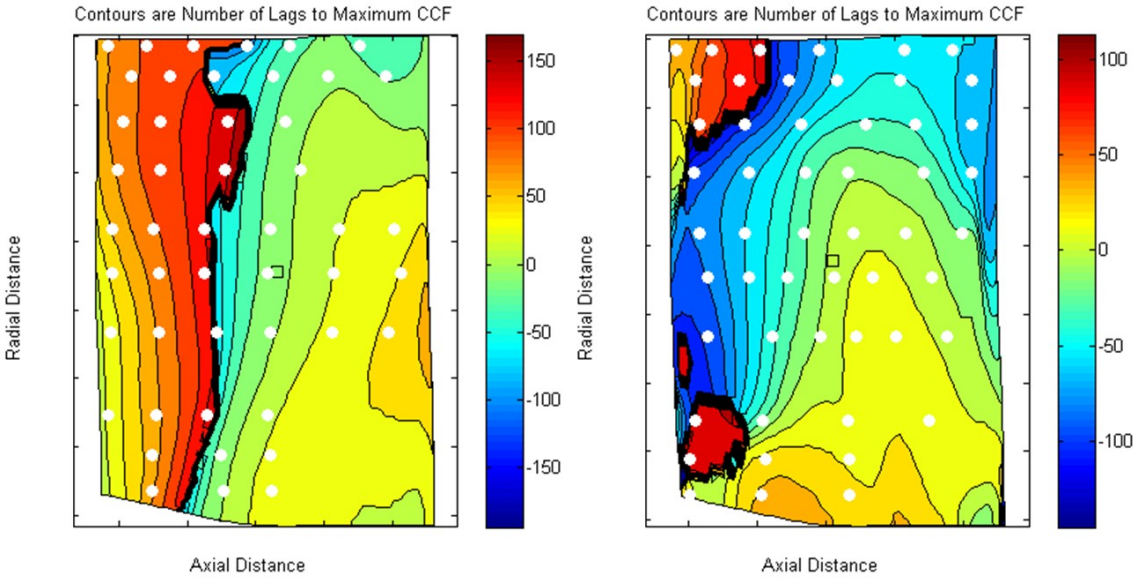

Figure 9: Cross-Correlation Analysis of the Pressure (left) and Suction (right) sides of the Second Vane

Future builds have been designed and manufactured and are ready to be tested. The goals of these builds are to reduce and/or relocate the high magnitude unsteadiness present on the first blade from interactions with the downstream vane. The architectures of the future builds include bowed, aspirated, clocked, and asymmetrically spaced downstream vanes. Combinations of the majority of these modifications are possible.

CHAPTER III

TWO-DIMENSIONAL BLADE FLOWFIELD

In this chapter, the midspan and quarter-tip sections of the HIT RT blade are investigated with numerical simulations and compared to experiment. The flow solver, Leo, was used to compute the numerical solution. The boundary conditions for the CFD simulation were informed by the experiment. The midspan and quarter-tip geometries were each run at various exit Mach and Reynolds numbers, as well as at three incidence angles. The effects of varying the incidence angle and the exit Mach number—or pressure ratio—of the blade on the pressure distribution were of particular interest and will be used during the post-test analysis of the stage-and-one-half experiments to determine whether or not the intended corrected speed and pressure ratio were achieved.

Experimental Methodology

The objective of the linear cascade experimental effort conducted at AFRL was to evaluate the performance of the HIT RT midspan and quarter-tip blade geometry for a range of exit Mach and Reynolds numbers at various angles of incidence under steady inflow conditions. The transonic cascade facility is a Turbine Engine Division asset located at Wright-Patterson Air Force Base. The test section of the facility is shown in Figure 10, and the air station flow diagram for the research cell that houses the linear cascade is shown in Figure 11. The air flows horizontally from right to left in the figure, fed from a settling chamber which is not shown, through the cascade and test section. The total contraction ratio from the settling chamber to the test section is 6.54. The flow then exits through the top of the test chamber after being turned by the airfoils. The test section—the rectangular insertion housing the airfoils—is bolted to a rotation ring, which allows for a large range of angle of attack configurations. The modular design of the test section enables an affordable method of building and installing additional airfoil packs for experimentation. The cascade is supplied with a continuous flow of air by an external air facility, which is capable of delivering over 30 lbm/s. The maximum inlet total pressure is limited by a rupture disk with a rating of 27 psig. The facility was designed for a maximum of 50 psig. The minimum exit static pressure is controlled by turbo- exhausters. When run in series, the exhausters can lower the exit pressure to approximately 3 psia. However, at higher mass flow rates, the minimum achievable exit pressure increases.

The HPT1B blade pack consists of nine airfoils at a 1.5x scale for the midspan geometry and 1.41x scale for the quarter-tip. The blades were scaled appropriately to match the flow area of the test section. The midspan and quarter-tip blade packs are shown in Figure 12. Three middle blades of the nine airfoil linear cascade are instrumented with static pressure taps in order to obtain the surface pressure distribution of the two inner most passages. It will be shown that periodicity is obtained for the middle four passages; therefore ensuring that the middle two passages are free from the effects of the bounding airfoils at the edges of the test section. Static pressure taps are also located on the endwalls up- and downstream of the cascade row. Total pressure and temperature measurements are taken upstream of the test article in the supply chamber. The downstream total and static pressure measurements are taken from a traversing rake and static pressure ports, respectively. For the midspan blade pack, the rake traverses parallel to the blade pack at 58% percent of the airfoil axial chord downstream of the trailing edge of the pack. The quarter-tip blade pack

traverse travels in a similar manner at 74% percent of one chord downstream of the trailing edges. The pressure measurements were made using NetScanner System pressure scanner, model 9116. The uncertainty of the measurements was provided by the manufacturer to be 0.05 percent of full scale, which equates to 0.0075 psid.

Exit Mach and Reynolds numbers and the angle of attack were varied to obtain the aerodynamic performance of the HPT1B. The Mach and Reynolds numbers were controlled primarily by varying the upstream and downstream pressures. Valves diverting the flow to exhaust vents and bypassing the test section were incrementally adjusted to set the upstream pressure. This also had some effect on the downstream pressure; however, the downstream pressure was primarily influenced by the turbo-exhausters.

Figure 10: Transonic Cascade Facility

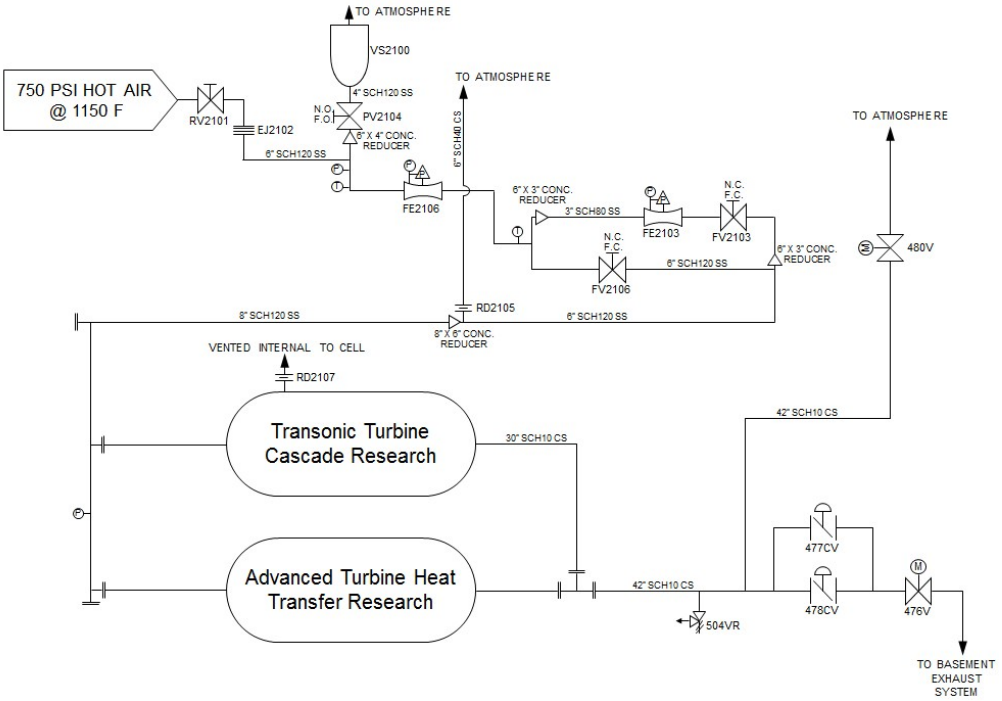

Figure 11: Research Cell Air Station Flow Diagram

Figure 12: Midspan (left) and Quarter-Tip (right) HPT1B Geometry

CFD Methodology

The CFD tool used was Leo, developed by AeroDynamic Solutions, Inc. Leo implements a Reynolds-Averaged Navier-Stokes method, using the two-equation k- Wilcox 1998 model for numerical closure. It is suitable for two- or three-dimensional geometries in steady or unsteady flow, with structured and/or unstructured meshes. One can also use Leo to perform conjugate heat transfer analysis [27], which takes into account solid conduction effects. A two-dimensional, steady, turbulent flow field was assumed to analyze the airfoils in the transonic linear cascade. The CFD domain extends one-half axial chords upstream and one axial chord downstream of the airfoil. The structured mesh contained approximately 13,500 elements. The mesh is shown in Figure 13. Leo runs a multi-block code [16][17], with the domain broken into O- and H-grids. Block 3 is the O-grid and wraps around the surface of

the airfoil, blocks 1 and 2 span the suction and pressure sides of the flow path, respectively, and blocks 4 and 5 cover the leading and trailing edge regions, respectively. Blocks 1, 2, 4, and 5 are H-grids; and there is point to point matching between blocks.

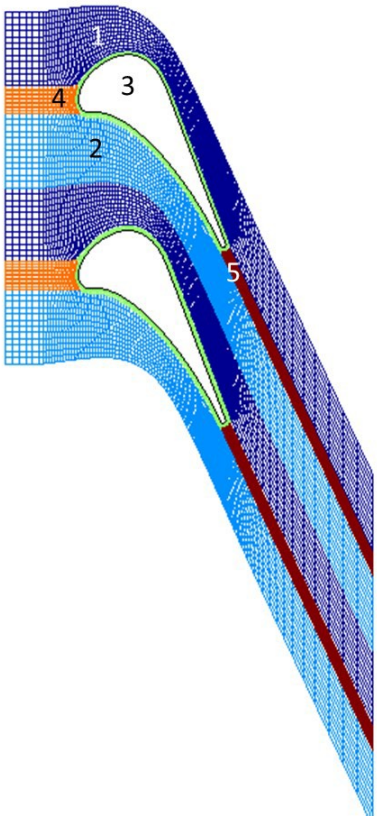

Figure 13: Leo five-block airfoil mesh used in the numerical analysis

A grid independence study was conducted prior to running the CFD comparison cases. Four meshes were created and the code was run for each. The grid sizes are listed in Table 1 and the resulting pressure distributions are shown in Figure 14. All cases were run to 4,000 iterations, which provided sufficient convergence of the density, momentum, and energy residuals to 10^{-5} or less. Increasing the number of elements showed very little change in the pressure distributions. The only area that was slightly sensitive to the grid size was the shock on the suction side. Grid 3 was chosen for use in the CFD simulations because there was an insignificant change in the pressure distribution when increasing the number of elements further.

Table 1: Grid sizes of meshes used in grid independence study.

Grid	Elements
1	5,330
2	9,010
3	13,522
4	19,090

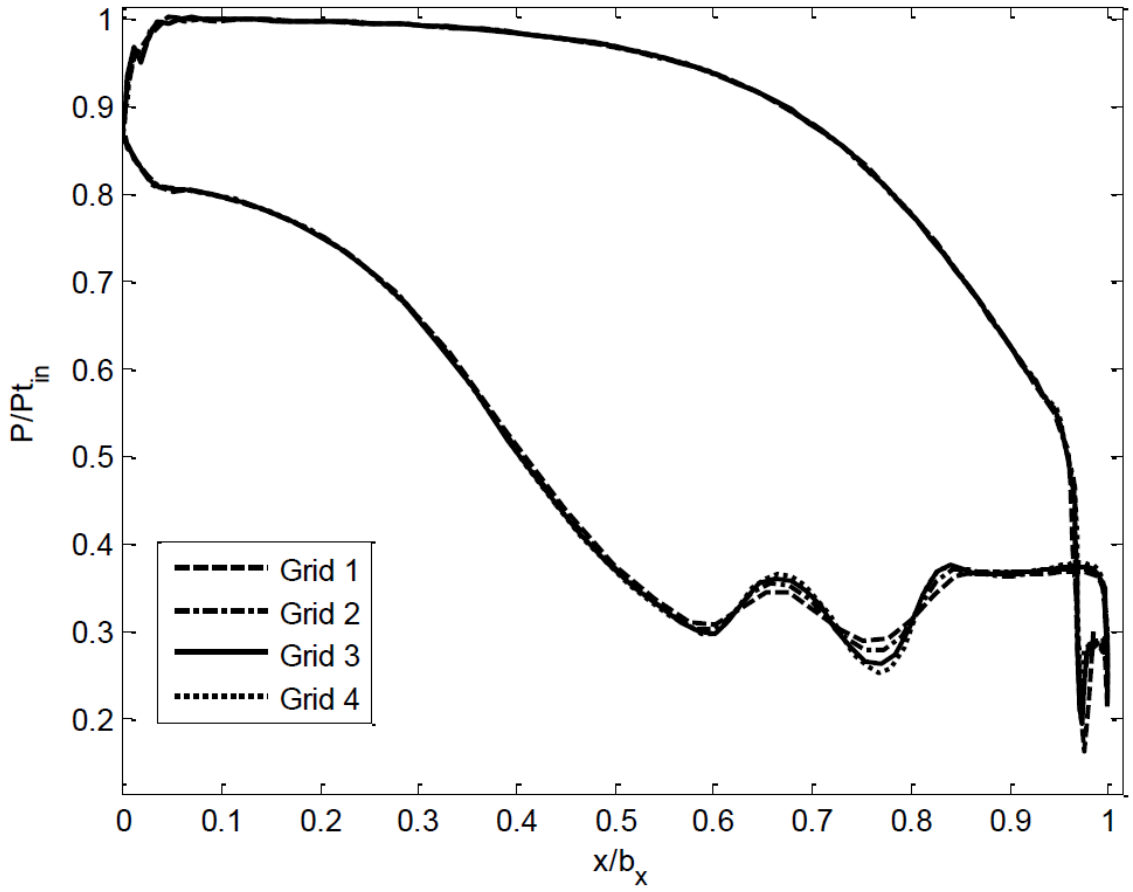

Figure 14: Pressure distributions of grid independence study

Midspan Geometry Experimental and CFD Cases

The exit Reynolds number was varied from $0.5x10^6$ to $1.5x10^6$ for an exit Mach number of 1.30. Nominal exit Mach numbers of 1.15, 1.30, and 1.45 were run at an exit Reynolds number of $1.3x10^6$. The experimental cases that will be compared to CFD are listed in Table 2. The inlet Mach number of 0.31 remained the same for all cases. Each case listed below includes incidence angles at design, as well as +/- five degrees off- design. The exception is Case 5, in which there is no experimental data for plus five degree incidence angle. The experimental flow path measurements are also listed in Table 2. The cases are graphically depicted in groupings in Figure 15, which plots the Mach and Reynolds number for each test.

Table 2: Experimental and Numerical Simulation Cases for the HPT1B Midspan Geometry

					Experiment		CFD	
	$\Delta\alpha$	M_{ex}	Re_{ex}	$T_{t,in}$	$P_{t,in}$ (psia)	$P_{s,ex}$ (psia)	$P_{t,in}$ (psia)	$P_{s,ex}$ (psia)
1	-5	1.29	1.29	541	24.4	8.87	36.6	13.3
1	0	1.30	1.29	545	24.6	8.92	36.9	13.4
1	5	1.30	1.29	542	24.4	8.81	36.6	13.2
2	-5	1.30	0.77	538	14.5	5.20	21.7	7.80
2	0	1.29	0.73	547	14.1	5.14	21.1	7.71
2	5	1.29	0.79	543	15.1	5.53	22.6	8.29
3	-5	1.30	1.55	539	29.1	10.54	43.6	15.8
3	0	1.30	1.48	550	28.6	10.35	42.9	15.5
3	5	1.29	1.54	540	29.0	10.57	43.6	15.9
4	-5	1.16	1.30	539	24.5	10.70	36.7	16.0
4	0	1.14	1.27	547	24.4	10.84	36.7	16.3
4	5	1.14	1.26	537	23.7	10.60	35.5	15.9
5	-5	1.46	1.30	540	25.2	7.29	37.7	10.9
5	0	1.45	1.27	550	25.1	7.40	37.7	11.1
6	-5	1.30	0.60	538	11.2	4.05	16.8	6.08
6	0	1.29	0.49	545	9.4	3.47	14.2	5.20
6	5	1.29	0.58	544	11.1	4.09	16.7	6.14

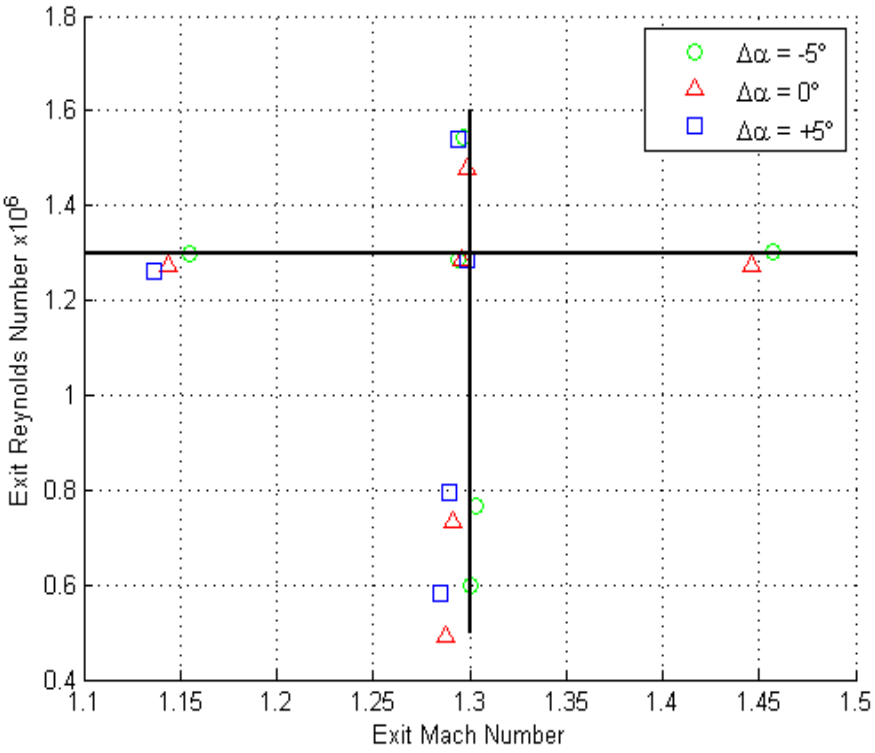

Figure 15: Exit Mach and Reynolds number groupings of the midspan blade pack

For each experimental case, the CFD analysis matched exit Mach and Reynolds numbers. The HPT1B midspan blade pack tested in the cascade was at 1.5x scale. In order to match the Reynolds number, the airfoils were at full-scale, the temperature between experiment and CFD was kept constant, and the inlet total pressure was increased by 150% of the experiment. The exit static pressure was also increased by the same factor in order to retain the Mach number, which is driven by the ratio of the aforementioned pressures. The pressure boundary conditions used for the corresponding experimental cases are also listed in Table 2.

When operating a linear cascade, a very important determination to make prior to investigating the airfoil pressure distributions concerns periodicity. One must ensure the passages with instrumentation are free from any effects due to bounding walls of the airfoil pack. The effects are caused by the walls of the cascade blocking the air flow over the pressure and suction surfaces of the top and bottom airfoils in the blade pack, respectively. The pressure losses of the wakes can be calculated by subtracting the downstream total pressure from the upstream total pressure and dividing that quantity by the latter. Examining the losses downstream of the airfoils reveals where periodicity is present, thereby finding the passages that are free from the bounding effects. The downstream pressure losses from a typical cascade test are shown in Figure 16, where the entire traverse distance is shown. The peaks in this plot represent higher losses and correspond to trailing-edge wakes from the airfoils, while passages are represented by troughs. The middle three blades bound the middle passages, and are represented by the peaks located at 6.5, 8.9, and 11.3 inches. It can be easily seen that the middle two passages, passages 4 and 5, whose airfoils are instrumented, are periodic. In

fact, the surrounding passages, passages 3 and 6, are also periodic. Therefore, the instrumented passages are decisively free from cascade bounding effects.

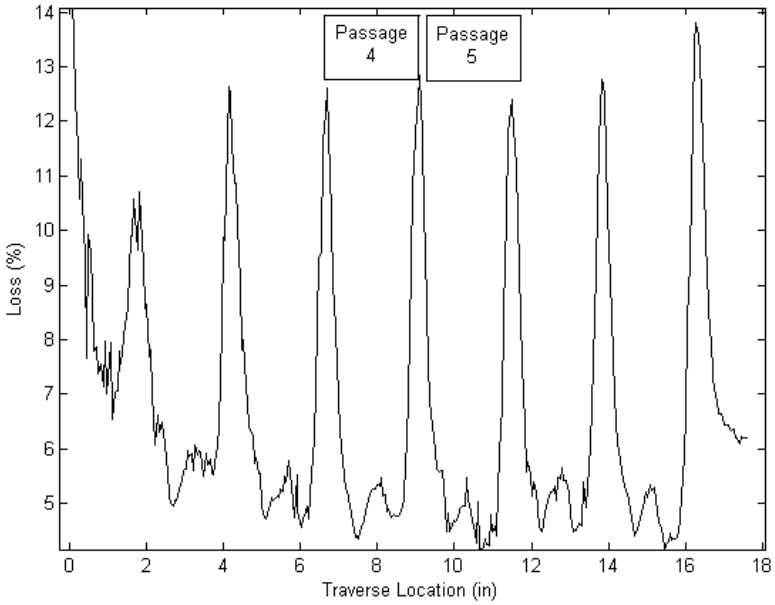

Figure 16: Wake losses of a typical cascade test measured by a traversing probe 58% of one chord length downstream of the trailing edge

The first case of the HPT1B midspan blade pack experimentally tested was the condition which had a Mach number of 1.30 and Reynolds number of 1.286×10^6. These conditions were run at the design angle of attack, as well as +/- 5 degrees incidence angle. The experimental and CFD pressure distributions for Case 1 are plotted in Figure 17 and show extremely good agreement across the entire airfoil. Error bars are included for the experimental data and represent one standard deviation above and below the mean for each pressure sensor. The standard deviations are so small that in many cases the error bars are difficult to see. This indicates that the flow is steady, which confirms that the assumption to run a time-independent CFD analysis was correct. The shock location is well captured by the analysis. Changing the incidence angle did not affect the ability of the CFD analysis to predict the loading. The experimental data and CFD predictions match considerably well for -5, 0, and +5 degrees of incidence. The loading from the leading edge halfway down the suction side was very slightly under predicted; however, that is the case for all incidence angles. This may be due to the experimental incidence angle deviating slightly from the intended setting during a given run. Increasing and decreasing the angle of attack increased and decreased, respectively, the loading measured on the airfoil on the suction side, from the leading edge to approximately 45 percent chord. The CFD results show a very similar trend.

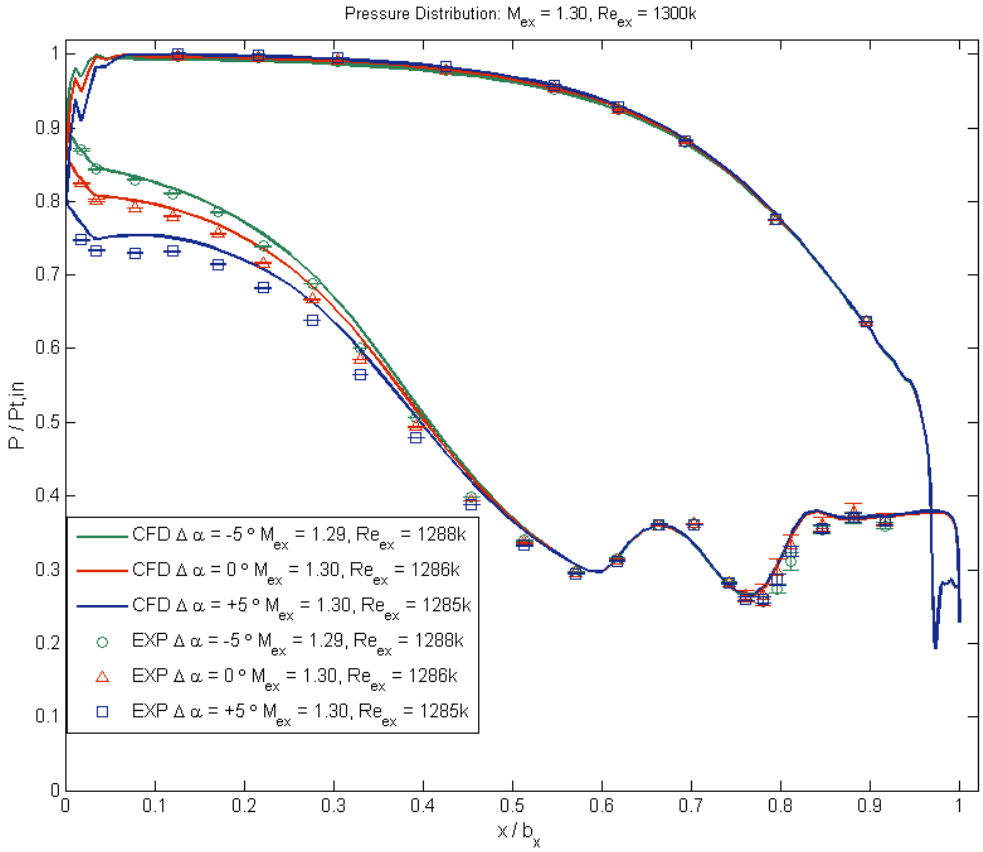

Figure 17: Pressure distribution for Case 1, whose nominal exit Mach and Reynolds numbers were 1.30 and 1.30×10^6, respectively, at three incidence angles

The pressure distributions of cases 2 through 6 are plotted in Figure 18 through Figure 22. For each case and angle of attack, the experimental and CFD pressure distributions show very close agreement. Expectedly, the exit Mach and Reynolds number sweep cases exhibit the same behavior as case 1 regarding the angle of attack and loading on the leading edge half of the suction side. Increasing the angle of attack produces an increased loading, and decreasing the angle of attack reduces the loading.

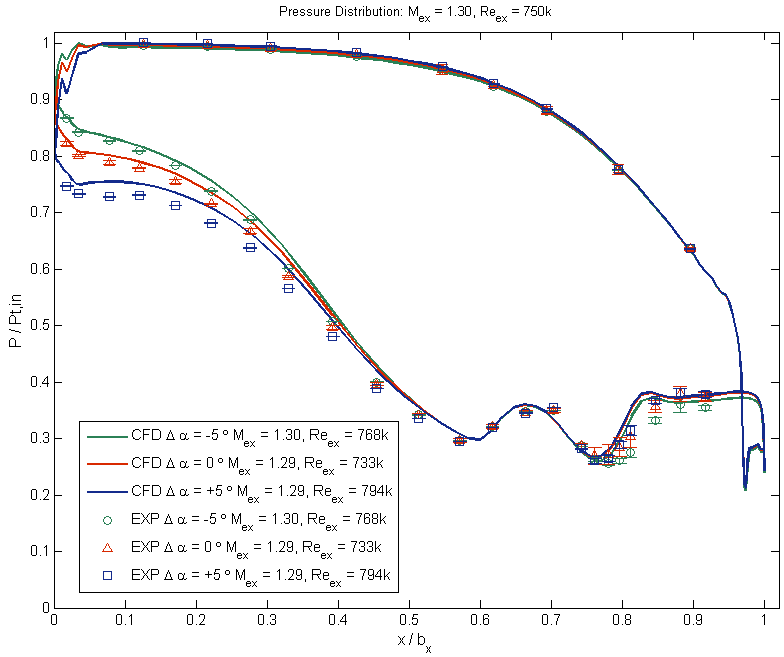

Figure 18: Pressure distribution for Case 2, whose nominal exit Mach and Reynolds numbers were 1.30 and 0.75x10^6, respectively, at three incidence angles

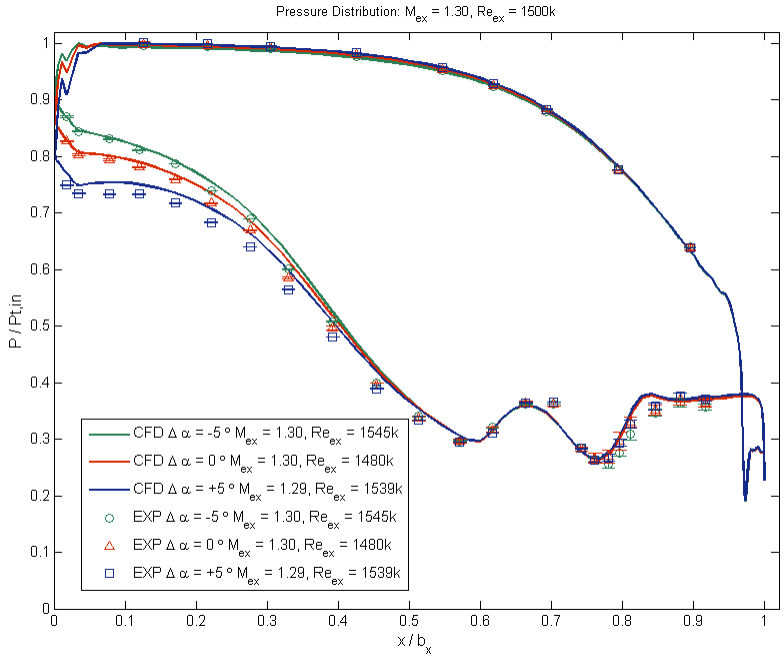

Figure 19: Pressure distribution for Case 3, whose nominal exit Mach and Reynolds numbers were 1.30 and 1.50x10^6, respectively, at three incidence angles

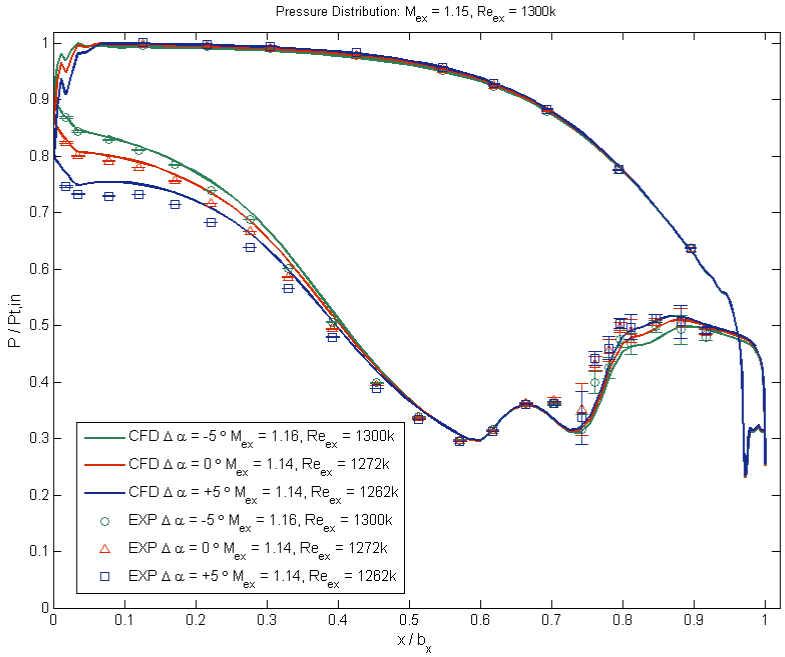

Figure 20: Pressure distribution for Case 4, whose nominal exit Mach and Reynolds numbers were 1.15 and 1.30x10^6, respectively, at three incidence angles

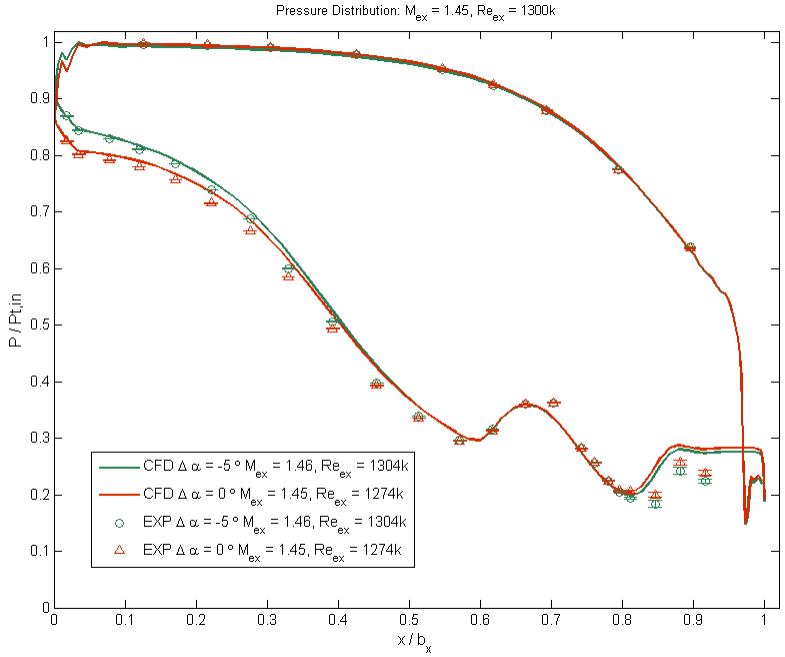

Figure 21: Pressure distribution for Case 5, whose nominal exit Mach and Reynolds numbers were 1.45 and 1.30x10^6, respectively, at two incidence angles

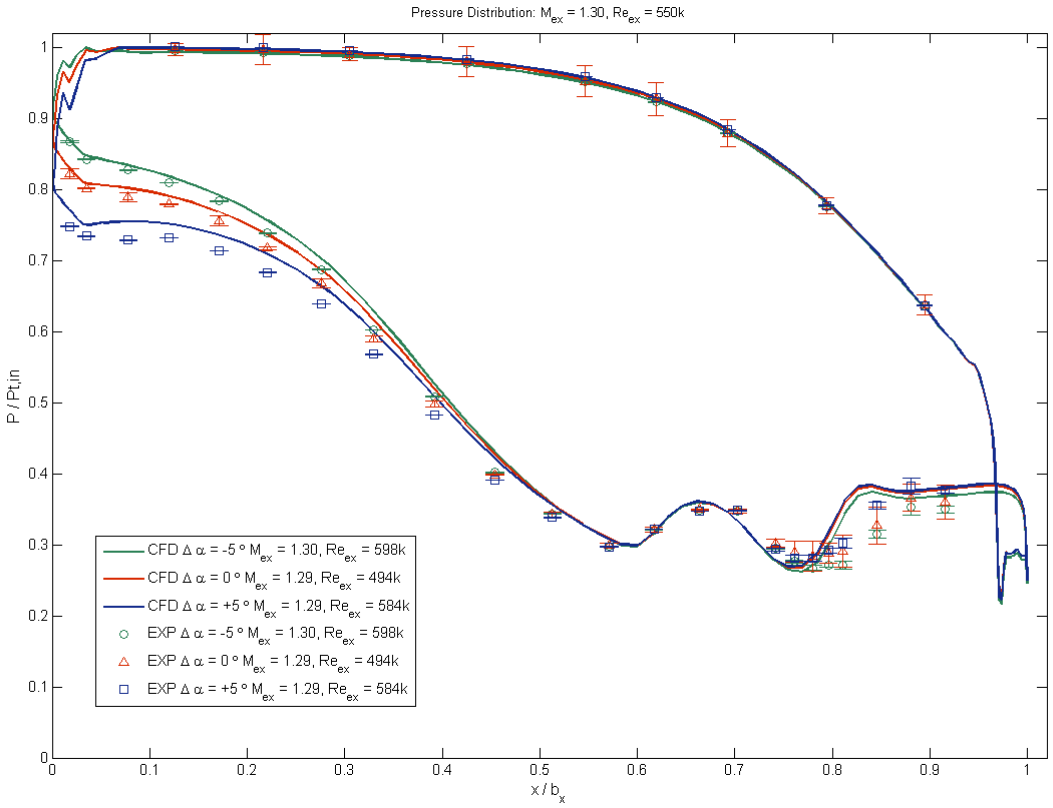

Figure 22: Pressure distribution for Case 6, whose nominal exit Mach and Reynolds numbers were 1.30 and 0.55×10^6, respectively, at three incidence angles

The data with an exit Reynolds number of 1.30×10^6 at design angle of attack with varying exit Mach numbers is grouped and plotted in Figure 23. As the Mach number deviates from design, the shock structure on the suction side is affected. Also, for lower exit Mach numbers, a greater adverse pressure gradient is encountered on the aft suction side of the airfoil. The pressure distribution is not affected at any other location on the airfoil by varying the exit Mach number. In a similar plot, variations of exit Reynolds number at an exit Mach number of 1.30 at design angle of attack are shown in Figure 24. Both the experimental and CFD pressure distributions remain unaffected by varying the exit Reynolds number. This is a desired result, which indicates that the airfoil is designed such that the boundary layer remains well-behaved over a large range of off-design conditions.

Comparing all cases reveals a telling observation. The error bars are larger for all cases with exit Mach numbers near unity, meaning that there was a larger distribution of pressure measurements recorded in the experiment. This indicates that there is inherent unsteadiness in the shock motion in the transonic regime and suggests engineers should avoid designing airfoils to exit Mach numbers near one.

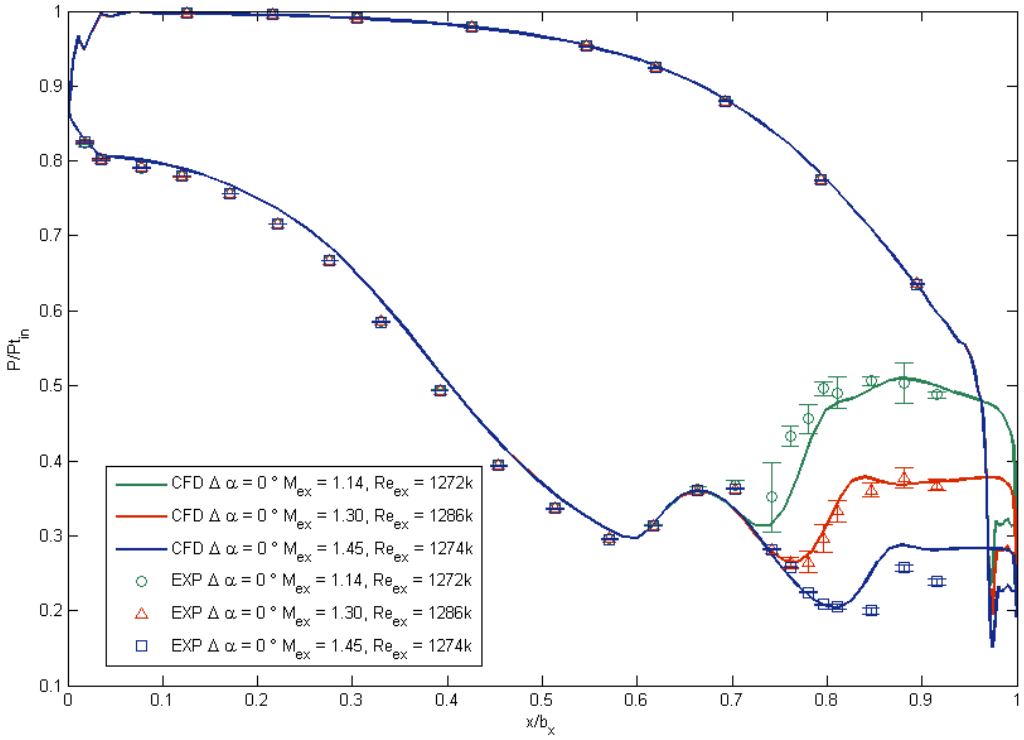

Figure 23: Pressure distributions of exit Mach numbers ranging from 1.15 to 1.45, at 1.30x10^6 exit Reynolds number and design incidence angle

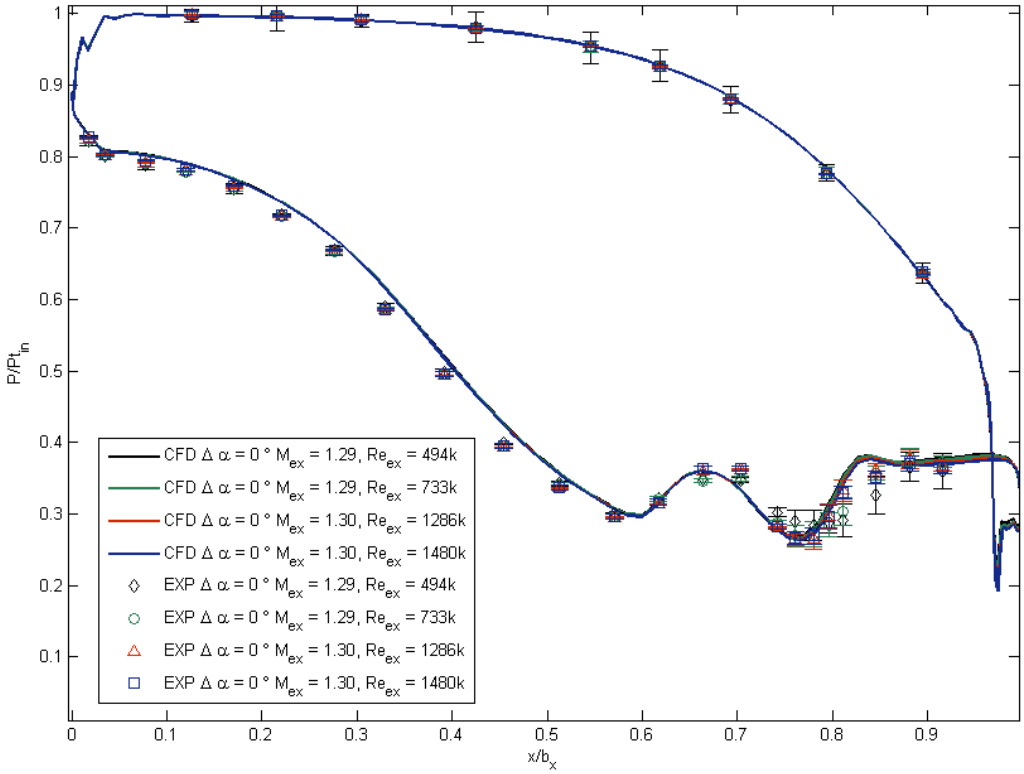

Figure 24: Pressure distributions of exit Reynolds numbers ranging from 0.55x10^6 to 1.50x10^6, at 1.30 exit Mach number and design incidence angle

The traversing rake measured the total pressure exiting the blade row at 58% of one chord length downstream of the trailing edge. The pressure loss in the wake for Case 1 is compared to the CFD pressure losses at the same axial location in Figure 25. Prior to the comparison, however, a modification was made to the raw measured pressure losses in order to correctly make the assessment. This is necessary because the relatively blunt leading edge of the traversing probe in the supersonic flow creates a bow shock, which locally can be assumed to behave like a normal shock. The total pressure measured by the probe is less than the actual total pressure of the flow at that location because there are additional pressure losses associated with the shock. The total pressure measured by the probe and the static pressure upstream of the shock measured by the endwall pressure taps were used with the normal shock relations [35] to calculate the total pressure upstream of the shock, which is the appropriate value to compare to the CFD results. The troughs in the figure are the two middle passages, passages 4 and 5. The loss is over predicted in the trailing edge wake, but under predicted in the passages by as much as 2 percent. It is also apparent that a change in the angle of attack does not affect the wake profile. This correlates to the pressure distribution having an effect only on the leading edge half of the suction side, as seen in the distribution plots presented above. The discrepancy could be attributed to several factors, including: the CFD results may not be accurate due to inadequate viscous modeling, the probe in the facility may not be oriented exactly parallel to the exiting flow, and/or the probe may be deflecting backwards slightly in the supersonic exit flow. Ongoing efforts continue to improve the understanding of the discrepancy between the computational and experimental loss profiles.

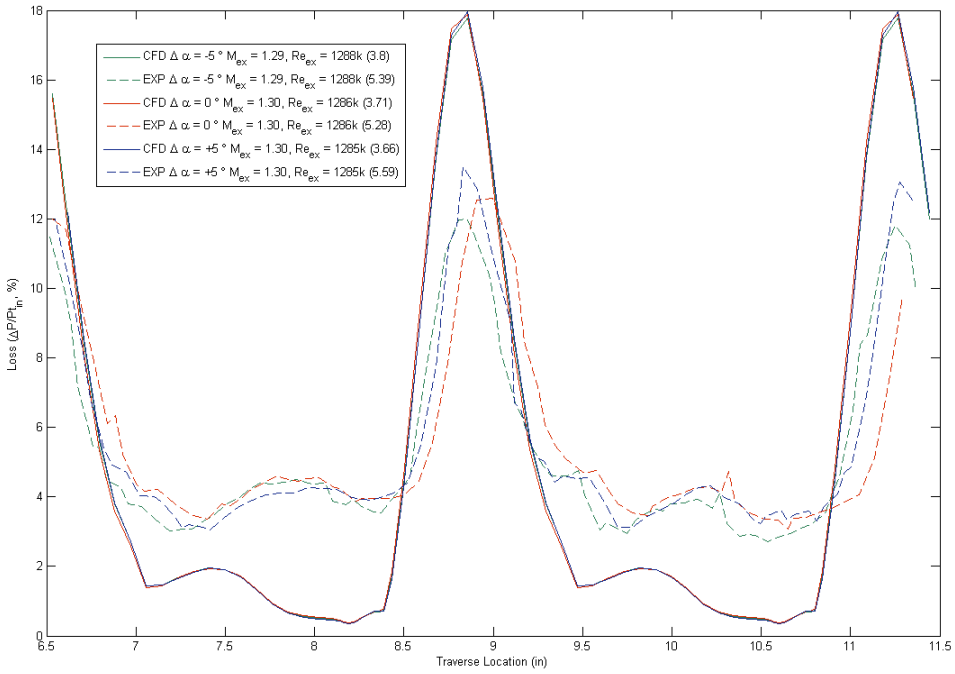

Figure 25: Loss profile of Case 1, with exit Mach and Reynolds numbers of 1.30 and 1.30×10^6, respectively, at three incidence angles

Quarter-Tip Geometry Experimental and CFD Cases

The exit Reynolds number for the quarter-tip geometry was varied from $0.8x10^6$ to $1.25x10^6$ for an exit Mach number of 1.45. Exit Mach numbers of 1.15, 1.30, 1.45, and 1.60 were run at an exit Reynolds number of $1.0x10^6$. Experimental cases at these conditions were compared to CFD results and are listed in Table 3. For each exit Mach and Reynolds number condition, the quarter-tip pack was run at the design angle of attack and +/- five degrees of incidence. The inlet Mach number for all cases was 0.25. The cases are plotted graphically—Mach number versus Reynolds number--in Figure 26.

Table 3: Experimental and Numerical Simulation Cases for the HPT1B Quarter-Tip Geometry

					Experiment		CFD	
Case	$\Delta\alpha$ (deg)		Re_{ex} ($x10^6$)	$T_{t,in}$	$P_{t,in}$ (psia)	$P_{s,ex}$ (psia)	$P_{t,in}$ (psia)	$P_{s,ex}$ (psia)
7	-5	1.45	0.99	540	22.7	6.66	32.0	9.38
7	0	1.45	1.00	531	22.4	6.59	31.6	9.28
7	5	1.45	1.00	531	22.4	6.51	31.5	9.18
8	-5	1.15	0.99	533	21.9	9.63	30.9	13.56
8	0	1.15	1.02	529	22.4	9.77	31.5	13.77
8	5	1.15	0.99	522	21.4	9.39	30.1	13.23
9	-5	1.30	0.99	536	22.1	7.95	31.2	11.2
9	0	1.30	1.02	530	22.5	8.07	31.6	11.4
9	5	1.30	1.00	525	21.6	7.79	30.4	11.0
10	-5	1.60	0.99	542	23.8	5.58	33.5	7.86
10	0	1.60	0.97	531	22.5	5.28	31.7	7.44
10	5	1.60	0.99	525	22.8	5.32	32.1	7.49
11	-5	1.45	1.25	534	28.4	8.29	40.0	11.7
11	0	1.43	1.45	526	32.0	9.72	45.1	13.7
11	5	1.45	1.28	528	28.7	8.34	40.4	11.8
12	-5	1.45	0.80	531	17.9	5.24	25.3	7.39
12	0	1.43	0.81	533	18.2	5.44	25.6	7.67
12	5	1.45	0.80	530	17.8	5.20	25.1	7.33

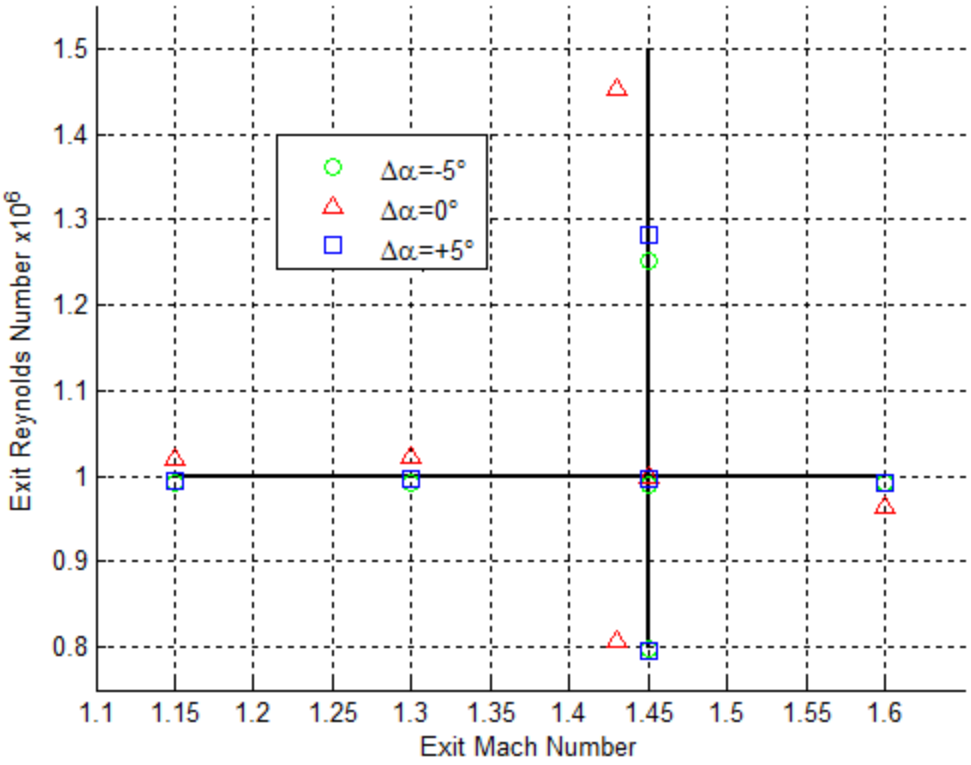

Figure 26: Exit Mach and Reynolds number groupings of the quarter-tip blade

Similar to the midspan blade pack, each experimental case run was compared against CFD analysis. The CFD analysis matched the exit Mach and Reynolds numbers. The scale of the HPT1B quarter-tip blade packed tested in the linear cascade was 1.41. The airfoils used in the numerical analysis were at full-scale. Therefore, in order to match the Reynolds number, the inlet total pressures of the CFD cases were increased by 141% of the experiment. The exit static pressures were also increased by the same factor in order to retain the exit Mach number. The pressures used for the CFD cases are also listed in Table 3.

The pressure loss profile of the quarter-tip blade pack for case 7 is shown in Figure 27. The loss percentage is calculated in the same manner as for the midspan blade pack, in which the downstream total pressure is subtracted from the upstream total pressure, and then the difference is divided by the latter. Once again, the peaks in this plot represent higher losses and correspond to the trailing-edge wakes. The troughs of low losses are flow from the passages between the airfoils. The quarter-tip pack is clearly periodic for passages 4 and 5. Therefore, the instrumented passages are free from the effects due to the walls bounding the linear cascade.

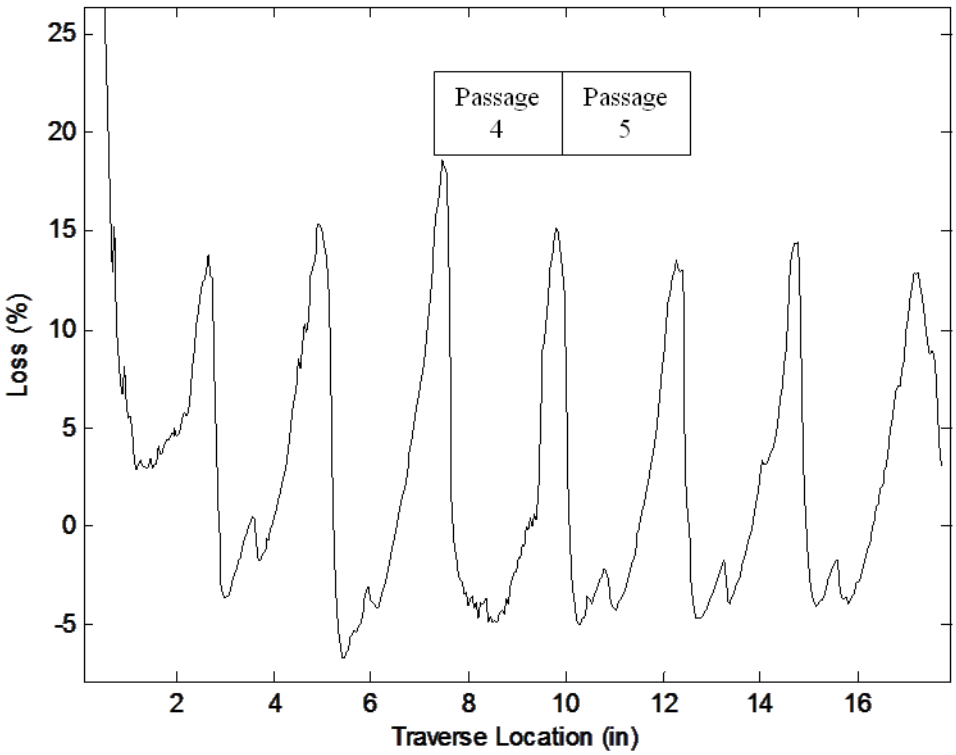

Figure 27: Wake losses of a typical cascade test measured by a traversing probe 74% of one chord length downstream of the trailing edge

Case 7, the first case for the quarter-tip blade pack, was nominally set at exit Mach and Reynolds numbers of 1.45 and $1.0x10^6$, respectively. The experimental pressure loading is shown in Figure 28 and compared to the numerical predictions. Off-design incidence angles of +/- 5 degrees are also included. The CFD predictions of the pressure distribution match the experimental data very well. Each experimental data point has error bars that represent one standard deviation above and below the mean pressure during the time period of data collection. For most of the data points, the error bars are difficult to detect, indicating extremely small variations in the pressures at those locations during data collection. Small variations are the desired result because the numerical solution was treated as a steady-state problem. The loading on the suction side forward of the first shock is the only area affected by the change of incidence angle. The loading increases and decreases for larger and smaller angles of attack, respectively. For this particular case, the CFD predictions differ from the experimental data downstream of the second shock for off-design incidence angles. The experimental data shows higher loading than the levels that the CFD predicts for the +5 degrees incidence case. The opposite is true for the -5 degrees incidence case. While the experimental data and CFD predictions match for the design incidence case, the experimental data experienced a relatively high amount of unsteadiness in the same location.

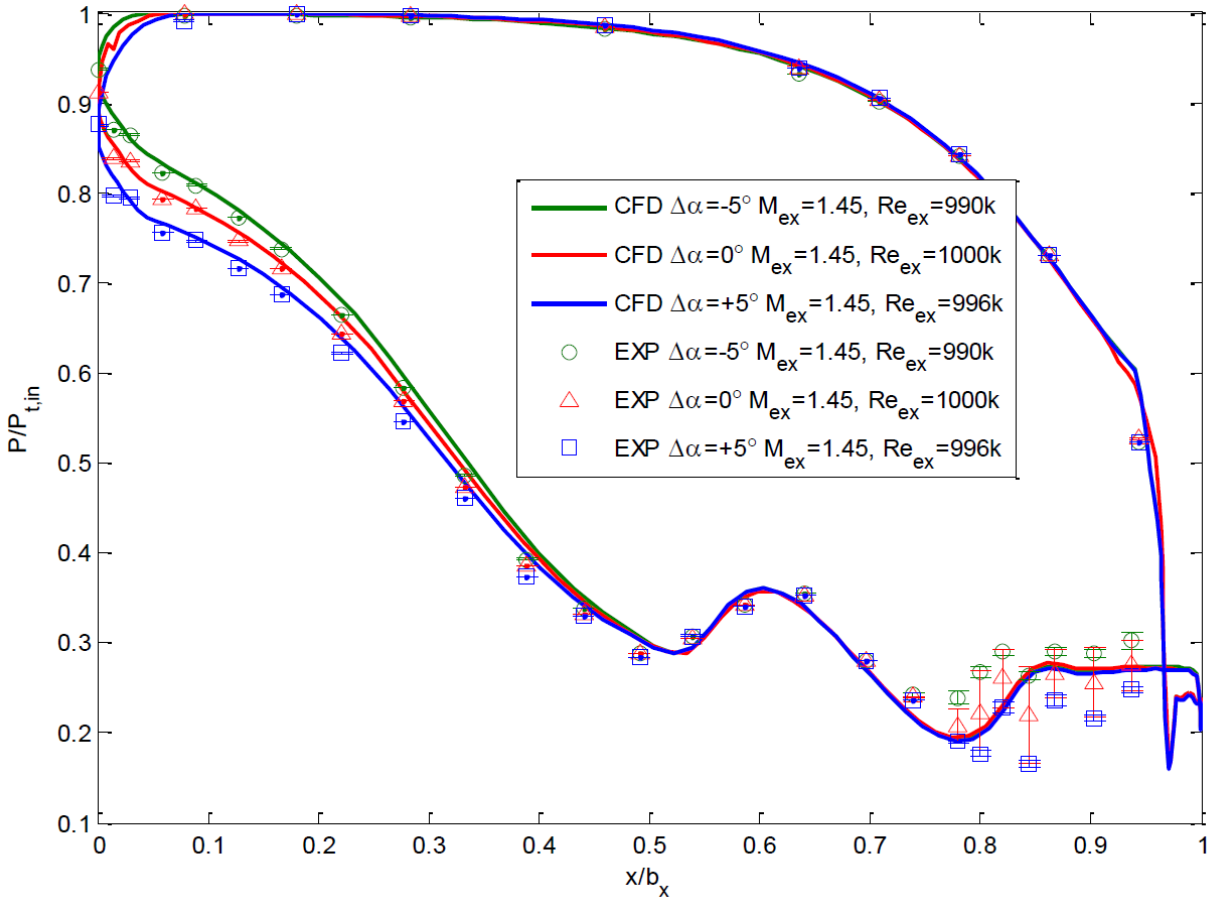

Figure 28: Pressure distribution for Case 7, whose nominal exit Mach and Reynolds numbers were 1.45 and 1.0x10^6, respectively, at three incidence angles

Pressure distributions for the remaining cases of the quarter-tip geometry are shown in Figure 29 through Figure 33. As expected, all cases exhibit an increase in loading when the angle of attack is increased, and a decrease in loading when the angle of attack is decreased. Each case shows very good agreement between the experimental data and simulations. Cases 8 and 10, shown in Figure 29 and Figure 31, respectively, have good agreement even in the area downstream of the second shock on the suction side. However, many of the other cases do not match with as much accuracy. The behavior could be explained by not measuring the experimental exit Mach number accurately. Case 11, shown in Figure 32, has nominal exit Mach numbers of 1.45. The on-design incidence angle case, however, was run at a Mach number of 1.43. This small difference in exit Mach number between the on- and off-design cases is very noticeable in the simulated pressure distributions. This illustrates that what appears to be a small difference in exit Mach number can create a fairly noticeable offset in the pressure distribution. For each case, the CFD simulations were run with matching boundary conditions with respect to the corresponding experimental case. Therefore, it is expected that the CFD and experimental results would line up. However, it is possible that small errors in measuring the flow variables used to calculate the experimental exit Mach number could result in the CFD being run at slightly differently conditions.

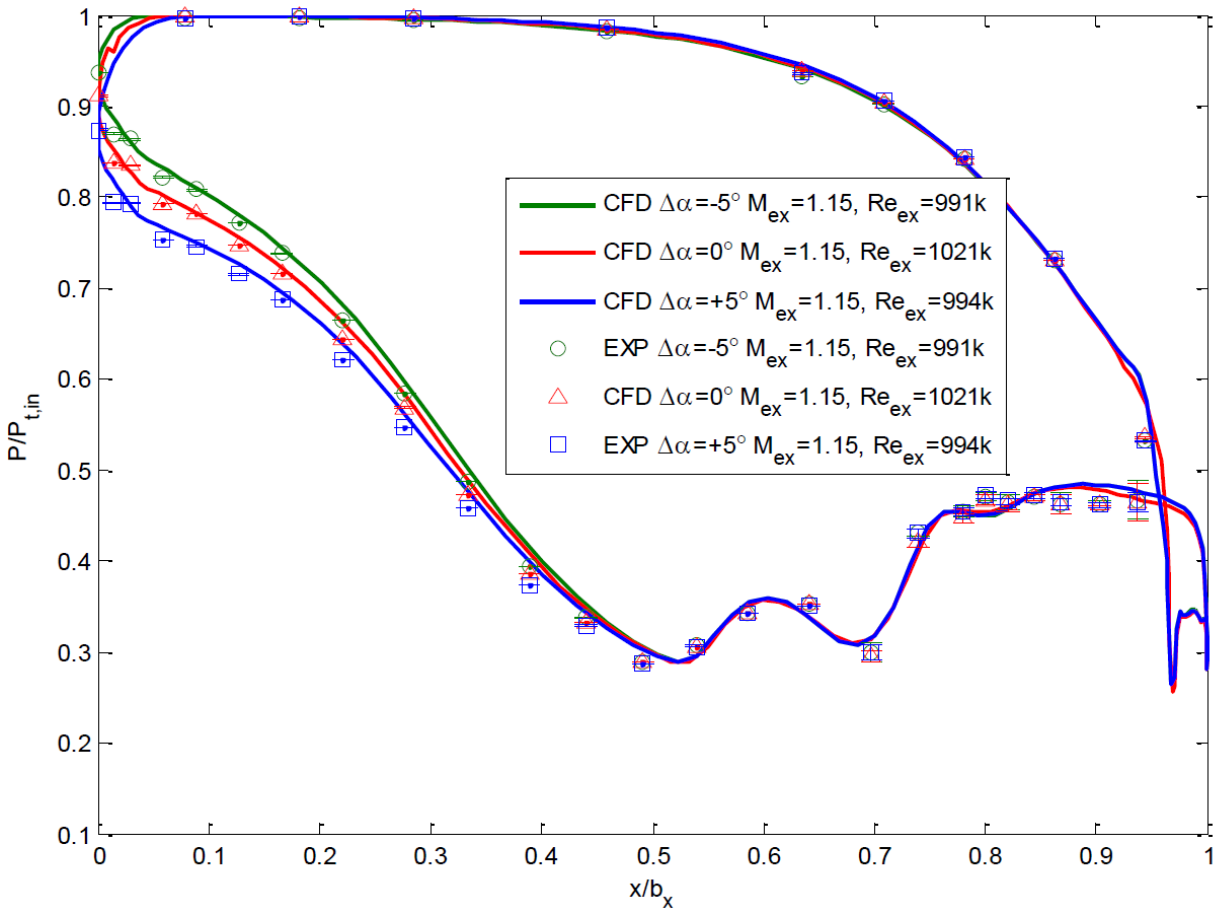

Figure 29: Pressure distribution for Case 8, whose nominal exit Mach and Reynolds numbers were 1.15 and 1.0×10^6, respectively, at three incidence angles

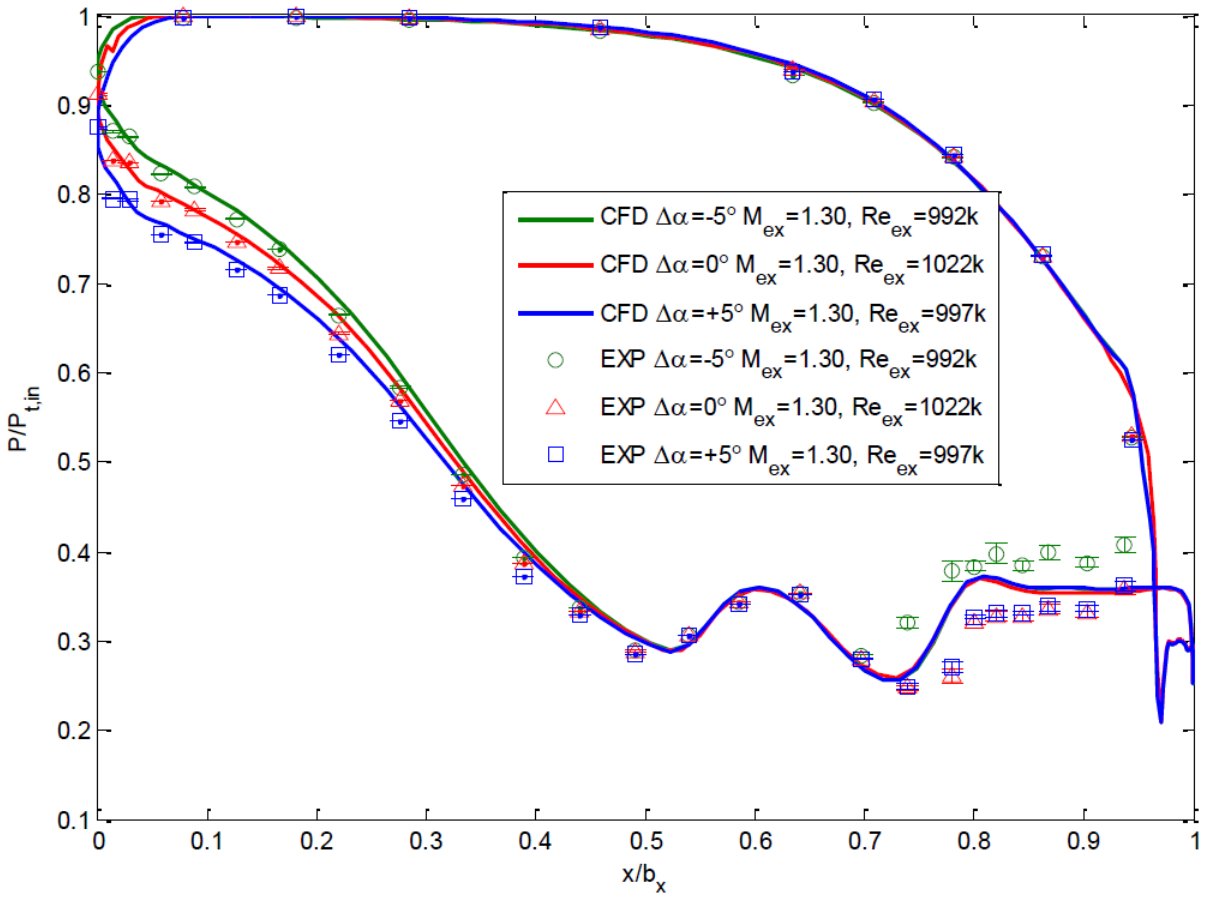

Figure 30: Pressure distribution for Case 9, whose nominal exit Mach and Reynolds numbers were 1.30 and 1.0×10^6, respectively, at three incidence angles

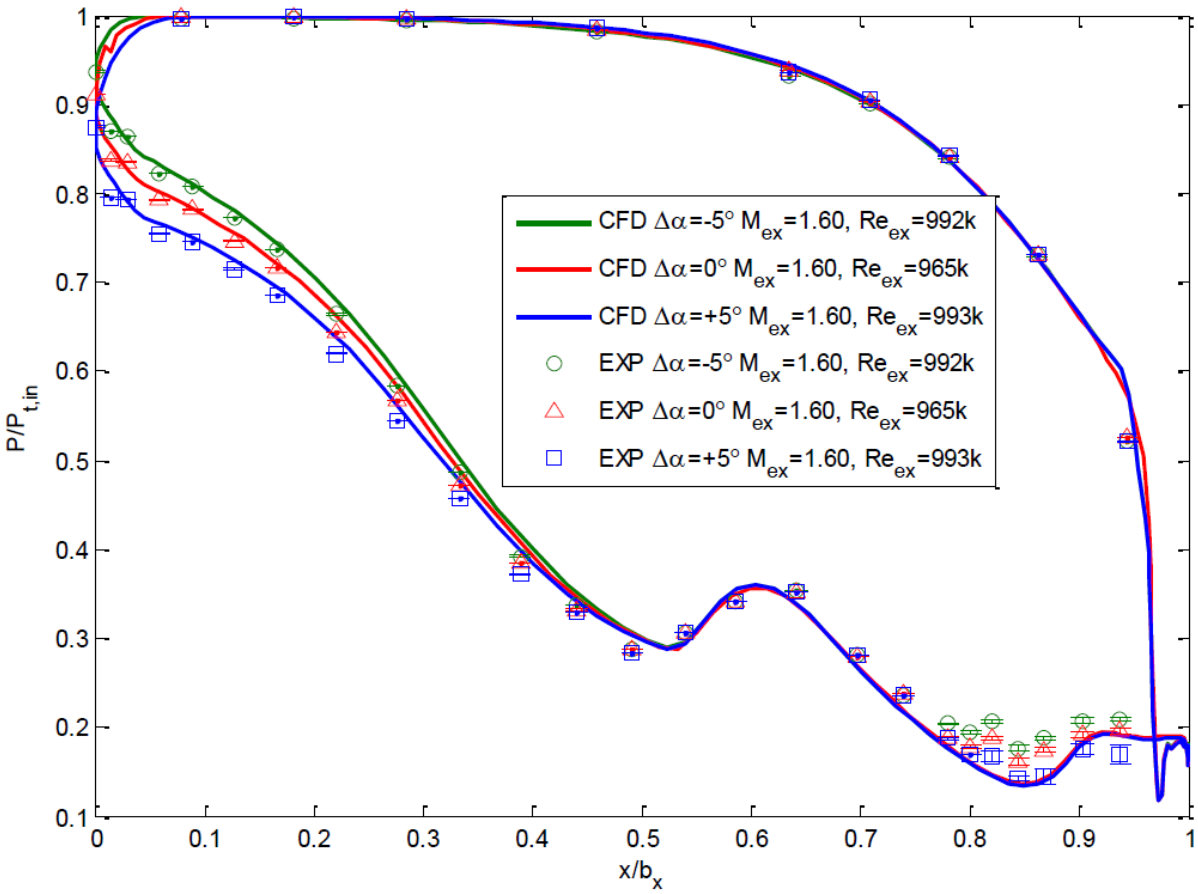

Figure 31: Pressure distribution for Case 10, whose nominal exit Mach and Reynolds numbers were 1.60 and 1.0×10^6, respectively, at three incidence angles

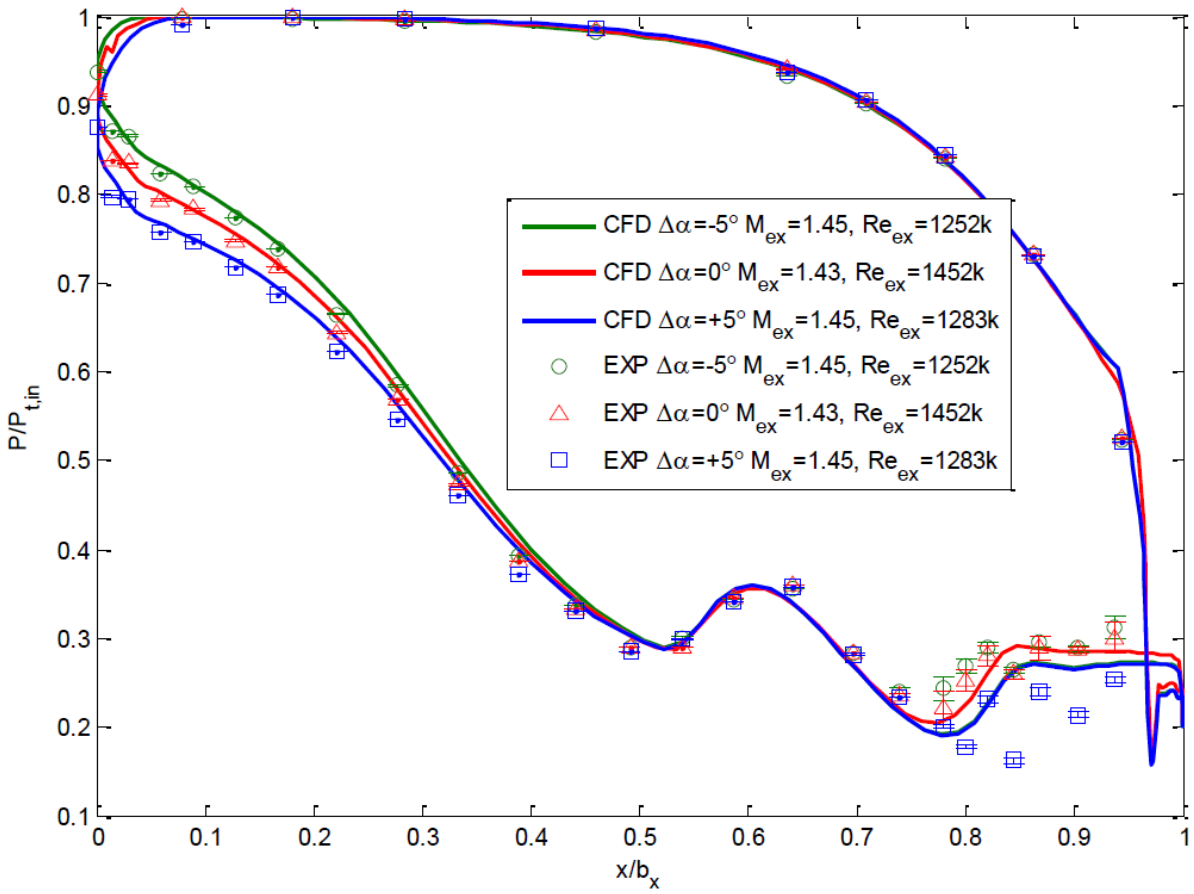

Figure 32: Pressure distribution for Case 11, whose nominal exit Mach and Reynolds numbers were 1.45 and 1.25×10^6, respectively, at three incidence angles

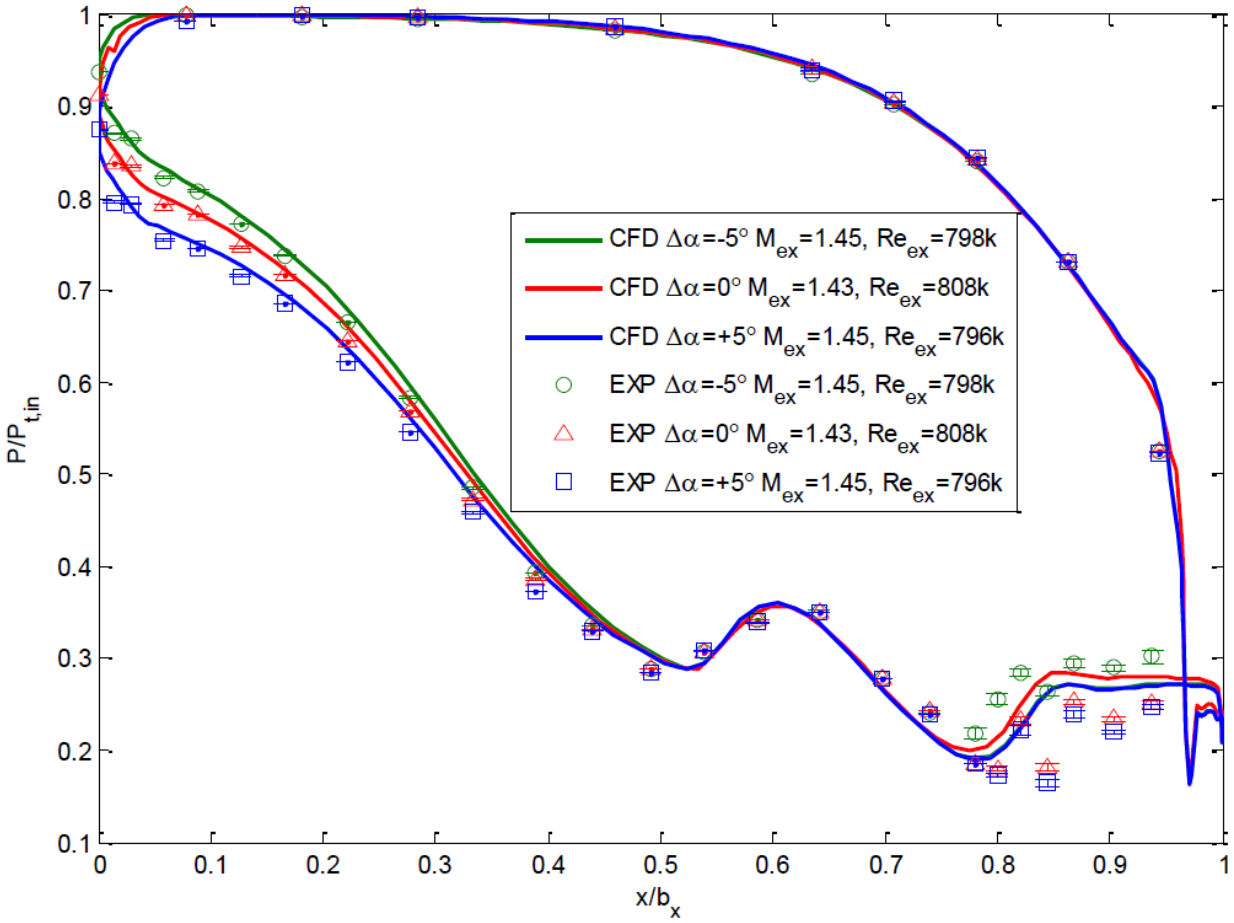

Figure 33: Pressure distribution for Case 12, whose nominal exit Mach and Reynolds numbers were 1.45 and 0.80x10^6, respectively, at three incidence angles

The experimental runs and CFD predictions for design angle of attack and exit Reynolds number of 1.0x10^6 were grouped and plotted in Figure 34. This figure illustrates the effect of varying the exit Mach number while holding the Reynolds number and incidence angle constant. The pressure loading is only affected downstream of the shock and decreases as the exit Mach number is reduced. In a similar plot, Figure 35 contains the experimental runs and CFD predictions for the design angle of attack and an exit Mach number of 1.45. This figure shows that varying only the exit Reynolds number has essentially no effect on the pressure distribution. A small variance in the loading on the suction side downstream of the shock is observed, however, that can be explained by the slight variation of the exit Mach numbers, two of which are at 1.43 rather than 1.45.

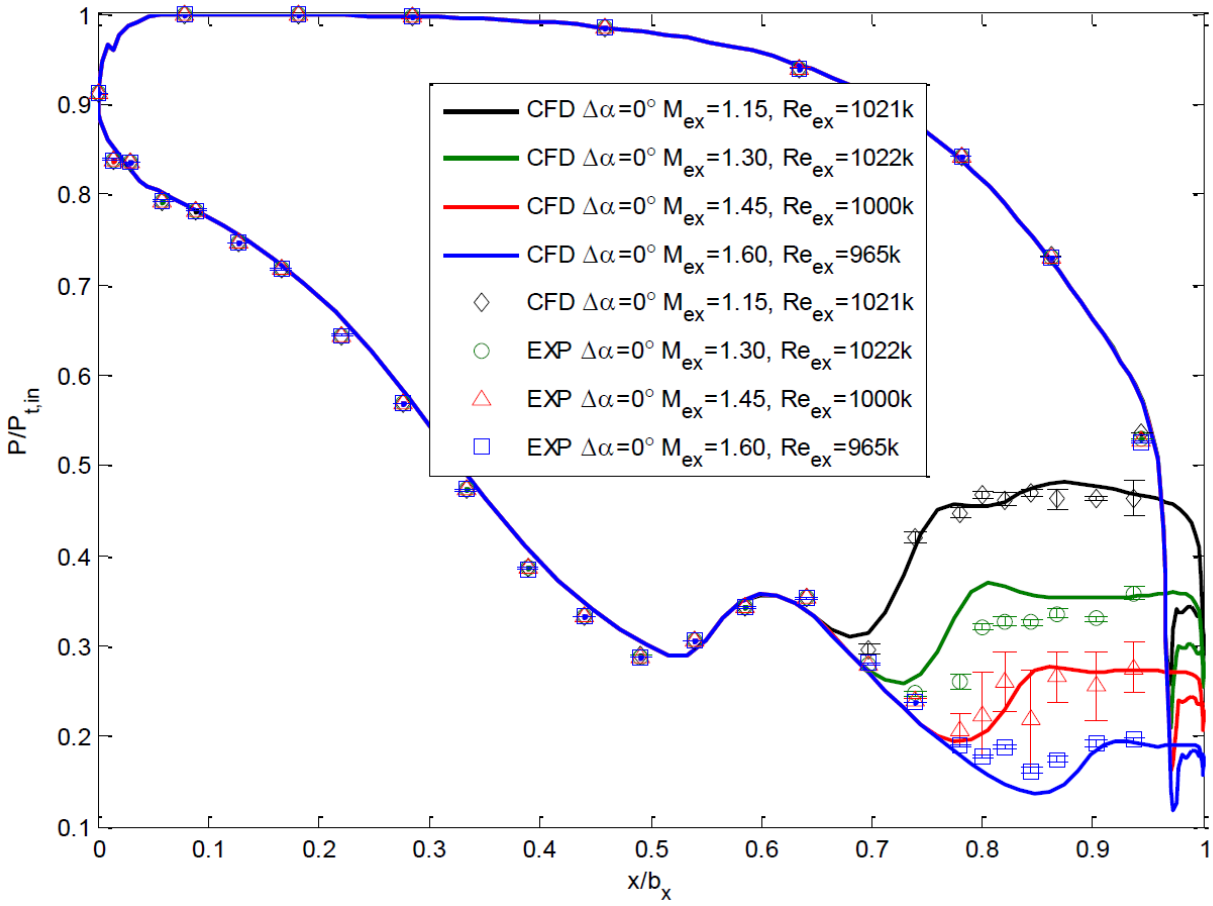

Figure 34: Pressure distributions of exit Mach numbers ranging from 1.15 to 1.60, at 1.0×10^6 exit Reynolds number and design incidence angle

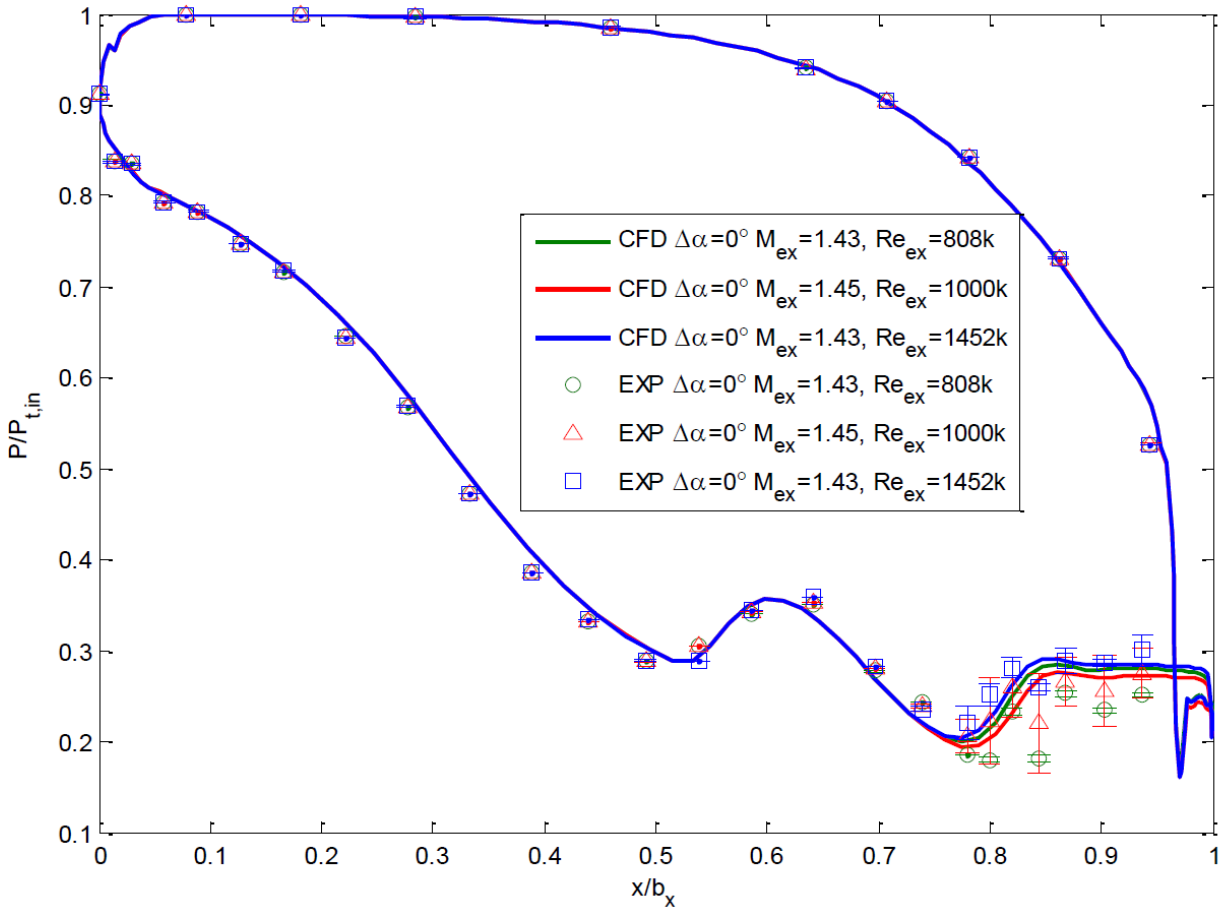

Figure 35: Pressure distributions of exit Reynolds numbers ranging from 0.80x10^6 to 1.25x10^6, at 1.45 exit Mach number and design incidence angle

The traversing rake measured the total pressure exiting the blade row at 74% of one chord length downstream of the trailing edges. The pressure loss in the wake for case 9 is compared to the CFD pressure losses at the same axial location in Figure 36. The experimental data shown in the figure was processed in the same manner as described in the midspan geometry section. Recall, there is a bow shock at the front of the probe in the supersonic flow. The total pressure recorded by the probe is actually the total pressure downstream of the shock, which can be approximated as a normal shock near the probe. Normal shock relations [35] were used to calculate the experimental total pressure as if no shock were present. Peaks correspond to blade wakes and the troughs in Figure 36 represent the flow passing through the middle two passages. The mean loss is shown in the legend. The wake losses were over predicted in the wakes of the quarter-tip blade pack and under predicted in the passages by the simulation. A shift in the loss peaks of the off-design incidence angles was seen in both the simulation and experiment. However, the magnitude of the shift was under predicted by the simulation. This could be due to several factors, including a slight misalignment of the traversing probe relative to the flow exiting the blade row. Ongoing efforts continue to improve the understanding of the discrepancy between the computational and experimental loss profiles.

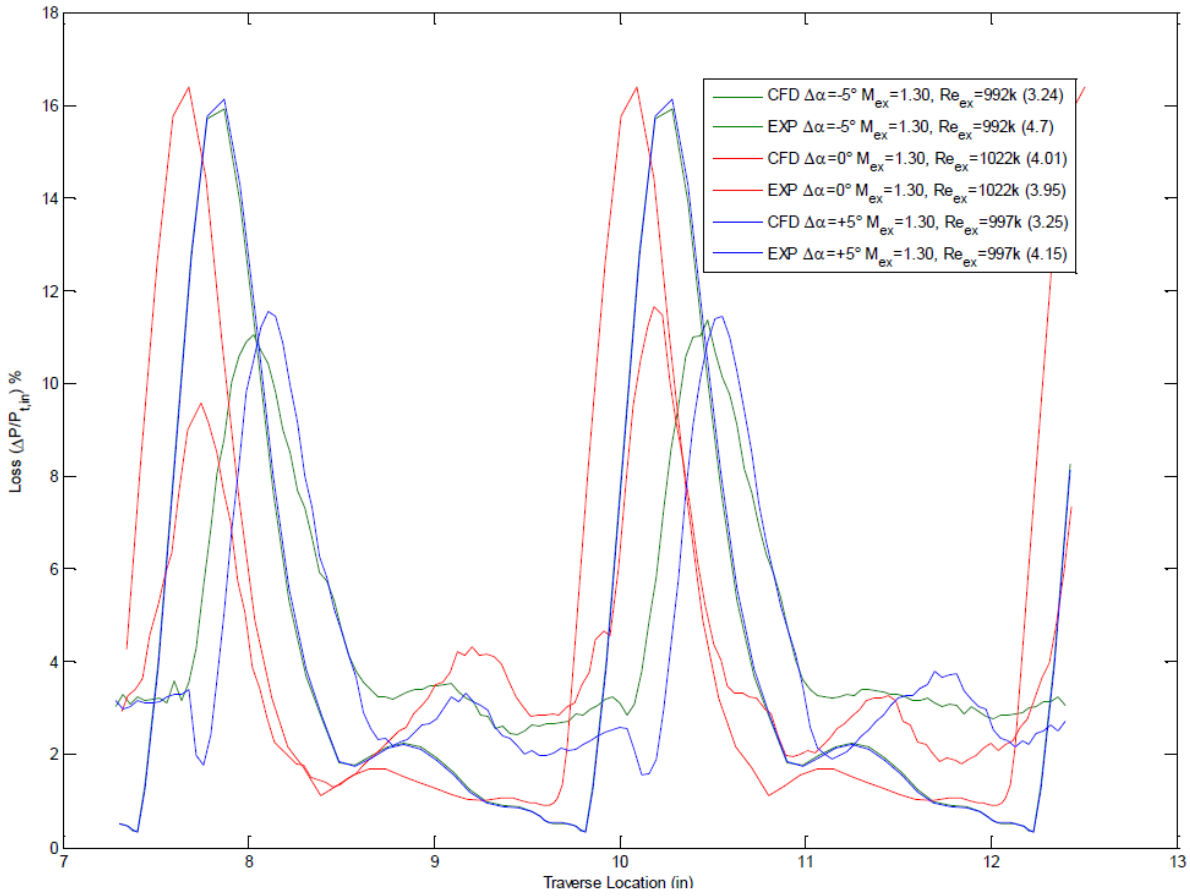

Figure 36: Loss profile of Case 9, with exit Mach and Reynolds numbers of 1.30 and $1.0x10^6$, respectively, at three incidence angles

Summary

The HPT1B midspan and quarter-tip blade packs were tested in the linear transonic cascade at AFRL. Pressure distributions and wake loss profiles for multiple exit Mach and Reynolds numbers and angles of attack were obtained and compared to CFD predictions with matching similarity parameters. The 2-D, steady component of a computational fluid dynamics code, known as Leo, was used for the computations. The CFD analysis showed similar trends and compared to the experimental data very well. Varying the angle of attack for constant exit Mach and Reynolds numbers only affected the leading edge half of the suction side. Airfoil loadings were increased as the angle of attack increased and decreased with decreasing incidence. When holding the exit Reynolds number and angle of attack constant, varying the exit Mach number affected the pressure distribution on the suction side towards the trailing edge only. The loading decreased in this area as the exit Mach number was reduced. This is consistent with the behavior of choked flows. When the throat is sonic—and indeed that is the case with the HPT1B for all cases explored—changes in the back pressure only propagate downstream. Exit Mach numbers near unity were also shown to have a higher degree of unsteadiness within the shock structure for the midspan blade pack. A well-designed airfoil performs well at a variety of Reynolds numbers, which is the behavior that the HPT1B exhibits. Varying the exit Reynolds number had very little effect on the experimental or

CFD pressure distributions. This indicates that the boundary layer is attached and not growing excessively on the airfoil.

The behavior of the pressure distribution due to varying the incidence angle and pressure ratio will be used in the post-test assessment of the stage-and-one-half. The effect on the suction side pressure distribution upstream of the shock will indicate whether or not the target test corrected speed was achieved. Achieving the target pressure ratio of the rotating tests will be assessed based on the effect on the suction side pressure distribution downstream of the shock.

Although further work can be done to improve the wake loss profile experimental measurement and/or computational analysis, the transonic cascade facility and the 2-D, steady package of Leo demonstrate exceptional data comparison for a range of exit Mach and Reynolds numbers and angles of attack. The aerodynamic performances of the blade during on- and off-design conditions have been modeled with CFD and validated successfully with experimental data.

CHAPTER IV

THREE-DIMENSIONAL VANE-ONLY FLOWFIELD

High pressure vane-only tests of the HIT RT were conducted in an annular cascade and compared to CFD predictions, and the results are highlighted in this chapter. Leo was, once again, the flow solver used to compute the numerical solution. The boundary conditions were derived from the experimental flow conditions. The experimental tests and comparison to predictions were conducted in order to characterize the flow field that will be delivered to the blade row during the subsequent stage-and-one half experiments.

Experimental Methodology

The objective of the experimental work performed in the Turbine Research Facility at WPAFB with the vane-only case was to characterize the flow field of the first vane without any rotating machinery. The TRF is a full-scale transient facility designed to obtain time-resolved pressure, surface temperature, and heat flux data from single- spool turbomachinery at flow conditions which are consistent with turbine environments in terms of non-dimensional parameters. The facility is shown in Figure 37. Nitrogen is pressurized and heated in the supply tank on the left side of the figure. The tank has a maximum pressure limit of approximately 100 psia and can heat the gas up to 1000ºR. Opening the fast-acting plug valve allows the flow to pass through the test section—from left to right in the figure—into the dump tanks. The dump tanks can be vacuum pumped, allowing back pressures ranging from 10 to 70 psia. An isolation valve downstream of the test section governs the mass flow and turbine pressure ratios. Previous simulations [36] of the flow passage in the TRF with varying isolation valve positions aided in determining the expected design pressure flowfield for the vane-only configuration. Typical runs for the vane-only cascade usually last on the order of six seconds. The Turbine Research Facility is described in greater detail in [34][37][38].

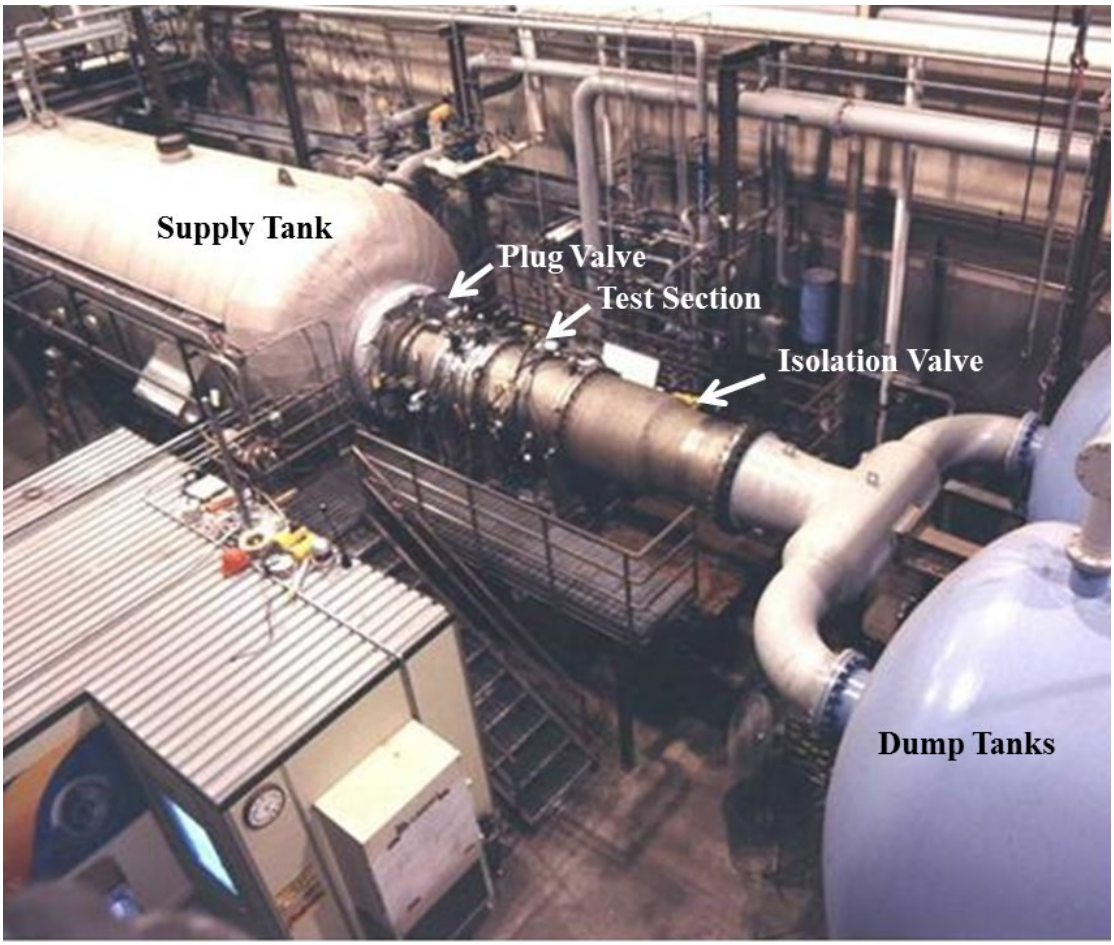

Figure 37: AFRL Turbine Research Facility

The static pressure data was obtained through pressure taps leading to flush-mounted Kulite piezo-resistive transducers. Surface temperatures and heat flux data were obtained using surface mounted thermocouples and thin-film double-sided heat flux gauges, respectively, although only pressure data is reported in this chapter. Total pressures up- and downstream of the vanes were each collected by a rake of nine pressure gauges at centers of equal area in the radial direction. The up- and downstream rakes swept 120 degrees of the annulus throughout the duration of the blowdown. The pressure transducers used in the Turbine Research Facility are Kulite transducers, model LQ-062. The uncertainty of the measurements was calculated using the method developed by Dunn and Haldeman [5]. Applied to the TRF, the uncertainty of the measurements is 0.05 percent of the full scale output, which equates to 0.05 psia [39]. The static pressure sensors used to obtain the surface pressures on the airfoil are listed in Table 4. The airfoil number that each sensor is on, the percent axial chord, percent span, and pressure or suction side designation is also shown. Most of the sensors that were connected for this test were located on the suction side toward the trailing edge.

Table 4: Vane-Only Pressure Sensors

Sensor	Airfoil	x/b_x	Span	Side
PVF14	19	0.916	0.500	SS
PVF16	19	0.980	0.500	SS
PVE1	20	0.800	0.500	PS
PVE2	20	0.000	0.500	PS
PVE10	20	0.719	0.250	SS
PVE11	20	0.800	0.250	SS
PVE12	20	0.887	0.250	SS
PVE13	20	0.920	0.250	SS
PVE14	20	0.950	0.250	SS
PVE15	20	0.980	0.250	SS
PVD2	21	0.000	0.050	PS
PVD10	21	0.250	0.050	SS
PVD11	21	0.677	0.050	SS
PVD12	21	0.822	0.050	SS

A typical total pressure time variation for a blowdown test is shown in Figure 38. As the gas empties from the pressurized tank, the total pressure heading into the vane row gradually drops off. The main valve opening and closing times are also highlighted on the figure. The static pressure on the airfoil surface exhibits a similar behavior, as seen in the example shown in Figure 39. Pressure data from PVF14 is shown in the figure. Referencing Table 4, the location of the sensor can be determined: on airfoil 19, at 91.6% axial chord and at 50% span on the suction side. An abnormality in the linearly decreasing pressure is seen here. This is due to the wake of the traversing upstream rake passing by vane 19 just prior to the 8 second mark of the test. In order to enable a comparison between a steady-state simulation and the experimental data, the surface pressures were normalized by the total pressures from the upstream traversing rakes using the following method. The pressure values from the total pressure rakes at various radial locations were averaged at every time sample, resulting in a spatially averaged upstream total pressure. Then, the surface pressure data on the airfoils was normalized by dividing the samples at each instant in time by the average upstream total pressure at the same instant in time. The result is an airfoil static-to-total pressure ratio as a function of time. Finally, the pressure ratio is time-averaged over the appropriate sampling time. This time- averaged static-to-total pressure ratio is used in the comparison to CFD because it should remain relatively constant for the duration of the blowdown despite the gradual drop in total pressure. This is proven to be the case in Figure 40, which is a plot of the static-to- total pressure ratio of the same gauge, PVF14, on airfoil 19. The pressure ratio remains constant after the main valve is opened and during the linear drop in total pressure. The vertical red lines in the figure represent the time interval in which the static-to-total pressure ratio is time averaged, from 9.00 seconds to 9.25 seconds. All airfoils that had surface pressures were clear of the traversing rake after 9 seconds and the cooling air was turned off shortly after 9.25 seconds.

In order to provide a closer inspection of the measured data, a magnified plot of the pressure data from PVF14 during the first two seconds of the test is shown in Figure 41. This cooling air is turned on at approximately 0.4 seconds. Prior to this point in time, the test section is in a near vacuum. The pressure fluctuations during the time at which the test section was in a near vacuum indicates the fluctuations due to uncertainty. The peak-to-peak fluctuations measure less than 0.025 psia.

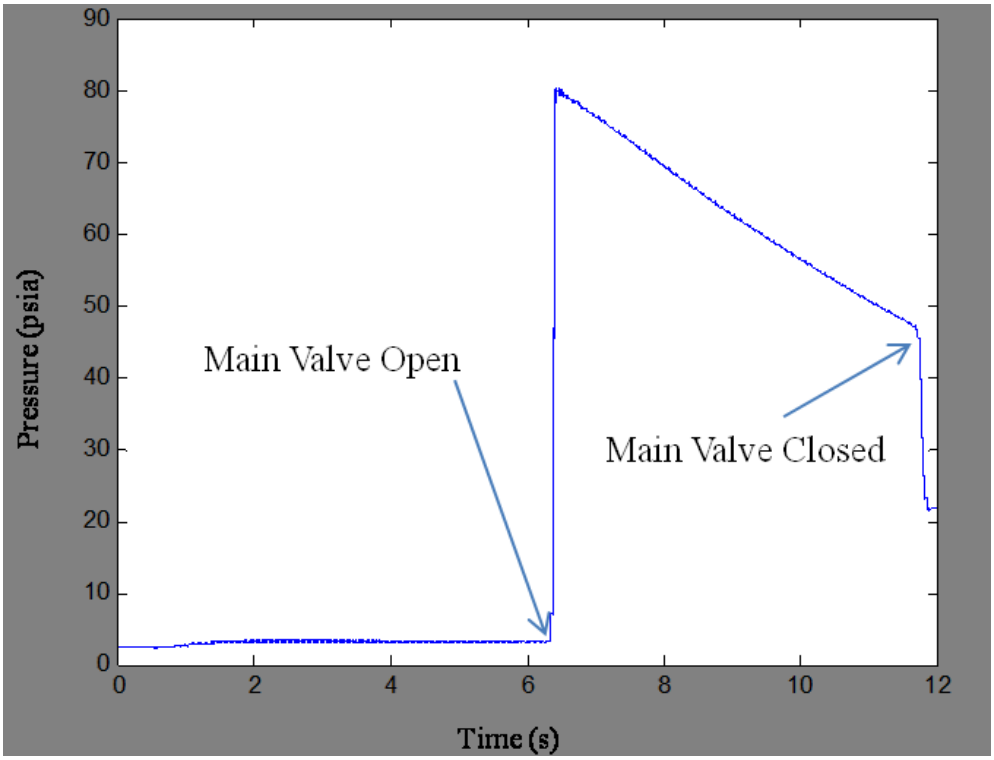

Figure 38: Upstream Total Pressure vs Time

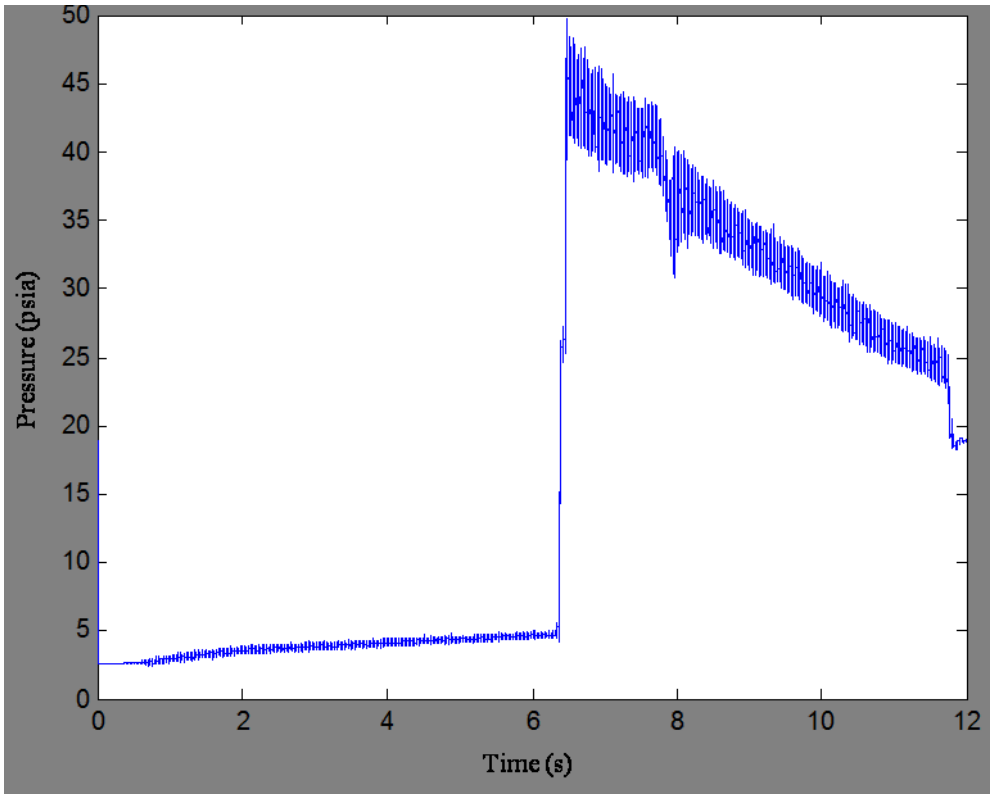

Figure 39: Static Pressure from PVF14 Airfoil 19, 92% Axial Chord, 50% Span

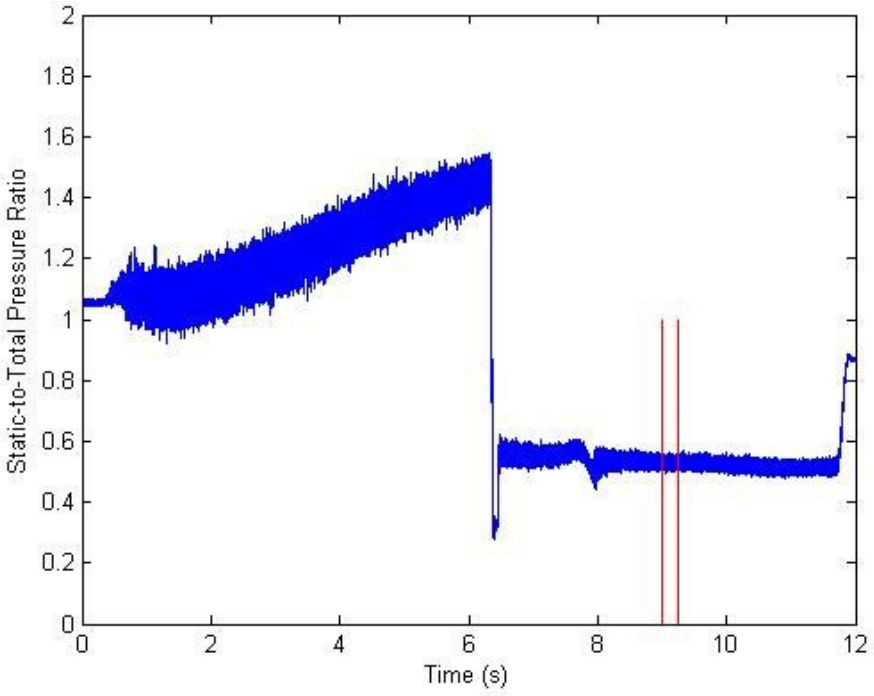

Figure 40: Static-to-Total Pressure Ratio from PVF14 Airfoil 19, 92% Axial Chord, 50% Span

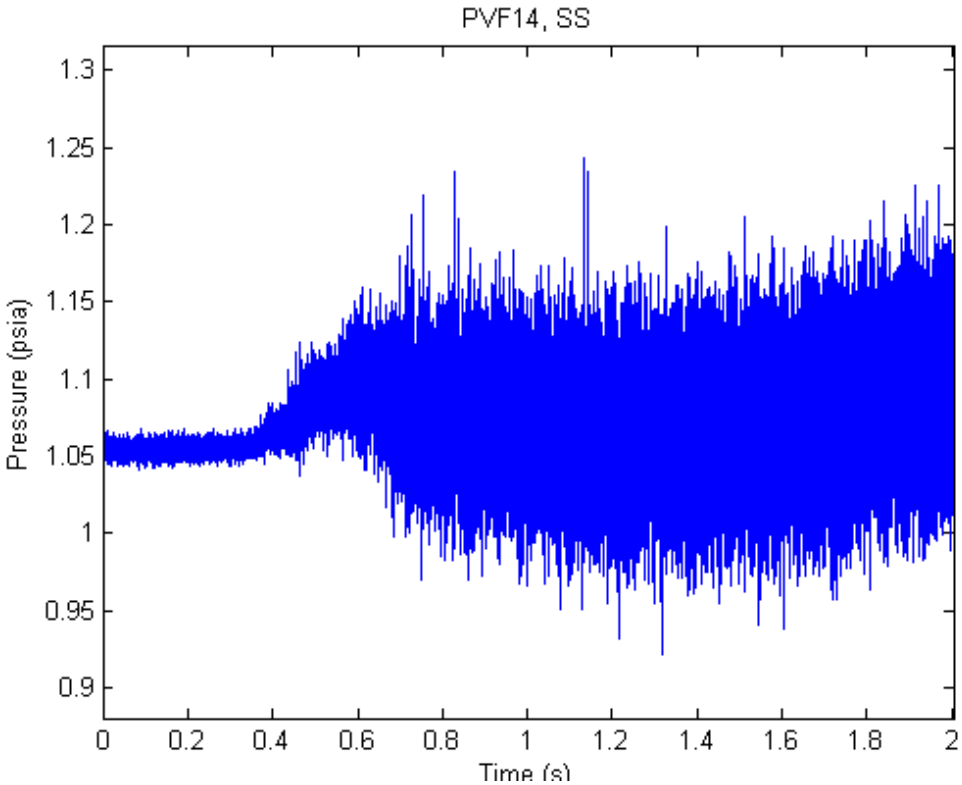

Figure 41: Magnified Plot of the Static Pressure from PVF14 Airfoil 19, 92% Axial Chord, 50% Span

The HIT RT first vane that was tested is shown in Figure 42. The HPT vane airfoil count is 23 and these are numbered such that vane 1 is at the top dead center, increasing in the clockwise direction, forward looking aft. The schematic of the vane shown in the figure is one of the 16 vanes that were cooled. Vanes 1 through 7 were uncooled and vanes 8 through 23 had cooling. The primary purpose for having both cooled and uncooled vanes was a heat transfer study not relevant to this research. However, it is important to mention here because all of the Kulites pressure transducers on the airfoils are on cooled vanes. A layout of the HPT vane ring illustrating the cooled and uncooled airfoils is shown in Figure 43. Vanes 10, 11, 19, 20, and 21 are identified as cooled vanes with pressure transducers. The pressure rise visible on the pressure traces prior to the main valve opening is due to the cooling. The cooling air is turned on prior to the main valve activation so that the cooling flow can be established.

The upstream and downstream flow conditions were measured and averaged over the duration of the time interval of interest, which was previously described. The total inlet pressure had a fairly constant radial profile of 65.5 psia. The inlet total temperature had a maximum value of 798 °R at the midspan and decreased to 793 °R at either endwall. The downstream static pressure was 39.43 psia. The wall temperature of the uncooled and cooled airfoils was 600.7 °R and 595.6 °R, respectively. The cooling pressure ratio, $P_{t,c}/P_{t,\infty}$, was 1.02.

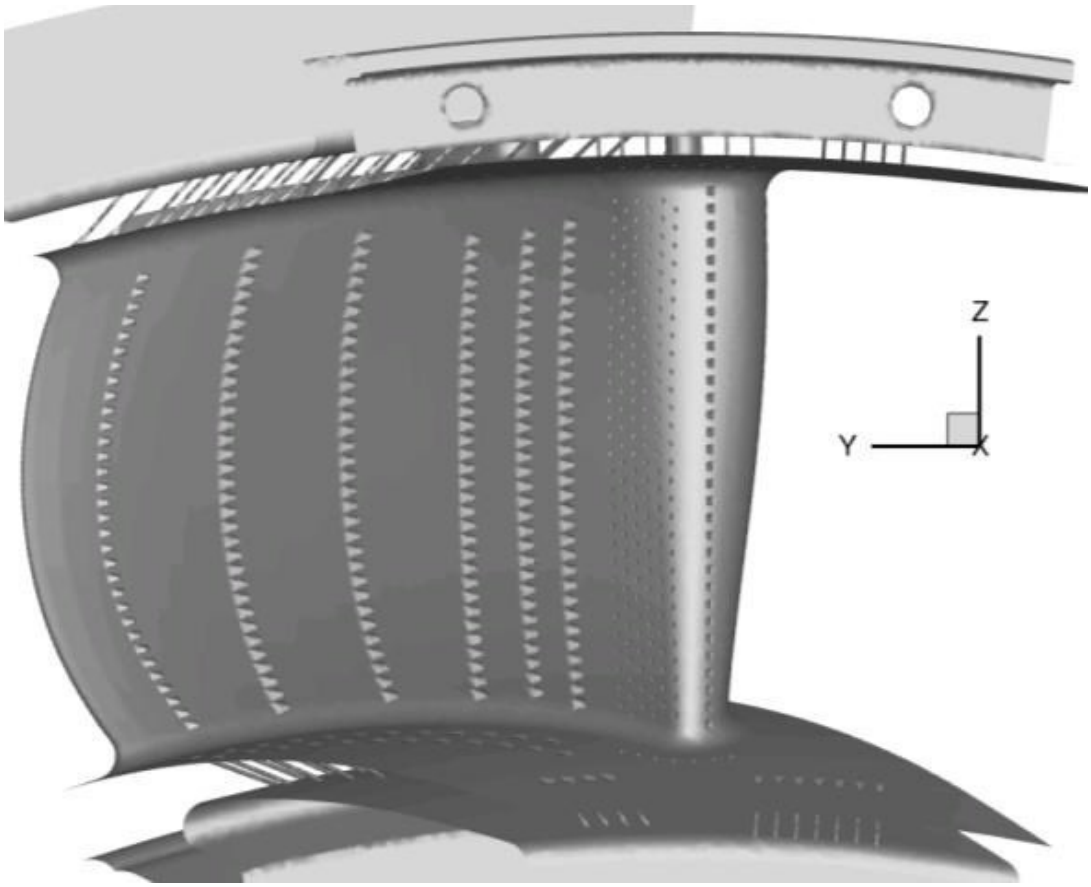

Figure 42: 3-D rendering of a cooled HIT RT 1V

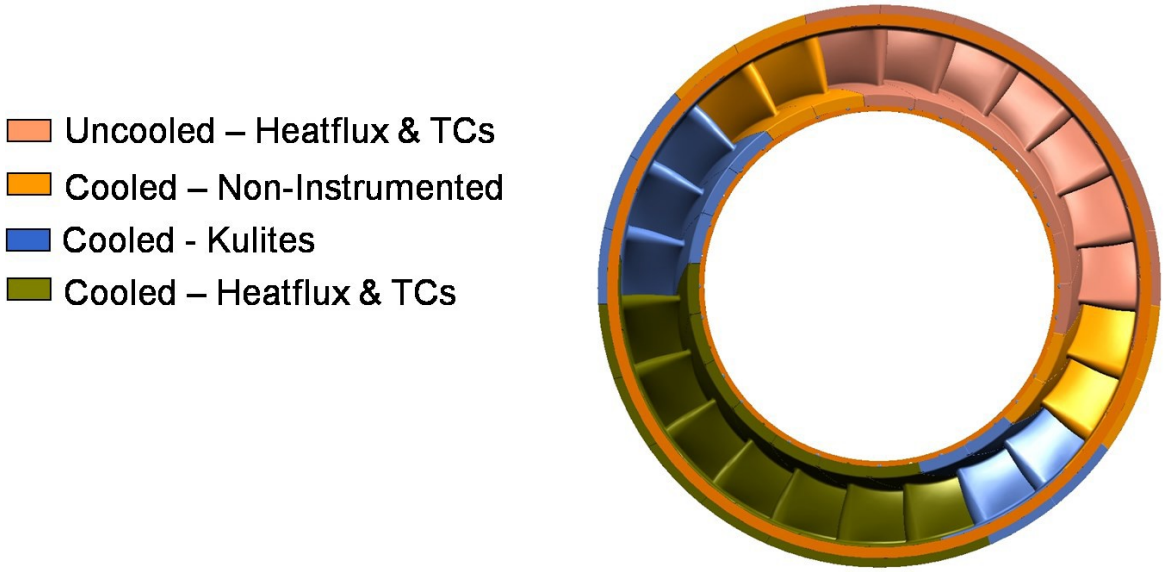

Figure 43: HIT RT 1V Ring Cooling Layout

CFD Methodology

Code Leo was also used for the three-dimensional, vane-only simulations. The 3- D version of Leo also implements a Reynolds-Averaged Navier-Stokes method with the two-equation Wilcox 1998 k-ω turbulence model. Leo was run in steady mode for comparisons to the experiment as described above. A radial slice of a typical grid generated from Leo is shown in Figure 44. Much like the 2-D cases, the grid is broken into H- and O-blocks. The difference is that the blocks extrude in the radial direction, or out of the plane as viewed in the figure. Block 3 is the O-grid, and blocks 1, 2, 4, and 5 are H-grids. Point to point matching exists between the blocks. The full length of the domain is not shown; however, the grid extends over two axial chord lengths upstream of the leading edge, and one and one-quarter axial chord lengths downstream of the trailing edge of the airfoil.

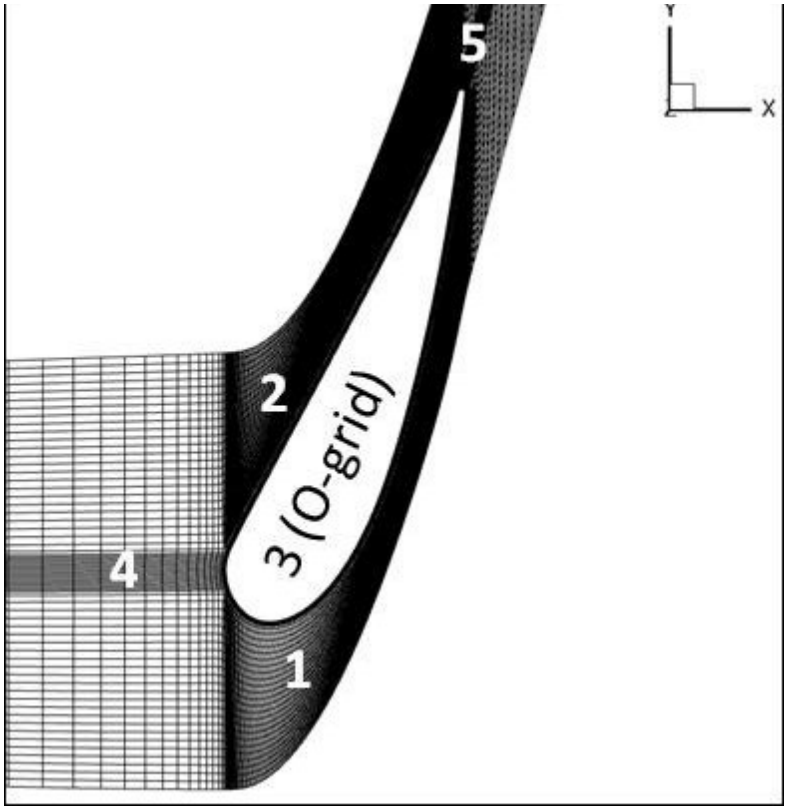

Figure 44: Radial Slice of 3D Computational Grid at Midspan

A grid independence study was conducted prior to comparing CFD data to the experimental results. Four meshes of varying grid densities were created and Leo was run for each. The details of each grid are listed in Table 5. All cases were run for 24,000 iterations, which proved sufficient for convergence of the density, momentum, and energy residuals to 10^{-3} or less. The inlet and exit mass flows and the loss in total pressure for each case are listed in Table 6. The mass flow in and out of the vane varied slightly in the cooled cases when compared to the uncooled cases due to the addition of the cooling air. Cooling air is not included in the inlet mass flow; therefore the inlet and exit mass flows were not equivalent for the cooled cases. The uncooled mass flows are nearly identical among the four grid sizes. There is also very little change in the cooled mass flows as well. As expected, the cooled cases

have more total pressure loss than the uncooled cases. The losses among the uncooled cases were very similar, and the losses among the cooled cases were also very similar to one another. The similar mass flows and losses for the uncooled cases indicate that grid independence has been achieved. Similarly, the cooled cases exhibit the same behavior and the solutions are also grid independent.

Table 5: Grid Dimensions for the 3-D Computational Grid Independence Study

	Grid 1	Grid 2	Grid 3	Grid 4
Axial upstream	25	29	29	33
Axial downstream	13	17	25	29
Tangential (pitch)	47	51	75	87
Radial	49	65	69	73
Axial on-vane	161	225	249	273
Wall-Normal in O-grid	21	25	41	53
Initial cell height (in)	$1x10^{-4}$	$1x10^{-4}$	$1x10^{-4}$	$1x10^{-4}$
Total Cells ($x10^3$)	419.2	858.1	1786.5	2751.5

Table 6: Mass Flow and Total Pressure Losses for a Single Uncooled Vane and a Single Cooled Vane for Varying Grid Densities

	Mass Flow Inlet (lb_m/s)	ass Flow Outlet (lb_m/s)	Loss ($\Delta P_t/P_{t,in}$)
Grid 1 (no cooling)	2.276	2.299	4.420
Grid 2 (no cooling)	2.271	2.275	3.929
Grid 3 (no cooling)	2.262	2.264	3.947
Grid 4 (no cooling)	2.261	2.261	3.794
Grid 1 (cooling)	2.092	2.336	5.684
Grid 2 (cooling)	2.081	2.326	5.292
Grid 3 (cooling)	2.074	2.316	5.289
Grid 4 (cooling)	2.075	2.316	5.159

Midspan pressure distributions from uncooled and cooled airfoils were also investigated, and are shown in Figure 45 and Figure 46, respectively. The loadings for each grid for the uncooled cases are nearly identical. It is very easy to conclude that grid independence has been achieved with Grid 3. However, the cooled pressure distributions have measureable variation among the grids in the area of cooling. The discontinuous behavior is a result of how the CFD code Leo introduces cooling into the flow. Leo uses three levels of fidelity for modeling cooling flow. Level 1 cooling, used in this study, adds the cooling flow at the airfoil surface as a flux [40]. The higher fidelity cooling modeling capabilities include the ability to model the flow in the cooling passages and a full conjugate analysis [27]. Areas on the cooled vane that do not have cooling holes show similar agreement when compared to the uncooled loadings. Taking into consideration of how Leo implements level 1 cooling, as well as the mass flow and total pressure loss data shown in Table 6, grid independence was considered to be achieved with Grid 3 for the cooled vane cases as well.

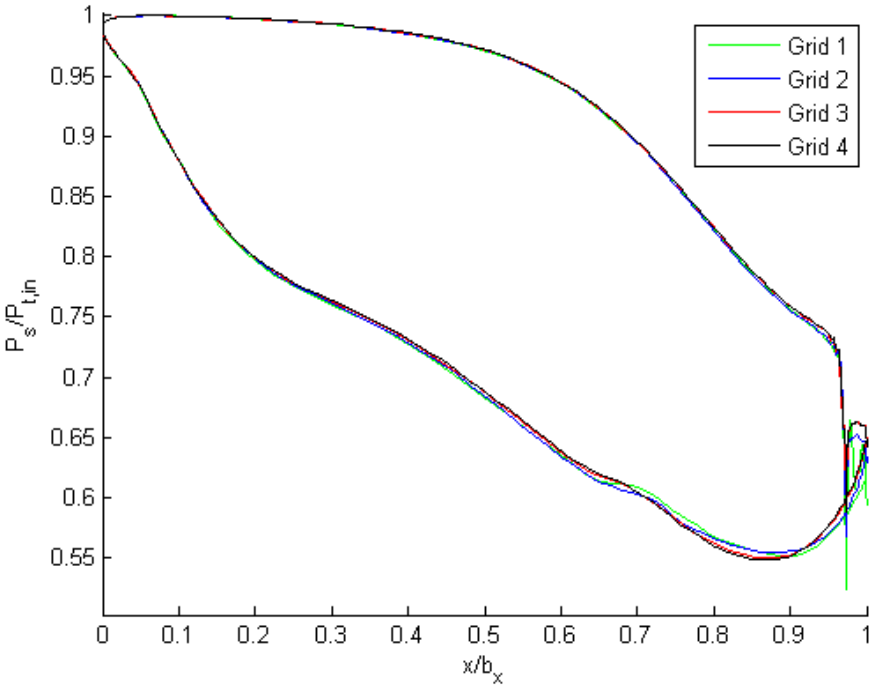

Figure 45: Midspan Pressure Distributions for Uncooled Vane Grid Independence Study

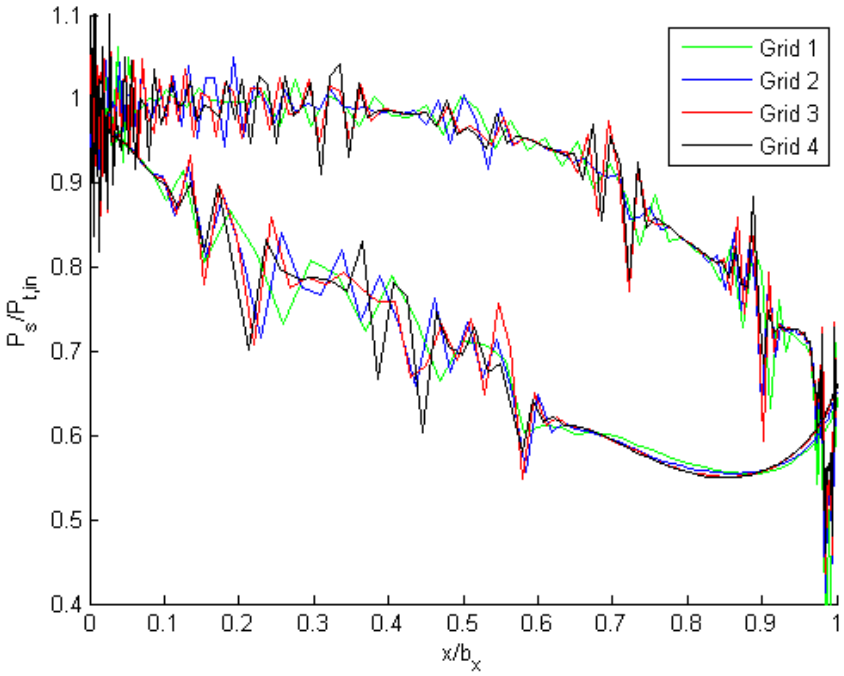

Figure 46: Midspan Pressure Distributions for Cooled Vane Grid Independence Study

Grid 3 was used to compare to the experimental data in this study because it has been shown to produce grid independent solutions and is not too computationally burdensome. The grid on the vane is shown in Figure 47. The boundary conditions for the CFD simulation were set to match the flow conditions described in the Experimental Methodology section.

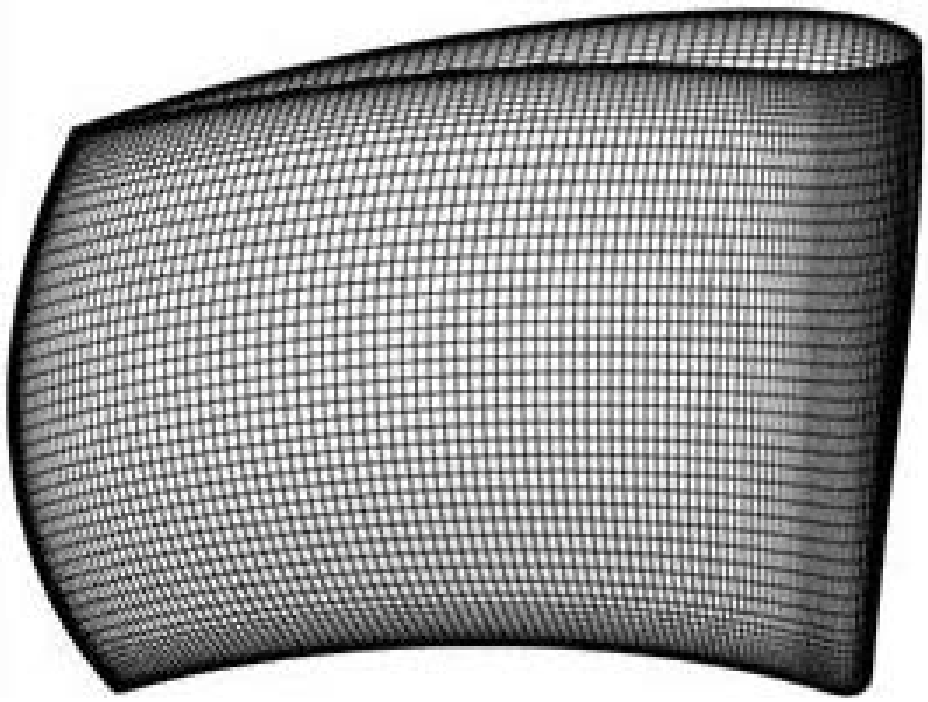

Figure 47: HIT RT 1V Modeled using Grid 3

Results

The experiment and CFD analysis were carried out as described in the previous sections. The static-to-total pressure ratios of experimental data and the numerical solution are shown in Figure 48. The three spans with pressure sensors—5%, 25%, and 50%—are compared to the corresponding spans from the CFD simulation. Although all pressure data was taken from cooled airfoils, the uncooled predictions are also shown in the figure. The vertical lines on the measured data indicate peak-to-peak pressure variation. Small peak-to-peak pressure variation was measured, indicating that the flow field is largely steady. The numerical solution matches the experimental measurements fairly well for all spans for which data was taken, and the flow field is well characterized.

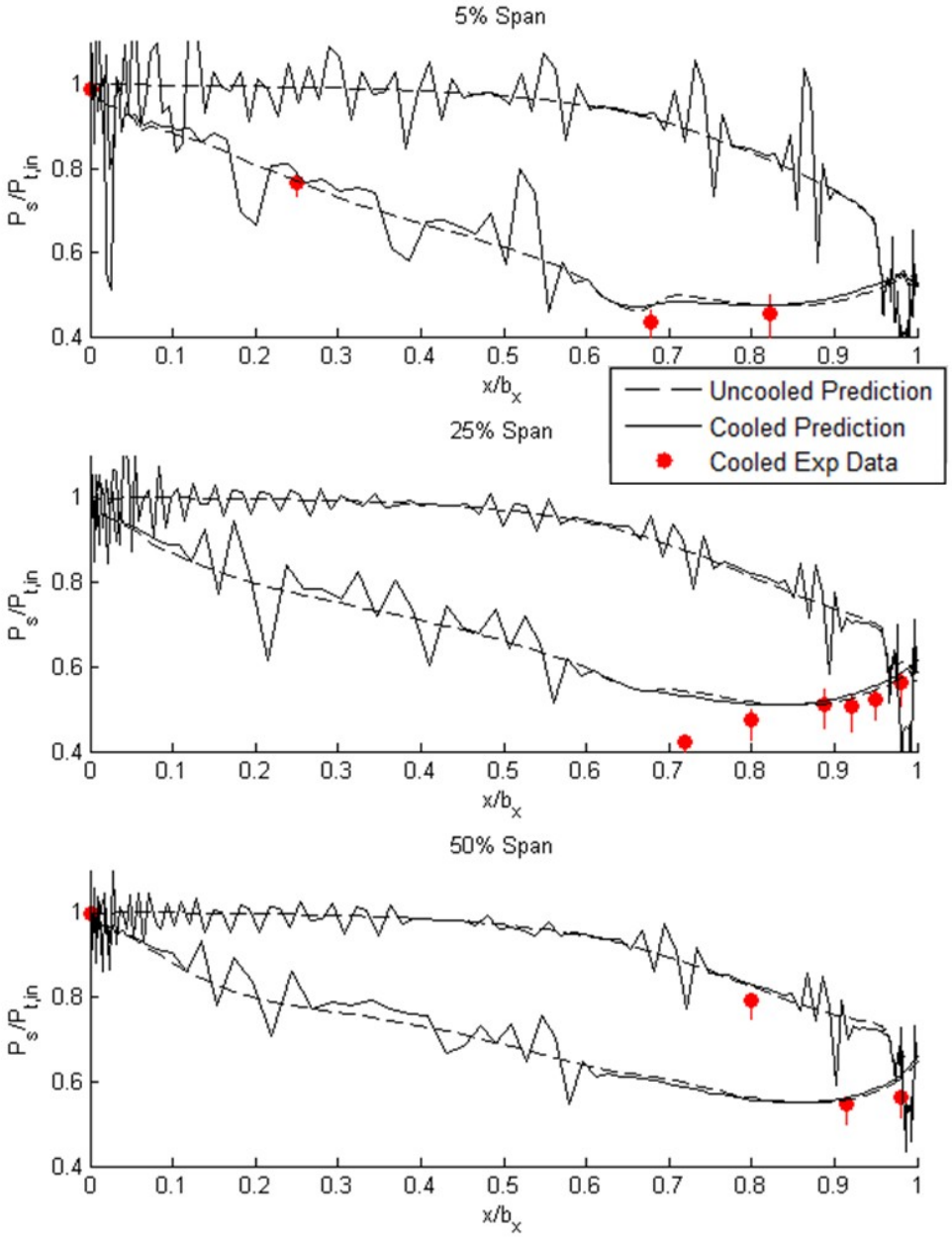

Figure 48: Cooled Pressure Loadings of the Vane-Only Case and Comparison to CFD

Fluctuations were seen in all of the pressure traces, similar to those seen in Figure 39 in the Experimental Methodology section. The pressure traces for many of the sensors are shown in Figure 49. The plots in the figure are organized by sensor location. The axial chord location increases from left to right, and the span location increases from bottom to top. Pressure side sensors are plotted in red, and suction side sensors are blue. Redundant sensors, or sensors very near the span and axial locations of others, were not included in the figure. The pressure fluctuations are larger for the sensors nearer to the endwall and trailing edges. This suggests that secondary flows may be the cause of the fluctuations. To distinguish between electronic noise and actual unsteadiness, the end of the pressure traces were investigated further.

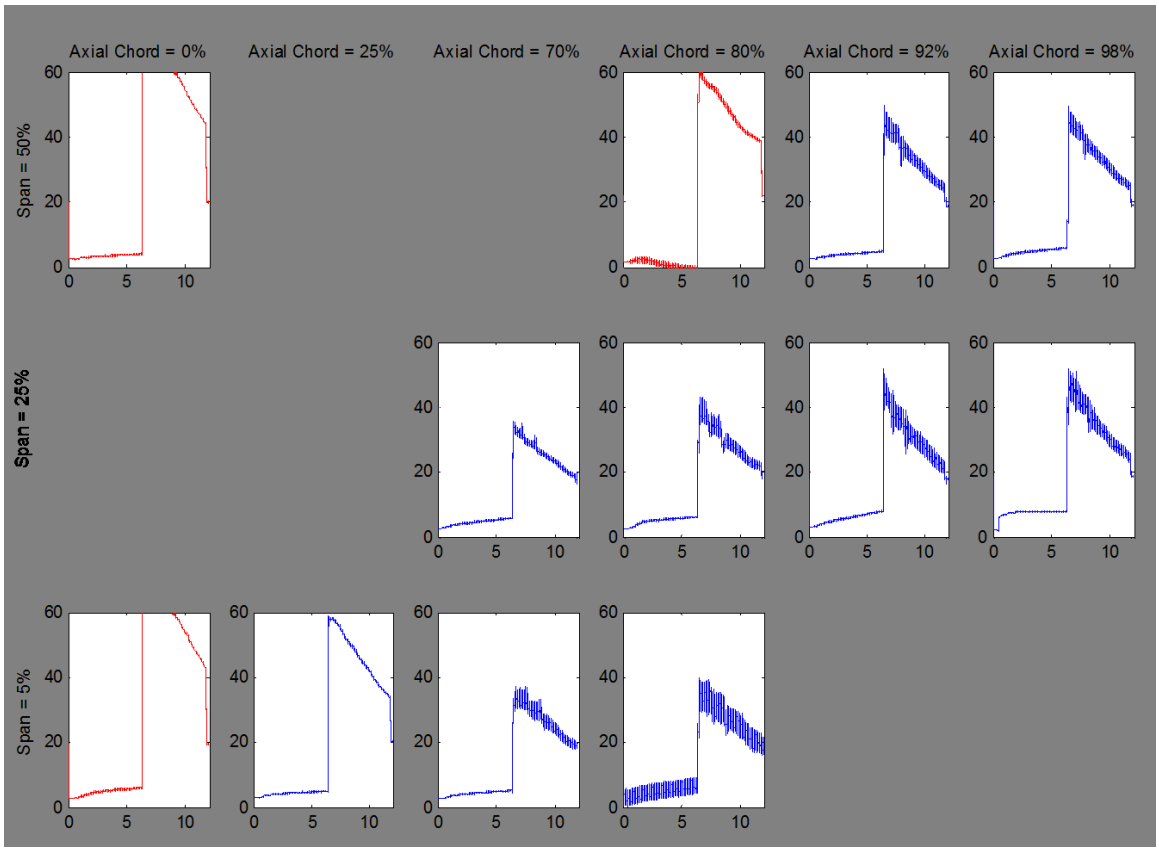

Figure 49: Pressure Traces for the Vane-Only Case at Various Axial and Span Locations

Summary

The HIT RT first vane-only case was tested in the Turbine Research Facility at AFRL. The TRF is a full-scale blowdown facility designed to obtain time-accurate unsteady pressure, surface temperature, and heat flux data from single-spool turbomachinery at flow conditions which are consistent with turbine environments in terms of non-dimensional parameters. The surface pressures at three spanwise locations were compared to the numerical solution of the CFD software, Leo. The blowdown is a transient event as the total pressure, and therefore airfoil surface static pressure, is linearly decreasing. However, after normalizing the surface pressure by the upstream total pressure at each sampling in time, the experimental data can be compared to steady- state CFD solutions. The Leo CFD solution matched the experimental pressure loadings fairly accurately. The fluctuations in the pressure traces were also investigated. Larger fluctuations were seen closer to the endwall and further

downstream due to secondary flow interaction. The three-dimensional, steady aerodynamics are well understood for the vane-only case, and the flow field that will be provided to the blade row during the subsequent stage-and-one-half tests is well characterized.

CHAPTER V

STAGE-AND-ONE-HALF CFD MODELING ASSESSMENT

When using computational fluid dynamics tools to simulate physical phenomena, it is extremely important to model the domain properly. Three-dimensional, unsteady numerical analyses of turbine engine components require sufficient spatial and temporal resolution, as well as choosing an appropriate sector of the wheel to model. However, there is a trade between the fidelity of the model and computational expense required to compute a solution. The purpose of this chapter is to conduct a rigorous evaluation of the CFD software that was used in order to determine a satisfactory method for the numerical analysis to be compared to experimental data. The grid, iterative, periodic, temporal, and geometric convergences are investigated.

Iterative convergence is achieved by computing the steady solution until the residuals of the flow variables are sufficiently small [42]. Assessing the grid and temporal convergences ensures that the spatial and time-step resolutions are sufficient for capturing the physics of the flowfield [42]. If significant differences in the solution are predicted by increasing the density of the grid or decreasing the time-step size, then the analysis has not achieved grid independence or temporal convergence, respectively. Periodic convergence is discussed in detail by Clark [7], and is assessed by investigating the time-mean signals, the amplitude and phase angle of Discrete Fourier Transforms, cross-correlation coefficient, and the power spectral density. High convergence values of the pertinent parameters indicate periodic convergence. Finally, geometric convergence refers to modeling the appropriate wheel sector of the turbine, depending on the airfoil count, cooling scheme, and other factors that could affect circumferential periodicity.

The HIT Research Turbine was designed to study unsteady aerodynamics as well as aerothermodynamics. For the study of the latter, which is not investigated in this thesis, cooled and uncooled airfoils were included in the first stage of the turbine. The Research Turbine cooling scheme for the first stage is shown in Figure 50. The mixed cooling scheme will affect the flow structure interacting with neighboring airfoil rows because the mass flow, boundary layers, and trailing edge shock strengths are affected by the presence of cooling flow. A turbine with 23 first vanes, 46 blades, and 23 second vanes would typically be modeled with a $1/23^{rd}$ sector, given the 1:2:1 airfoil-per-row ratio. However, the mixed cooling scheme of the Research Turbine potentially requires modeling a larger sector of the wheel for unsteady forcing analysis of cases involving cooling flow.

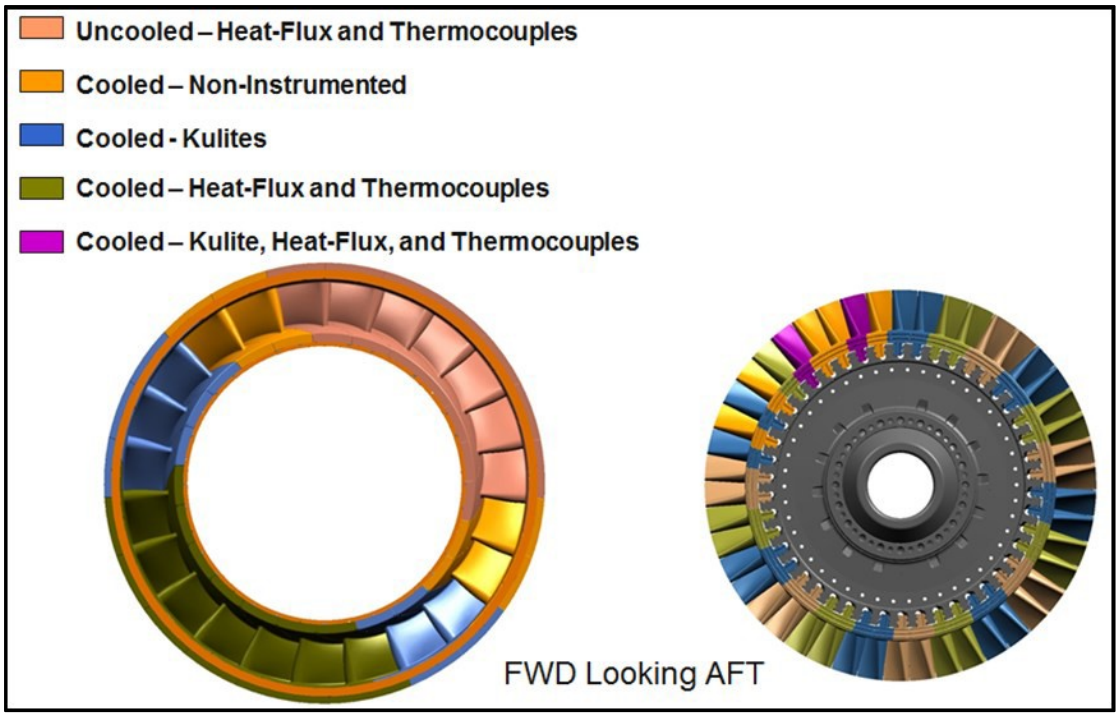

Figure 50: HIT RT Vane and Blade Cooled Schematic

Grid and Iterative Convergence

The CFD software, Leo, was used to provide the numerical analysis for the time-accurate, three-dimensional, stage-and-a-half cases. Recall that the 3-D version of Leo also implements a Reynolds-Averaged Navier-Stokes method with the two-equation Wilcox 1998 k-ω turbulence model. A grid convergence study was conducted prior to evaluating the appropriate portion of the wheel that is necessary to model. An uncooled, 1/23rd sector—1 vane: 2 blades: 1 vane—was used to complete the grid convergence study. Five grid densities were investigated, and the details of each grid are shown in Table 7. Note that the total cell count for each grid represents a 1:2:1 sector, and the blade cell count listed in the table represents one airfoil only. The initial cell height was kept constant throughout the study.

Table 7: Grid Dimensions for Stage-and-One-Half Grid Independence Study

	Grid 1			Grid 2			Grid 3			Grid 4			Grid 5		
	1V	1B	2V	1V	1B	2V	1V	1B	2V	1V	1B	2V	1V	1B	2V
Axial upstream	25	13	13	27	15	15	29	17	17	29	25	25	33	29	29
Axial downstream	13	13	25	15	15	27	17	17	29	25	25	33	29	29	37
Tangential (pitch)	47	31	47	51	35	51	51	35	51	75	51	75	87	55	87
Radial	49			57			65			69			73		
Axial on-vane	161			193			225			249			273		
Wall-Normal in O-grid	21			25			25			41			53		
Initial cell height (in)	$1x10^{-4}$			$1x10^{-4}$			$1x10^{-4}$			$1x10^{-4}$			$1x10^{-4}$		
Total Cells per Airfoil ($x10^3$)	419.2	318.7	419.2	661.8	527.5	661.8	858.1	684.2	858.1	1786.5	834.1	1807.2	2751.5	1174.3	2776.9
Total Cells ($x10^3$)	1475.8			2378.5			3084.6			5261.9			7877.1		

Each simulation was initially converged to steady state before running time-accurate simulations. As shown in Figure 51, the largest residual was reduced to at most 10^{-3} for any variable of interest. The cases were then run until periodic convergence was obtained. A more formal process of achieving periodic convergence is discussed in a following section. However, for the purposes of evaluating grid convergence—prior to establishing periodic convergence—a simple and qualitative assessment of periodic convergence is exercised here. Mass flow, mass- and area-averaged total pressure and temperature, efficiency, and static pressure are plotted against iteration number in Figure 52. All quantities have attained periodicity during the last four-plus cycles. The unsteady analysis was then continued for exactly two blade-passing cycles. The two-period cycles of the aforementioned flow variables are shown in Figure 53. Signal processing was conducted using the results from the two-cycle runs, after previously achieving periodic convergence. The cases were also spatially averaged after running for two complete cycles, in order to calculate mass-averaged quantities. Grid 5 is represented in Figure 51 through Figure 53; however, the simulations were conducted as described above for each grid case.

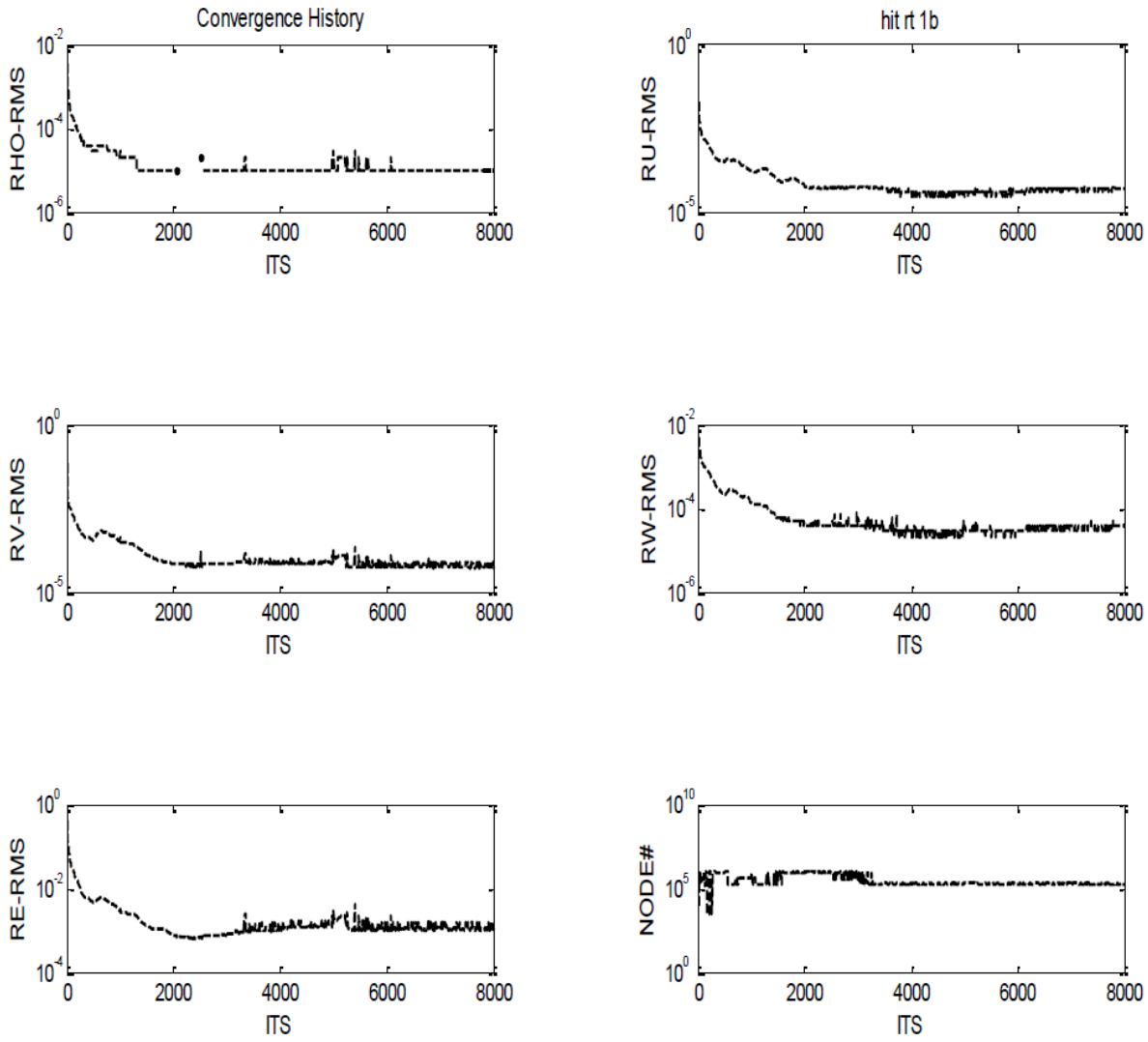

Figure 51: Convergence History of the Steady-State Simulation used for the Convergence Assessment

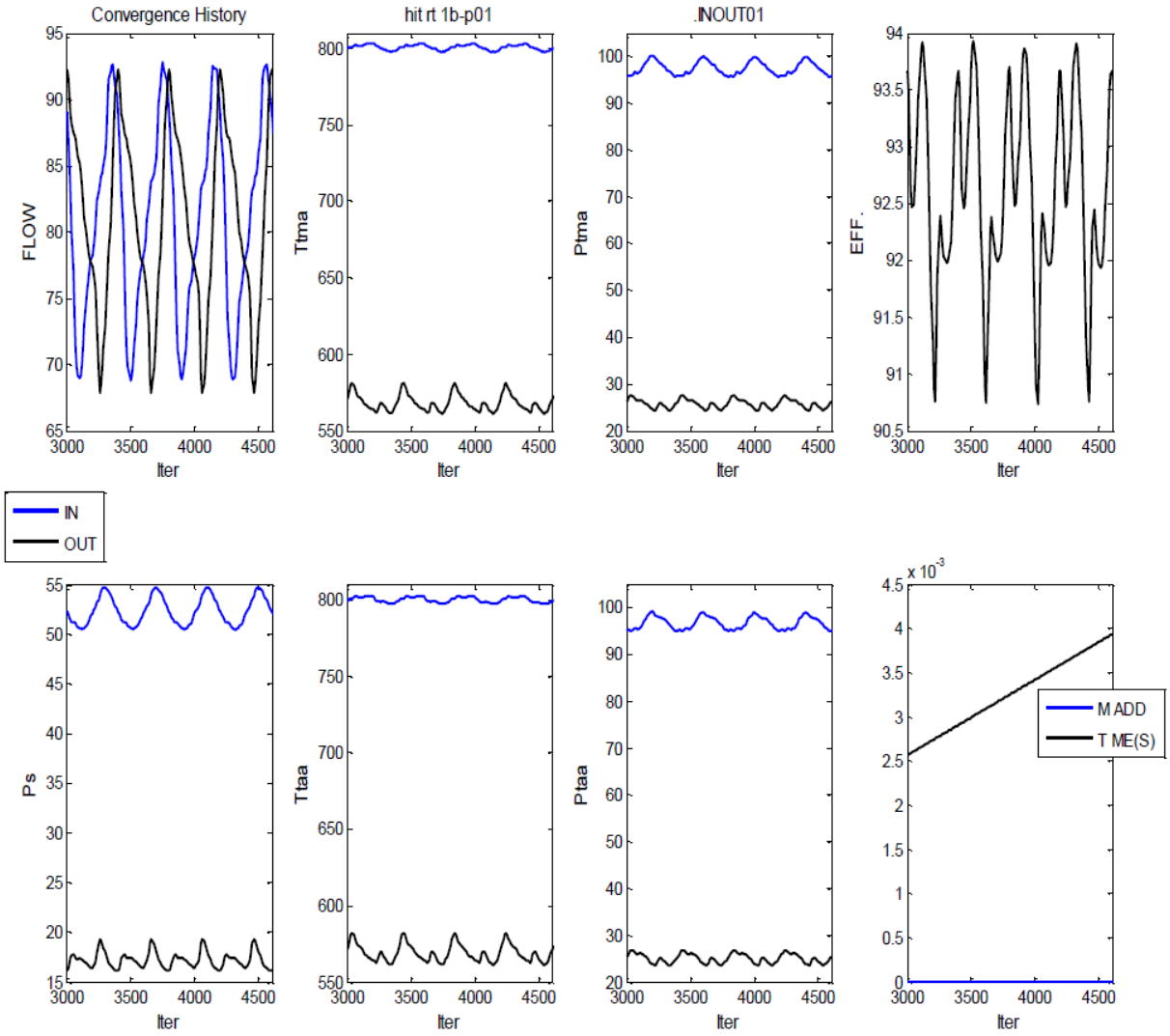

Figure 52: Development of Flowfield Periodicity in Unsteady Analysis used for the Convergence Assessment

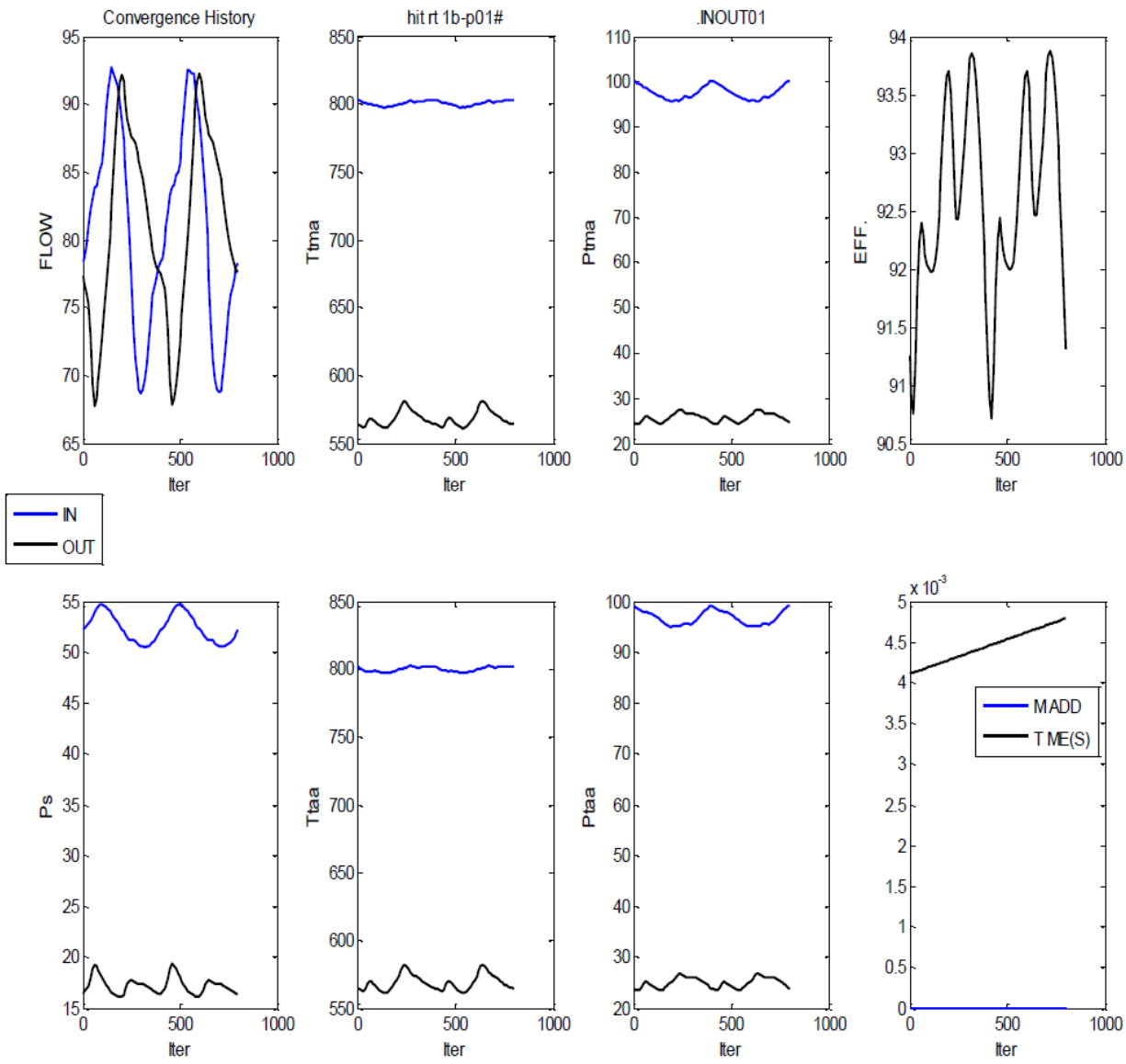

Figure 53: Periodicity of the Flowfield used for the Convergence Assessment

The objective of the grid independence study was to determine the least computationally expensive grid that captured the unsteady physics in the turbine sufficiently. The physics of interest in this study are the unsteady pressures and the signal analysis of those pressures. A power spectral density analysis of the blade suction side at 23 engine order (23E) and 46 engine order (46E) is shown in Figure 54. Relative to the blade, 23E and 46E are the fundamental and first harmonic frequencies of the upstream and downstream vanes, respectively. For a design rotational speed of 7617 rpm, 23E and 46E correspond to frequencies of approximately 2.92 and 5.84 kHz. The cross-passage shock is clearly visible in the figure. Upstream of the shock, the unsteadiness is largely dominated by 23E. However, interaction between the blade and downstream vane is mainly driven by 46E. Therefore, in order to determine a grid suitable for capturing the unsteady aerodynamics of the blade and downstream vane, the time-accurate pressures and signal analysis at 46E were investigated.

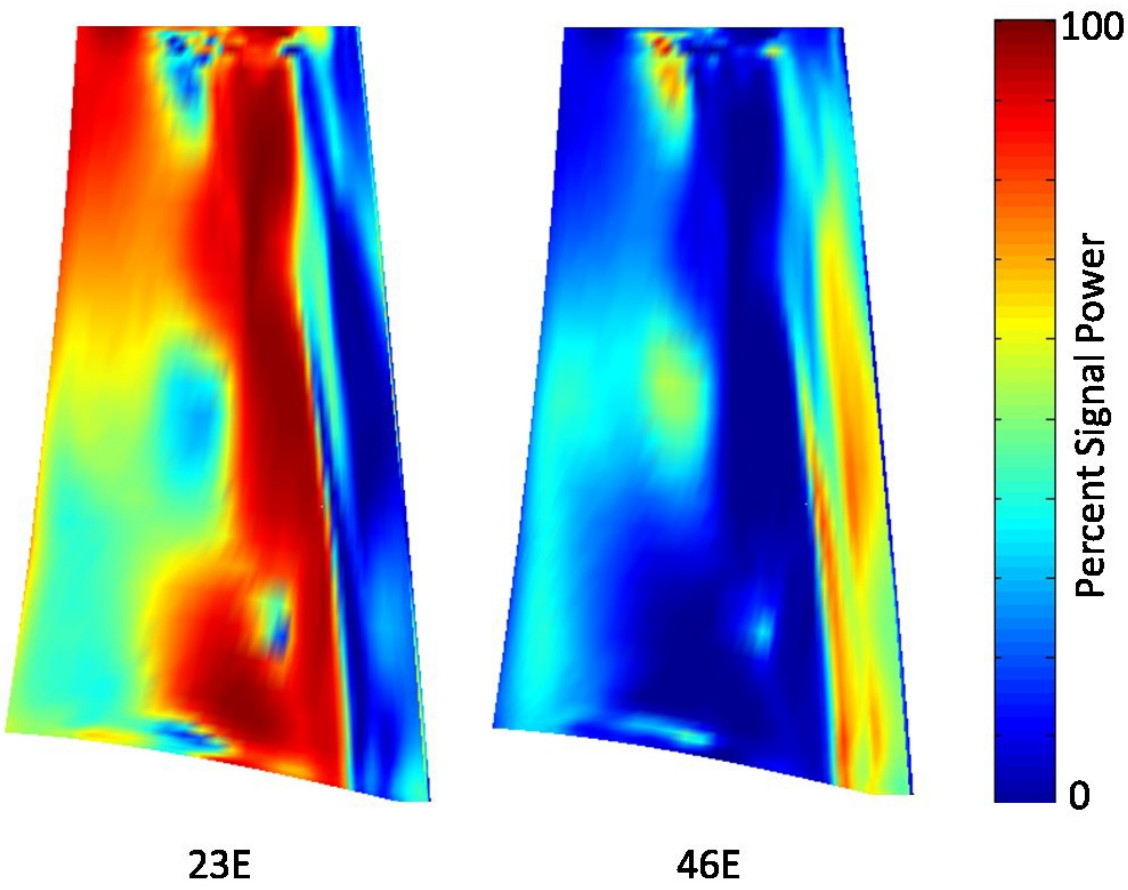

Figure 54: Power Spectral Density Analysis of Blade SS at 23E and 46E

Contours of normalized Discrete Fourier Transform (DFT) of the blade suction side at 5.84 kHz are shown in Figure 55. The five points also shown on the figure are the locations at which time accurate pressure traces and signal analysis were investigated. The points were chosen such that areas of high unsteadiness would be evaluated. As previously described and shown in Figure 54, the unsteadiness at the targeted locations on the blade suction side downstream of the cross passage shock are largely due to the first harmonic of the downstream vane—46E.

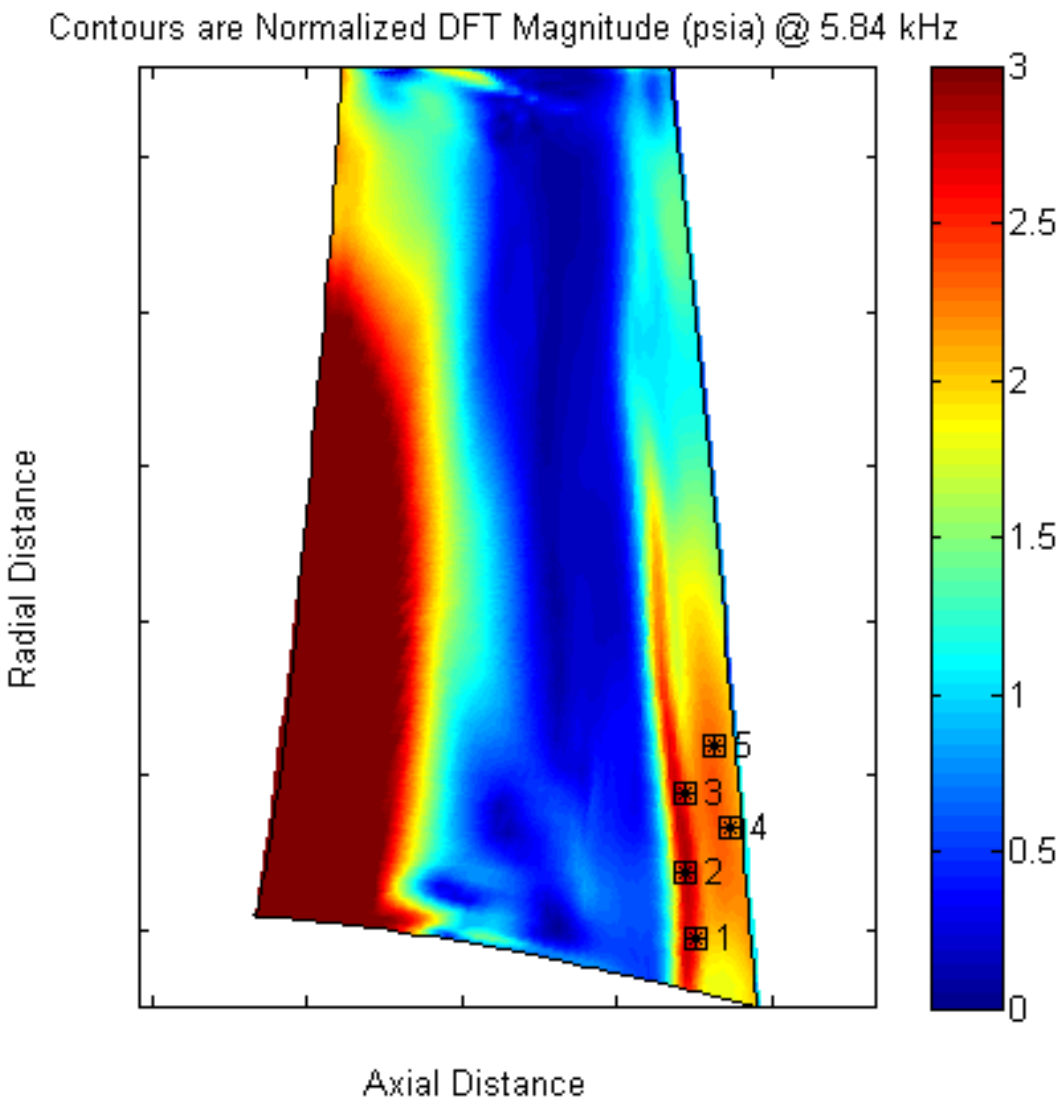

Figure 55: Blade SS Contours of Normalized DFT Magnitude (psia) at 5.84 kHz

Time-accurate static pressures at the five targeted locations on the blade for each grid are shown in Figure 56. The pressure traces shown are from the time-accurate, two- cycle simulation after the unsteady analyses were run to periodic convergence. At the first three points of interest, the pressure traces from Grids 1 through 3—while falling nearly on top of one another—do not quite predict the peaks and valleys as the more dense Grids 4 and 5 do. The latter two grids show very good agreement at all five points. This suggests that Grids 4 and 5 are picking up on physics that the less dense grids are unable to resolve. However, because Grids 4 and 5 are computationally expensive, it is important to investigate the frequencies at which the less dense grids differ from Grids 4 and 5. This is because the frequencies of interest in this study are associated with 23E and 46E. If it can be shown that Grid 3 matches well at these frequencies but misses the higher frequencies, it could be worth choosing Grid 3 rather than the more dense grids because of the computational expense of Grids 4 and 5.

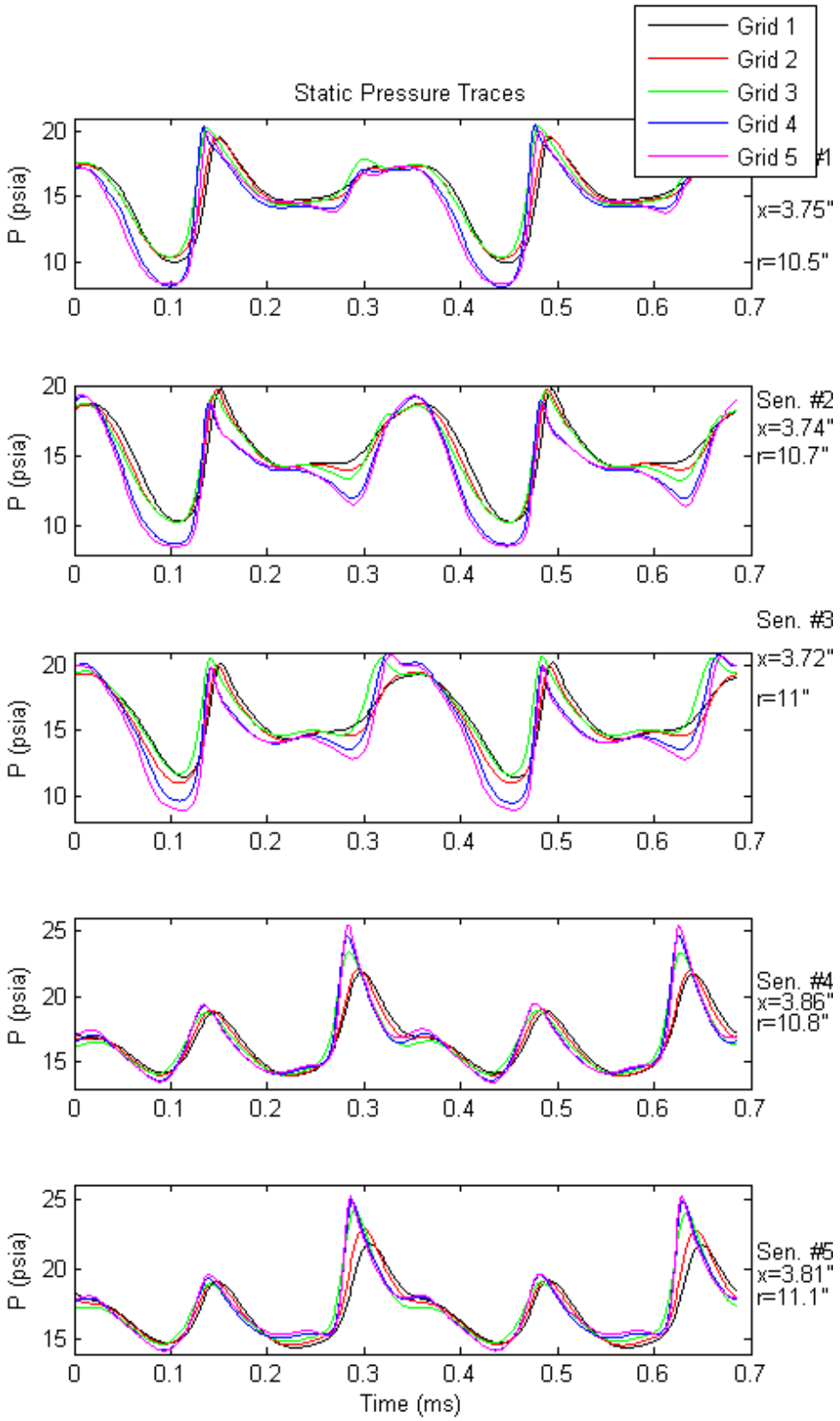

Figure 56: Two-Cycle Time-Accurate Static Pressures at Targeted Locations

Discrete Fourier Transforms (DFT) of the signal at the selected locations were performed for Grids 3, 4, and 5, and are shown in Figure 57 through Figure 61. Pressure traces are shown in the figures as well. Once again, the time-accurate, two-cycle simulation was used for this analysis. The DFT compares the magnitude of the unsteadiness against frequency. The first spike in the DFT plots is at 2.92 kHz, which corresponds to the fundamental frequency of the downstream vane—23E. Similarly, the second spike is the 46E, or first harmonic of the downstream vane, and so on. By investigating the DFTs at each point, it is clear that Grid 3 is not sufficiently resolving the unsteady flow physics of the interaction between the blade and downstream vane. The unsteady magnitudes at 23E and 46E are consistently under predicted relative to Grids 4 and 5. The unsteady magnitudes of Grid 4 and 5 show excellent agreement for not only 23E and 46E, but all other resonant frequencies as well.

Finally, Grid 4 was proven to be in the region of asymptotic grid convergence [41]. This was accomplished by plotting, for each grid, a flow metric against the number of nodes in each grid raised to a fractional quantity. The fractional quantity is determined by dividing the order of accuracy of the code by the number of dimensions involved in the solution, then multiplying by negative one. Since Leo is a second-order accurate code calculating a solution in three-dimensional space, the exponent in this case is negative two-thirds. The flow metric used was the average DFT magnitude on the suction side surface for each grid. A linear relationship between the flow metric and the number of nodes raised to the fractional quantity among three or more grids indicates that those grids are in the region of asymptotic convergence—the point at which no new physics is being resolved by the more dense grids. This is shown in Figure 62, with Grid 1 through 5 depicted from right to left. A linear curve was fit to Grids 3 through 5, illustrating that these grids are in the region of asymptotic convergence. Grid 4 was chosen not only because it was in the region of convergence, but also due to very little change in the time- accurate pressure signals and DFT magnitudes at all frequencies when increasing the density to Grid 5. Grid 4 was used for the remaining analysis in this chapter, as well as in the following chapter for simulations of the unsteady interaction and comparison to experiment.

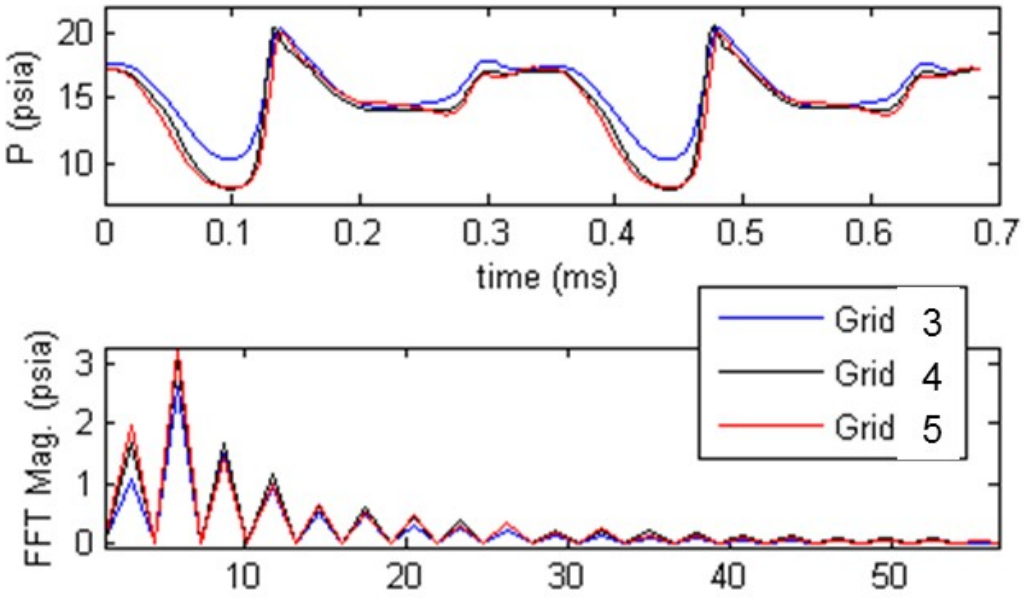

Figure 57: Static Pressure Trace and Fourier Transform Magnitude at Point 1

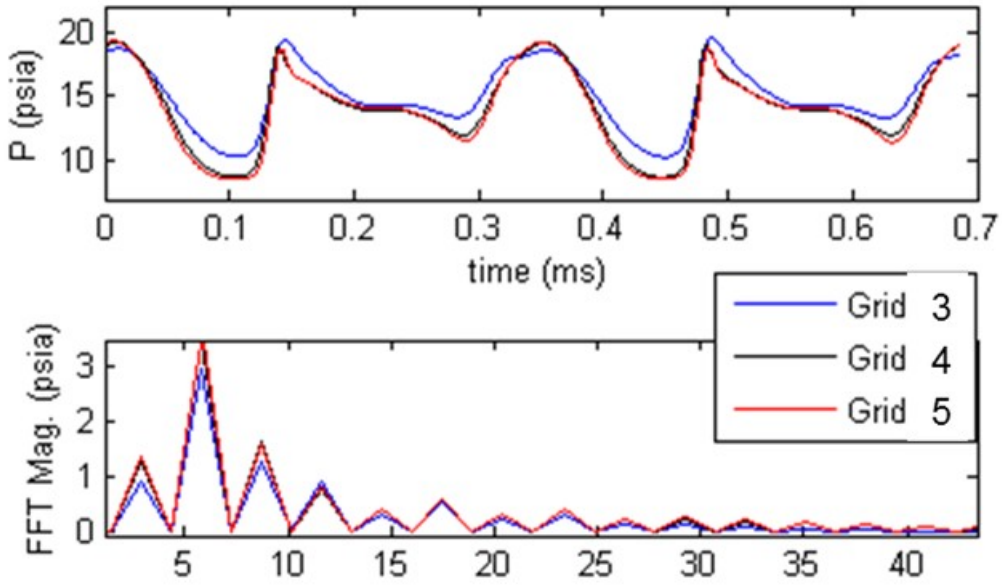

Figure 58: Static Pressure Trace and Fourier Transform Magnitude at Point 2

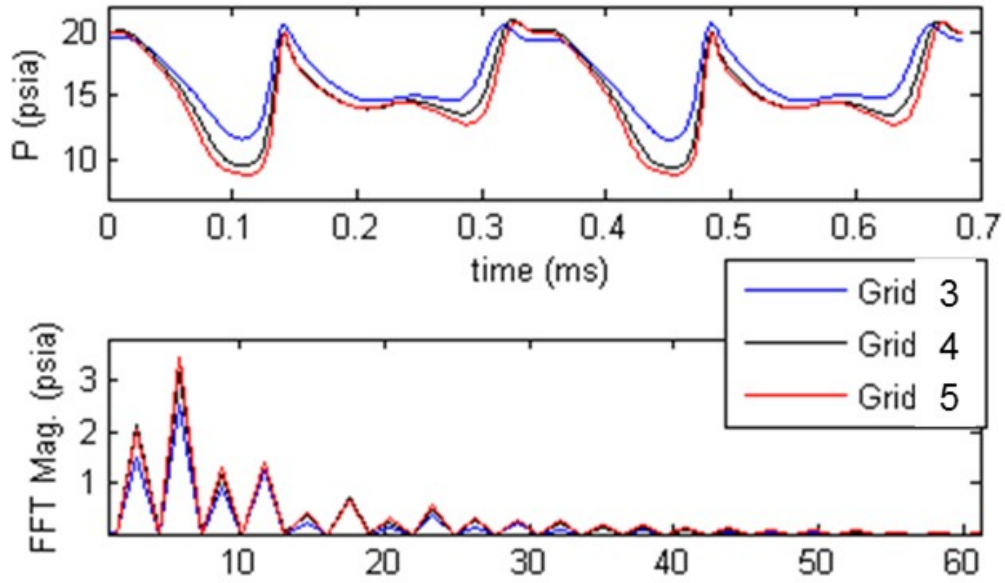

Figure 59: Static Pressure Trace and Fourier Transform Magnitude at Point 3

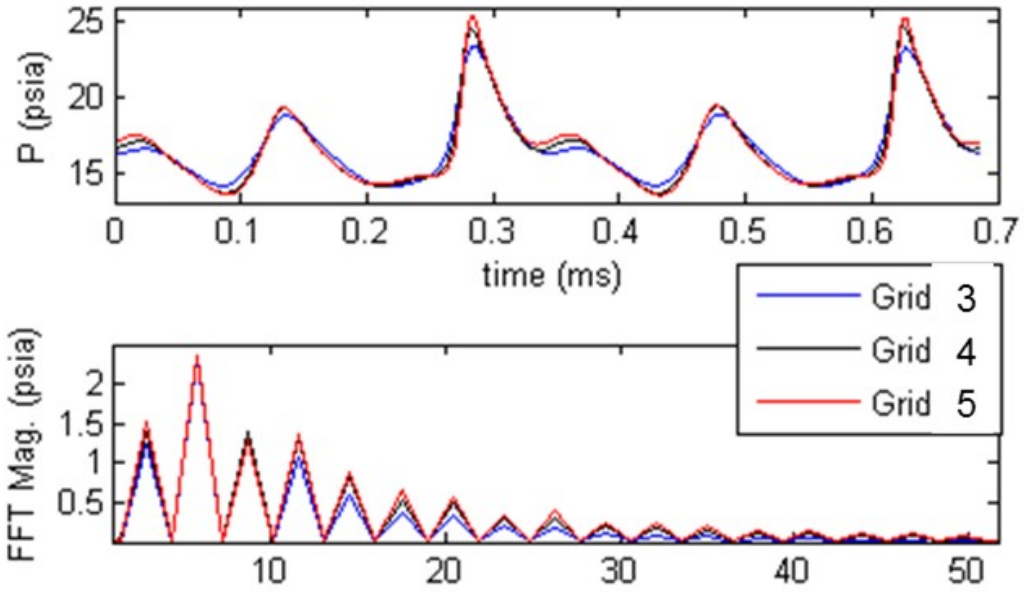

Figure 60: Static Pressure Trace and Fourier Transform Magnitude at Point 4

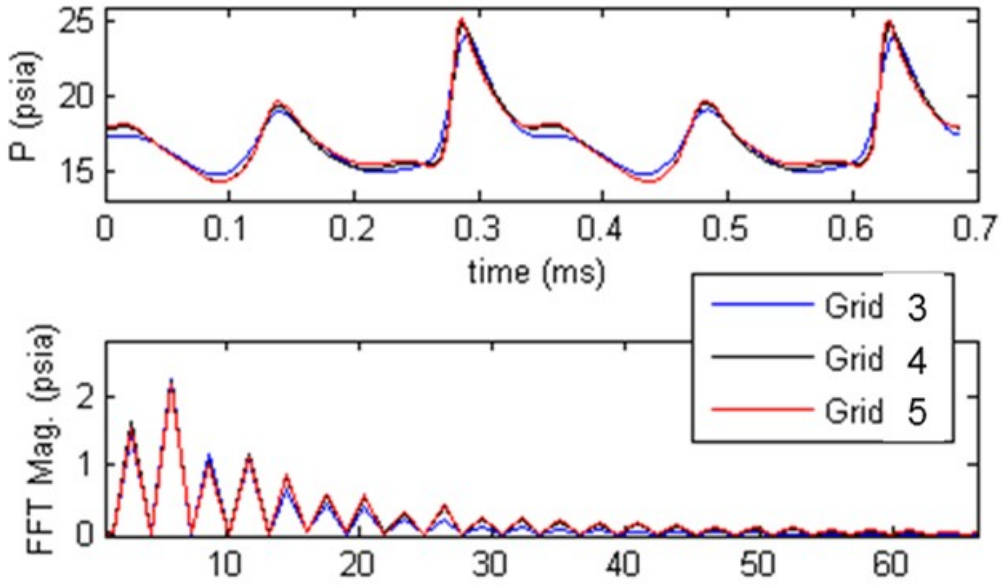

Figure 61: Static Pressure Trace and Fourier Transform Magnitude at Point 5

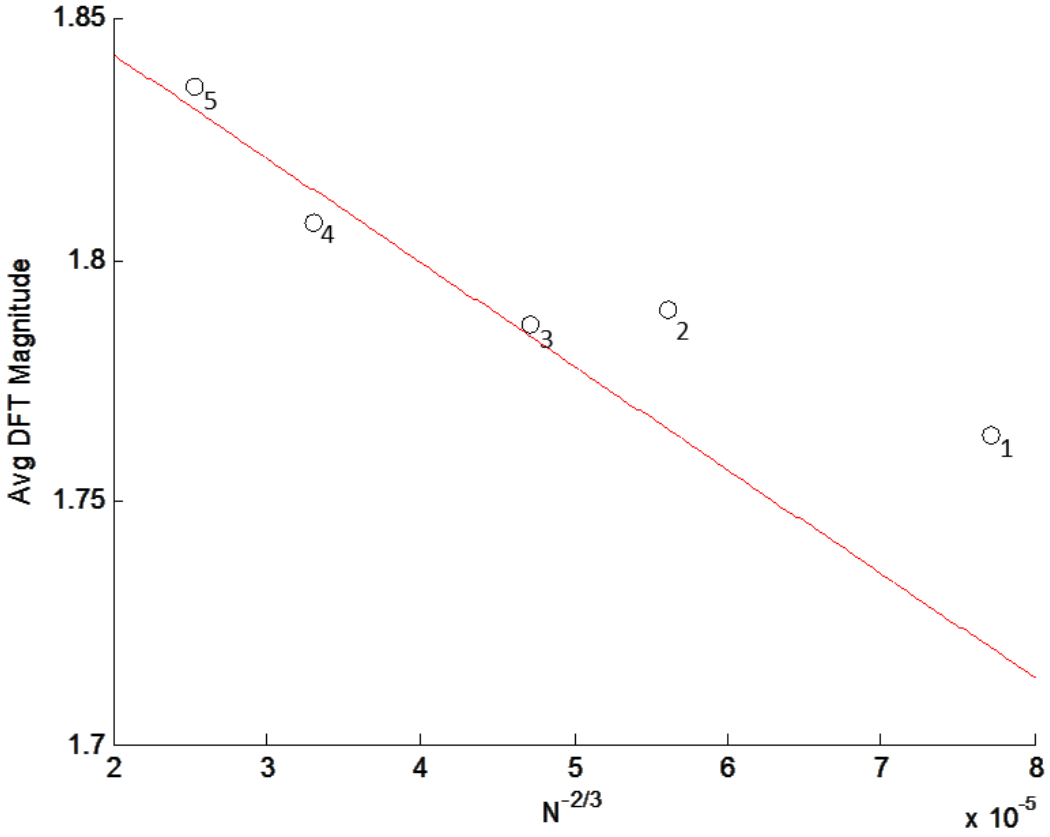

Figure 62: Stage-and-a-Half Region of Asymptotic Grid Convergence

Periodic Convergence

After selecting the appropriate grid density and iterative convergence in the previous section, an assessment of the periodic convergence was completed. A fuzzy logic technique—detailed by Clark [7] was used in this assessment. In this method, the time-mean values over each cycle, f_M; the amplitude, f_A, and phase, f_ϕ, of the Discrete Fourier Transform (DFT); the cross-correlation coefficient (CCF), f_S; and the power spectral density (PSD), f_P;of the surface pressure at the five locations shown in Figure 55—and discussed in the previous section—were analyzed. The values of the signal operations at a given cycle are compared to that of the previous cycle to calculate a convergence value for that cycle. The signal operations listed above were used on the two-cycle post-processing run conducted in the Grid and Iterative Convergence section, and a fuzzy parameter is calculated for each operation at each point. As Clark [7] describes, the overall fuzzy convergence, f_C, is then assessed by taking the minimum value of the fuzzy parameter set. Also, a fuzzy parameter of 95 percent or higher is generally considered well converged.

The fuzzy parameters calculated at each point for the two-cycle post-processing case are shown in Table 8. Note that the fundamental frequency and the first five harmonic frequencies were included in the signal analysis, which captured at least 97 percent of the signal power for each point, as seen in the table. The overall fuzzy convergence is above 95 percent—e.g., "well converged"—for all points, with the exception of Point 3. The 115E DFT amplitude parameter is approximately 93 percent, which is the minimum fuzzy set value for Point 3, and therefore the overall convergence value. A crucial takeaway from a fuzzy set periodic convergence analysis—and hence the power of the tool—is that the most important quantities are sufficiently converged. In this study, the critical parameters are the 23E and 46E DFT magnitude and phase parameters, along with the time-mean, CCF, and PSD parameters. This is because the focus is on the vane-blade interaction driven for the most part by the fundamental and the first harmonic frequencies. It is shown in Table 8 that the critical parameters are very well converged, all of which are greater than 97 percent. Therefore, this method of running the unsteady numerical analysis and the subsequent post-processing cycles provide sufficient periodic convergence.

Table 8: Fuzzy Set Convergence

	Parameter Value				
Fuzzy Set	Point 1	Point 2	Point 3	Point 4	Point 5
f_M	99.73%	99.50%	99.53%	99.87%	99.91%
f_A(23E)	98.83%	96.94%	98.82%	95.55%	97.61%
f_ϕ(23E)	98.32%	97.30%	98.37%	99.06%	98.94%
f_A(46E)	99.41%	99.55%	99.66%	99.75%	99.90%
f_ϕ(46E)	99.20%	99.30%	99.09%	99.47%	99.32%
f_A(69E)	99.54%	97.69%	98.08%	99.08%	98.19%
f_ϕ(69E)	99.07%	99.07%	99.16%	99.04%	98.68%
f_A(92E)	96.96%	99.51%	99.51%	98.92%	98.70%
f_ϕ(92E)	97.85%	97.40%	97.90%	98.85%	98.34%
f_A(115E)	98.09%	98.02%	93.15%	99.40%	99.96%
f_ϕ(115E)	99.49%	98.39%	99.43%	98.13%	97.23%
f_A(138E)	95.45%	96.89%	97.91%	96.01%	96.95%
f_ϕ(138E)	97.63%	97.13%	96.55%	97.80%	97.46%
f_S	99.92%	99.90%	99.86%	99.93%	99.91%
f_P	98.04%	97.99%	97.48%	98.28%	98.03%
f_C	**95.45%**	**96.89%**	**93.15%**	**95.55%**	**96.95%**

Temporal Convergence

Cooled and uncooled cases were used to determine the appropriate temporal resolution for modeling the full stage-and-a-half Research Turbine using 3-D, time-accurate computation. A 1/23rd sector—1 vane: 2 blades: 1 vane—was used to complete the temporal convergence study. The rainbow cooling configuration of the first vane and blade allows for many cooled and uncooled combinations of the first stage airfoils. For the cooled case in this study, the first vane and both blades were cooled. Recall that the second vane is uncooled in the rig and, therefore, not cooled in any numerical computation.

The cases that were used in this study are shown in Table 9. Temporal resolutions of 100, 200, 400, and 800 time-steps per cycle were run for both the cooled and uncooled configurations. Based on the vane and blade counts of the Research Turbine, a cycle consists of the movement of the blade through a 1/23rd sector of the wheel. Cooled airfoils were included in this study to investigate whether the addition of cooling flow affected the convergence of a solution for a given temporal resolution.

Table 9: Temporal Resolution Study

Cooling	Temporal Resolution (Time-steps per cycle)
Uncooled	100
Uncooled	200
Uncooled	400
Uncooled	800
Cooled	100
Cooled	200
Cooled	400
Cooled	800

Each of the time-accurate, uncooled cases originated from the same uncooled, steady case discussed in the Grid and Iterative Convergence section. Following the convergence of the steady-state computation, the steady solution was used as an initial condition for each of the four temporal resolution cases. For each of these cases, the time- steps per cycle were set to the corresponding values and the simulation was run until periodic convergence was evident. The periodic convergence of the uncooled, 400 time- steps per cycle case is shown in Figure 63. Mass flow, mass- and area-average total pressure and temperature, efficiency, and static pressure of the blade row are plotted against iteration number. The figure illustrates that the numerical solution has attained at least four cycles of periodicity. The two-period cycles of the aforementioned flow variables are shown in Figure 64. Once again, the blade row of the uncooled, 400 time-steps per cycle case is shown in the figure. Signal processing was conducted using the results from the two-cycle runs.

The cooled cases were run in the same manner. The unsteady periodic convergence and two-period cycle periodicity of the blade row for the cooled, 400 time- steps per cycle cases are shown in Figure 65 and Figure 66, respectively. As seen in the figures, the cooled and uncooled cases achieved periodic convergence prior to signal processing, and the signal processing was conducted on an exact two-cycle period for each case.

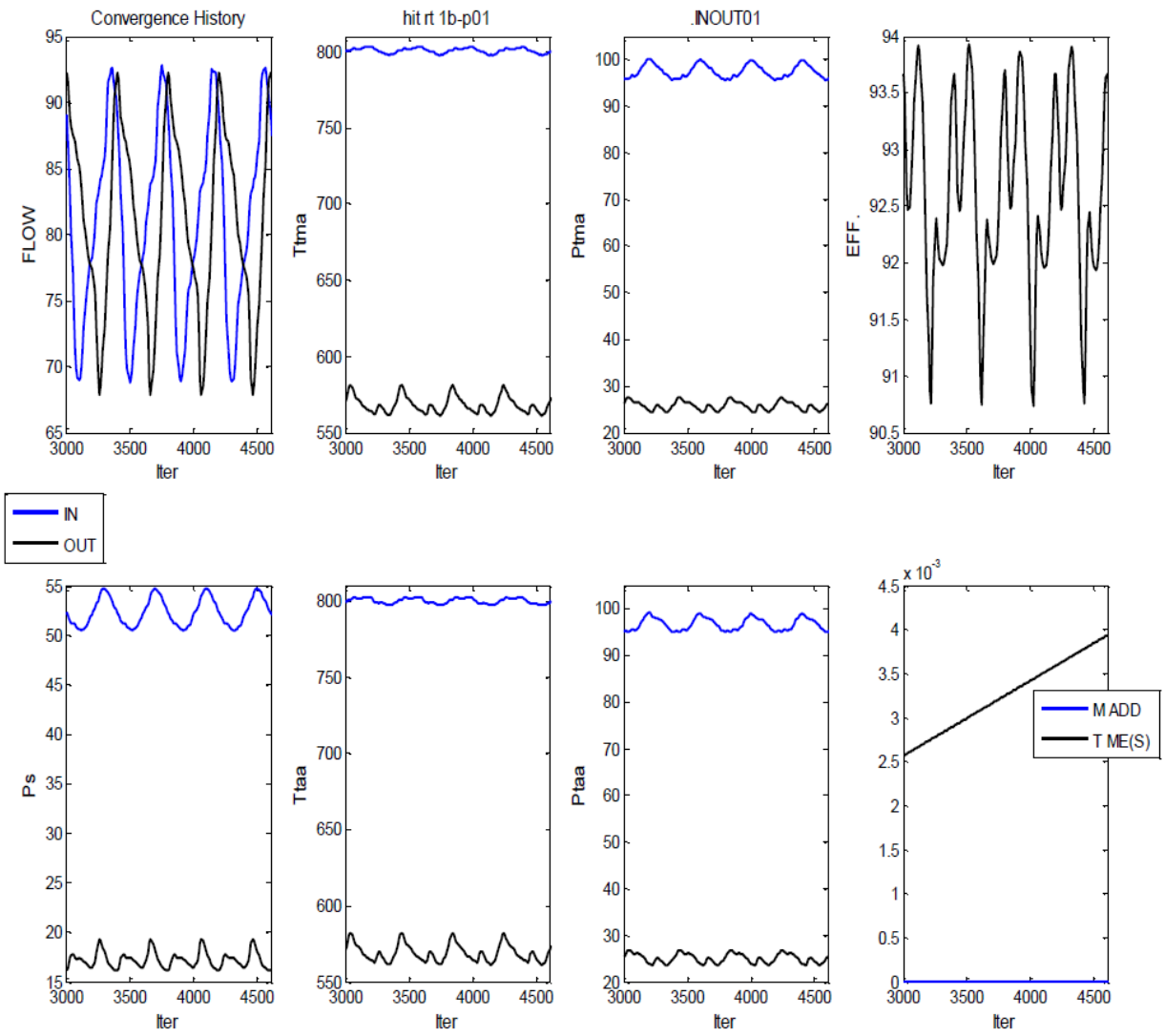

Figure 63: Unsteady Stage-and-a-Half Periodic Convergence of the 1B in the Uncooled, 400 Time-steps per Cycle Case

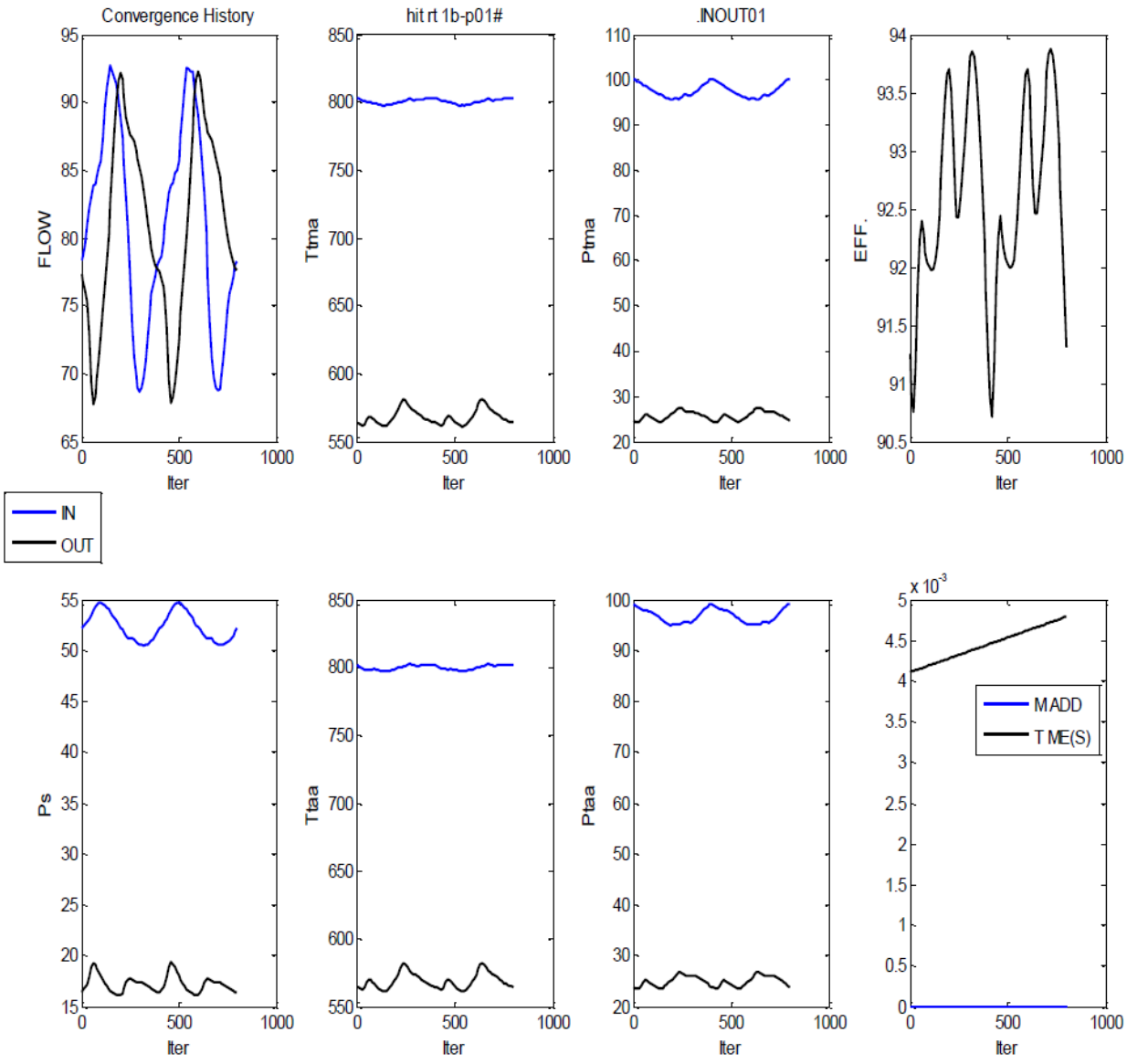

Figure 64: Unsteady Stage-and-a-Half Periodicity of the 1B in the Uncooled, 400 Time-steps per Cycle Case

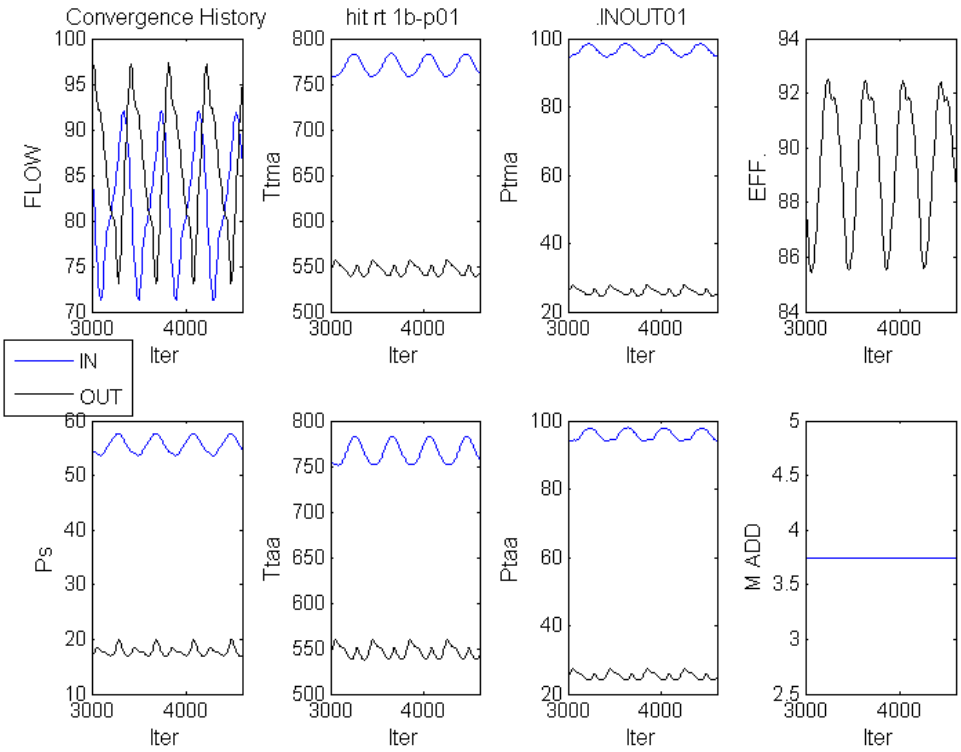

Figure 65: Unsteady Stage-and-a-Half Periodic Convergence of the 1B in the Cooled, 400 Time-steps per Cycle Case

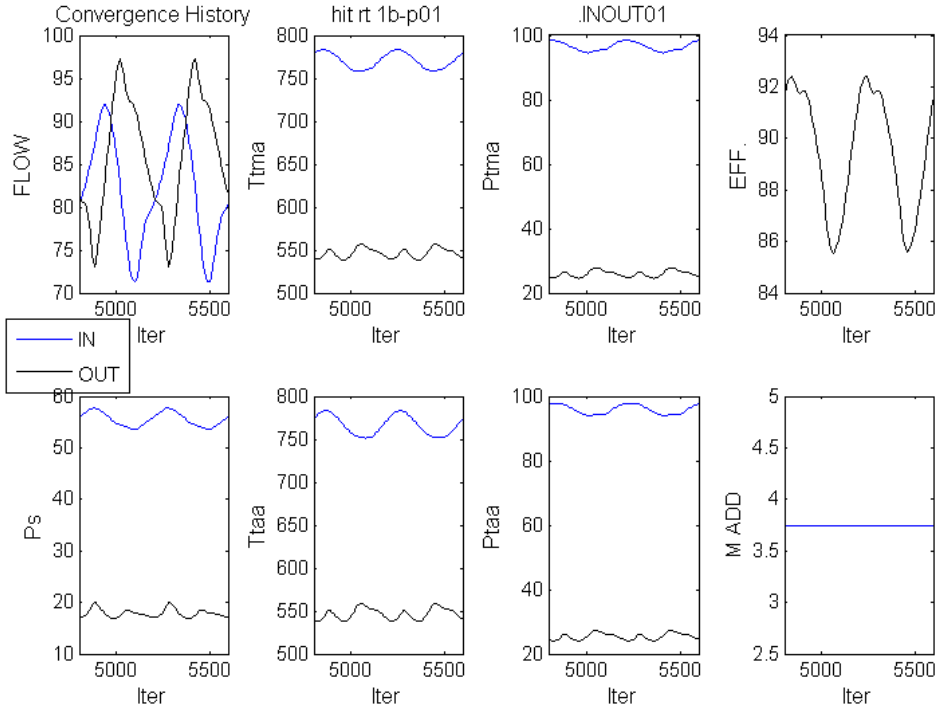

Figure 66: Unsteady Stage-and-a-Half Periodicity of the 1B in the Cooled, 400 Time-steps per Cycle Case

The objective of the temporal resolution study was to determine the least computationally expensive resolution that was sufficient to model accurately the unsteady interaction between the blade and downstream vane. Larger numbers of time-steps per cycle correlates to more time required to execute the numerical analysis, therefore, fewer time-steps are desirable from a computer resource standpoint. As shown in the previous section regarding spatial resolution, the interaction between the blade and downstream vane are largely driven by the first harmonic of the blade, or the 46^{th} engine order at 5.84 kHz. Therefore, the temporal resolution study also focuses on the convergence of the unsteady pressures at this frequency.

Normalized Discrete Fourier Transforms (DFT) at 5.84 kHz of the blade suction side for the uncooled cases are shown in Figure 67. The numbered points on the figures are locations in which pressure traces were analyzed and will be discussed later in this section. Upon close investigation of the uncooled DFT contours, the differences in the 100 and 200 time-step contours are significant. Also, there are noticeable changes when comparing the 200 and 400 time-step cases, though not as distinct as the previous two cases. When comparing the 400 and 800 time-step cases, the DFT contours are nearly identical. The differences between the DFT contours can be more easily visualized in Figure 68, which plots the percent difference between the 800 time-step per cycle case and the 100, 200, and 400 time-steps per cycle cases from left to right, respectively, at each grid point. Values near zero indicate small changes from each time-step case compared to the 800 time-step case. The differences between the DFT contours of the 400 and 800 time-step per cycle cases are extremely small, especially downstream of the shock in which the interaction with the second vane dominates. This indicates that the 400 time-step solution is capturing the physics sufficiently at 5.84 kHz, within the limits of the RANS model.

Similarly, the normalized Discrete Fourier Transforms at 5.84 kHz of the blade suction side for the cooled cases are shown in Figure 69. The percent differences between the 800 time-step per cycle case and the 100, 200, and 400 time-steps per cycle cases at each grid point are plotted in Figure 70 from left to right, respectively. As with the uncooled analysis, the 400 time-step per cycle case shows very little difference in the DFT when compared to the 800 time-step case. This indicates that the 400 time-step solution is sufficiently capturing the physics at 5.84 kHz for the cooled turbine as well.

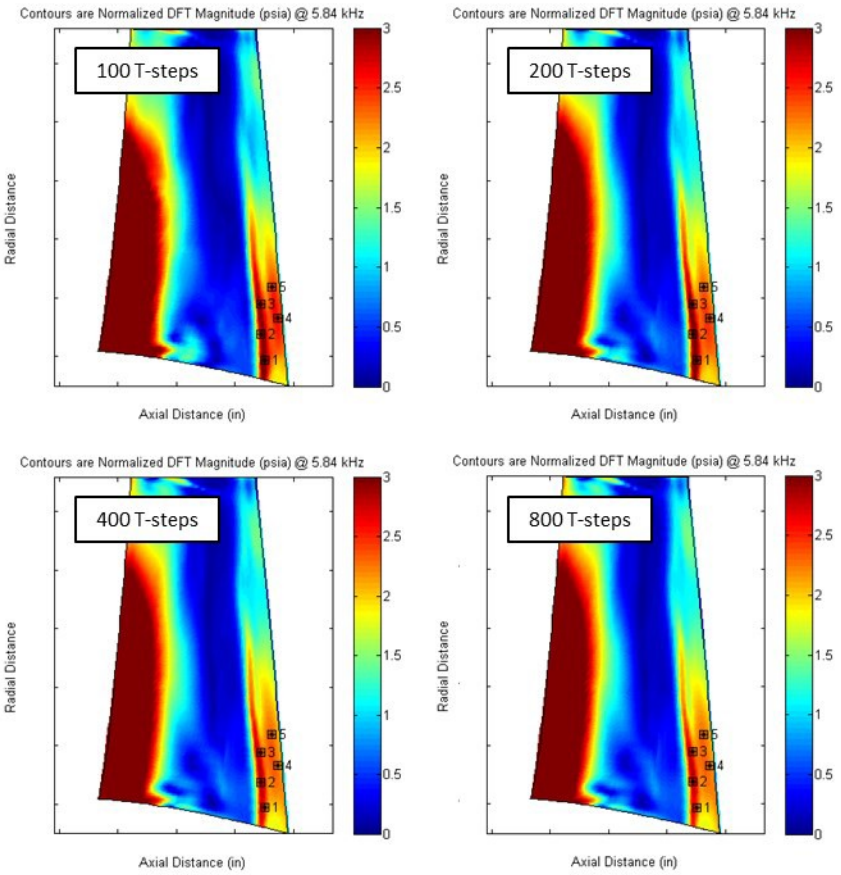

Figure 67: Normalized Discrete Fourier Transforms of the Blade SS at 5.84 kHz for Uncooled Temporal Resolution Analysis

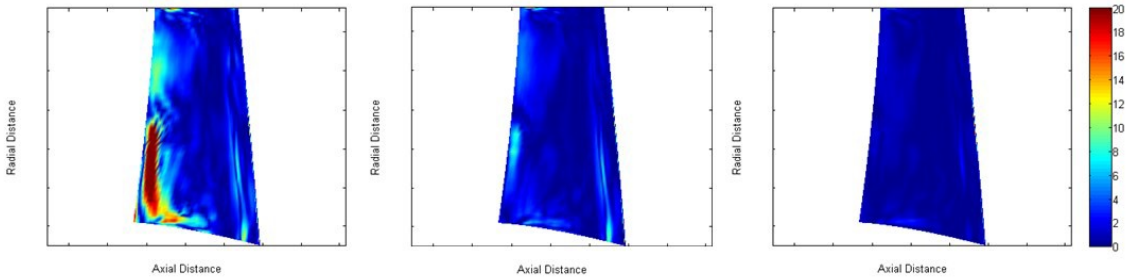

Figure 68: Percent Differences of the Normalized Discrete Fourier Transform of the Uncooled 800 Time-Steps per Cycle Case Compared to the 100 (left), 200 (center), and 400 (right) Time-Steps per Cycle Cases

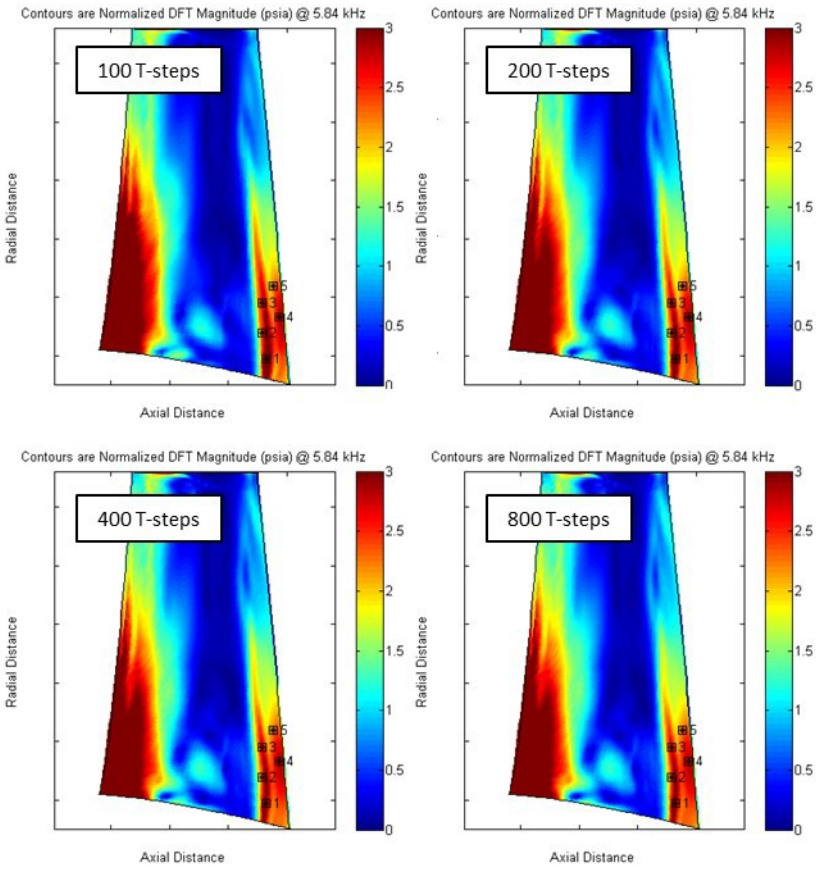

Figure 69: Normalized Discrete Fourier Transforms of the Blade SS at 5.84 kHz for Cooled Temporal Resolution Analysis

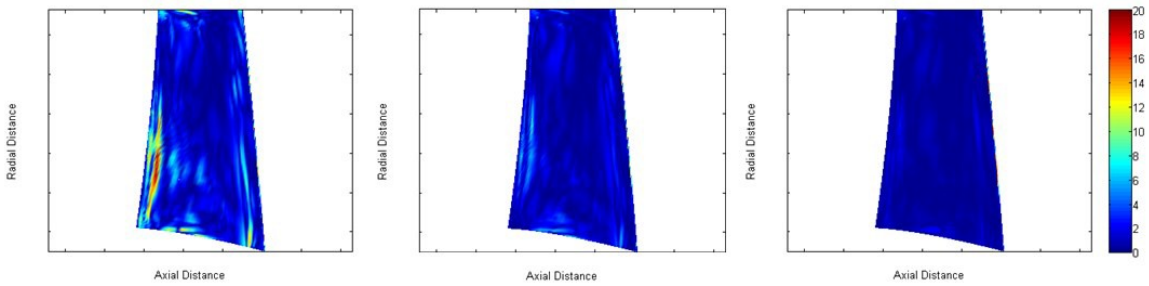

Figure 70: Percent Differences of the Normalized Discrete Fourier Transform of the Cooled 800 Time-Steps per Cycle Case Compared to the 100 (left), 200 (center), and 400 (right) Time-Steps per Cycle Cases

Static pressure traces at five locations on the blade suction side were also investigated during the temporal resolution analysis. The locations are shown and numbered in Figure 67 and Figure 69. The coordinates are identical between the uncooled and cooled cases. The static pressures for the uncooled cases over the two-period cycle for points 1 through 5 are shown in Figure 71 through Figure 75, respectively. The Fast Fourier Transforms of the two-period cycle are also plotted in the figures. As the number of time-steps

per cycle increases, the pressure traces begin to align with one another. Very little difference is evident between the 400 and 800 time-steps per cycle cases. The Fourier transform can indicate which frequencies are the sources of the physics that may not be captured if the static pressure traces differ between time-step resolutions. The Fourier Transforms of the 100 and 200 time-steps per cycle cases differ from those of the 400 and 800 time-step cases at two crucial frequencies: the fundamental (2.92 kHz) and first harmonic (5.84 kHz) frequencies. The interaction between the downstream vanes is largely dominated by the first harmonic, but the fundamental frequency influences the reaction downstream of the shock as well. For a particular time resolution to be considered to have sufficiently captured the physics for the research of interest being investigated in this thesis, the fundamental and first harmonic frequencies should be converged. There is very little difference in the static pressure traces and Fourier transform signal analysis between the 400 and 800 time-steps per cycle cases.

The static pressures and Fourier Transforms for the cooled cases over the two- period cycle for points 1 through 5 are shown in Figure 76 through Figure 80, respectively. The results of the cooled cases are very similar to those of the uncooled cases. As the number of time-steps per cycle increases, the static pressure traces and signal analyses converge. The 400 and 800 time-steps per cycle cases show very good correlation and are considered converged.

For both the uncooled and cooled cases, the 400 time-steps per cycle cases are sufficiently converged compared to the 800 time-steps per cycle cases. The normalized DFT magnitude of the blade suction side at 5.84 kHz, pressure traces, and Fourier signal analyses between the two resolutions showed very little difference. Therefore, 400 time- steps per cycle will be used to model the unsteady interaction between the blade and downstream vane.

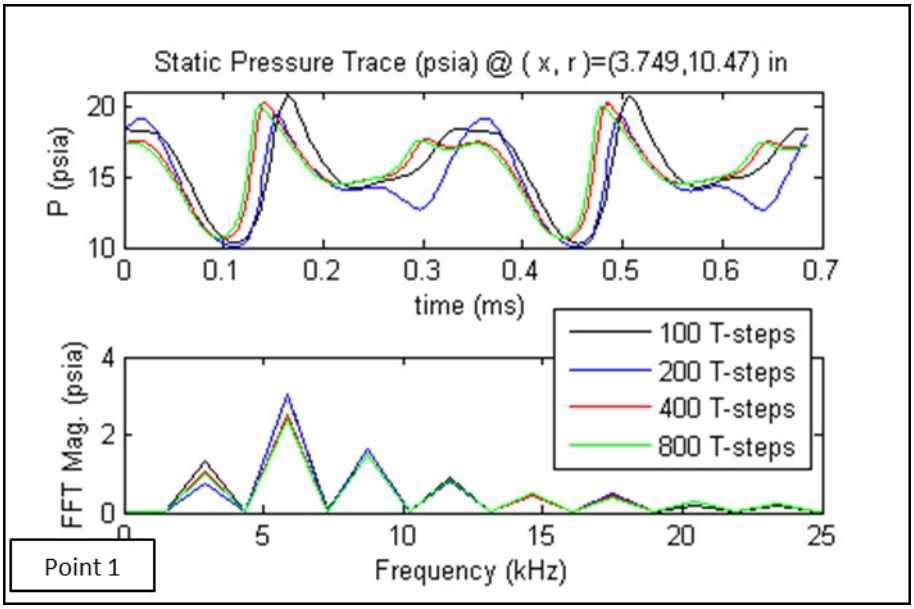

Figure 71: Uncooled Static Pressure Trace and Fourier Transform Analysis for Temporal Resolution Study at Point 1

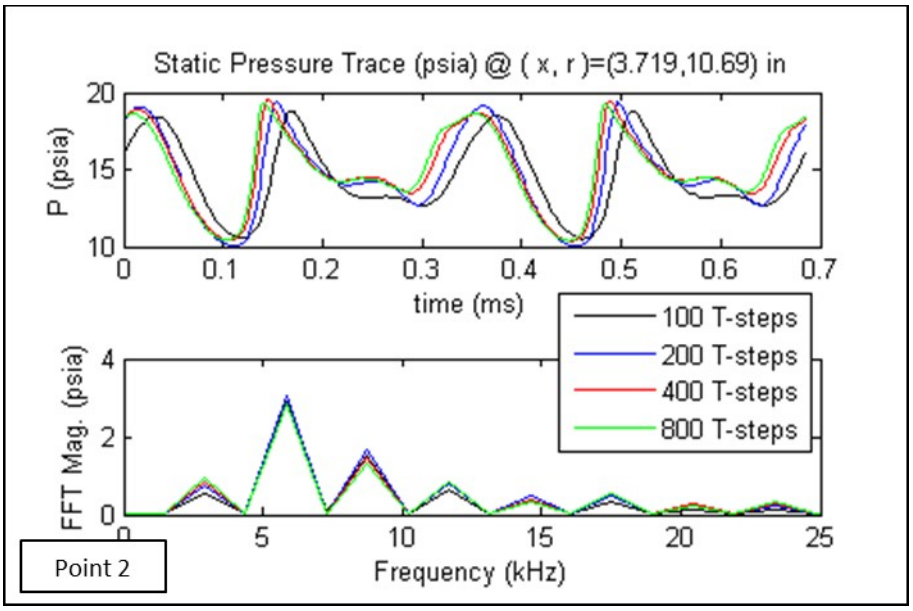

Figure 72: Uncooled Static Pressure Trace and Fourier Transform Analysis for Temporal Resolution Study at Point 2

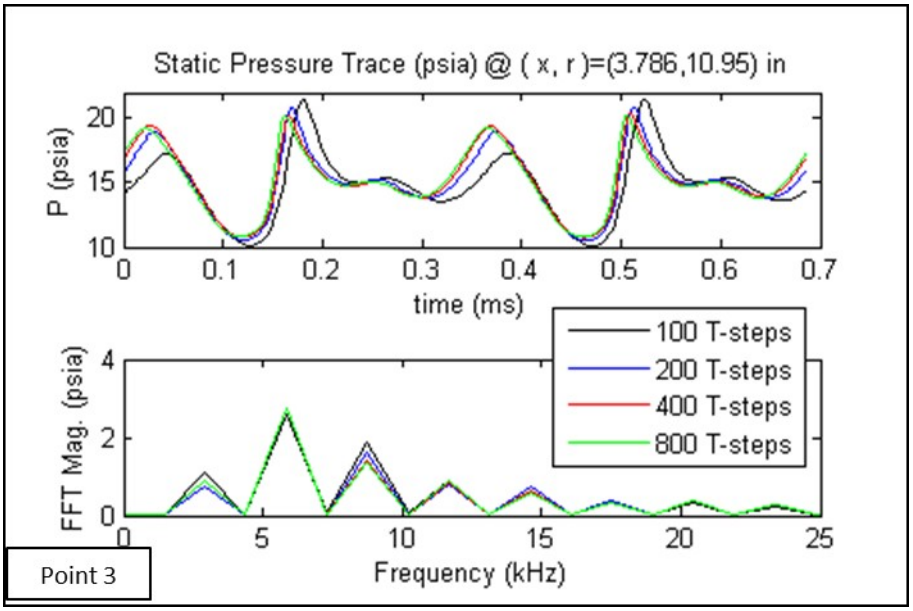

Figure 73: Uncooled Static Pressure Trace and Fourier Transform Analysis for Temporal Resolution Study at Point 3

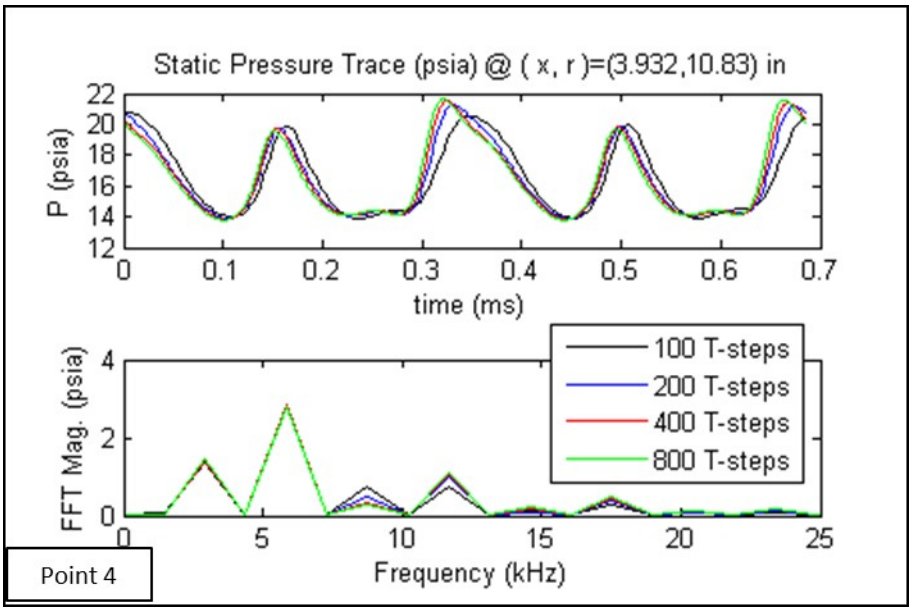

Figure 74: Uncooled Static Pressure Trace and Fourier Transform Analysis for Temporal Resolution Study at Point 4

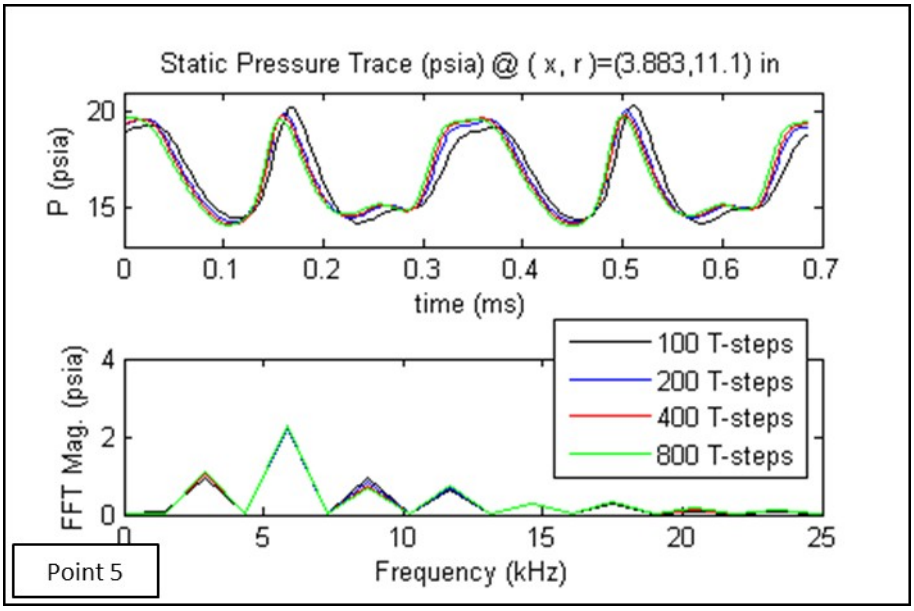

Figure 75: Uncooled Static Pressure Trace and Fourier Transform Analysis for Temporal Resolution Study at Point 5

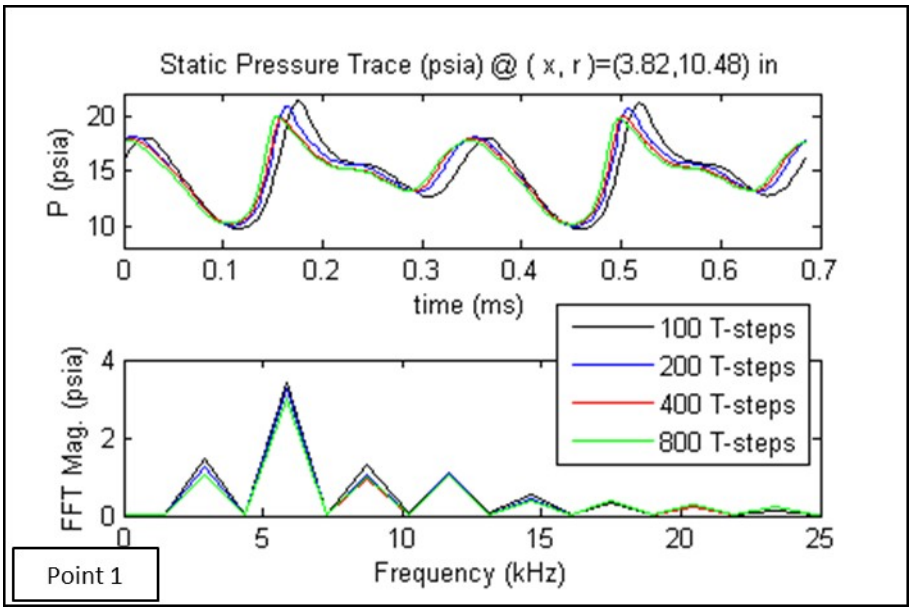

Figure 76: Cooled Static Pressure Trace and Fourier Transform Analysis for Temporal Resolution Study at Point 1

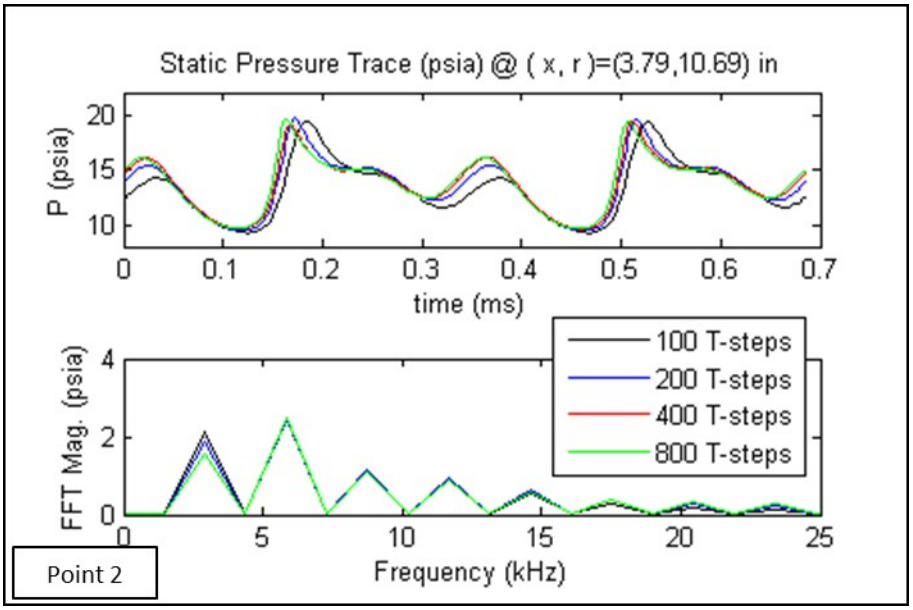

Figure 77: Cooled Static Pressure Trace and Fourier Transform Analysis for Temporal Resolution Study at Point 2

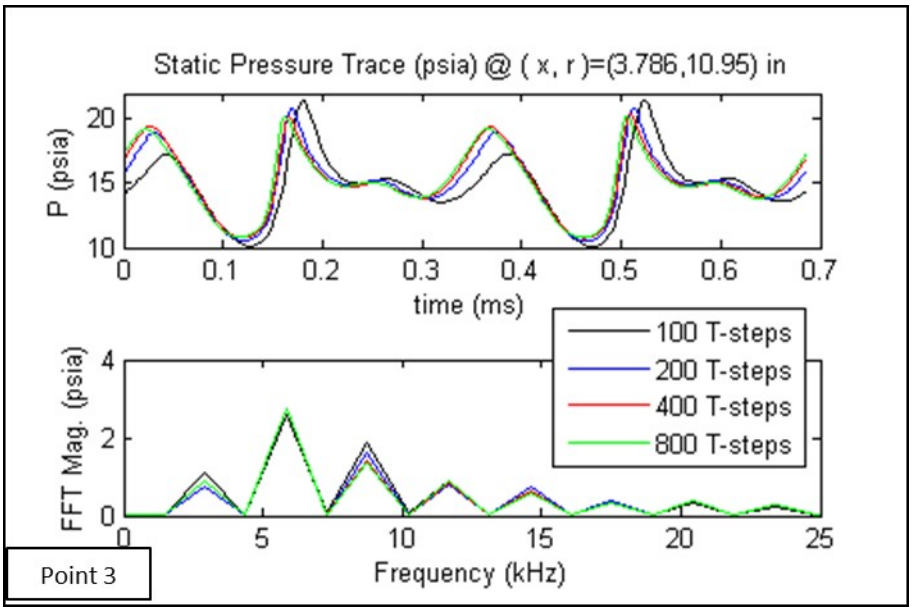

Figure 78: Cooled Static Pressure Trace and Fourier Transform Analysis for Temporal Resolution Study at Point 3

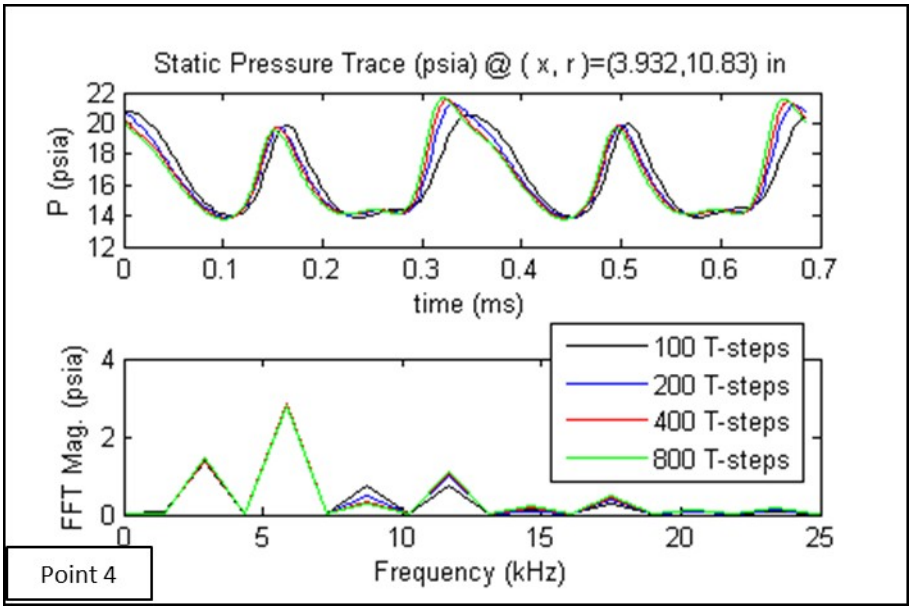

Figure 79: Cooled Static Pressure Trace and Fourier Transform Analysis for Temporal Resolution Study at Point 4

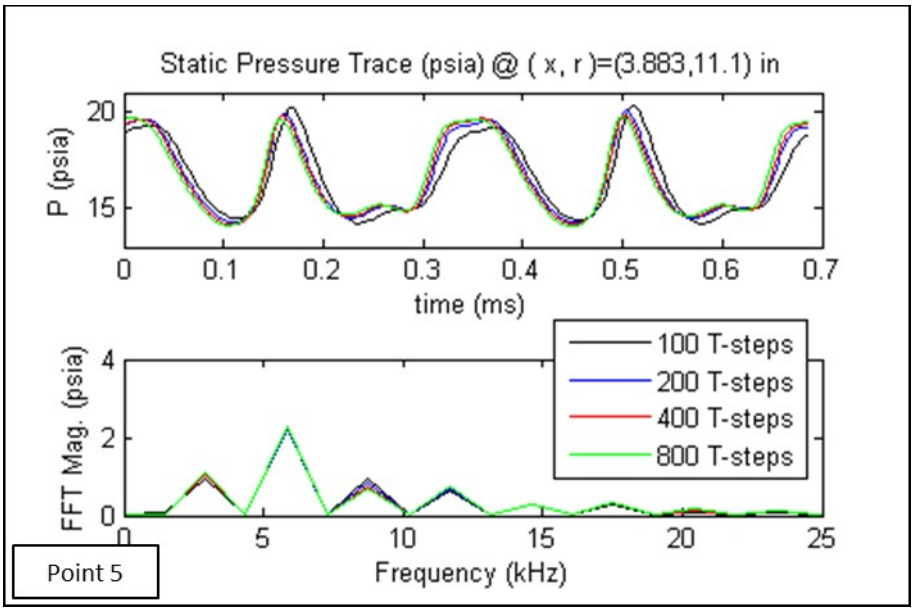

Figure 80: Cooled Static Pressure Trace and Fourier Transform Analysis for Temporal Resolution Study at Point 5

Geometric Model Convergence

The determination of a sufficient wheel section for modeling the stage-and-one- half Research Turbine was made by evaluating a number of varying wheel sectors with varying degrees of cooling. The rainbow cooling configuration of the first vane and blade allows for several cooled and uncooled combinations of the first stage airfoils when modeling only a fraction of the wheel. The cooled and uncooled airfoils for the first stage are shown once again in Figure 81. The cases used in this study are shown in Table 10.

Three wheel sectors were used, all of which maintained the 1:2:1 airfoil ratio: a 1/23rd sector, a 3/23rd sector, and a full wheel. The 1/23rd and 3/23rd sectors are compared to the full wheel analysis to determine whether either wheel fraction can provide sufficient accuracy while saving the computational resources that would be required to model a full wheel. The spatial resolution of the grids for each sector was identical. In other words, the full wheel simulation contains twenty-three times the number of cells as the simulations modeling only 1/23rd sector of the wheel.

For each sector, the most prominent cooled and uncooled combinations were modeled. As shown in Figure 81, the cooled and uncooled first vanes are grouped. Therefore, in the cases outlined in Table 10, the vanes are either all cooled or all uncooled. The blades generally follow a pattern of four cooled airfoils and two uncooled airfoils. The 1/23rd sector approximates this by modeling both blades as cooled or uncooled. The 3/23rd sector models four cooled and two uncooled blades. The full wheel simulation matches exactly the cooling scheme shown in Figure 81 for the vanes and blades. Recall that the second vane is uncooled in the rig and, therefore, not cooled in any numerical computation.

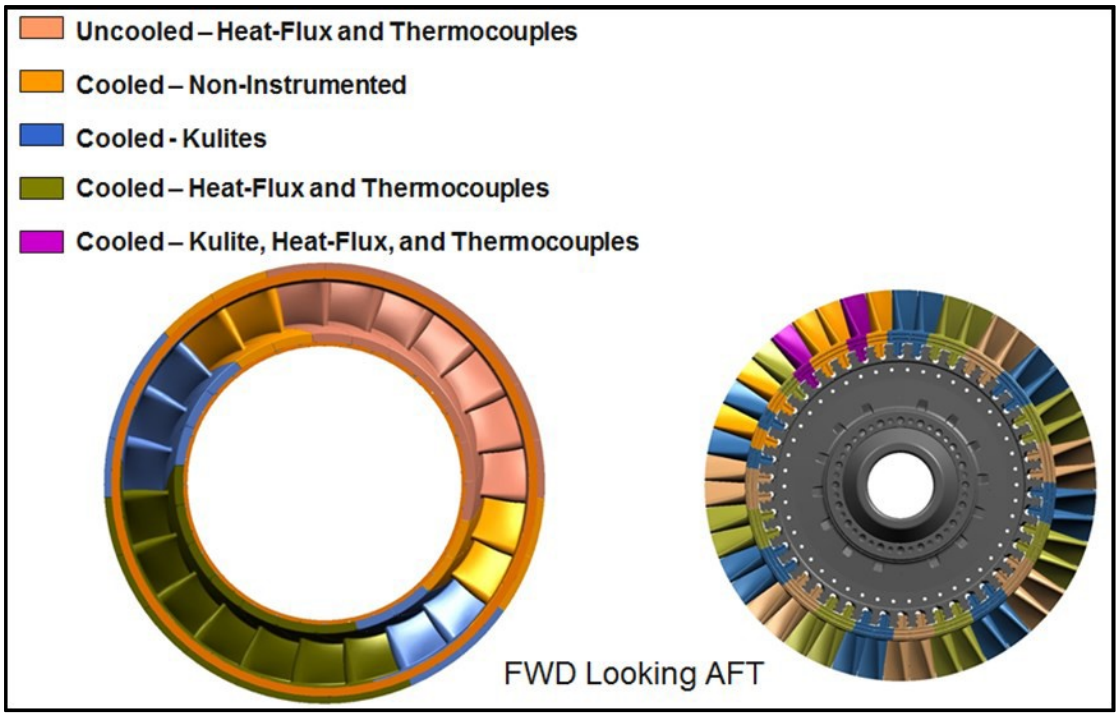

Figure 81: HIT RT Vane and Blade Cooled Schematic

Table 10: Wheel Sector Study Cases

Case	1V		1B		2V	
	N_{af}	Cooling	N_{af}	Cooling	N_{af}	Cooling
1	1	uncooled	2	uncooled	1	uncooled
2	1	cooled	2	uncooled	1	uncooled
3	1	uncooled	2	cooled	1	uncooled
4	1	cooled	2	cooled	1	uncooled
5	3	uncooled	6	2u/4c	3	uncooled
6	3	cooled	6	2u/4c	3	uncooled
7	23	7u/16c	46	12u/34c	23	uncooled

Each sector case was converged to a steady-state before running time-accurate solutions. All numerical solutions were run with 400 time-steps per cycle. As shown in Figure 82, the residuals were reduced to at most 10^{-3} for each variable of interest. Case 1 is shown in the figure; however, each sector case was run in the same specified manner. The cases were then run until periodic convergence was evident. Mass flow, mass- and area-average total pressure and temperature, efficiency, and static pressure are plotted against iteration number in Figure 83. All quantities have attained periodicity during the last four-plus blade passings. The unsteady analysis was then continued for at least one blade-passing cycle, depending on the sector size. A cycle is defined as the movement of the blade across the entire sector domain. In the 1/23rd wheel sector, a cycle is two blade pitches, the cycle of the 3/23rd wheel sector is six blade pitches, and the cycle of the full wheel case is one entire revolution. Cases 1 through 4 (1/23rd wheel sector) were run for an additional two cycles, while the remaining cases (3/23rd

wheel sector and full wheel) were run for only one addition cycle. These cycles are referred to as post-processing cycles. The post-processing cycles of the aforementioned flow variables are shown in Figure 84. Signal processing was conducted using the results from the post-processing cycle runs, after previously achieving periodic convergence.

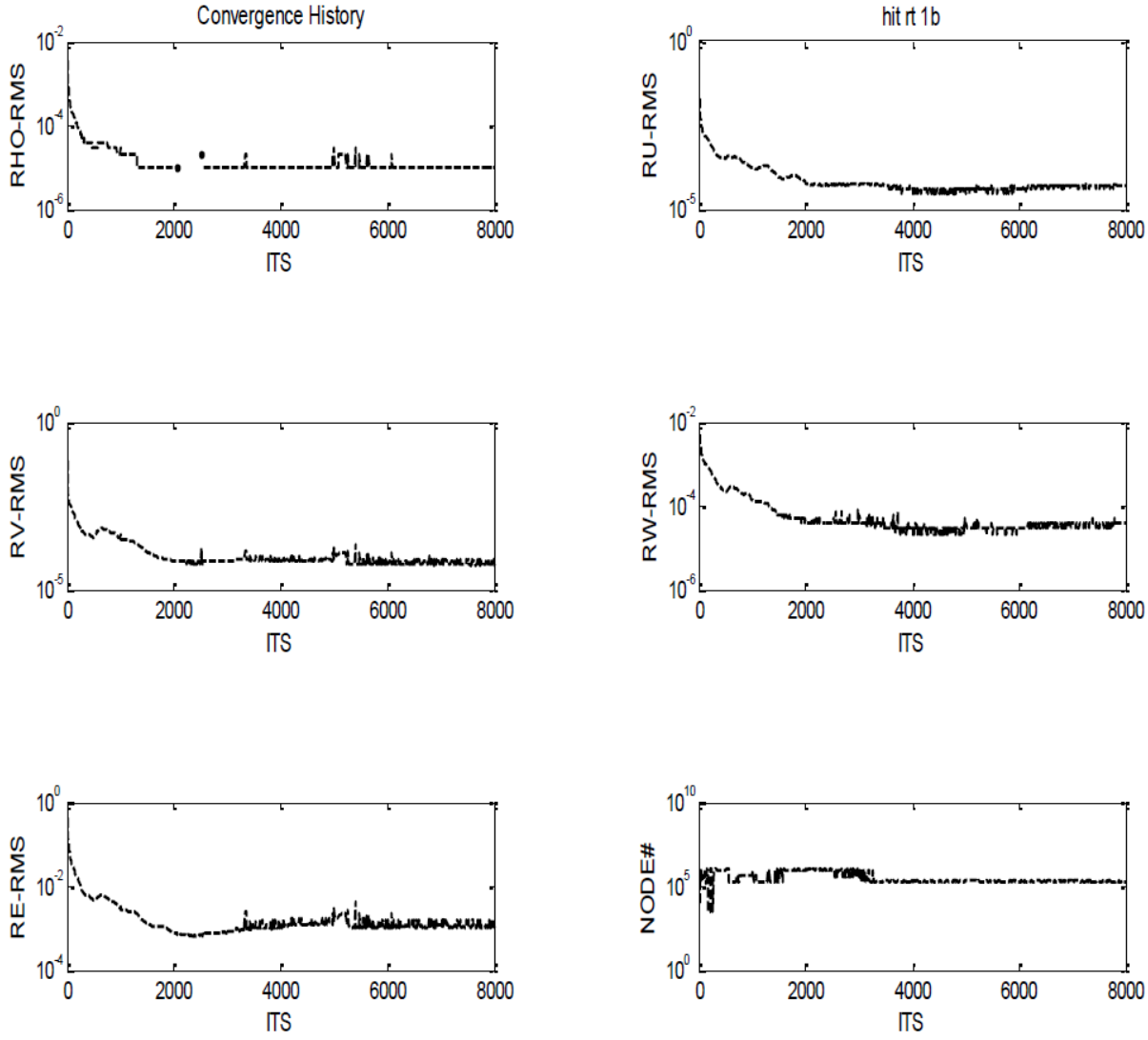

Figure 82: Steady Stage-and-a-Half Convergence History of Residuals (Case 1)

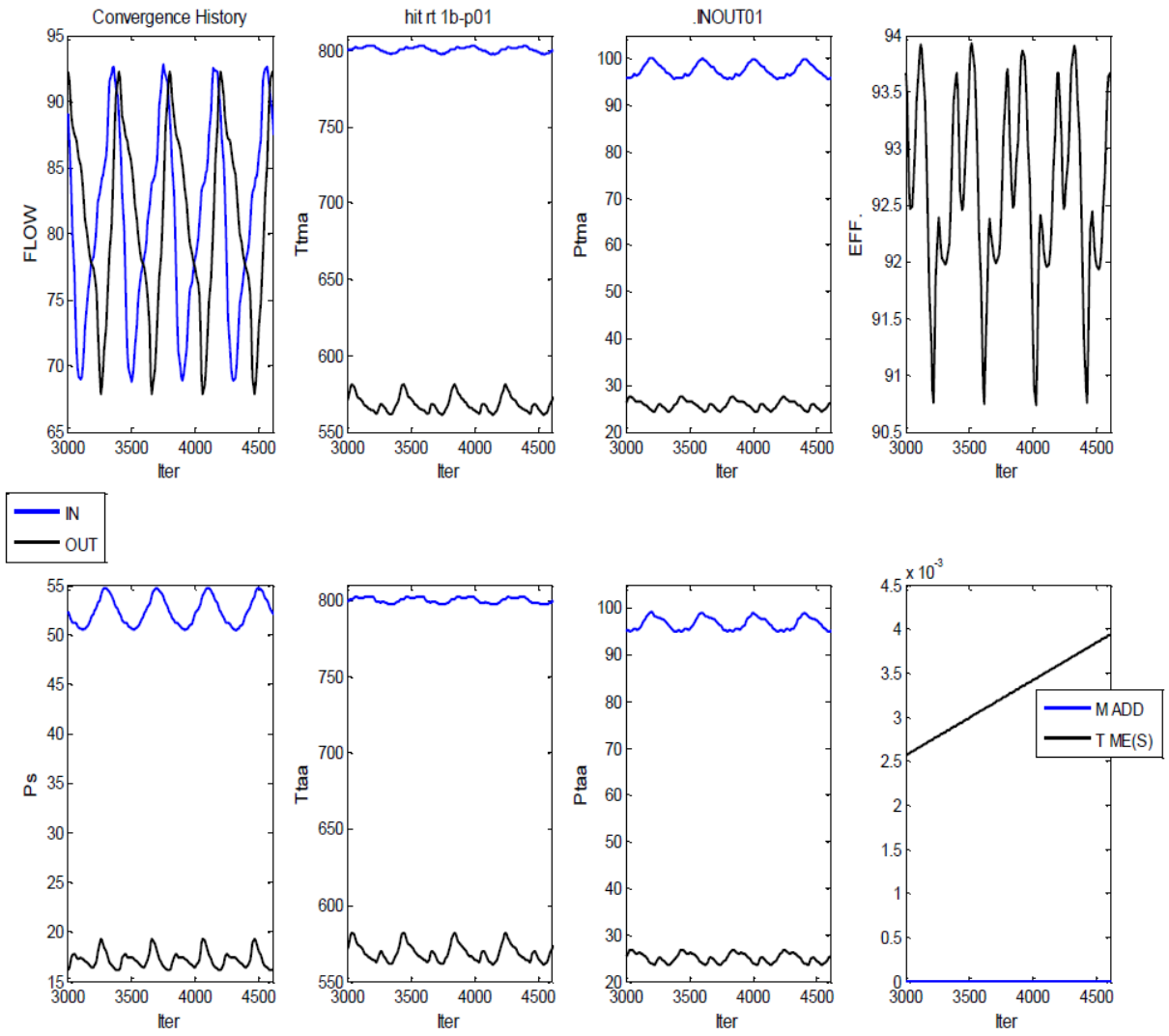

Figure 83: Unsteady Stage-and-a-Half Periodicity (Case 1)

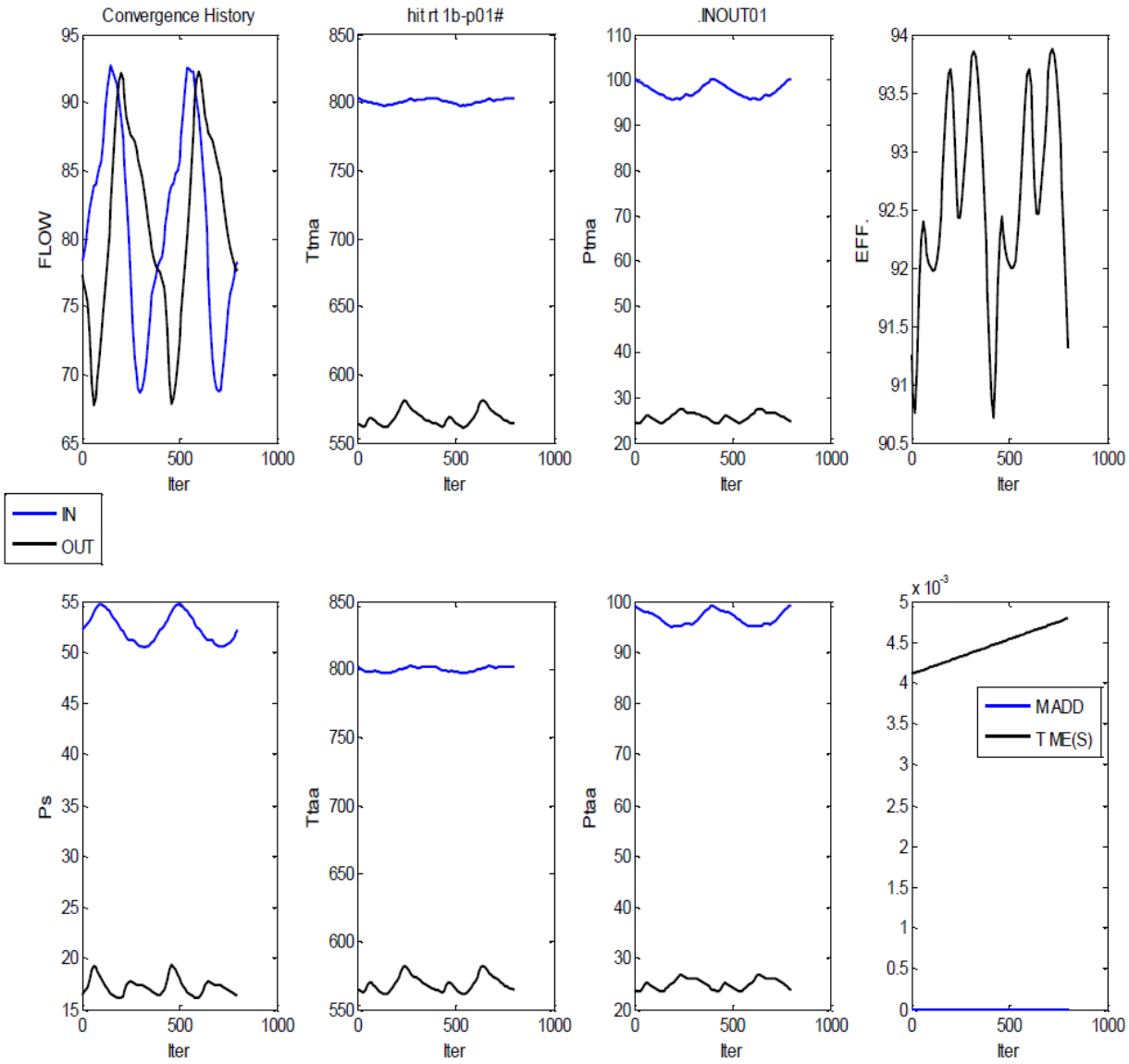

Figure 84: Unsteady Stage-and-a-Half Post-Processing Cycles (Case 1)

The objective of the wheel sector study was to determine the least computationally expensive sector size that was sufficient to model accurately the unsteady interaction between the blade and downstream vane. Larger sectors used in CFD modeling correlates to more time and CPU resources required to execute the numerical analysis, therefore, smaller sectors are desirable from a computer resource standpoint. In fact, the airfoil counts of the Research Turbine were directly influenced by the ability to model only a small sector of the wheel for an accurate representation of the full wheel without the computational expense. However, the mixed cooling scheme incorporated by the Research Turbine in order to allow engineers to study aerothermal effects introduces the need to investigate whether a 1/23rd sector provides a sufficient representation of the full wheel analysis. For uncooled cases—or cooled cases if the cooling was uniform for all airfoils in a given row—the appropriate sector is simply the reduced ratio of the airfoils counts. The study in this section focuses

exclusively on cooled cases because the mixed cooling scheme introduces complexities that may require more than the most reduced ratio of the airfoil counts to model properly the turbine flowfield. As shown in the previous sections regarding spatial and temporal resolutions, the interaction between the blade and downstream vane are largely driven by the first harmonic of the blade, or the 46th engine order at 5.84 kHz. Therefore, the wheel sector study also focuses on the convergence of the unsteady pressures at this frequency.

The Normalized Discrete Fourier Transforms (DFT) of the blade suction side at 5.84 kHz for each case are shown in Figure 85. The transforms are computed from the post-processing cycles of each case. The five points shown on the contours are once again at the same locations as the previous studies. Although close investigation of this figure reveals the differences of the unsteady magnitude between each case, it can be more easily visualized in Figure 86. The differences of the unsteady magnitude contours of each case compared to that of the full wheel analysis (Case 7) as a percentage of the maximum full-wheel unsteady magnitude are shown in Figure 86. Among the first four cases—the 1/23rd sector cases—Case 4 has the least difference in unsteady magnitude in the area of interest when compared to the full wheel analysis. Recall, as shown in Table 10, Case 4 was run with cooled vanes and blades. Therefore, it is not surprising that the cooled vane and blade case among the 1/23rd sectors compares best with the full wheel analysis because the full wheel contains more cooled airfoils in the first stage than uncooled airfoils. However, there is a sizable region near the root trailing edge in which the difference in magnitude compared to the full-wheel analysis is near or above 10%.

Tripling the sector width, as was done in Cases 5 and 6, allows for a more accurate representation of the full wheel cooling scheme. A 3/23rd sector contains six blades, which allows for the modeling of four cooled blades and 2 uncooled blades. This is significant because the majority of the cooling on the blade wheel follows the four cooled, two uncooled blade pattern. Cases 5 and 6 differ by modeling the first vanes as uncooled and cooled, respectively. Both Cases 5 and 6 further reduce the difference to the full-wheel analysis of the unsteady magnitude in the region of interest compared to the 1/23rd sector models. In particular, Case 6 compares best with the full wheel analysis. This is also intuitive because the majority of the first vanes are cooled in the full wheel; therefore, Case 6, which models the vanes as cooled, more accurately represents the cooling scheme of the full wheel.

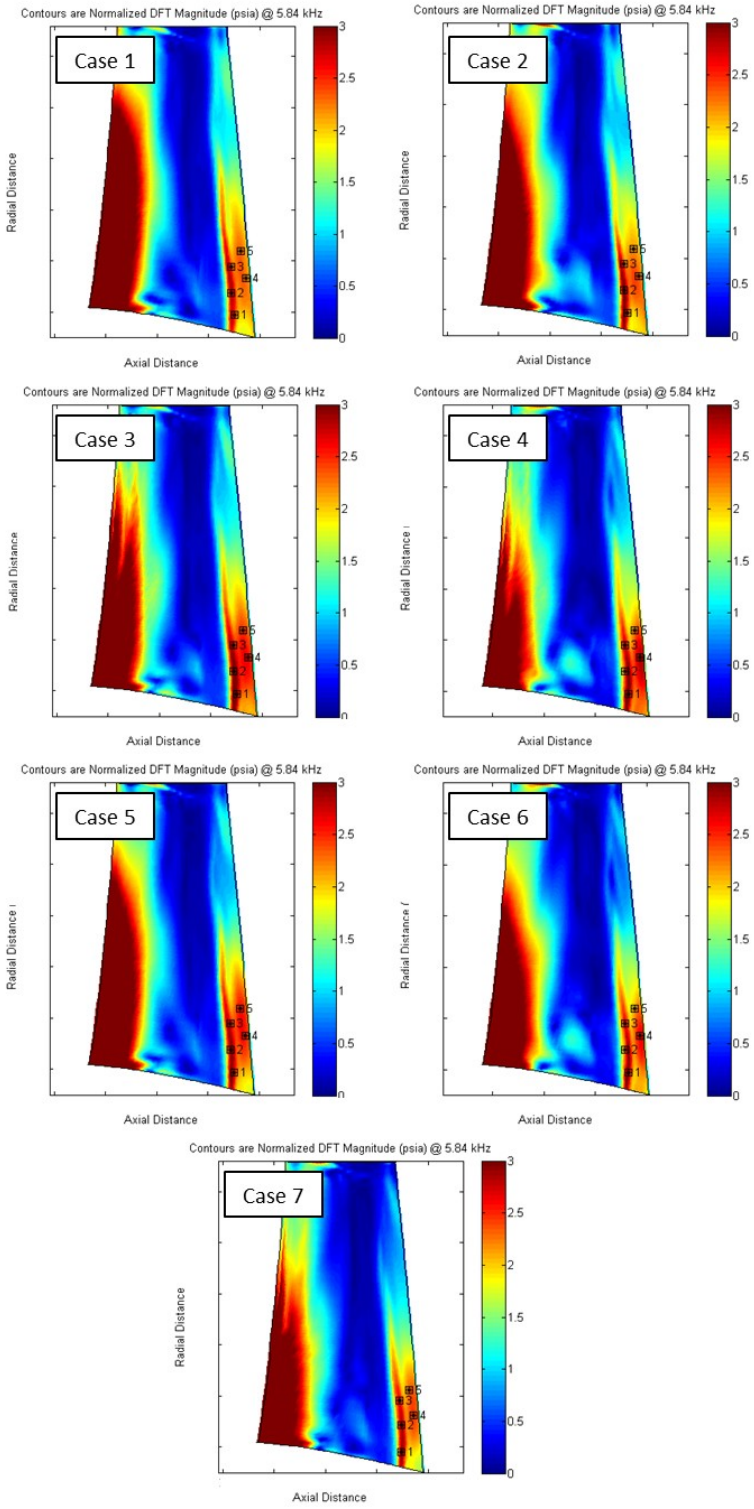

Figure 85: Normalized Discrete Fourier Transforms of the Blade SS at 5.84 kHz for the Sector Analysis Study

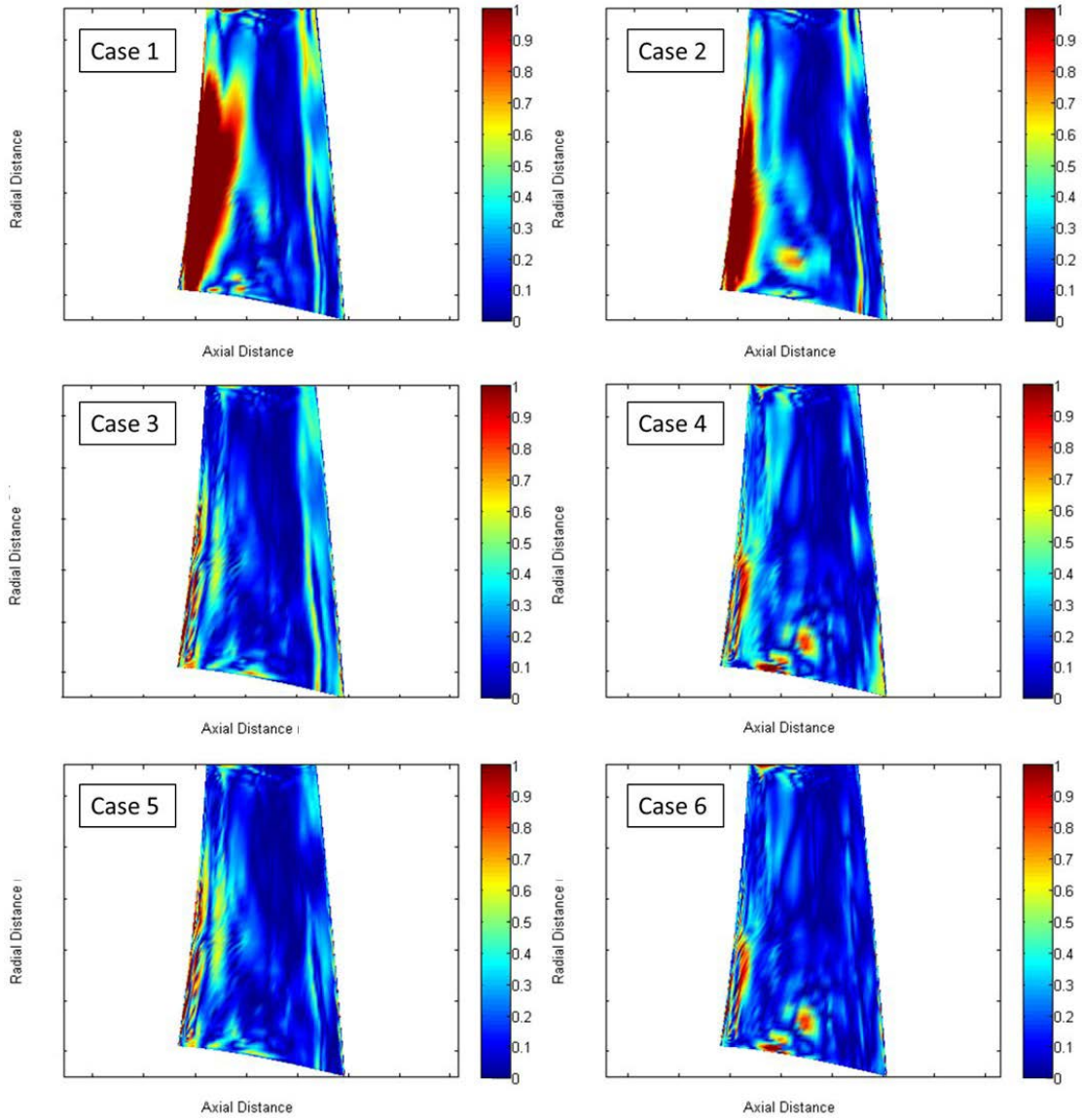

Figure 86: Differences of the Normalized Discrete Fourier Transform of the Full-Wheel Analysis (Case 7) and Each Sector Case as a Percentage of the Maximum Unsteadiness of the Full-Wheel Analysis

The time-accurate static pressure traces and Fourier Transforms of the signal from the post-processing cycles for points 1 through 5 are shown in Figure 87 through Figure 91, respectively. Refer to Figure 85 for the actual locations of each point. Every sector case is plotted for each point in the figures. Throughout most of the pressure traces and Fourier Transforms, Cases 4 and 6 agree closest with the full-wheel analysis. Although at certain instances in time Case 4 exhibits a closer agreement with the full-wheel traces, Case 6 is shown to be an accurate representation of the full-wheel analysis in the pressure traces and Fourier Transform. The occasional shortcomings of Case 6 can be explained by the fact that while Case 6 most accurately represents the full wheel cooling scheme, there are small portions of the full wheel cooling that are represented by other cooling patterns that exist in Cases 4 and 5.

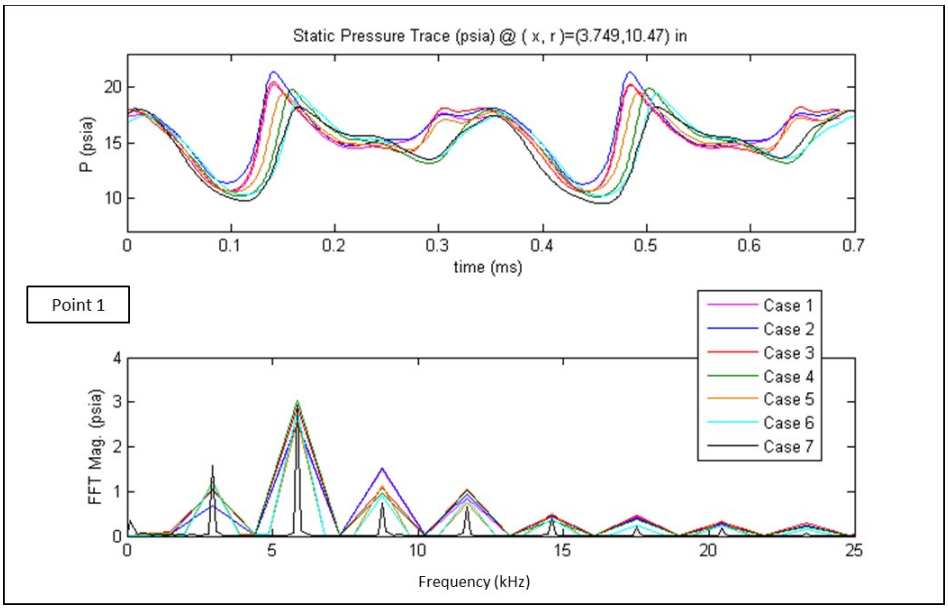

Figure 87: Static Pressure Trace and Fourier Transform Analysis for Wheel Sector Study at Point 1

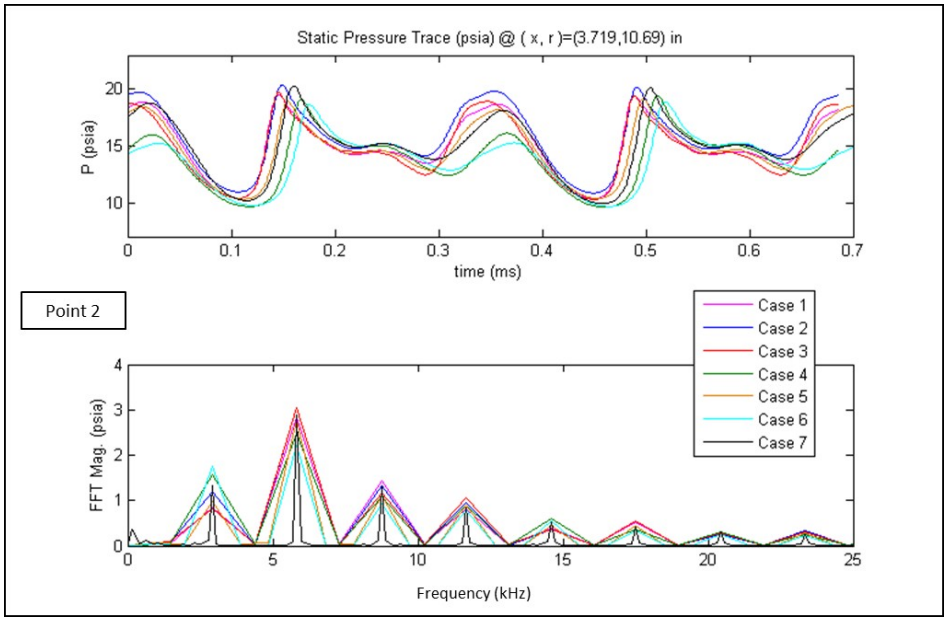

Figure 88: Static Pressure Trace and Fourier Transform Analysis for Wheel Sector Study at Point 2

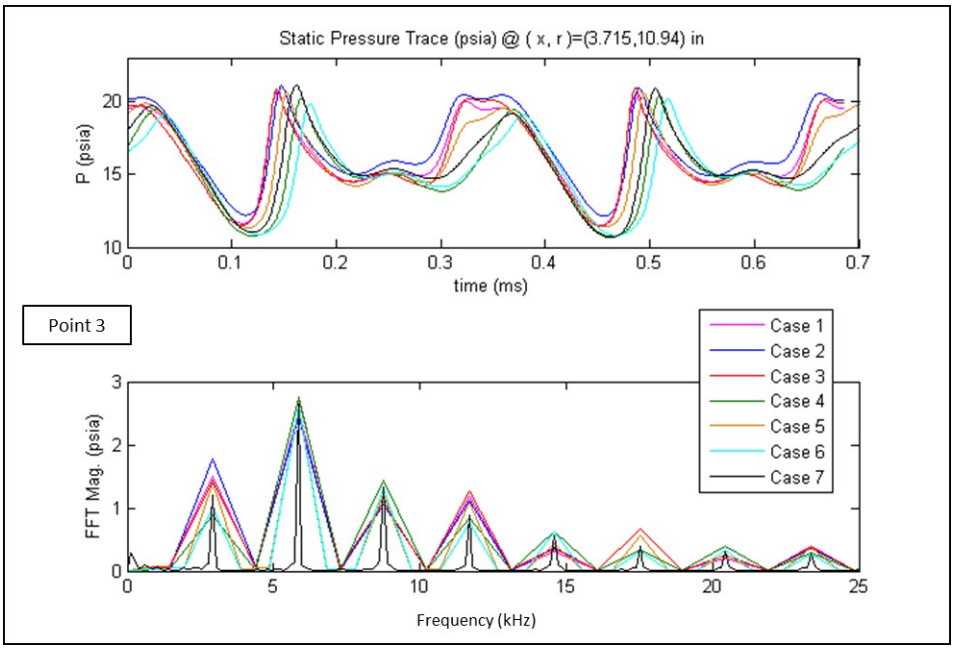

Figure 89: Static Pressure Trace and Fourier Transform Analysis for Wheel Sector Study at Point 3

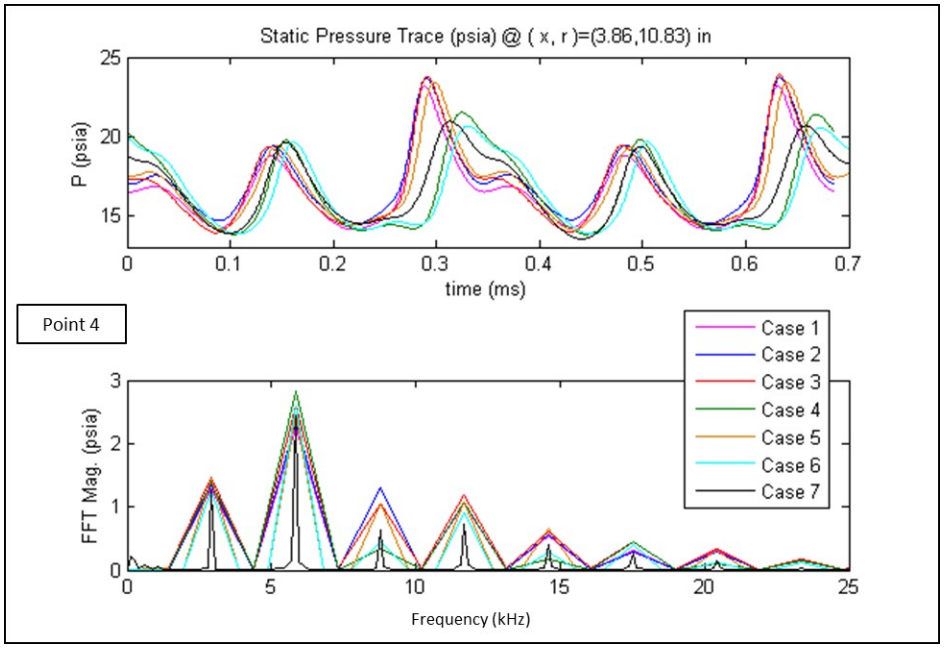

Figure 90: Static Pressure Trace and Fourier Transform Analysis for Wheel Sector Study at Point 4

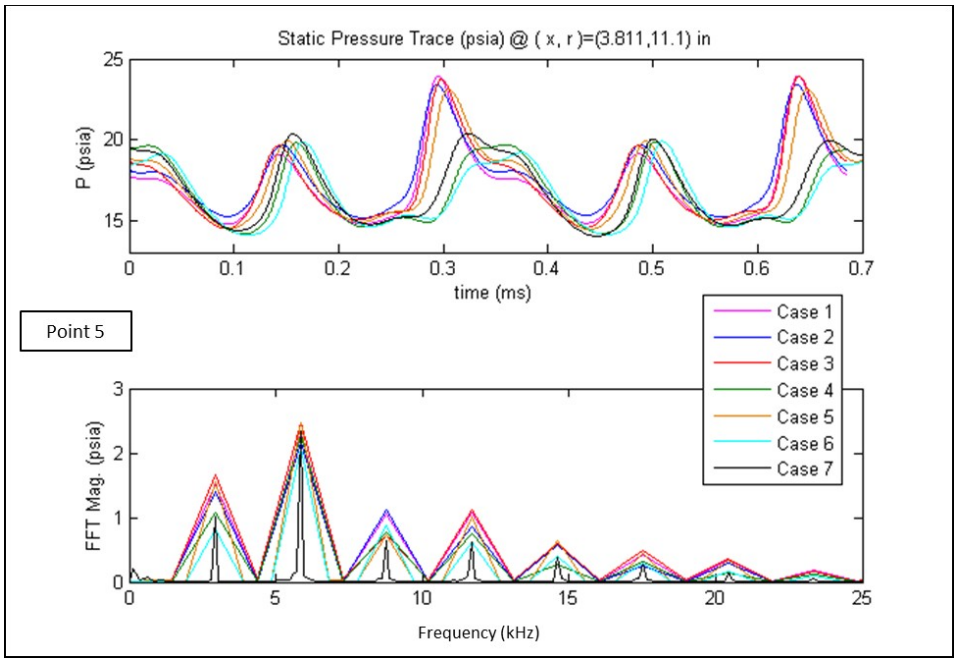

Figure 91: Static Pressure Trace and Fourier Transform Analysis for Wheel Sector Study at Point 5

Cases 4 and 6 were shown to have only small deviations with respect to the time-accurate pressure trace and the Fourier Transform for the points analyzed. The percent difference of the normalized Discrete Fourier Transform between the full-wheel analysis and Case 6 is minimal in the region of interest for this study. However, the most accurate 1/23rd sector—Case 4—had sizeable areas in which the difference between the full-wheel Discrete Fourier Transform was unacceptable (near or above 10%) despite tracking accurately with the time-accurate pressure traces. Therefore, Case 6 was chosen to conduct further time-accurate simulations because of the optimal trade between computational expense and acceptable accuracy of the solution.

Summary

A rigorous study was conducted in order to determine the appropriate manner in which the stage-and-a-half Research Turbine will be modeled. As with any computational modeling system, there is a tradeoff between the fidelity of the solution and computational expense required to arrive at that solution. The spatial resolution of the grid, temporal resolution, periodic convergence, and the appropriate wheel sector to model was investigated. The spatial and temporal resolution analyses were evaluated using a 1/23rd sector of the wheel. It was determined that a grid containing approximately 5 million nodes for the entire sector was sufficient and 400 time-steps per cycle was found to accurately capture the unsteady interaction without compromising the accuracy of the solution. The method in which the unsteady numerical analysis was conducted, which included a two-cycle post-processing run, was proven to achieve periodic convergence.

Typically, a stage-and-a-half airfoil count of 23:46:23 would be modeled rather with a 1/23rd sector of a 1:2:1 count. This would be true of the Research Turbine if it were run uncooled or the cooling scheme was uniform for each airfoil row. However, in order to study

unsteady aerothermal dynamics, the Research Turbine was implemented with a rainbow cooling scheme. It was determined, through a wheel sector analysis of varying cooling patterns based on the rainbow cooling scheme implemented on the full wheel, that a 3/23rd sector of count 3:6:3 provided a sufficiently accurate solution when compared to the full-wheel analysis, while saving computational expense. The 3/23rd sector that will be used to model the Research Turbine will use cooled first vanes and four cooled and two uncooled blades. Recall that the grid chosen for the spatial resolution study contained approximately 5 million nodes. Therefore, the grid size of the 3/23rd sector that will be used for all further analysis will contain approximately 15 million nodes.

CHAPTER VI

THREE-DIMENSIONAL, TIME-ACCURATE INTERACTION AND COMPARISON TO EXPERIMENT

The full stage-and-one-half HIT Research Turbine rig tests were conducted in the Turbine Research Facility at WPAFB, Ohio. The flow solver Leo was used to compute the numerical solution. The method in which the numerical analysis was conducted was determined by work presented in the previous chapter. The boundary conditions for the CFD analyses were derived from the experimental flow conditions. The experimental results and comparisons to the numerical analyses are highlighted in this chapter.

Experimental Methodology

The objective of the experimental work performed in the Turbine Research Facility at WPAFB with the full stage-and-one-half was to characterize the flow field of the Research Turbine. The TRF is a full-scale transient facility designed to obtain time- resolved pressure, surface temperature, and heat flux data from single-spool turbomachinery at flow conditions which are consistent with turbine environments in terms of the relevant non-dimensional parameters. The facility is described in greater detail in the "Experimental Methodology" section of the "Three-Dimensional Vane-Only Flow Field" chapter and is shown in Figure 37. The HIT RT first vane, blade, and second vane assembles are shown in Figure 92through Figure 94, respectively.

Figure 92: First Vane Assembly

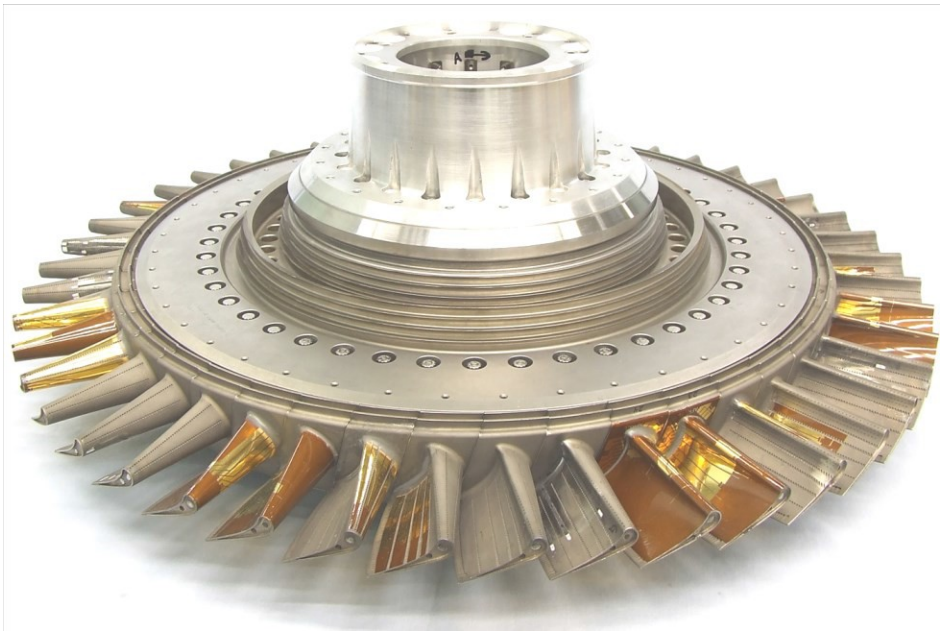

Figure 93: First Blade Assembly

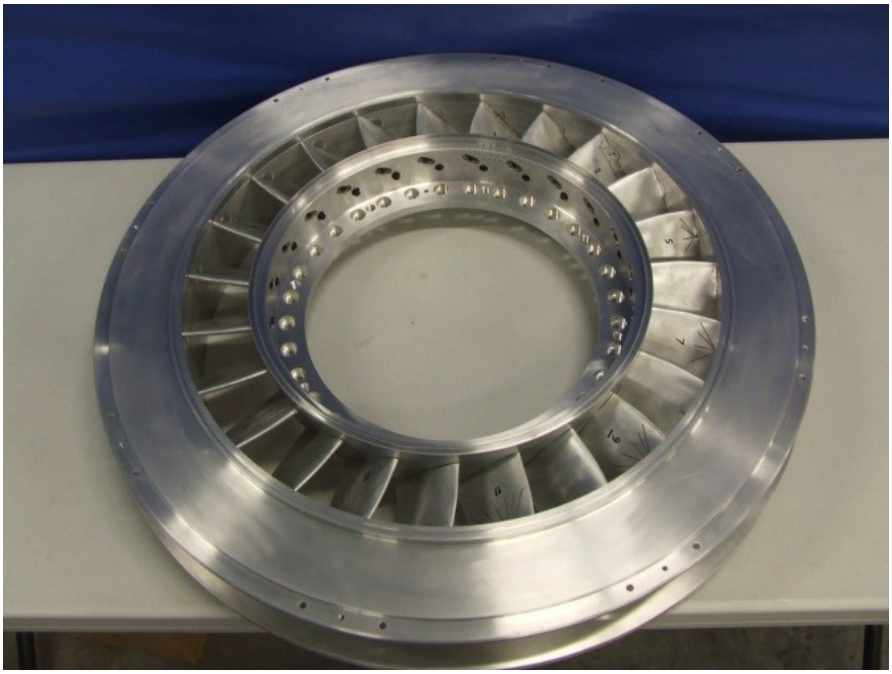

Figure 94: Second Vane Assembly

The static pressure data was obtained through pressure taps leading to flush-mounted Kulite piezo-resistive transducers. Surface temperatures and heat flux data were obtained using surface mounted thermocouples and double-sided thin-film heat-flux gauges, respectively, although only pressure data is reported in this chapter. Total pressures up- and downstream of the Research Turbine were each collected by a rake of nine pressure gauges at centers of equal area in the radial direction. The up- and downstream rakes swept 120 degrees

of the annulus throughout the duration of the blowdown experiment and measured the total pressure to the inlet of the first vane and the total pressure exit of the second vane. The pressure transducers used in the Turbine Research Facility are Kulite transducers, model LQ-062. The uncertainty of the measurements was calculated using the method developed by Dunn and Haldeman [5]. Applied to the TRF, the uncertainty of the measurements is 0.05 percent of the full scale output, which equates to 0.05 psia and 0.025 on the first stage and downstream vane, respectively [39]. The pressure data was sampled at a rate of 800 kHz.

Collection of a complete set of static pressure data on the blade required three instrumentation patches due to slip ring channel limitations. TRF blowdowns designated as experiments 280100, 280200, and 280300 were run at a matching turbine pressure ratio and speed parameter of 3.754 and 269.4 $\frac{RPM}{\sqrt{K}}$, respectively. The Kulites used to obtain the surface pressures on the first vane are listed in Table 11. The pressure sensors on the blade are listed in Table 12, and these are organized by the TRF experiment in which they were connected. The sensor locations on the second vane are given in Table 13. Data was obtained via pressure sensors on both vanes during all experiments. The airfoil number in which each sensor is located, percent axial chord, percent span, and pressure side or suction side designation is also shown in the instrumentation tables. Surface static pressures were also measured on the inner (ID) and outer diameter (OD) endwalls of the low pressure vane. There were 34 and 45 sensors on the ID and OD endwalls, respectively, located within one vane passage. The pressure sensors were clustered closely together in a single passage to get a detailed measurement of the unsteady pressures and to resolve reflected shock motion in that channel. The axial chord, pitch, and ID/OD flag of each endwall sensor are shown in Table 14. The pitch is measured as a fraction of the pitch of the second vane relative to a trailing edge zero point. The instrumented endwall passage is shown in Figure 95.

Table 11: First Vane Kulite Instrumentation

Sensor	Airfoil	x/b_x	Span	Side
PVQ10	10	0.250	0.900	SS
PVQ11	10	0.642	0.900	SS
PVQ12	10	0.883	0.900	SS
PVQ13	10	0.948	0.900	SS
PVQ14	10	0.980	0.900	SS
PVP1	11	0.800	0.900	PS
PVP2	11	0.000	0.900	PS
PVP10	11	0.686	0.620	SS
PVP11	11	0.778	0.620	SS
PVP12	11	0.930	0.620	SS
PVP13	11	0.950	0.620	SS
PVP14	11	0.980	0.620	SS
PVF10	19	0.250	0.500	SS
PVF11	19	0.612	0.500	SS
PVF12	19	0.700	0.500	SS
PVF13	19	0.775	0.500	SS
PVF14	19	0.916	0.500	SS
PVF15	19	0.950	0.500	SS
PVF16	19	0.980	0.500	SS
PVE1	20	0.800	0.500	PS
PVE2	20	0.000	0.500	PS
PVE10	20	0.719	0.250	SS
PVE11	20	0.800	0.250	SS
PVE12	20	0.887	0.250	SS
PVE13	20	0.920	0.250	SS
PVE14	20	0.950	0.250	SS
PVE15	20	0.980	0.250	SS
PVD1	21	0.800	0.050	PS
PVD2	21	0.000	0.050	PS
PVD10	21	0.250	0.050	SS
PVD11	21	0.677	0.050	SS
PVD12	21	0.822	0.050	SS
PVD13	21	0.944	0.050	SS
PVD14	21	0.980	0.050	SS

Table 12: First Blade Kulite Instrumentation

Run 280100					Run 280200					Run 280300				
Sensor	Airfoil	x/b_x	Span	Side	Sensor	Airfoil	x/b_x	Span	Side	Sensor	Airfoil	x/b_x	Span	Side
PRAA5	1	0.205	0.150	PS	PRMM10	26	0.389	0.746	SS	PRAA5	1	0.205	0.150	PS
PRAA4	1	0.308	0.150	PS	PRJJ10	32	0.27	0.97	SS	PREE10	39	0.089	0.746	SS
PRAA3	1	0.460	0.150	PS	PRJJ11	32	0.374	0.97	SS	PRXX3	7	0.222	0.350	PS
PRAA2	1	0.688	0.150	PS	PRJJ12	32	0.487	0.97	SS	PRZA10	2	0.321	0.150	SS
PRAA1	1	0.843	0.150	PS	PRJJ13	32	0.71	0.97	SS	PRZA11	2	0.585	0.150	SS
PRZA10	2	0.321	0.150	SS	PRJJ14	32	0.789	0.97	SS	PRZA12	2	0.789	0.150	SS
PRZA11	2	0.585	0.150	SS	PRJJ15	32	0.874	0.97	SS	PRZA13	2	0.836	0.150	SS
PRZA12	2	0.789	0.150	SS	PRJJ16	32	0.978	0.97	SS	PRZA14	2	0.877	0.150	SS
PRZA13	2	0.836	0.150	SS	PRMM11	26	0.586	0.746	SS	PREE14	39	0.185	0.970	SS
PRZA14	2	0.877	0.150	SS	PRMM12	26	0.697	0.746	SS	PRFF10	37	0.000	0.150	SS
PRZA15	2	0.924	0.150	SS	PRMM13	26	0.78	0.746	SS	PRFF11	37	0.088	0.150	SS
PRZA16	2	0.985	0.150	SS	PRMM14	26	0.82	0.746	SS	PRFF13	37	0.072	0.495	SS
PRWX10	8	0.104	0.350	SS	PRMM15	26	0.868	0.746	SS	PRFF14	37	0.252	0.495	SS
PRWX11	8	0.350	0.350	SS	PRMM16	26	0.937	0.746	SS	PRFF15	37	0.330	0.495	SS
PRWX12	8	0.606	0.350	SS	PRQQ10	20	0.103	0.6	SS					
PRWX13	8	0.790	0.350	SS	PRQQ11	20	0.25	0.6	SS					
PRWX14	8	0.820	0.350	SS	PRQQ12	20	0.548	0.6	SS					
PRWX15	8	0.877	0.350	SS	PRQQ13	20	0.78	0.6	SS					
PRWX16	8	0.973	0.350	SS	PRQQ14	20	0.81	0.6	SS					
PRTT10	14	0.454	0.495	SS	PRQQ15	20	0.839	0.6	SS					
PRTT11	14	0.664	0.495	SS	PRQQ16	20	0.912	0.6	SS					
PRTT12	14	0.742	0.495	SS										
PRTT13	14	0.780	0.495	SS										
PRTT14	14	0.811	0.495	SS										
PRTT15	14	0.881	0.495	SS										
PRTT16	14	0.951	0.495	SS										

Table 13: Second Vane Kulite Instrumentation

Sensor	Airfoil	x/b_x	Span	Side	Sensor	Airfoil	x/b_x	Span	Side	Sensor	Airfoil	x/b_x	Span	Side
P2VA1	1	0.789	0.957	PS	P2VU1	7	0.614	0.721	PS	P2VM1	13	0.866	0.407	PS
P2VA2	1	0.583	0.957	PS	P2VU2	7	0.392	0.721	PS	P2VM2	13	0.698	0.407	PS
P2VA3	1	0.459	0.957	PS	P2VU3	7	0.204	0.721	PS	P2VM3	13	0.520	0.407	PS
P2VA4	1	0.301	0.957	PS	P2VU4	7	0.077	0.721	PS	P2VM4	13	0.360	0.407	PS
P2VA5	1	0.164	0.957	PS	P2VT6	8	0.905	0.721	SS	P2VM5	13	0.192	0.407	PS
P2VA6	1	0.051	0.957	PS	P2VT5	8	0.768	0.721	SS	P2VM6	13	0.051	0.407	PS
P2VZ6	2	0.851	0.957	SS	P2VT4	8	0.547	0.721	SS	P2VL6	14	0.828	0.407	SS
P2VZ5	2	0.711	0.957	SS	P2VT3	8	0.421	0.721	SS	P2VL5	14	0.681	0.407	SS
P2VZ4	2	0.462	0.957	SS	P2VT2	8	0.257	0.721	SS	P2VL4	14	0.563	0.407	SS
P2VZ3	2	0.291	0.957	SS	P2VT1	8	0.098	0.721	SS	P2VL3	14	0.459	0.407	SS
P2VZ2	2	0.150	0.957	SS	P2VS1	9	0.887	0.605	PS	P2VL2	14	0.321	0.407	SS
P2VZ1	2	0.046	0.957	SS	P2VS2	9	0.723	0.605	PS	P2VL1	14	0.132	0.407	SS
P2VY1	3	0.865	0.898	PS	P2VS3	9	0.522	0.605	PS	P2VK1	15	0.507	0.249	PS
P2VY2	3	0.695	0.898	PS	P2VS4	9	0.331	0.605	PS	P2VK2	15	0.331	0.249	PS
P2VY3	3	0.535	0.898	PS	P2VS5	9	0.182	0.605	PS	P2VK3	15	0.180	0.249	PS
P2VY4	3	0.361	0.898	PS	P2VS6	9	0.061	0.605	PS	P2VK4	15	0.040	0.249	PS
P2VY5	3	0.232	0.898	PS	P2VQ6	10	0.875	0.605	SS	P2VJ4	16	0.772	0.249	SS
P2VY6	3	0.119	0.898	PS	P2VQ5	10	0.712	0.605	SS	P2VJ3	16	0.535	0.249	SS
P2VX6	4	0.906	0.898	SS	P2VQ4	10	0.559	0.605	SS	P2VJ2	16	0.289	0.249	SS
P2VX5	4	0.698	0.898	SS	P2VQ3	10	0.417	0.605	SS	P2VJ1	16	0.090	0.249	SS
P2VX4	4	0.513	0.898	SS	P2VQ2	10	0.243	0.605	SS	P2VH1	17	0.512	0.175	PS
P2VX3	4	0.372	0.898	SS	P2VQ1	10	0.111	0.605	SS	P2VH2	17	0.366	0.175	PS
P2VX2	4	0.232	0.898	SS	P2VP1	11	0.902	0.522	PS	P2VH3	17	0.167	0.175	PS
P2VX1	4	0.101	0.898	SS	P2VP2	11	0.707	0.522	PS	P2VG3	18	0.537	0.175	SS
P2VW1	5	0.570	0.813	PS	P2VP3	11	0.514	0.522	PS	P2VG2	18	0.293	0.175	SS
P2VW2	5	0.399	0.813	PS	P2VP4	11	0.328	0.522	PS	P2VG1	18	0.074	0.175	SS
P2VW3	5	0.202	0.813	PS	P2VP5	11	0.195	0.522	PS	P2VF1	19	0.514	0.106	PS
P2VW4	5	0.094	0.813	PS	P2VP6	11	0.057	0.522	PS	P2VF2	19	0.372	0.106	PS
P2VV6	6	0.908	0.813	SS	P2VN6	12	0.785	0.522	SS	P2VF3	19	0.165	0.106	PS
P2VV5	6	0.742	0.813	SS	P2VN5	12	0.614	0.522	SS	P2VE3	20	0.534	0.106	SS
P2VV4	6	0.600	0.813	SS	P2VN4	12	0.502	0.522	SS	P2VE2	20	0.281	0.106	SS
P2VV3	6	0.410	0.813	SS	P2VN3	12	0.364	0.522	SS	P2VE1	20	0.072	0.106	SS
P2VV2	6	0.248	0.813	SS	P2VN2	12	0.252	0.522	SS					
P2VV1	6	0.112	0.813	SS	P2VN1	12	0.134	0.522	SS					

Table 14: 2nd Vane Endwall Kulite Instrumentation

Sensor	x/b_x	ID/OD	Pitch
P2VYI11	-0.138	ID	0.382
P2VYI12	-0.138	ID	0.220
P2VYI13	-0.138	ID	0.059
P2VYI14	-0.138	ID	0.898
P2VYI15	-0.138	ID	0.736
P2VYI16	-0.138	ID	0.575
P2VYI17	-0.138	ID	0.414
P2VYI21	-0.018	ID	0.304
P2VYI22	-0.018	ID	0.116
P2VYI23	-0.018	ID	0.927
P2VYI24	-0.018	ID	0.739
P2VYI25	-0.018	ID	0.550
P2VYI31	0.062	ID	0.223
P2VYI32	0.062	ID	0.081
P2VYI33	0.062	ID	0.938
P2VYI34	0.062	ID	0.795
P2VYI35	0.062	ID	0.652
P2VYI41	0.182	ID	0.255
P2VYI42	0.182	ID	0.131
P2VYI43	0.182	ID	0.008
P2VYI44	0.182	ID	0.884
P2VYI45	0.182	ID	0.761
P2VYI51	0.302	ID	0.345
P2VYI52	0.302	ID	0.180
P2VYI53	0.302	ID	0.015
P2VYI54	0.302	ID	0.850
P2VYI61	0.462	ID	0.523
P2VYI62	0.462	ID	0.348
P2VYI63	0.462	ID	0.174
P2VYI64	0.462	ID	0.999
P2VYI71	0.621	ID	0.705
P2VYI72	0.621	ID	0.528
P2VYI73	0.621	ID	0.350
P2VYI74	0.621	ID	0.173

Sensor	x/b_x	ID/OD	Pitch
P2VYO11	0.101	OD	0.093
P2VYO12	0.101	OD	0.977
P2VYO13	0.101	OD	0.861
P2VYO14	0.101	OD	0.744
P2VYO15	0.101	OD	0.628
P2VYO16	0.101	OD	0.512
P2VYO17	0.101	OD	0.396
P2VYO18	0.101	OD	0.338
P2VYO21	0.211	OD	0.116
P2VYO22	0.211	OD	0.018
P2VYO23	0.211	OD	0.920
P2VYO24	0.211	OD	0.822
P2VYO25	0.211	OD	0.724
P2VYO26	0.211	OD	0.626
P2VYO27	0.211	OD	0.528
P2VYO28	0.211	OD	0.479
P2VYO31	0.321	OD	0.179
P2VYO32	0.321	OD	0.080
P2VYO33	0.321	OD	0.980
P2VYO34	0.321	OD	0.880
P2VYO35	0.321	OD	0.781
P2VYO36	0.321	OD	0.681
P2VYO37	0.321	OD	0.581
P2VYO41	0.481	OD	0.246
P2VYO42	0.481	OD	0.194
P2VYO43	0.481	OD	0.092
P2VYO44	0.481	OD	0.989
P2VYO45	0.481	OD	0.886
P2VYO46	0.481	OD	0.783
P2VYO47	0.481	OD	0.680
P2VYO48	0.481	OD	0.577
P2VYO51	0.641	OD	0.300
P2VYO52	0.641	OD	0.250
P2VYO53	0.641	OD	0.199
P2VYO54	0.641	OD	0.098
P2VYO55	0.641	OD	0.997
P2VYO56	0.641	OD	0.896
P2VYO57	0.641	OD	0.795
P2VYO58	0.641	OD	0.694
P2VYO62	0.801	OD	0.404
P2VYO63	0.801	OD	0.288
P2VYO64	0.801	OD	0.172
P2VYO65	0.801	OD	0.057
P2VYO66	0.801	OD	0.941
P2VYO67	0.801	OD	0.825

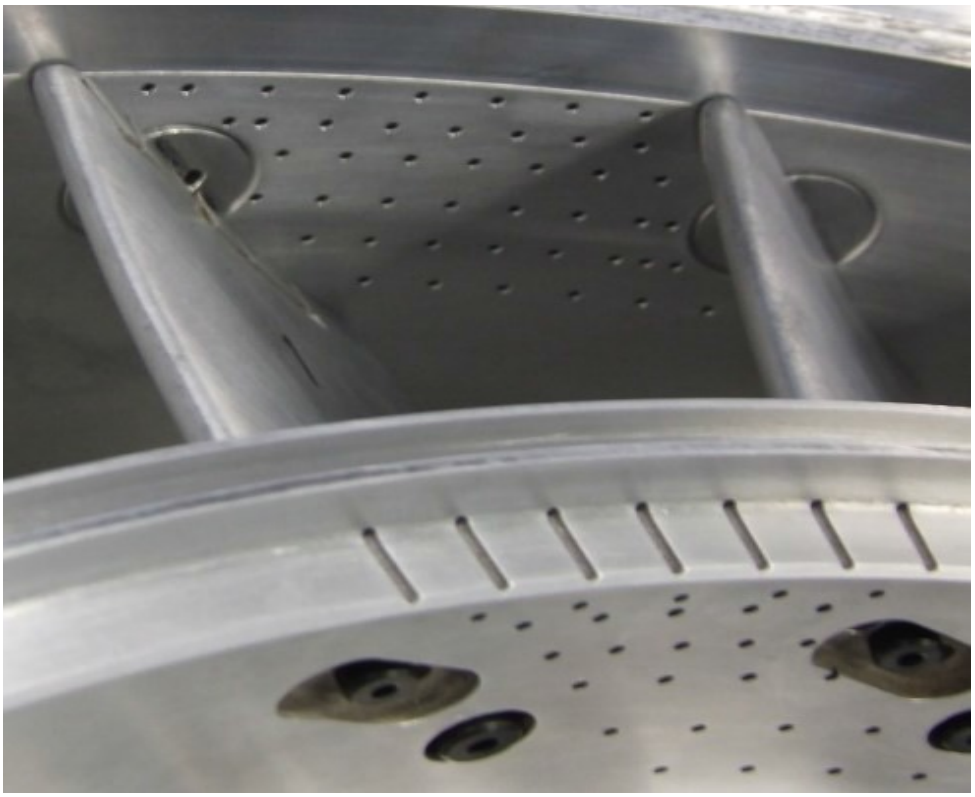

Figure 95: Instrumented Endwall Passage of the Second Vane

A plot of RPM versus time for a typical experiment is shown in Figure 96. The majority of the time is spent accelerating the turbine prior to the blowdown. The turbine is accelerated to one percent above the target test speed, and then allowed to coast back down to test speed. Then, at time zero, an eddy current brake speed control system is engaged, and this results in a sharp deceleration until the target speed parameter is achieved. Cooling air is then initiated to the vanes and blades, and this slightly accelerates the turbine. Recall that the turbine is in a near vacuum with little air resistance, allowing the cooling air to increase the speed of the rotor. At two seconds, a plug valve at the turbine inlet is opened, and this allows the air to enter the test section and power the turbine. During the blowdown, the turbine speed is controlled by the eddy current brake system that, through a feedback loop, operates the turbine at a constant speed parameter. After the prescribed test period has ended, the eddy current brake is used to decelerate the turbine below all rotor dynamic critical speeds. Data was acquired throughout the test sequence, but only a portion of the data collected during the blowdown was used to compare to CFD data. The window was determined by the time required to achieve 100 turbine revolutions in the latter half of the blowdown, after the cooling flow had time to establish, and is identified by two vertical red lines in the figure. The inlet and exit conditions for the turbine, averaged across all three experiments, are shown in Table 15.

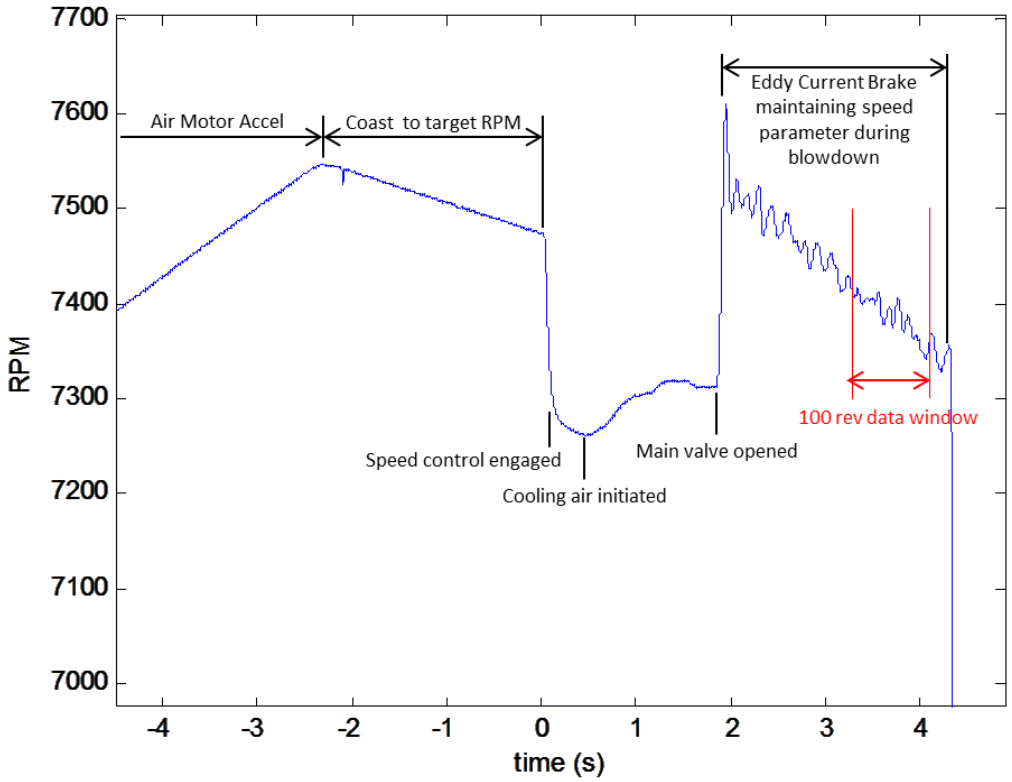

Figure 96: RPM of Stage-and-a-Half Blowdown

Table 15: Averaged Blowdown Boundary Conditions

	Run 280100	Run 280200	Run 280300	Averaged
1V P_{T_IN} (psia)	55.75	56.19	56.05	55.60 psia
1V T_{T_IN} (deg R)	751.1	747.8	748.1	749.0 deg R
1V P_{S_EX} (psia)	30.09	30.38	30.36	30.28 psia
1V M_{IN}	0.052	0.052	0.052	0.052
1B P_{T_IN} (psia)	52.96	53.38	53.25	53.19 psia
1B T_{T_IN} (deg R)	736.1	732.8	733.1	734.0 deg R
1B P_{S_EX} (psia)	11.42	11.58	11.45	11.48 psia
1B M_{IN}	0.985	0.983	0.982	0.983
RPM	7386.4	7386.4	7386.4	7386.4
Tip Clearance (in)	0.010	0.010	0.010	0.010 in
2V P_{S_EX} (psia)	10.87	11.03	10.92	10.94 psia
2V M_{IN}	0.628	0.625	0.627	0.627

Two cooling tanks supplied the cooling air for the inlet guide vanes and blades during the blowdown experiment, one each for the inner diameter (ID) and outer diameter (OD) feeds. The ID supply tank fed the vane inner endwall, the forward vane airfoil cavity, and the blade. The OD tank supplied cooling air to the vane outer endwall and the aft vane airfoil cavity. The cooling holes for the vane and blade are shown and identified in Figure 97 through Figure 100. The forward vane airfoil cavity includes the showerhead holes (rows HA-HF), suction side holes (rows SA-SD), and two rows of the pressure side holes (rows PE and PF). The remaining pressure side holes (row PA-PD) and the trailing edge holes (row TE) are fed by the aft vane airfoil cavity.

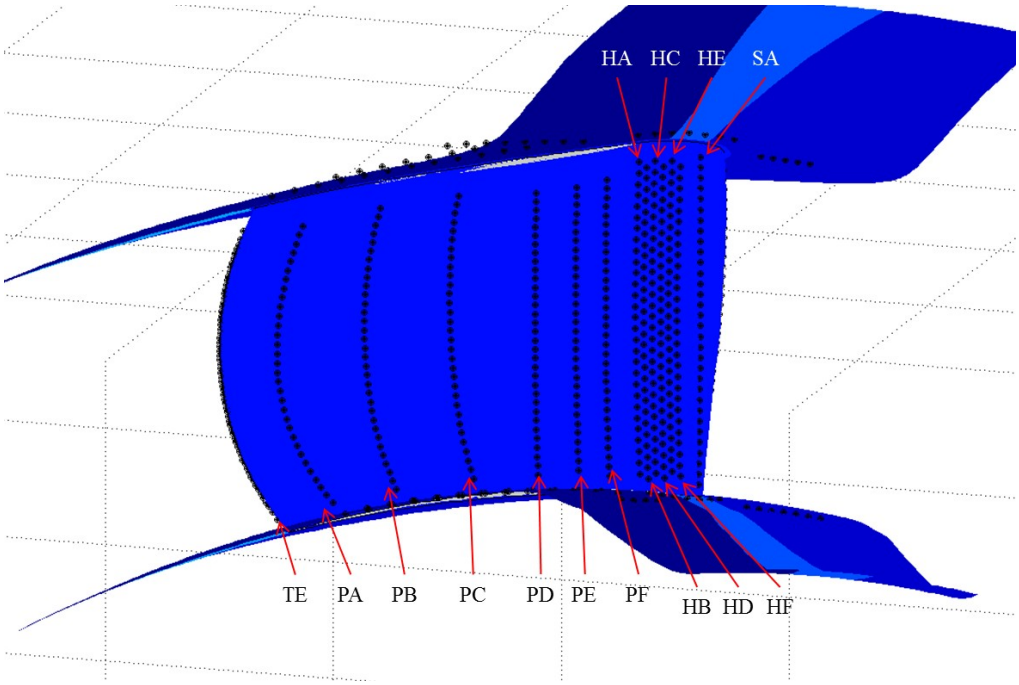

Figure 97: First Vane Pressure Side Cooling Rows

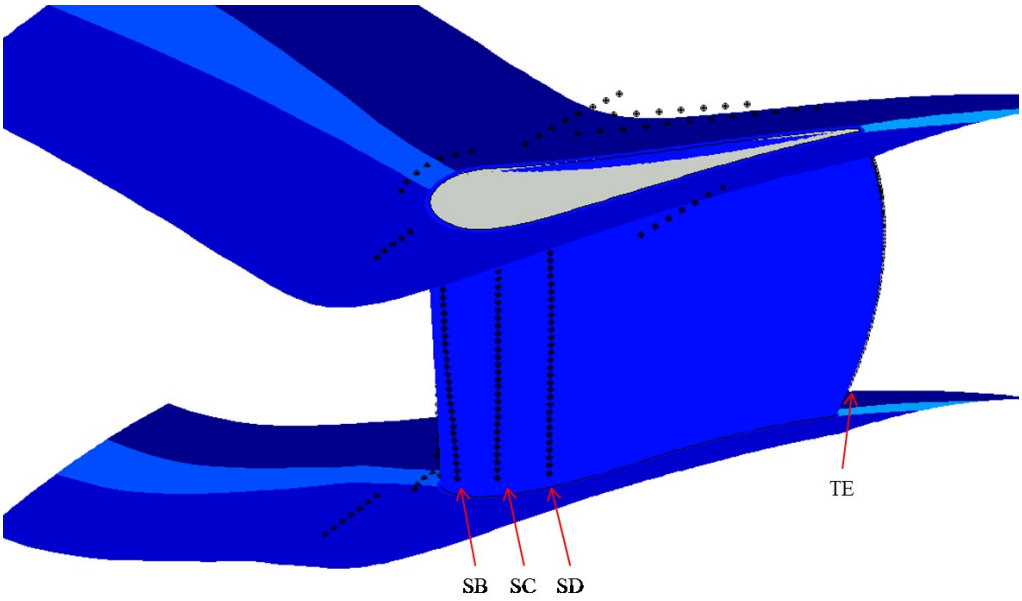

Figure 98: First Vane Suction Side Cooling Rows

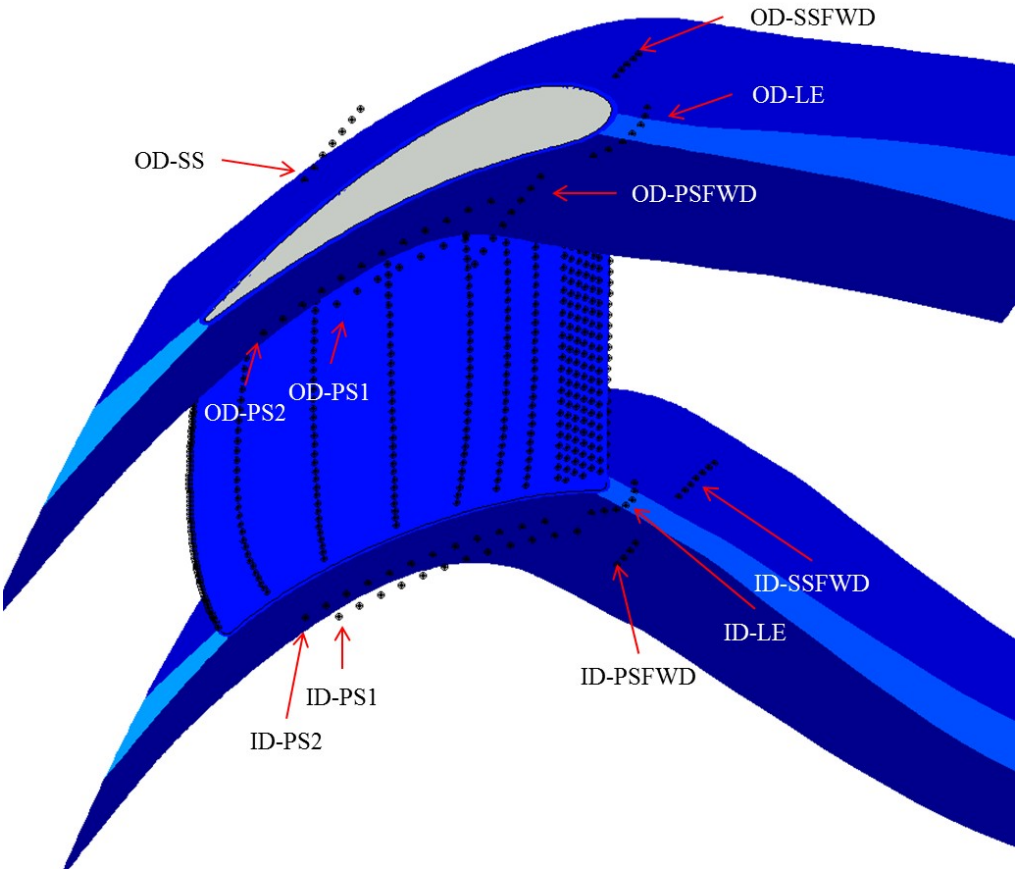

Figure 99: First Vane Inner and Outer Endwall Cooling Rows

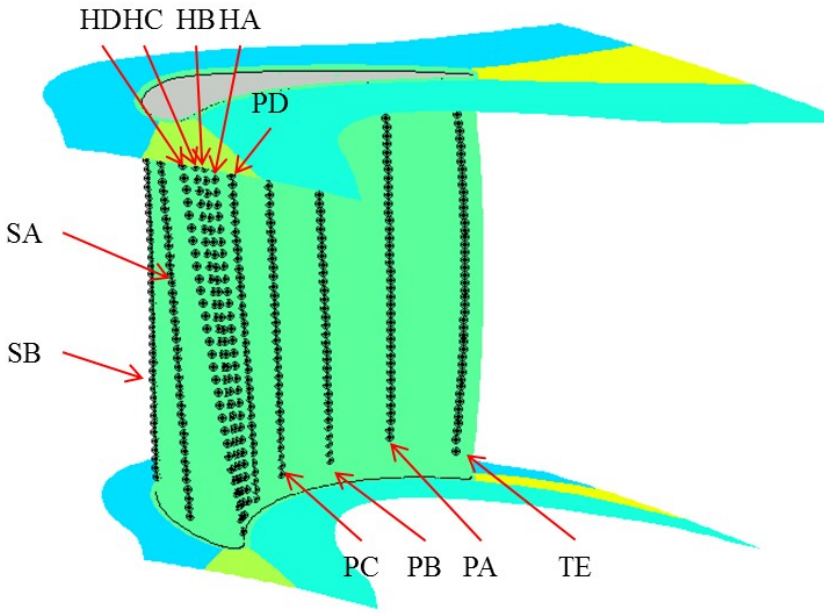

Figure 100: First Blade Cooling Rows

The conditions of the cooling air were closely monitored prior to the blowdown and kept at a constant fraction of inlet mass flow for each of the three tests. The total mass flows delivered to the first vane and blade from each tank are shown in Table 16. The cooling flows, pressures, and temperatures delivered to each row and the compound ejection angles are also listed in Table 16. The cooling rows are organized under the appropriate tank cooling source. The angle α is the angle off the surface of the airfoil, while angle β is the off-downstream-axial angle. Positive β angles point toward the OD and negative β angles point toward the ID. Note that the vane shower head rows are split at the midspan, and that both the ID and OD portions of the shower head rows point towards the midspan, as indicated by the positive and negative 90° β angles for the ID and OD halves, respectively. The number of holes in each row is also shown in the table. The pressures and temperatures were measured at both the ID and OD plenum of the vane and the blade. Therefore, the rows that share a common plenum have the same values. It should also be noted—although not shown in Table 16 but included in the mass flow numbers shown—that the trailing edge row for the vane and blade contain two holes that flow two and three times the mass flow as the rest of the holes as listed in the table. The outside-most holes—closest to the ID and OD endwall—flow three times the mass flow. The second-most outside holes—second closest to the ID and OD endwall—flow two times the mass flow. The mass flow values listed for each row reflect the amount of cooling flow for a single airfoil. In order to determine the row mass flows to the ID and OD cooling tank flows, one would need to multiply the vane and blade cooling rows by 16 and 34, respectively, which represents the number of cooled vanes and blades.

Table 16: Cooling Specifications for TRF Experiments 280100, 280200, and 280300

Inner Diameter Cooling Tank Total Mass Flow: 2.330 lb_m/s						
Cooling Row	Holes in Row	P_{t_c} (psia)	T_{t_c} (deg R)	Mass Flow (lb_m/s)	α (deg)	β (deg)
Vane PE	32	60.14	544.7	0.00529	30	0
Vane PF	33	60.14	544.7	0.00528	30	0
Vane HA ID	14	60.14	544.7	0.00206	30	90
Vane HA OD	15	60.14	544.7	0.00221	30	-90
Vane HB ID	15	60.14	544.7	0.00220	30	90
Vane HB OD	14	60.14	544.7	0.00205	30	-90
Vane HC ID	14	60.14	544.7	0.00205	30	90
Vane HC OD	15	60.14	544.7	0.00219	30	-90
Vane HD ID	15	60.14	544.7	0.00220	30	90
Vane HD OD	14	60.14	544.7	0.00205	30	-90
Vane HE ID	14	60.14	544.7	0.00208	30	90
Vane HE OD	15	60.14	544.7	0.00223	30	-90
Vane HF ID	15	60.14	544.7	0.00231	30	90
Vane HF OD	14	60.14	544.7	0.00216	30	-90
Vane SA	32	60.14	544.7	0.00675	55	0
Vane SB	33	60.14	544.7	0.01278	50	0
Vane SC	32	60.14	544.7	0.01349	45	0
Vane SD	33	60.14	544.7	0.01447	30	0
Vane ID PSFWD	4	60.14	544.7	0.00091	30	70
Vane ID SSFWD	7	60.14	544.7	0.00160	30	0
Vane ID LE	7	60.14	544.7	0.00151	90	0
Vane ID PS1	12	60.14	544.7	0.00410	30	65
Vane ID PS2	12	60.14	544.7	0.00410	30	67
Blade PA	42	50.81	525.4	0.00189	30	55
Blade PB	43	50.81	525.4	0.00223	30	55
Blade PC	42	50.81	525.4	0.00177	30	55
Blade PD	43	50.81	525.4	0.00235	30	55
Blade HA	31	50.81	525.4	0.00101	20	90
Blade HB	32	50.81	525.4	0.00105	20	90
Blade HC	31	50.81	525.4	0.00102	20	90
Blade HD	32	50.81	525.4	0.00128	20	90
Blade SA	42	50.81	525.4	0.00333	24	51
Blade SB	41	50.81	525.4	0.00338	24	51
Blade TE	46	50.81	525.4	0.00401	0	0

Outer Diameter Cooling Tank Total Mass Flow: 0.938 lb_m/s						
Cooling Row	Holes in Row	P_{t_c} (psia)	T_{t_c} (deg R)	Mass Flow (lb_m/s)	α (deg)	β (deg)
Vane PA	32	60.35	531.2	0.01011	30	0
Vane PB	33	60.35	531.2	0.00788	30	0
Vane PC	32	60.35	531.2	0.00504	30	0
Vane PD	33	60.35	531.2	0.00398	30	0
Vane TE	65	60.35	531.2	0.02196	0	0
Vane OD LE	7	60.35	531.2	0.00085	90	0
Vane OD SSFWD	5	60.35	531.2	0.00065	30	0
Vane OD PSFWD	8	60.35	531.2	0.00103	30	0
Vane OD PS1	7	60.35	531.2	0.00171	40	90
Vane OD PS2	12	60.35	531.2	0.00293	40	90
Vane OD SS	7	60.35	531.2	0.00246	30	60

CFD Methodology

The CFD solver, Leo, was used to provide the numerical analysis for the time-accurate, three-dimensional, stage-and-a-half experiments. Recall that the 3-D version of Leo is a Reynolds-Averaged Navier-Stokes solver that uses the two-equation Wilcox 1998 k-ω turbulence model for closure. A rigorous computational analysis was conducted in the previous chapter to determine the proper grid, temporal, and geometric model resolutions for the stage-and-one-half Research Turbine CFD cases. The results of that study were used for the numerical analysis conducted in this chapter. Recall that a 3/23rd section of the wheel will be modeled, which is a 3:6:3 airfoil count. Over 15 million nodes will comprise the computational domain, and there will be 400 time-steps per cycle. The cell count for each airfoil is shown in Table 17. Note that the total cell count is a sum of the cells in the three upstream vanes, six blades, and three downstream blades.

Table 17: Grid Cell Count

	1V	1B	2V
Axial upstream	29	25	25
Axial downstream	25	25	33
ngential (pitch)	75	51	75
Radial	69		
Axial on-vane	249		
Wall- Normal in O-grid	41		
Initial cell height (in)	$1x10^4$		
Total Cells per Airfoil ($x10^3$)	1786.5	834.1	1807.2
tal Cells ($x10^6$)	15.786		

Three TRF blowdown experiments at the same operating conditions were conducted to obtain a full set of static pressure data on the blade row. The boundary conditions were derived from taking an average of experiments 280100, 280200, and 280300. The boundary conditions listed in Table 15 were used for the numerical solution.

Convergence of the CFD simulation was achieved as described in the previous chapter. First, the steady-state flowfield was computed, and this solution was used as an initial condition for time-accurate simulation. The largest residual in the steady-state solution was reduced to at most 10^{-3} for any variable of interest, as shown in Figure 101. The cases were then run time accurately until periodic convergence was obtained. Mass flow, mass- and area-average total pressure and temperature, efficiency, and static pressure are plotted against iteration number in Figure 102. All quantities have attained periodicity. The unsteady analysis was then continued for exactly two blade-passing cycles, and the aforementioned flow variables are shown in Figure 103. Signal processing was conducted using the results from the two-cycle post-processing runs, after previously achieving periodic convergence.

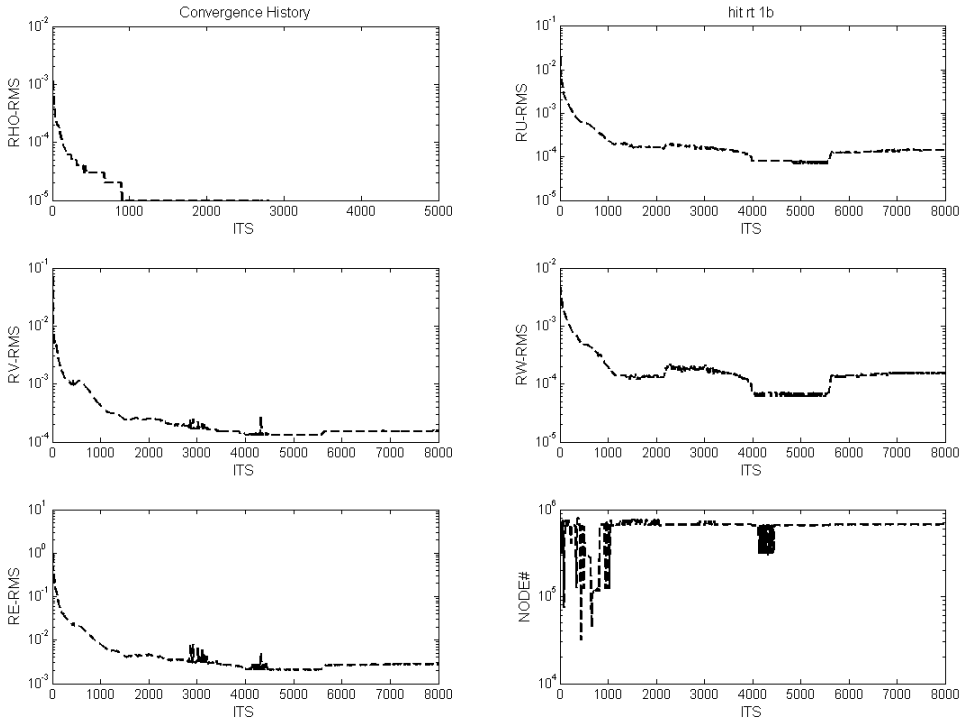

Figure 101: Convergence Histories of the Steady-State Simulation

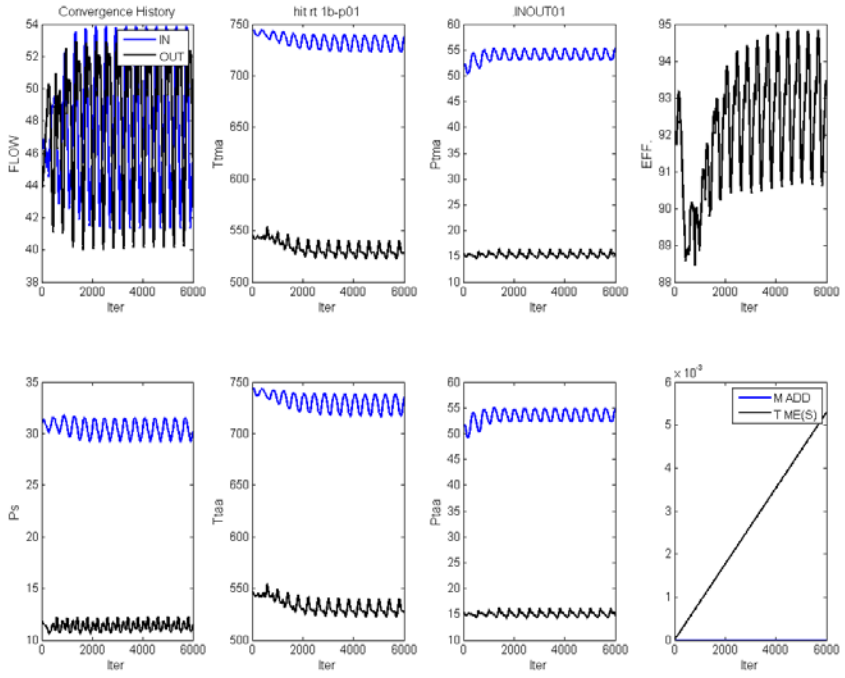

Figure 102: Development of Flowfield Periodicity in Unsteady Analysis

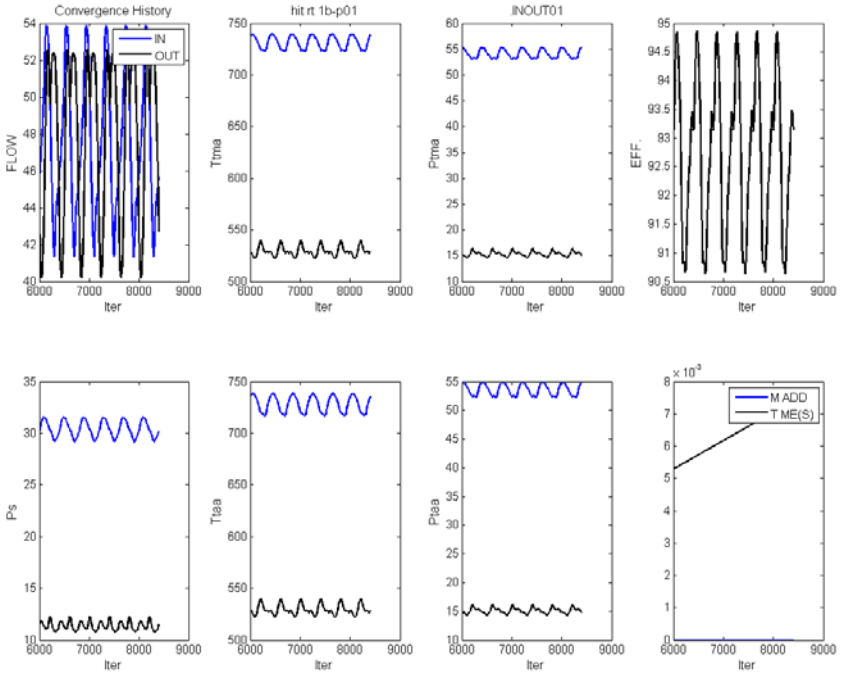

Figure 103: Periodicity of the Flowfield used for Detailed Comparison Against Experimental Results

Results

The physical and numerical experiments were carried out as described in the previous sections. Unless otherwise noted, all numerical data presented in this section is from the two-cycle post-processing run. The time-averaged surface pressure envelopes for the first vane, blade, and second vane are shown in Figure 104 through Figure 106, respectively. The solid lines represent averaged surface pressures and the dashed lines are the predicted peak-to-peak values. Colored circles represent averaged experimental data, and the error bars are the peak-to-peak values measured. Pressure side and suction side sensors are red and blue, respectively. Note that the pressure in all three plots is non-dimensionalized by the inlet total pressure to the first vane.

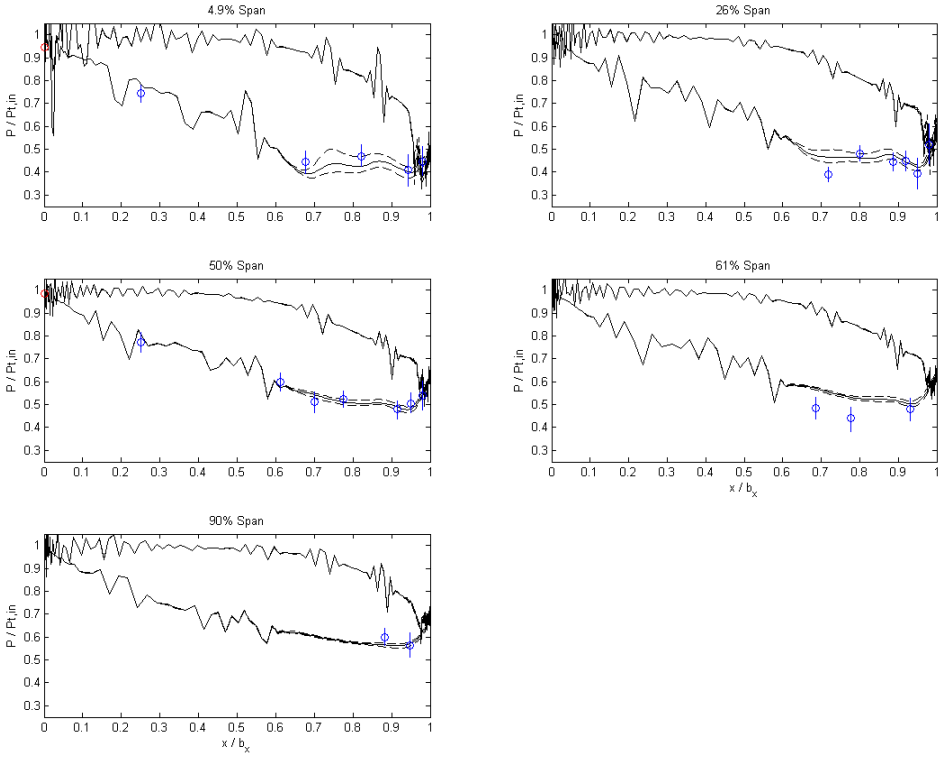

Figure 104: First Vane Unsteady Pressure Envelopes

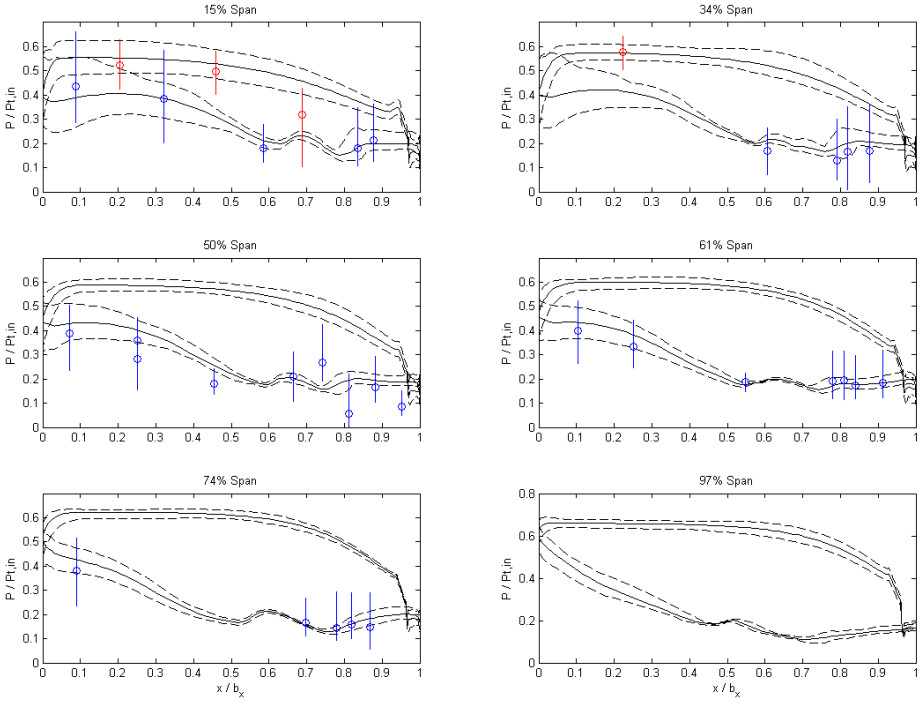

Figure 105: Blade Unsteady Pressure Envelopes

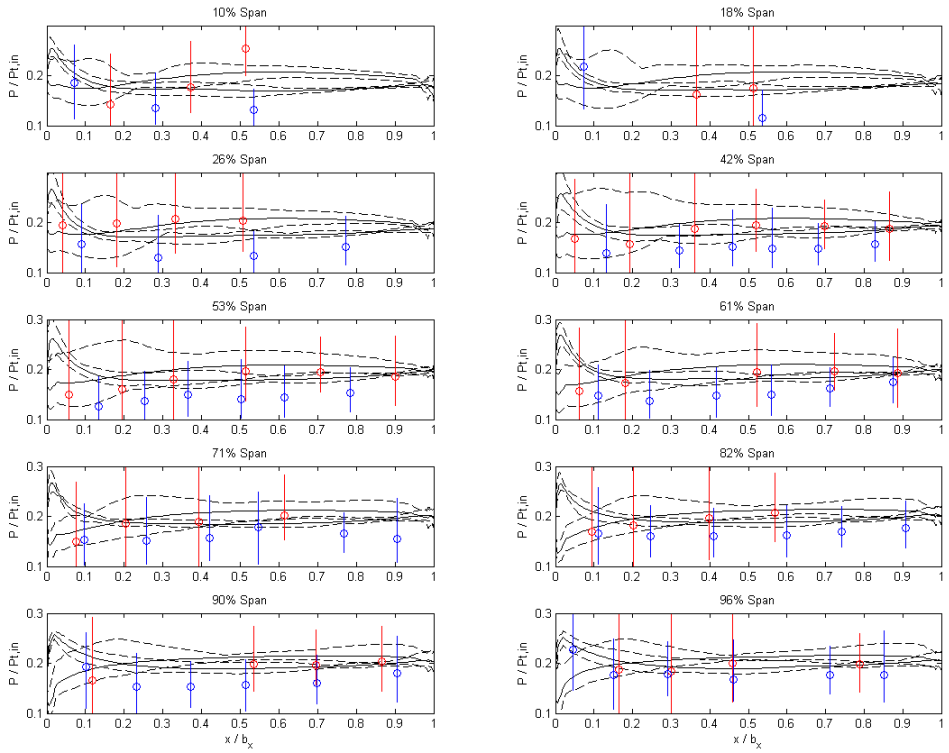

Figure 106: Second Vane Unsteady Pressure Envelopes

The time-mean experimental surface pressure data is predicted reasonably well, both qualitatively and quantitatively. In fact, the predictions for the first vane are extremely close to the experimental data, with a few notable exceptions, as can be seen in Figure 104. At 61 percent span, the numerical analysis over predicted the pressure on the suction side at approximately 70 and 80 percent of the axial chord. The same is also true at 26 percent span and approximately 72 percent axial chord. Overall, however, the experiment and predictions compare very well for the first vane. Both CFD and experimental data indicated relatively low magnitudes of unsteadiness, as depicted by the range of peak-to-peak values in the figure. The unsteadiness on the first vane was located downstream of the throat on the suction side, and this was consistent with the potential field interaction with the first blade. Also, the magnitude of the peak-to-peak unsteadiness is both predicted and measured to range from approximately 3 percent of the total inlet pressure to as high as 15 percent in some locations. The highest unsteadiness is found at the root and decreases toward the tip of the vane. Evidence of cooling injection can be seen on the first vane via the sharp fluctuations in predicted surface pressures.

Blade time-averaged pressures and the unsteady envelopes are shown in Figure 105. The experimental data and the predicted values of the time-averaged surface pressures are in good trend-wise agreement throughout all of the radial spans. The agreement on the pressure distribution on the suction side aft of the shock indicates that the target pressure ratio of the turbine was achieved. In addition, the agreement on the suction side upstream of the shock indicates that the target corrected speed of the rotor was achieved. The numerical analysis tended to predict lower peak-to-peak pressures than were measured. This is not an unexpected outcome because the RANS solver captures the unsteadiness only in the harmonics, whereas the pressure sensors measure the random fluctuations in addition to the unsteadiness in the harmonics. Also, the prediction and experiment both have similar patterns

of high and low peak unsteadiness across the surface of the airfoil. For example, both experimental and predicted data have the highest variation in the peak-to-peak surface pressures at the root of the blade and this decreases at spans closer to the blade tip. The unsteadiness is generally lower in magnitude on the pressure side compared to the suction side. Also, the greater magnitudes are located on the suction side near the leading and trialing edges, due to the interactions of the up- and downstream vanes.

The predicted and measured time-averaged pressures on the second vane are similar in trend, however shifted in magnitude, as seen in Figure 106. This is indicative of a small difference in the first stage pressure ratio between the experiment and numerical analysis, most likely caused by a mismatch in predicted and measured blade losses. The pressure on the second vane is highly unsteady on both the pressure and suction sides. Similar to the blade, the peak-to-peak unsteadiness was measured higher than the predictions in most instances on the second vane. The predicted peak-to-peak unsteady pressures range from 10 to 20 percent of the first vane inlet total pressure near the leading edge, and 5 to 8 percent near the trailing edge. The measured peak-to-peak unsteady pressures range from 15 to 30 percent at the leading edge, and approximately 10 to 15 percent near the trailing edge. Despite the difference in magnitude, both the predictions of the peak-to-peak unsteadiness and the measured values trend similarly: the highest unsteadiness is found near the leading edge, and it decreases towards the trailing edge.

Also, the unsteadiness does not change significantly in the radial direction on the second vane, which is in contrast to the behavior seen on the first vane.

The time-accurate solution and unsteady experimental data were also heavily investigated. Eight time slices of the numerical solution at the midspan section of a single blade rotating across a vane passage—or one complete periodic cycle—are shown in Figure 107. The figure is indicative of the complex flow field between the blade and the downstream vane that occurs as the blade completes one vane passing. Each subplot advances the numerical simulation 50 time-steps—one-eighth of a cycle—starting at the top left subplot and progressing counter-clockwise. Recall that the simulation used 400 time-steps for each vane passing. Therefore, the “Initial” subplot would follow the “+350 Its” subplot to begin the next cycle, with exception to the shock and blade labels. The colored shading is the static pressure field and the contours are changes in entropy from the inlet, calculated via the Gibbs equation [43]. The static pressure is used to identify shocks, and trailing-edge wakes are easily visualized by the changes in entropy. The reflected shocks are labeled with a subscript indicating the blade in which the shock originated.

Fundamentally, the shocks from the blade travel downstream and impinge on the pressure side of the downstream vane and reflect onto the suction side of the neighboring blade. As the blade rotates, the impinging shock moves from the trailing edge of the pressure side of the downstream vane toward the leading edge and the reflected shock moves upstream in the vane passage. After the reflected shock leaves the downstream vane passage, it continues upstream and impacts the suction side of the blade.

In greater detail, beginning with the “Initial” subplot in the top left corner, one can truly visualize the high complexity of the flowfield between the blade and downstream vane. The shock in between the airfoils, S_A, has already reflected off of the downstream vane and is traveling upstream, interacting with trailing-edge wakes from the blades. Shock S_B has just

reflected off of the vane. Shock S_B is at a shallower angle than shock S_A at this point in its development. In the "+50 Its" frame, the blades have rotated upwards and the shocks have progressed upstream towards the blade. Note that as the shocks travels further upstream, their orientation becomes more aligned with the circumferential direction. The "+100 Its" subplot shows the impact of shock S_A on blades C and D. Shock S_B has traveled through the passage of the vane. The shock traveling the passage caused a high pressure region—particularly on the pressure side—to move along the airfoil from the trailing edge to the leading edge. In frame "+150 Its," Shock S_B has moved completely off of the downstream vane and shock S_C is clearly recognized and reflecting off of the vane at a shallow angle. During the next two frames, "+200 Its" and "+250 Its," shock S_B approaches the blade row while shock S_C continues to progress upstream through the downstream vane passage. Shock S_B has impacted blades D and E in subplot "+300 Its." This marks the second time during the current cycle that blade D has experienced a high degree of unsteadiness due to the blade and downstream vane shock interaction. Subplot "+350 Its" shows shock S_C has progressed out of the vane passage and continues to move upstream toward the blade row. Also, shock S_D is clearly visible, having just reflected off of the vane. This cycle would repeat itself by continuing to the "Initial" frame and substituting the blade and shock labels. Shock S_A and S_B become S_C and S_D, respectively, and blades B, C, D, and E become D, E, F, and G respectively, in the new "Initial" frame.

Therefore, during each vane passing, a blade is impacted twice by reflected shocks that have originated from the second and third preceding vanes. For example, in the vane passing cycle shown in Figure 107, blade D is impacted by reflected shocks from blade A and blade B. Recall that a cycle consists of one complete vane passing by the blades, and that there are 23 downstream vanes. Therefore, during one revolution, each blade is impacted 46 times and hence the strong 46E driver on the suction side of the blade, downstream of the throat. Also, the pressure and suction sides of the downstream vane are impacted by one incident or reflected shock per blade passing, respectively. There are 46 blades on the rotor, which leads to the strong 46E driver on the downstream vane.

The percent signal power variation derived from the power spectral density predicted at 46E is shown in Figure 108. Note that the pressure sides of each airfoil are shown in the upper portion of the figure, and the suction sides are shown in the lower portion. The pressure and suction sides are grouped as described for the convenience of the researcher when selecting sensor locations to interrogate. This is contrary to what one would actually see looking circumferentially from one direction and seeing the pressure, suction, and pressure sides of the first vane, blade, and downstream vane respectively. Also, selected sensors are identified on the figure for reference later in the chapter.

Based on the unsteady flow characteristics described with reference to Figure 107, it is not a surprise that the majority of the unsteadiness on the downstream vane occurs at 46E. A shock from each of the 46 blades reflects from the downstream vane passage along the pressure and suction side prior to impacting the blade, as previously discussed. Similarly, the 46E frequency is the major driver for most of the suction side of the blade aft of the throat, which is impacted by the aforementioned reflected shocks. As shown in Figure 109, the vast majority of the unsteadiness on the remaining areas of the blade is from the 23E frequency, due to the 23 vanes up- and downstream of the blade row.

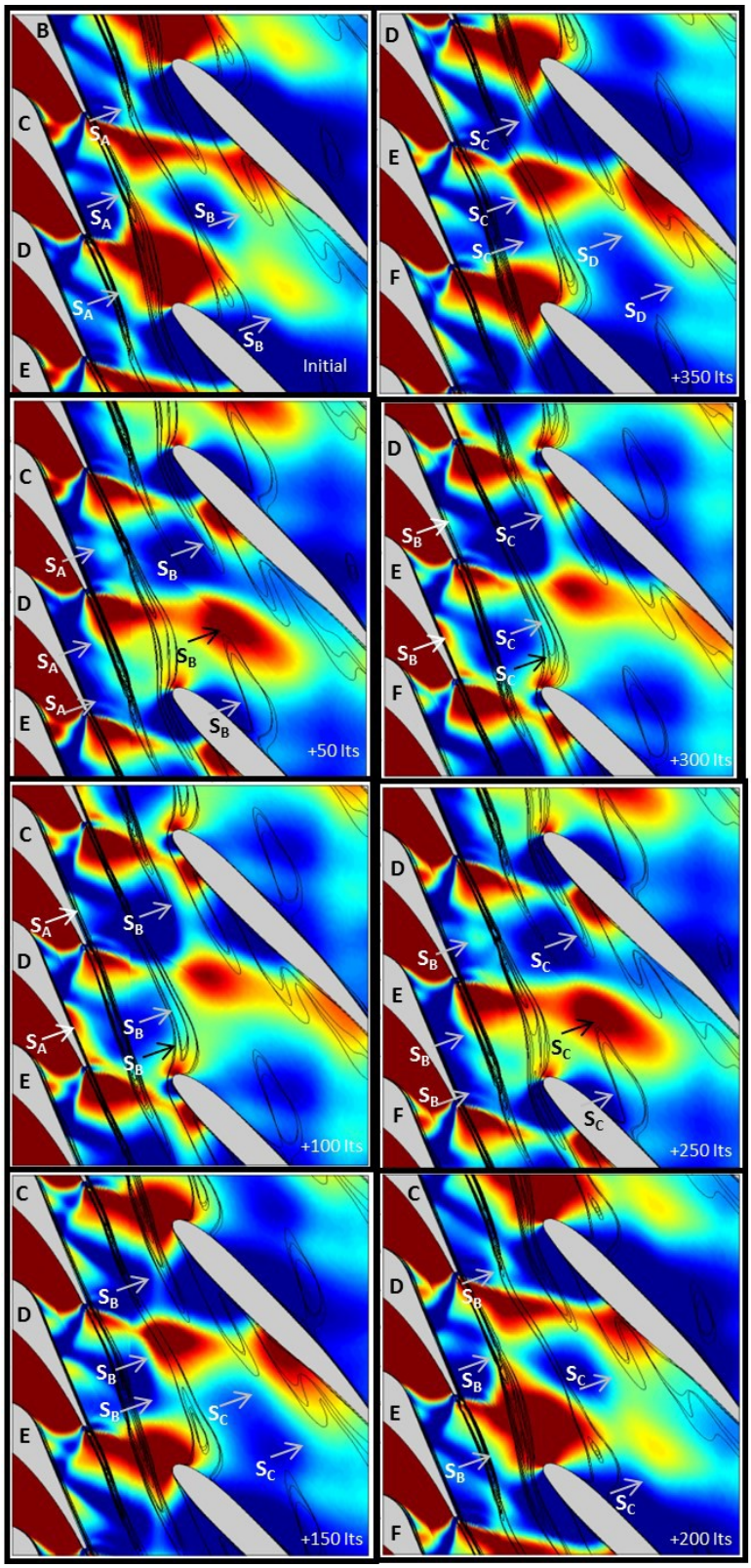

Figure 107: Unsteady CFD Flowfield of Blade and Downstream Vane

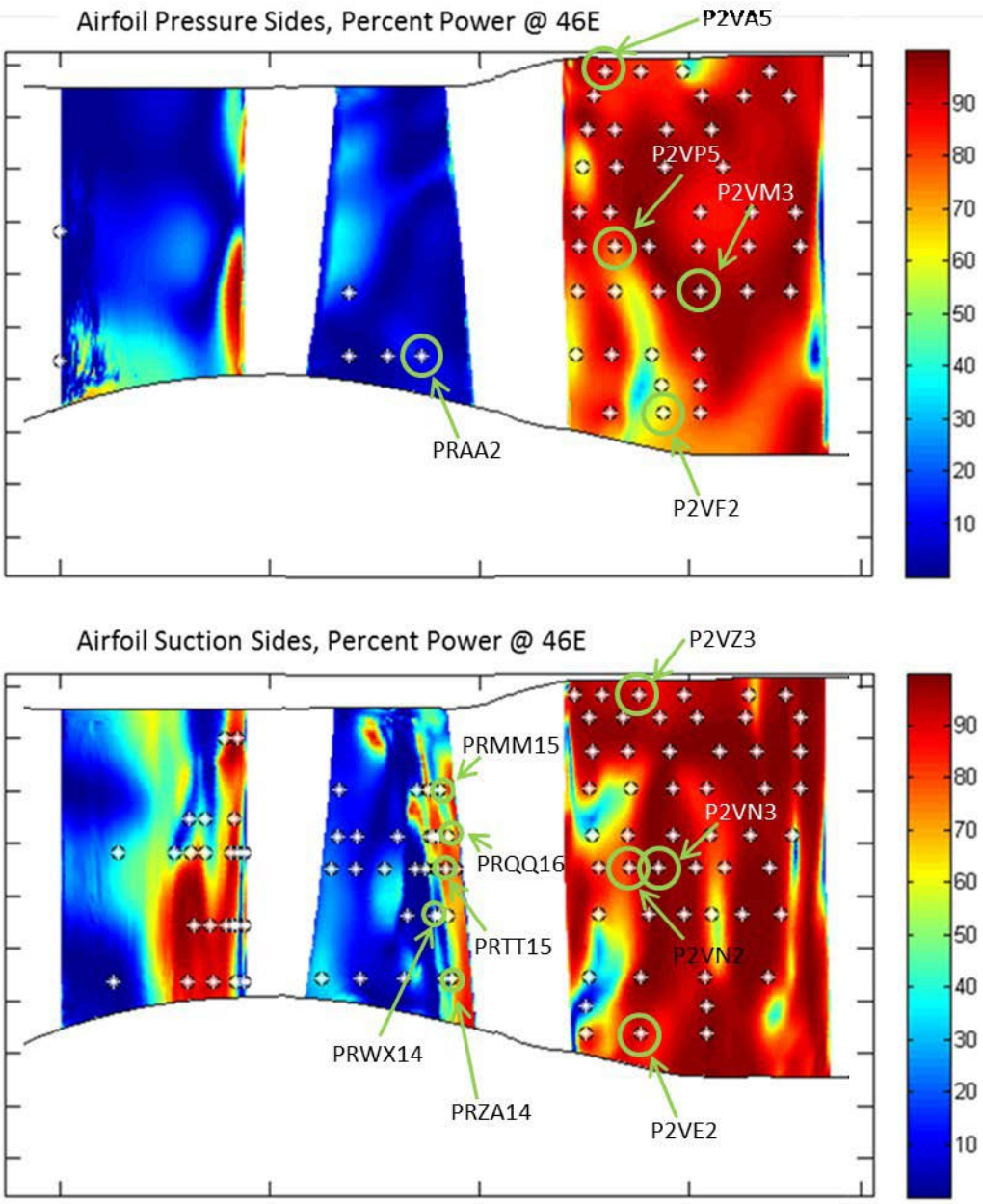

Figure 108: Predicted Percent Signal Power on the Airfoils at 46E

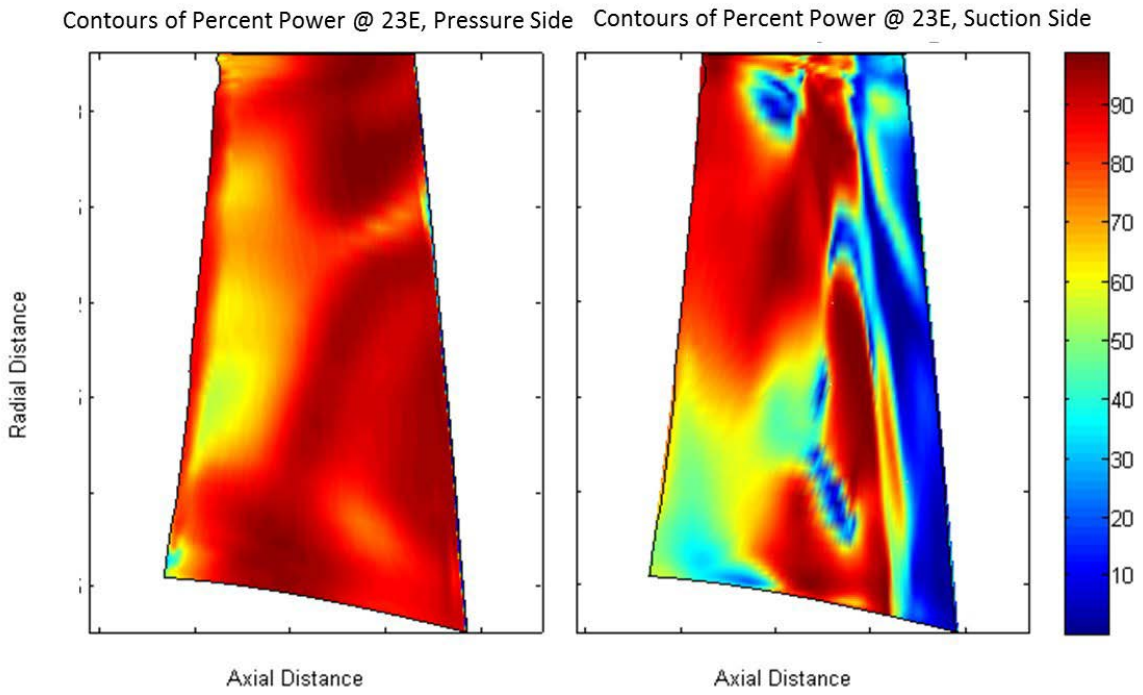

Figure 109: Percent Signal Power on Blade Surfaces at 23E

The Discrete Fourier Transforms (DFT) of the unsteady predicted and measured signals were also compared. The DFT of sensor PRZA14 is shown in Figure 110. Sensor PRZA14 is located on the suction side of the blade at 15 percent span, downstream of the shock at 87.7 percent axial chord. Recall that all sensor locations are listed in Table 12. In the upper graph, the time traces of the experimental and predicted surface pressure are plotted for one revolution. The surface pressures are normalized by the total inlet pressure of the first vane. The first complete revolution of the experimental data is shown in red and the ensemble average of 99 revolutions is shown in blue. Both are compared to the predicted surface pressure plotted in black. The black and green dashed line represents the cyclical repeated prediction. The signal shapes of the experiment—both the single revolution and the ensemble average—and the predicted variation match extremely well.

Both sets of time traces clearly indicate similar unsteady, periodic pressure rises due to the interaction of the downstream vane. The magnitude of the surface pressure time traces is slightly offset. The average of the predicted time trace for sensor PRZA14 is approximately 20 percent of the first vane inlet total pressure, and the experimental average is approximately 15 percent. Also, the rise of the measured pressure during the revolution from approximately 5 to 6.5 ms is attributed to the instrumentation unique to the facility that was not modeled in the simulation.

The DFT magnitudes of the predicted and experimental signals of PRZA14 are shown in the bottom graph. Once again, the black line represents the predicted data and the blue line the ensemble averaged experimental data. One difference from the upper plot, however, is that the red line represents the DFT of the entire experimental time trace during the test window—3.722 to 10.73 seconds for TRF experiment 280100, as shown in the figure—as opposed to just one revolution. The DFT of the three signals indicate relatively high magnitudes of

unsteadiness at 23E (2.92 kHz) and 46E (5.84 kHz). Other than very low frequency drivers detected on the experimental data—most likely driven by the facility or test instrumentation—the 46E and 23E are the greatest in magnitude. This is more evident in the experimental data than the predicted signal.

One should note that the ensemble average data should be more consistent with the predictions in the case of DFT analysis due to the assumptions behind such an analysis. The DFT of the entire pressure signal was calculated using a period equal to the time interval of all revolutions. However, the RPM varied slightly over the test period, and this can have a negative impact on the DFT analysis. Calculating the DFT over the full period would result in the sharing of signal power over a range of frequencies. On the other hand, a DFT analysis was conducted for each revolution using the appropriate time scale. Thus, in this case, the DFT of the ensemble average is a truer indicator of the magnitudes of unsteadiness for the experimental data. As shown in Figure 110, the ensemble average DFT matches very closely with the predicted DFT for the 23E and 46E unsteadiness. Recall that there are 23 vanes up- and downstream of the blade row. Both the experimental and predicted data are capturing the unsteadiness of the interaction of the blade and downstream vane.

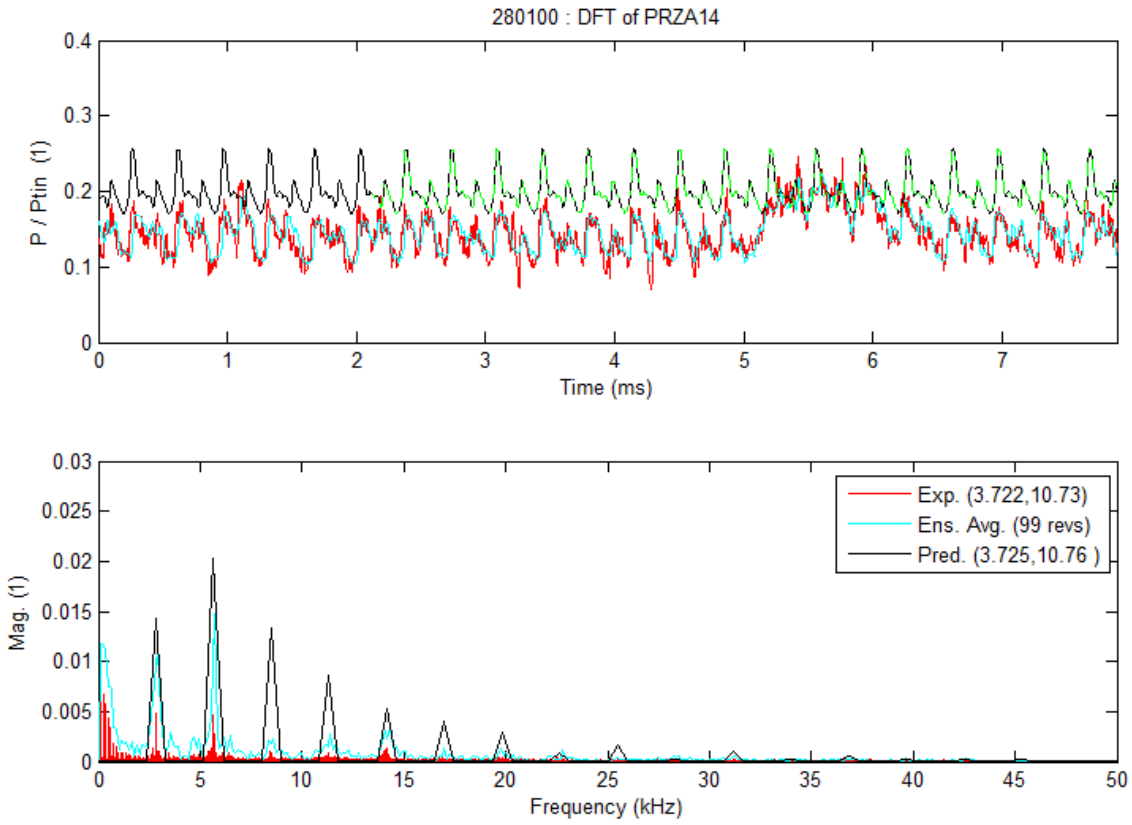

Figure 110: Experimental and Predicted DFT of PRZA14 (Blade SS, 15% Span, 87.7% Axial Chord)

In order to illustrate the difference of the up- and downstream drivers, the time-accurate surface pressure traces and DFT analyses of sensors PRFF14 and PRAA2 are shown in Figure 111 and Figure 112, respectively. As listed in Table 12, sensor PRFF14 is located on the suction side of the blade at 49.5 percent span, upstream of the throat at 25.2 percent axial

chord. Sensor PRAA2 is located on the pressure side of the blade at 15 percent span and 68.8 percent axial chord. The DFT analyses clearly indicate that the main driver for unsteadiness at these locations is the 23E frequency. As previously discussed, the upstream interaction seen by the blade will be dominated by 23E because the blade passes through each of the 23 upstream potential fields. Downstream of the throat, the interaction seen by the blade will consist heavily of 46E as well, due to the shock reflection from the downstream vanes.

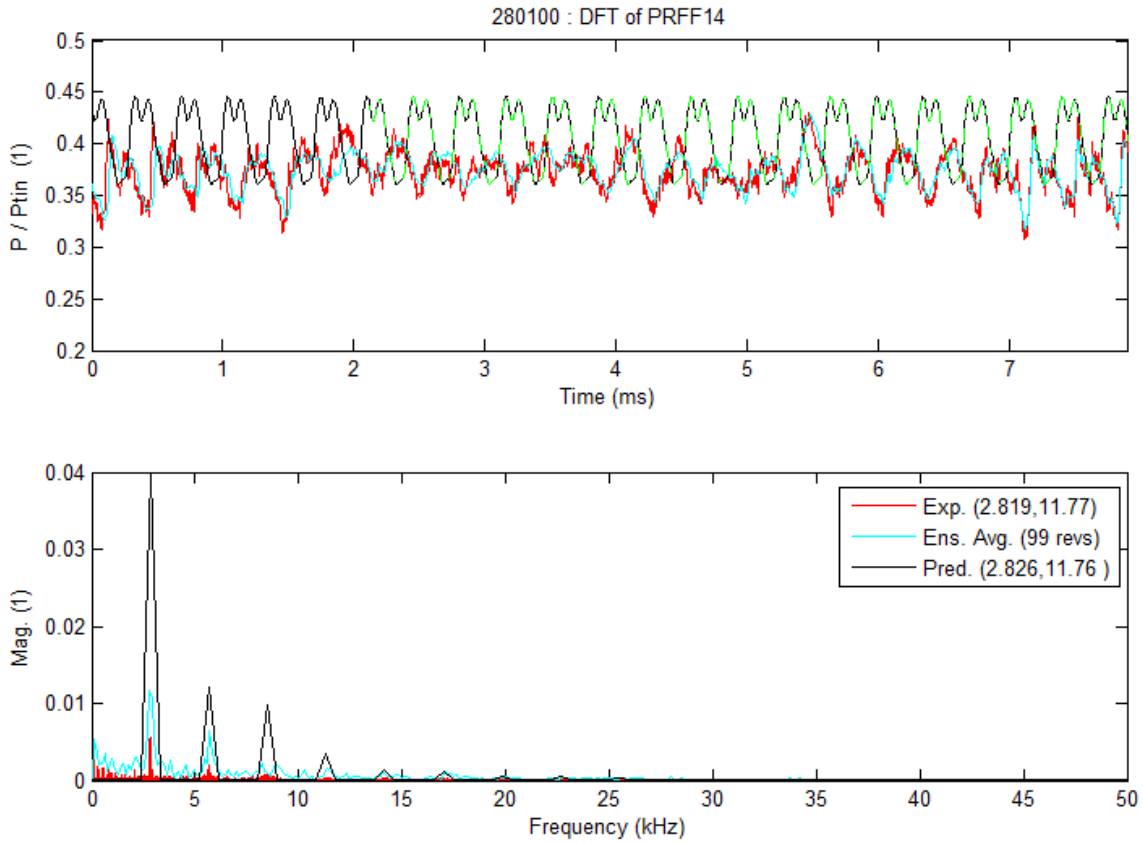

Figure 111: Experimental and Predicted DFT of PRFF14 (Blade SS, 49.5% Span, 25.2% Axial Chord)

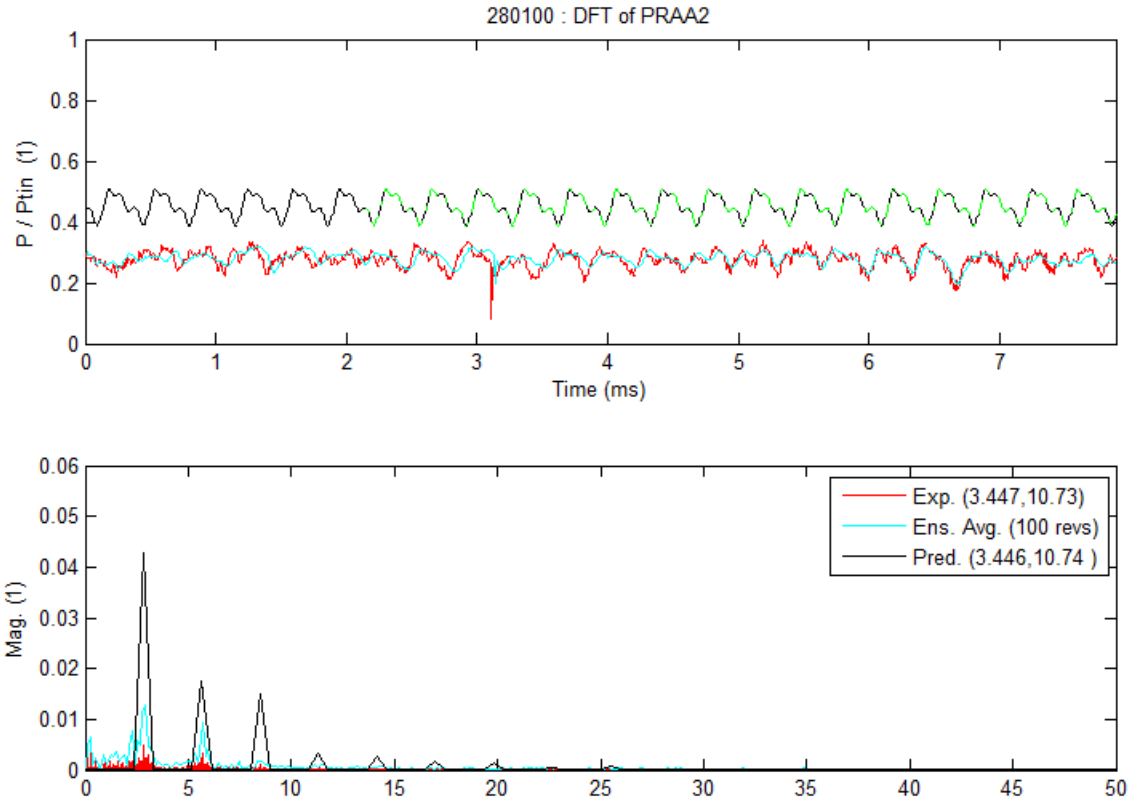

Figure 112: Experimental and Predicted DFT of PRAA2 (Blade PS, 15% Span, 68.8% Axial Chord)

Sensors PRWX14, PRTT15, PRQQ16, and PRMM15 are also on the blade suction side and axially located very near or aft of the cross-passage shock, but at various spans relative to PRZA14. The DFT analyses of the signals recorded by these sensors are shown in Figure 113 through Figure 116, respectively. Each of the experimental signals and DFT analyses shown of the surface pressure traces matches the predictions very well. Note that sensors PRTT15 (Figure 114) and PRMM15 (Figure 116) also have a slight offset in the magnitude of the surface pressure traces. The experimental DFT analyses capture a very low engine order mode, just as previously shown for sensor PRZA14. This is most likely driven by the facility or instrumentation, and can be seen in the pressure traces as a temporary rise in the average pressure. The relative magnitudes of the fundamental (23E) and first harmonic (46E) frequencies of the vane interaction are captured well by the predictions. The presence of higher harmonics aft of the shock on the suction side was also predicted well. However, the actual magnitudes at the harmonics were predicted with mixed results. The fundamental and second harmonic of the blade were significantly over predicted on sensor PRWX14 (Figure 113). Although, as shown in Figure 108, this sensor is located very near—but just upstream of—the cross- passage shock. This is confirmed by the experimental data in that the 23E response is much greater than that of the 46E. Even small fluctuations of the shock in this vicinity could significantly alter the pressure magnitude at these frequencies. Other significant misses in the prediction include the second harmonic of the blade on sensors PRTT15 (Figure 114) and PRMM15 (Figure 116). The predicted magnitude was far greater than was measured. Also, the higher order frequencies were measured to have higher unsteadiness than predicted

at the location of sensor PRMM15. Overall, however, the numerical analysis captured the physics of the vane-blade interaction very well. There was a very good match in the remaining sensor locations and frequencies not identified above. Sensor PRQQ16 (Figure 115) was predicted very well, in particular. The magnitudes at each frequency are nearly identical and the predicted and measured pressure traces are aligned. Also, the fundamental and first harmonic of the blade at the locations of sensors PRTT15 and PRMM15 were predicted accurately.

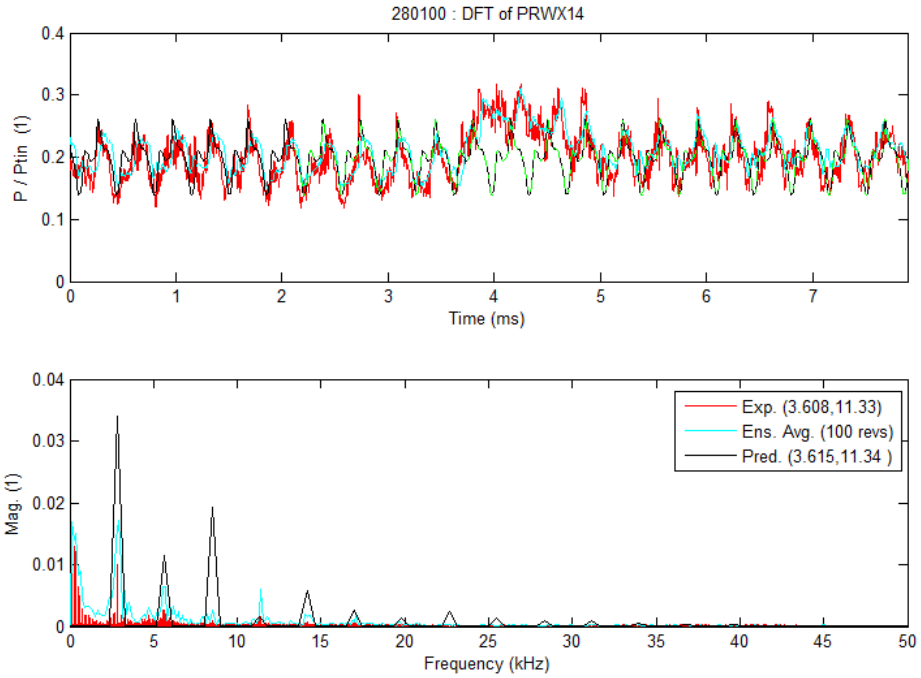

Figure 113: Experimental and Predicted DFT of PRWX14 (Blade SS, 35% Span, 82% Axial Chord)

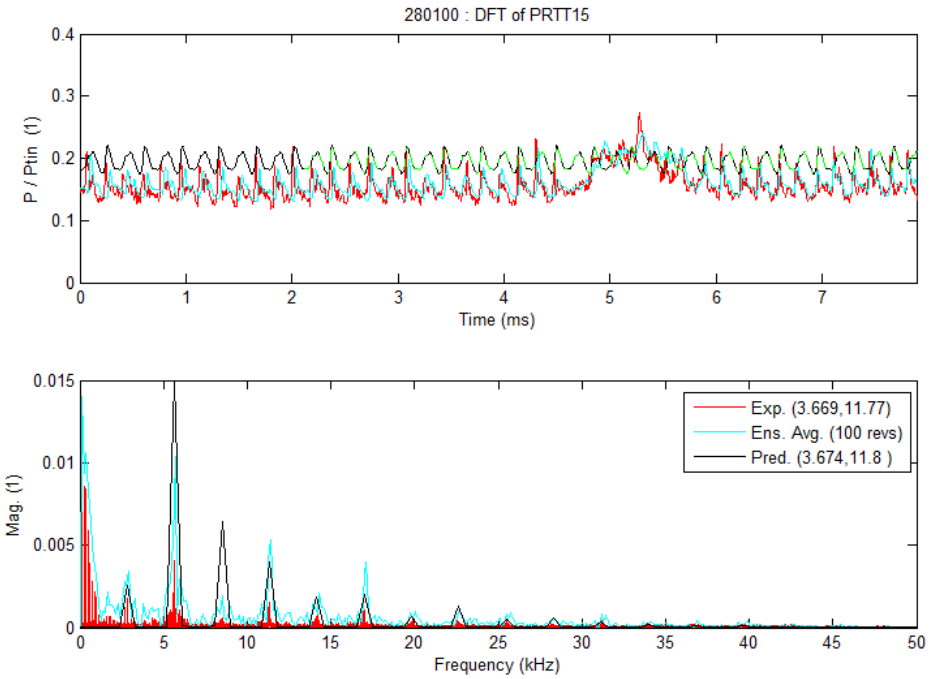

Figure 114: Experimental and Predicted DFT of PRTT15 (Blade SS, 49.5% Span, 88.1% Axial Chord)

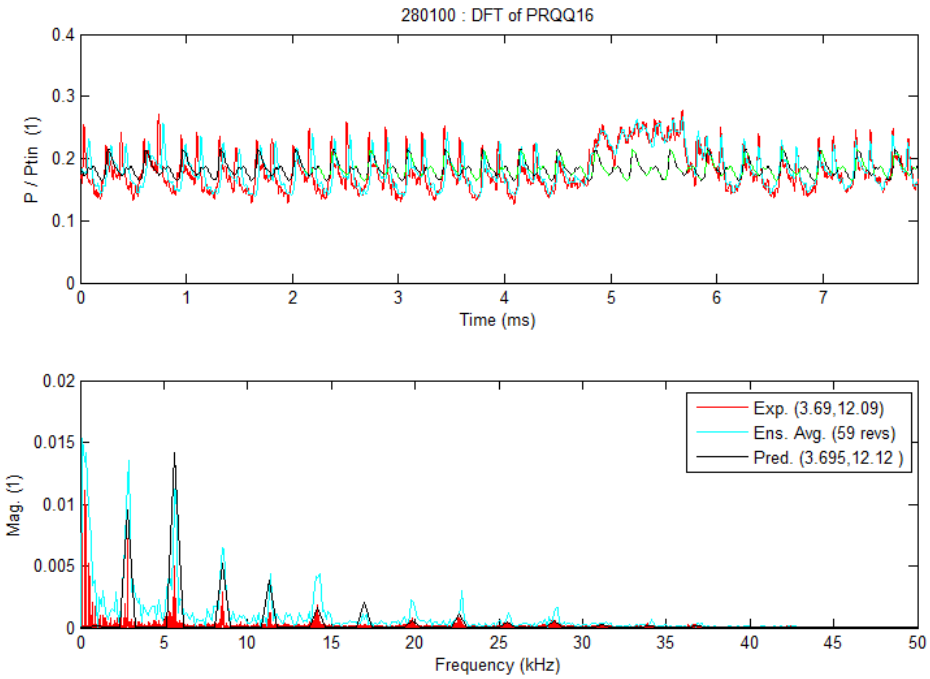

Figure 115: Experimental and Predicted DFT of PRQQ16 (Blade SS, 60% Span, 91.2% Axial Chord)

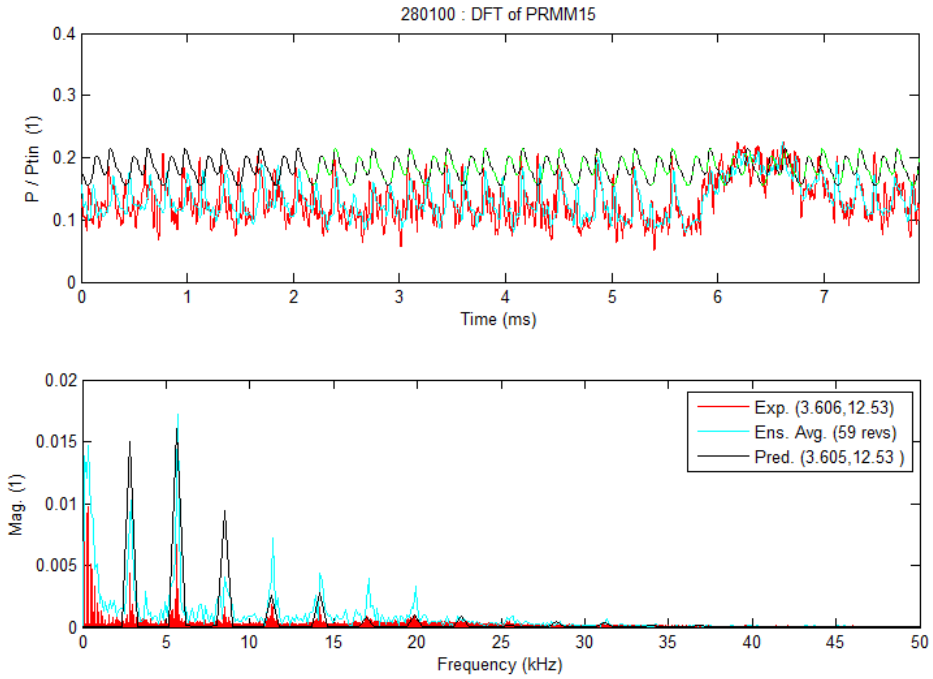

Figure 116: Experimental and Predicted DFT of PRMM15 (Blade SS, 74.6% Span, 86.8% Axial Chord)

The pressure traces and Discrete Fourier Transforms were also investigated on the downstream vane, and these are shown in Figure 117 through Figure 122. The figures represent sensors P2VF2, P2VM3, and P2VA5 on the pressure side, and P2VE2, P2VN2, and P2VZ3 on the suction side, respectively. For all pressure and suction side sensors on the downstream vane, the 46E frequency had the highest magnitude response. This was also true for the predictions—which one can also see in Figure 108—and the measurements from the experiment. The second highest responder was the first harmonic frequency of the upstream blade, or 92E (11.68 kHz). Although there were some sensors in which the absolute magnitude of the responses at each frequency were under or over predicted, the prediction and measured values do show good qualitative agreement when comparing the relative strength of each response with respect to each frequency. The predicted pressure traces on the pressure side were in very good agreement with the ensemble averaged data. However, despite the shape of the traces looking very similar on the suction side, there was an offset of the predicted and measured pressure. The unsteady pressure was over predicted on the suction side by as high as five percent of the first vane inlet total pressure in some cases. This is likely due to a difference in the predicted and measured pressure losses in the first stage. A similar effect was seen when examining the predicted and measured pressure envelopes in Figure 106.

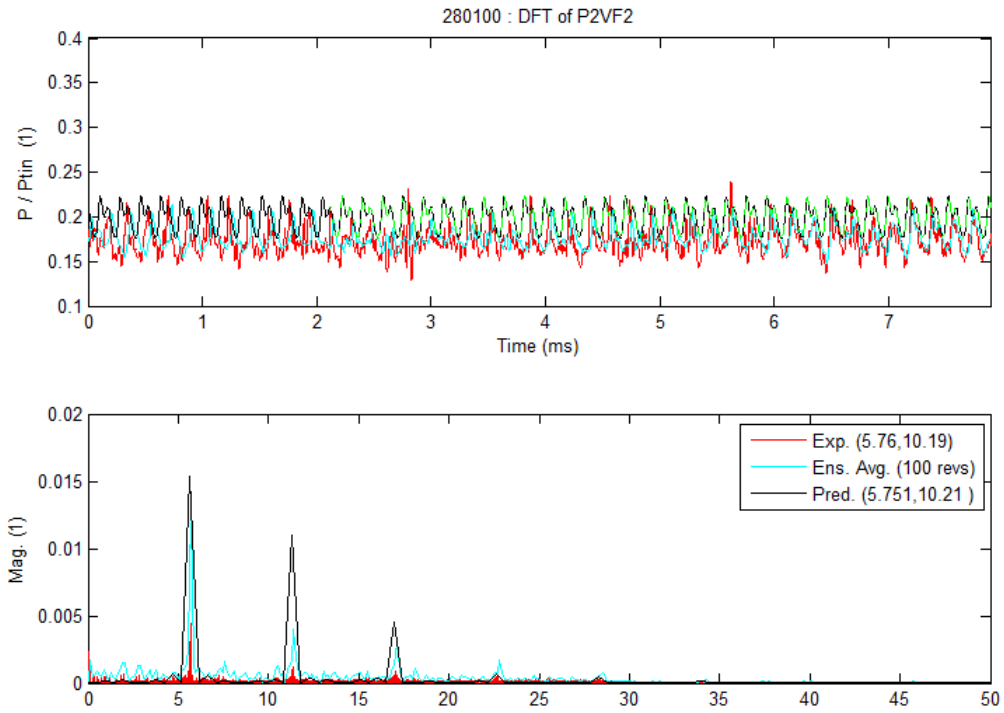

Figure 117: Experimental and Predicted DFT of P2VF2 (Downstream Vane PS, 10.6% Span, 37.2% Axial Chord)

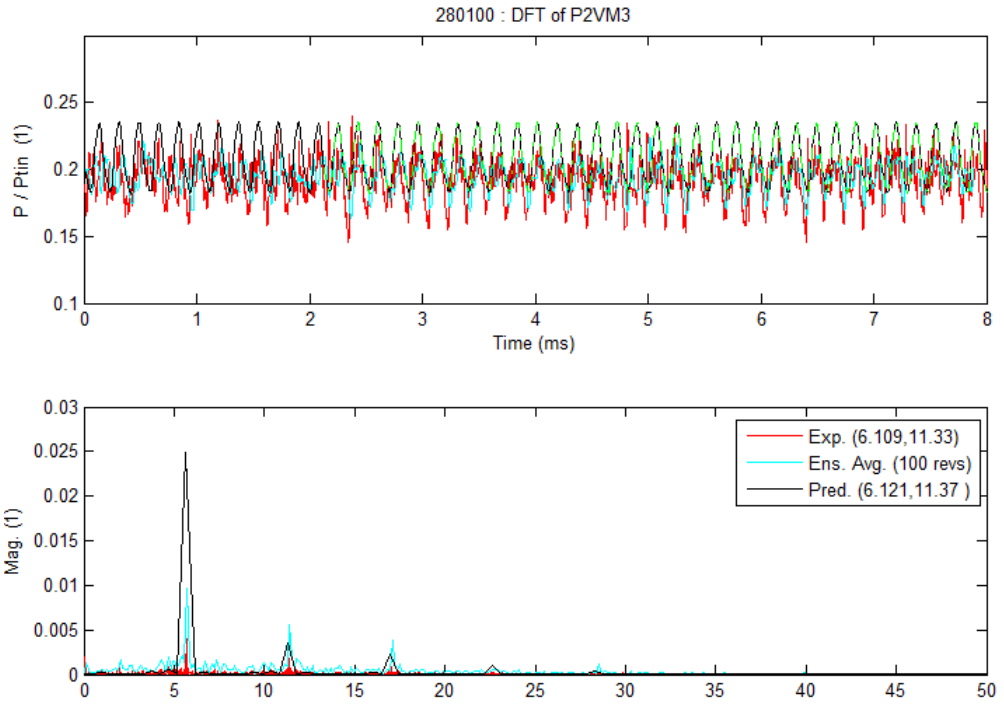

Figure 118: Experimental and Predicted DFT of P2VM3 (Downstream Vane PS, 40.7% Span, 52% Axial Chord)

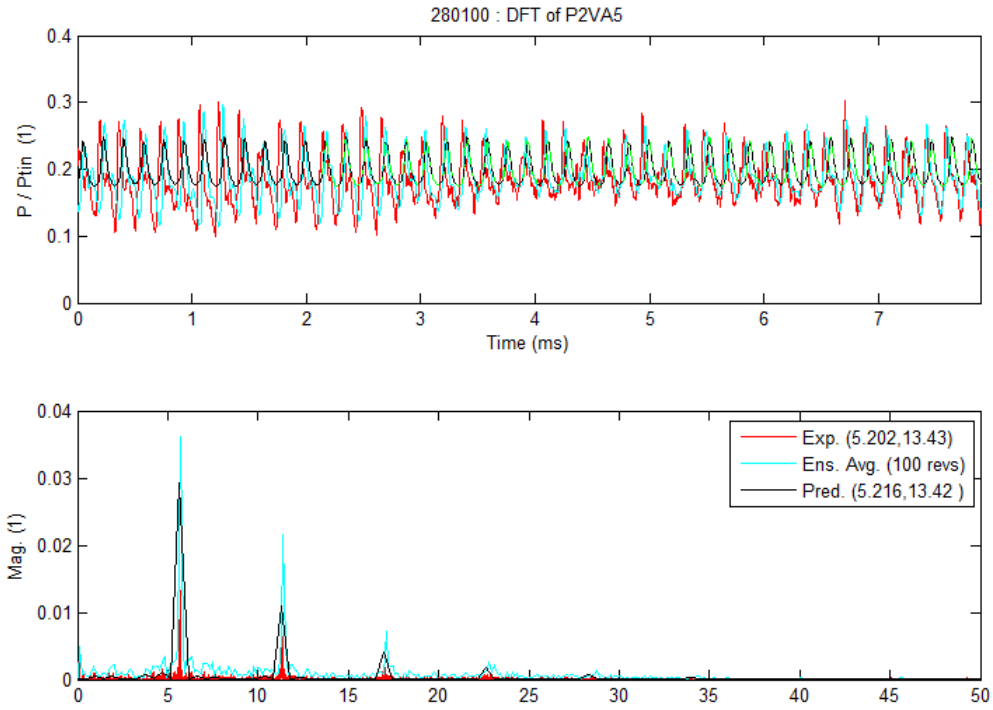

Figure 119: Experimental and Predicted DFT of P2VA5 (Downstream Vane PS, 95.7% Span, 16.4% Axial Chord)

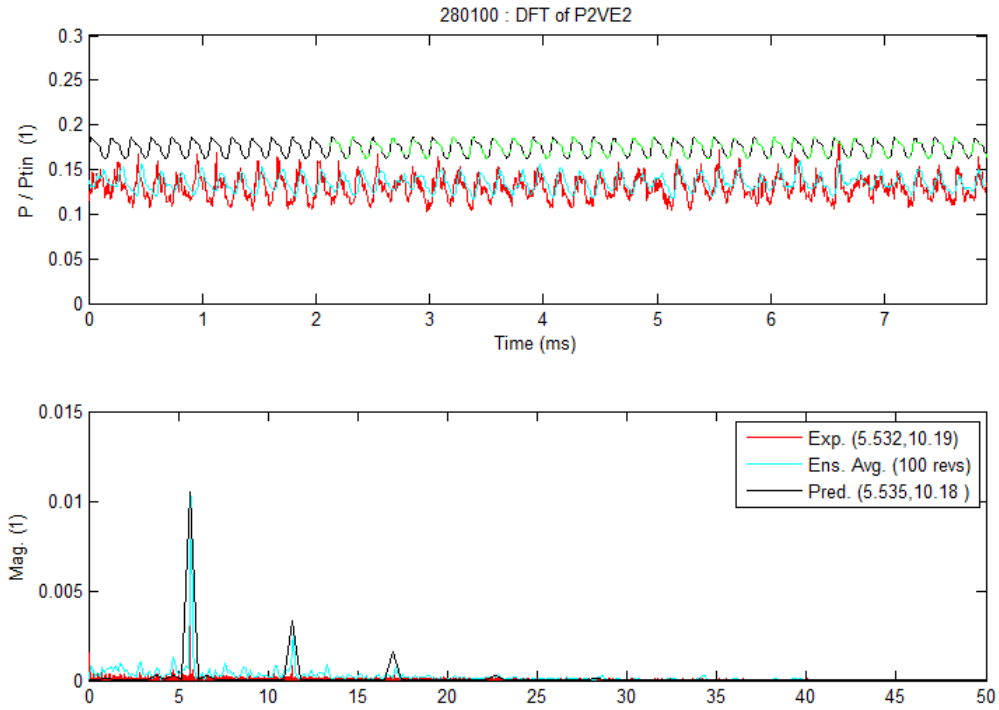

Figure 120: Experimental and Predicted DFT of P2VE2 (Downstream Vane SS, 10.6% Span, 28.1% Axial Chord)

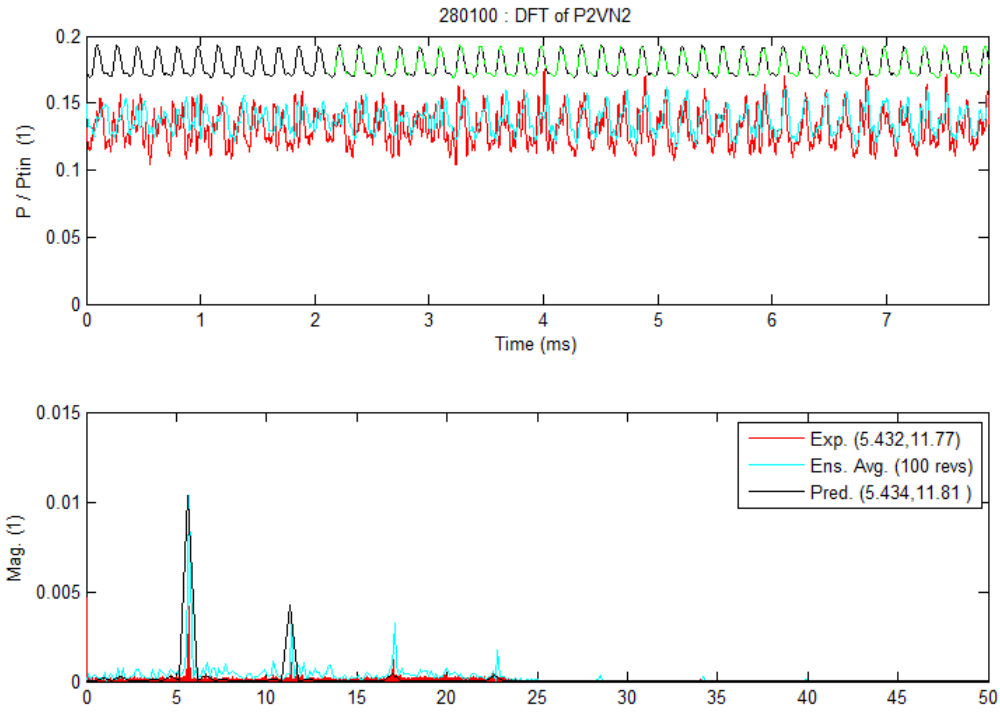

Figure 121: Experimental and Predicted DFT of P2VN2 (Downstream Vane SS, 52.2% Span, 25.2% Axial Chord)

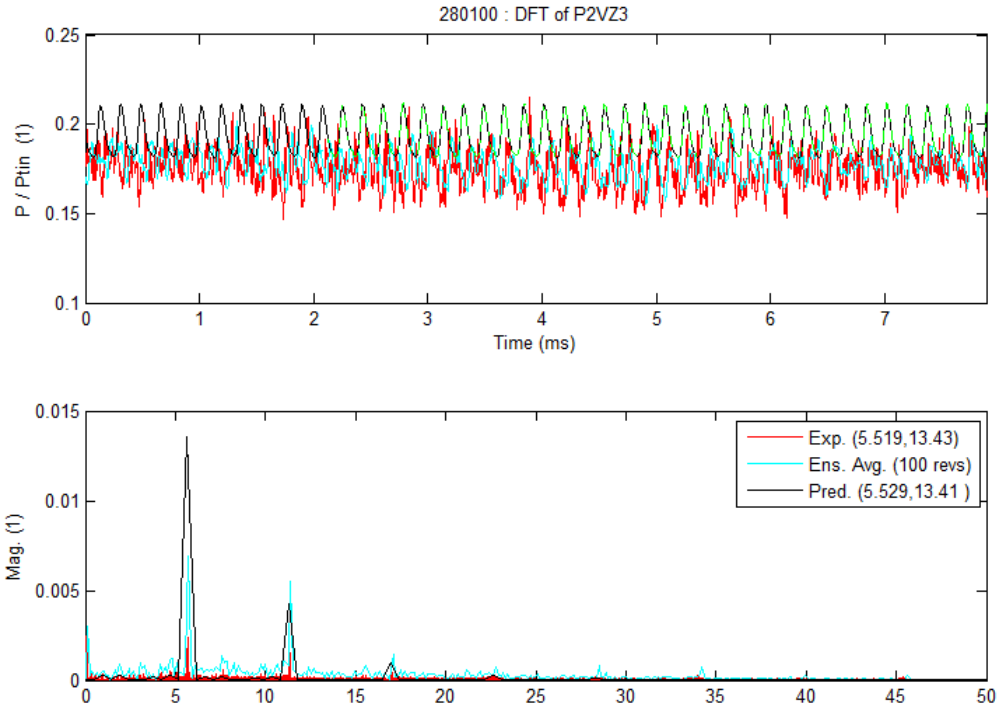

Figure 122: Experimental and Predicted DFT of P2VZ3 (Downstream Vane SS, 95.7% Span, 29.1% Axial Chord)

Contours of the maximum cross-correlation coefficient (CCF) on the pressure side of the downstream vane are shown on the left side of Figure 123. The maximum CCF plotted in the figure is with respect to the center of the pressure side, as indicated on the plot. On the right side of Figure 123, the contours represent the number of time lags to the maximum CCF. Again, this is with respect to the center of the pressure side as indicated by the black square in the left figure. Similarly, the contours of maximum CCF and lags to maximum CCF for the downstream vane suction side are shown in Figure 124. Each time lag increment represents one time-step taken in the prediction, which is 8.83×10^{-4} ms for this simulation. For example, point A and point B have a maximum CCF at -100 lags, which implies that the signal measured at point A was 100 lags—or, in this case, 8.83×10^{-2} ms—prior to that same signal being measured at point B. The sensors on the downstream vane pressure side are shown on each plot as white circles. The lags to maximum CCF plot appears to be discontinuous at approximately the quarter-chord, shifting from negative to positive lags traversing from aft forward. However, this is not the case: it is simply a "wrapping" effect. The predicted lags were compared to the center reference point on either side of the lag sign shift—as indicated on the plot by the green circle. The predicted pressure traces and CCF at these locations and the reference point are shown in Figure 125 and Figure 126. The downstream side of the lag shift is shown in Figure 125, and the upstream side is shown in Figure 126. The maximum CCF values relative to the reference point is -68 lags for the downstream side and 124 lags for the upstream side—a difference of 192 time-steps. Recall, that blade passing occurs at 200 cycles. Therefore, the shift from negative to positive lags—aft looking forward—is a numerical artifact that simply indicates a switching of the unsteady driver from one traveling shock to the one that preceded it. Subtracting 200 time-steps—one blade passing—from the upstream side of the lag shift would result in continuous lag contour plot, as expected. This can also be seen by determining the number of lags to the second highest CCF for the upstream location, which is -75 lags.

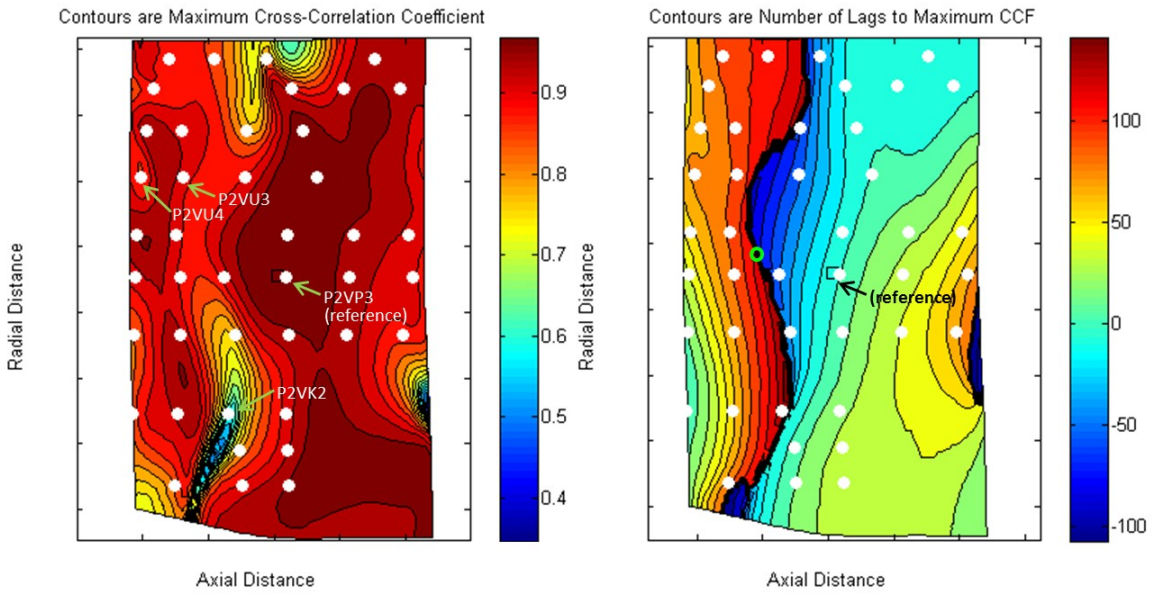

Figure 123: Contours of Maximum Cross-Correlation Coefficient (CCF) (left) and Lags to Maximum CCF (right) on the Downstream Vane Pressure Side

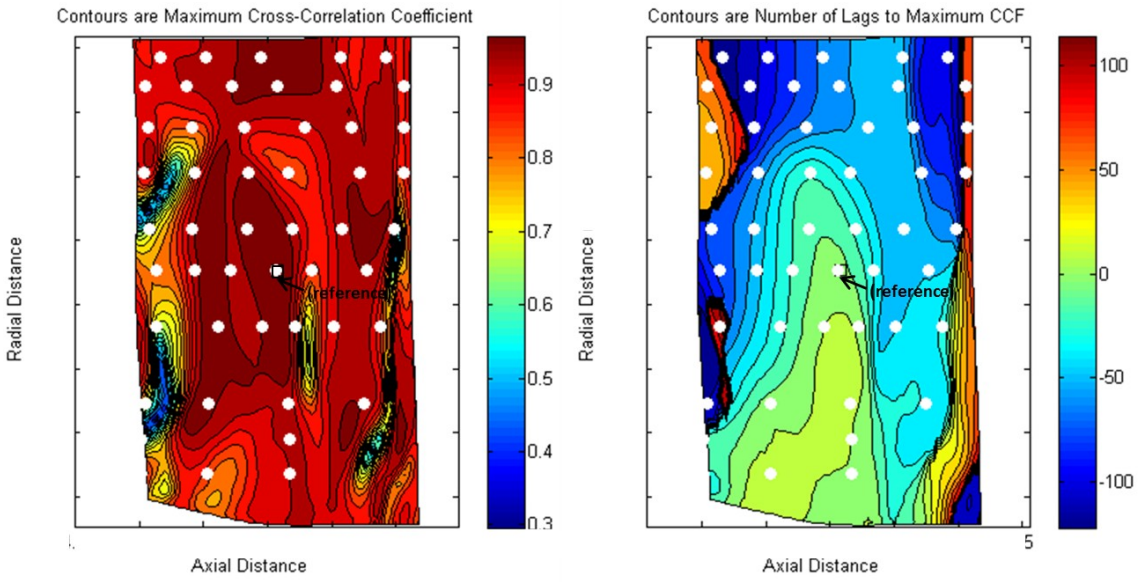

Figure 124: Contours of Maximum Cross-Correlation Coefficient (CCF) (left) and Lags to Maximum CCF (right) on the Downstream Vane Suction Side

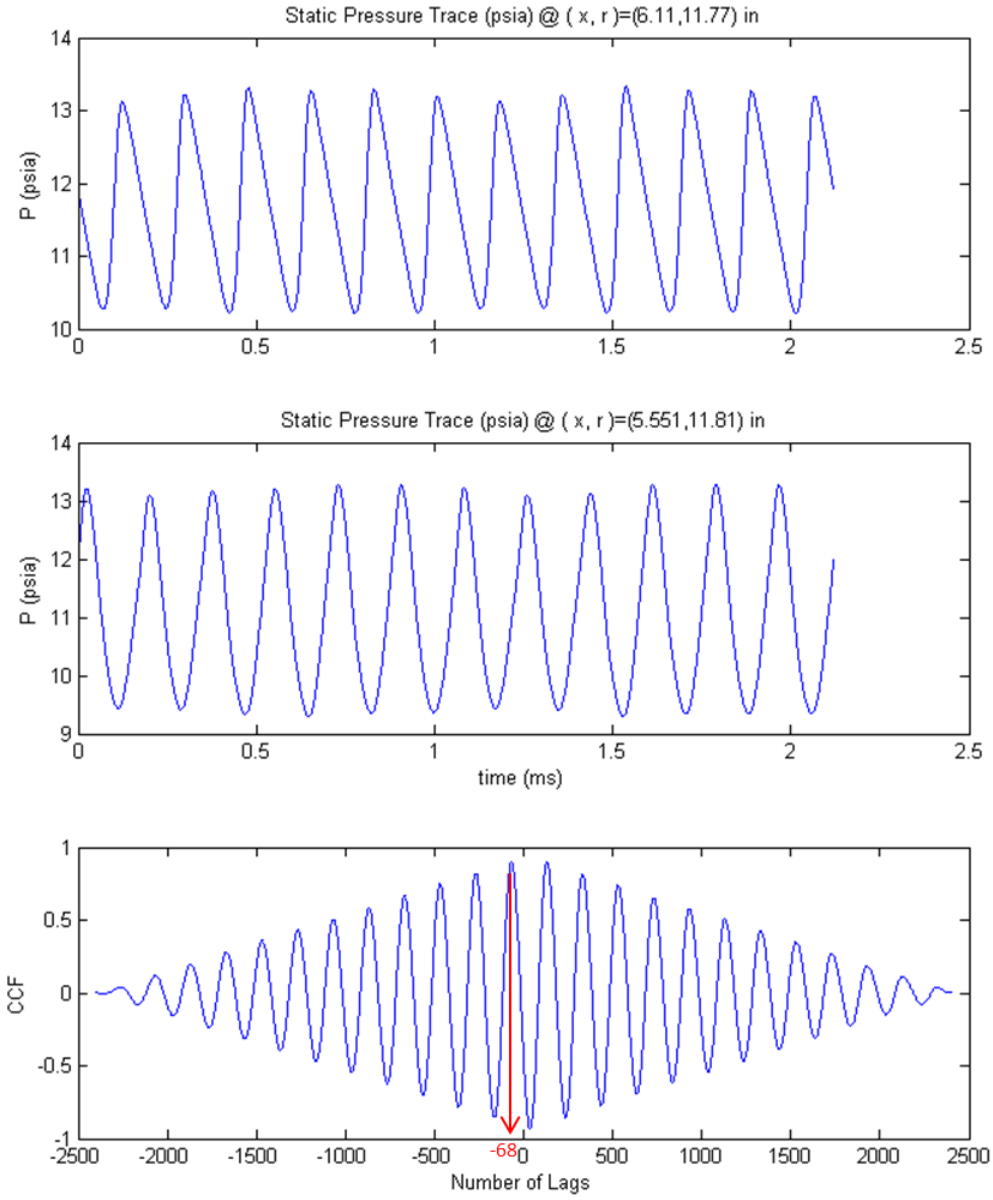

Figure 125: Pressure Traces of Reference Point (top) and Downstream of Lag Sign Shift (middle) and CCF (bottom)

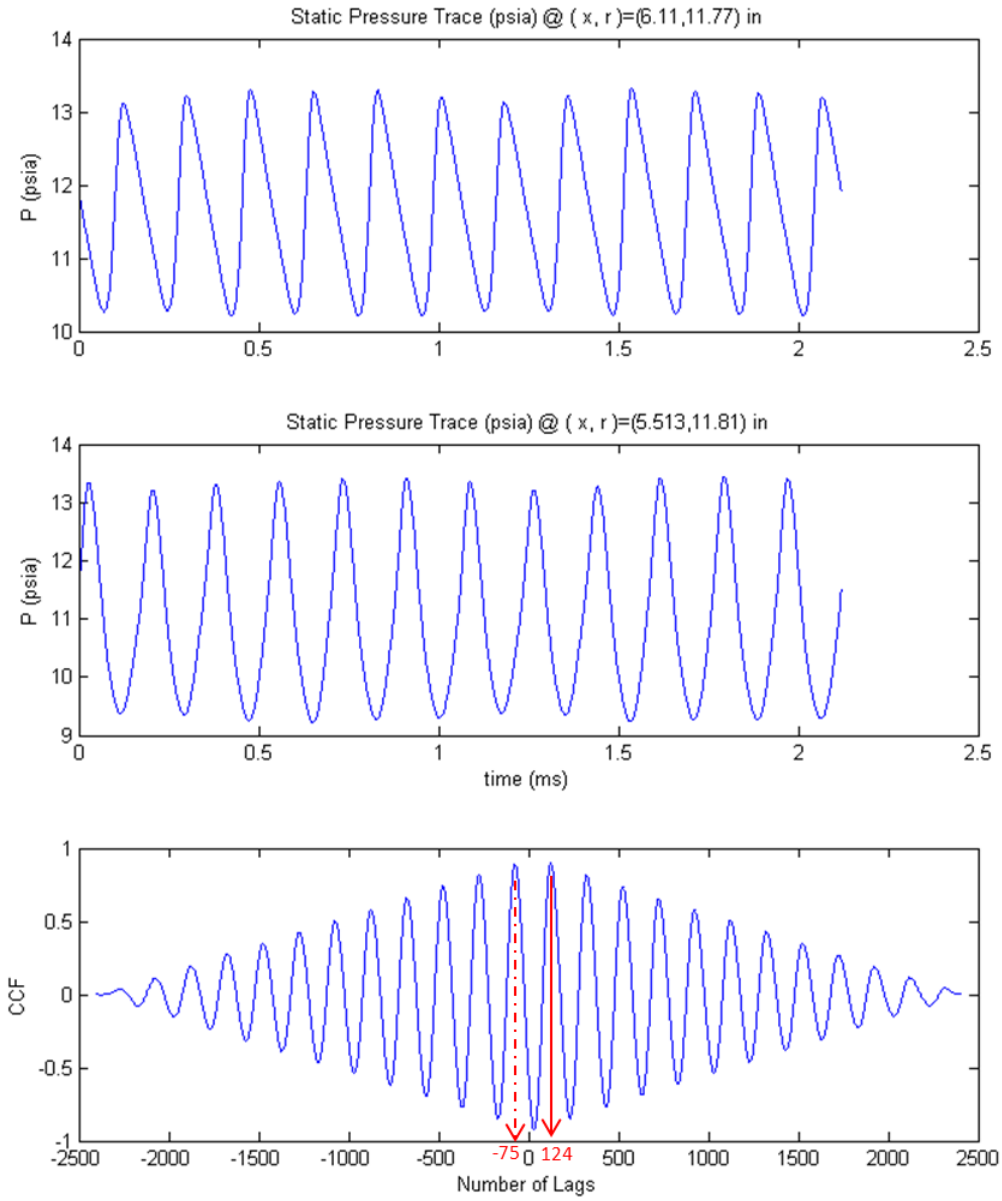

Figure 126: Pressure Traces of Reference Point (top) and Upstream of Lag Sign Shift (middle) and CCF vs Lags (bottom)

Most of the pressure side was predicted to have a high correlation with the center point chosen for evaluation. There were islands of relatively low correlation predicted, with the largest region being located at the quarter-chord near the root of the airfoil. The correlation among the experimental measurements was not as high. This result is not surprising considering the additional sources of unsteadiness and noise in the experimental facility. Sensors P2VU3 and P2VU4 are in locations that were predicted to have high CCF values with respect to the reference point, collocated with sensor P2VP3. The predicted and experimental pressure traces and CCF of the reference point and sensors P2VU3 and P2VU4 are shown in Figure 127 and Figure 128, respectively. The predicted pressure traces are shown in black in the upper and middle portions of the figure. The green lines represent a periodic

repetition of the predicted variation. Once again, the red and blue lines represent the raw experimental signal and the ensemble average of the traces over 100 revolutions, respectively.

The predicted maximum CCF of sensors P2VP3 and P2VU3 is approximately 0.90, as shown in Figure 123 and Figure 127. However, the measured CCF of the ensemble average is approximately 0.50. The same trend is seen when comparing sensors P2VP3 and P2VU4. Once again, the mismatch in the predicted and experimental CCF is due to the additional sources of unsteadiness and noise in the facility that are not modeled in the simulation. The predicted pressure traces are relatively clean signals, for which a high degree of correlation would be expected. On the other hand, the experimental measurements contain low frequency sources of excitation such as instrumentation and facility struts and random fluctuations and uncertainty that drive the correlation to a much lower value. As shown in Figure 123, sensor P2VK2 is located in an area in which the CCF is predicted to be relatively low. The predicted and experimental pressure traces and CCF of the reference point and sensors P2VK2 are shown in Figure 129. For these sensors, the predicted CCF aligns more closely with the measured CCF. However, the measured CCF of the reference point and P2VK2 is very near the values of the reference point and sensors P2VU3 and P2VU4. Due to the location of sensor P2VK2 in the predicted low correlation area, one would expect the measured CCF of sensor P2VK2 to be lower relative to P2VU3 and P2VU4, but this is not the case. All three measured CCF relative to the reference point are approximately 0.50.

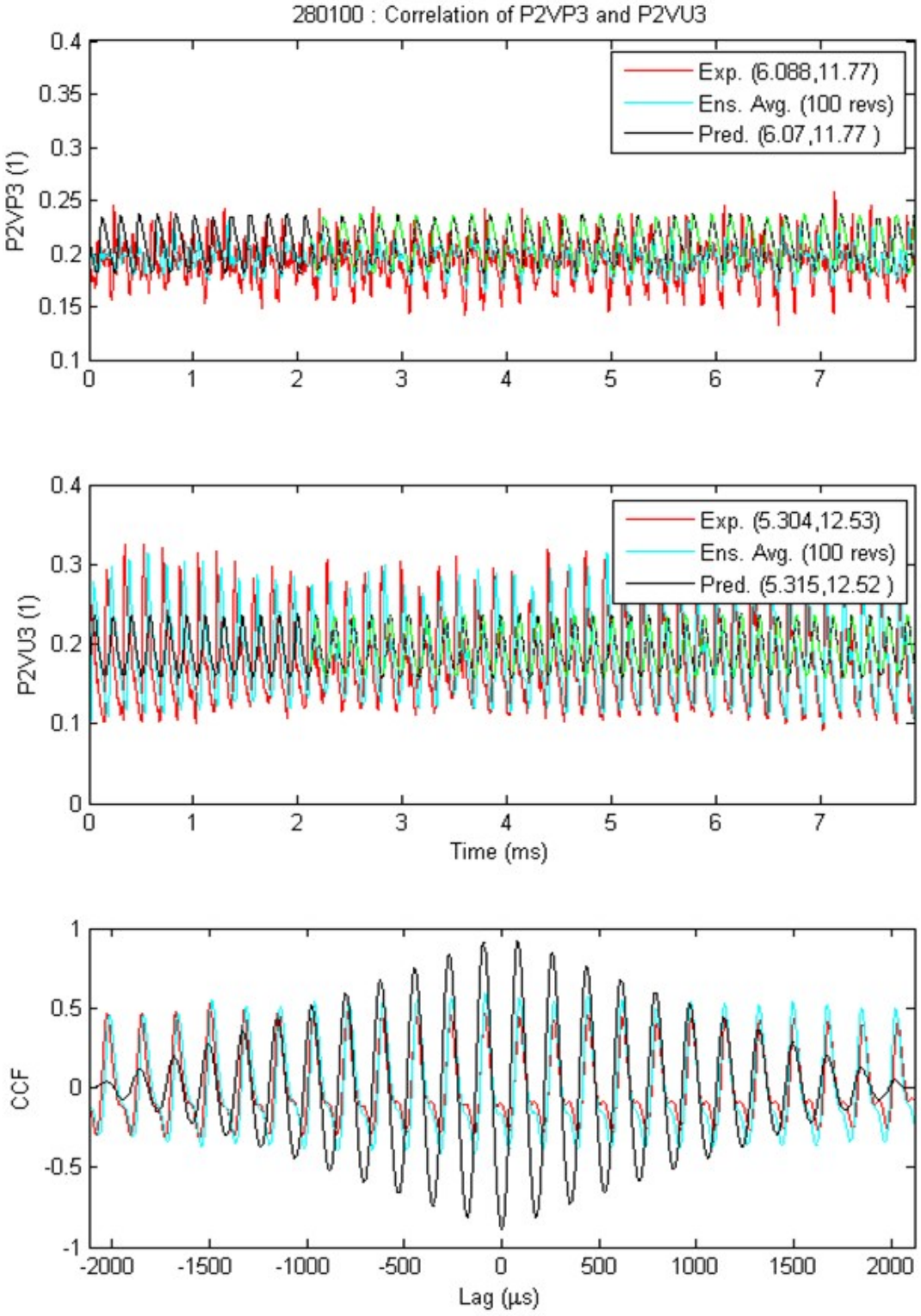

Figure 127: Pressure Traces of Reference Point P2VP3 (top) and P2VU3 (middle) and CCF vs Lag (bottom)

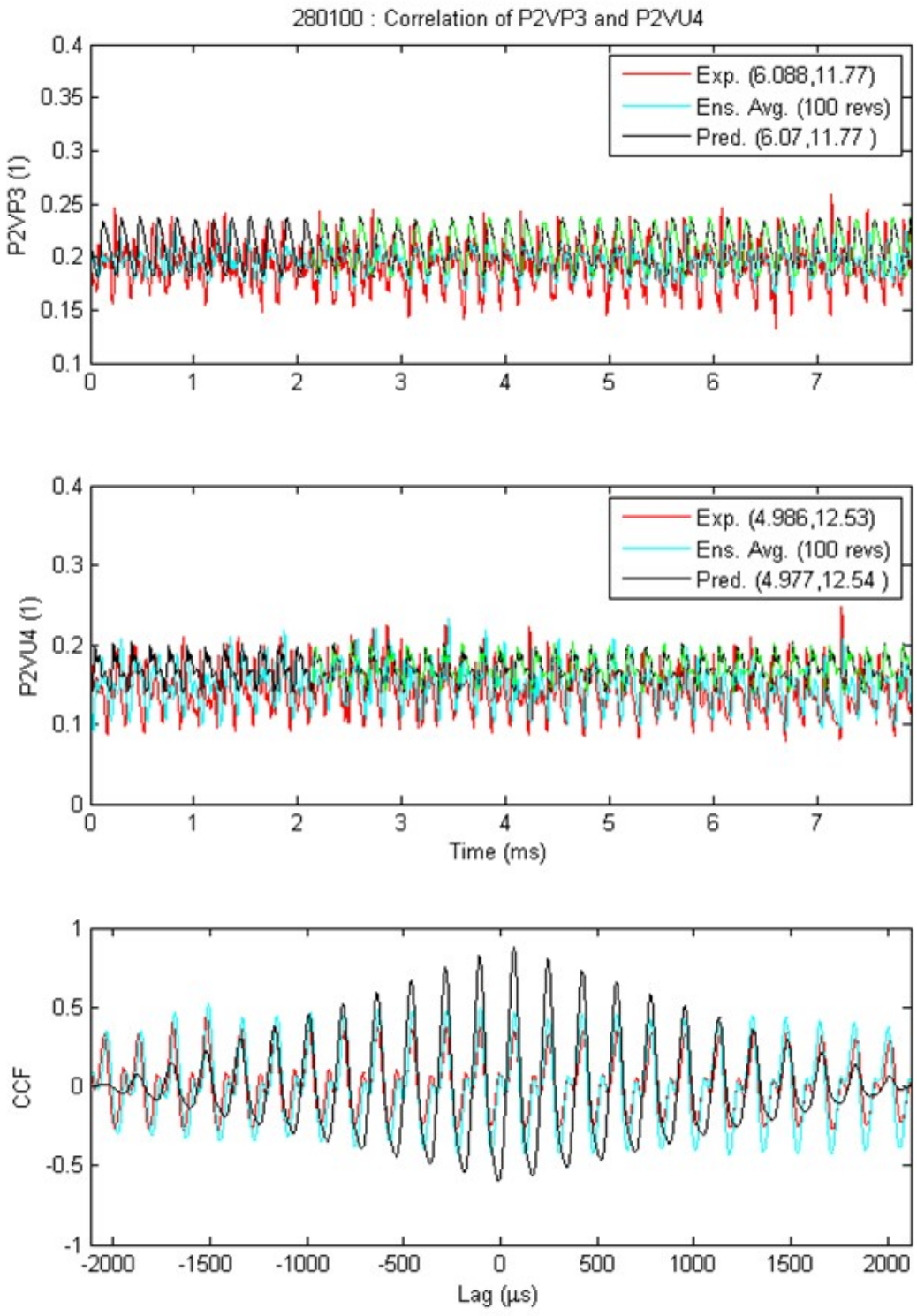

Figure 128: Pressure Traces of Reference Point P2VP3 (top) and P2VU4 (middle) and CCF vs Lag (bottom)

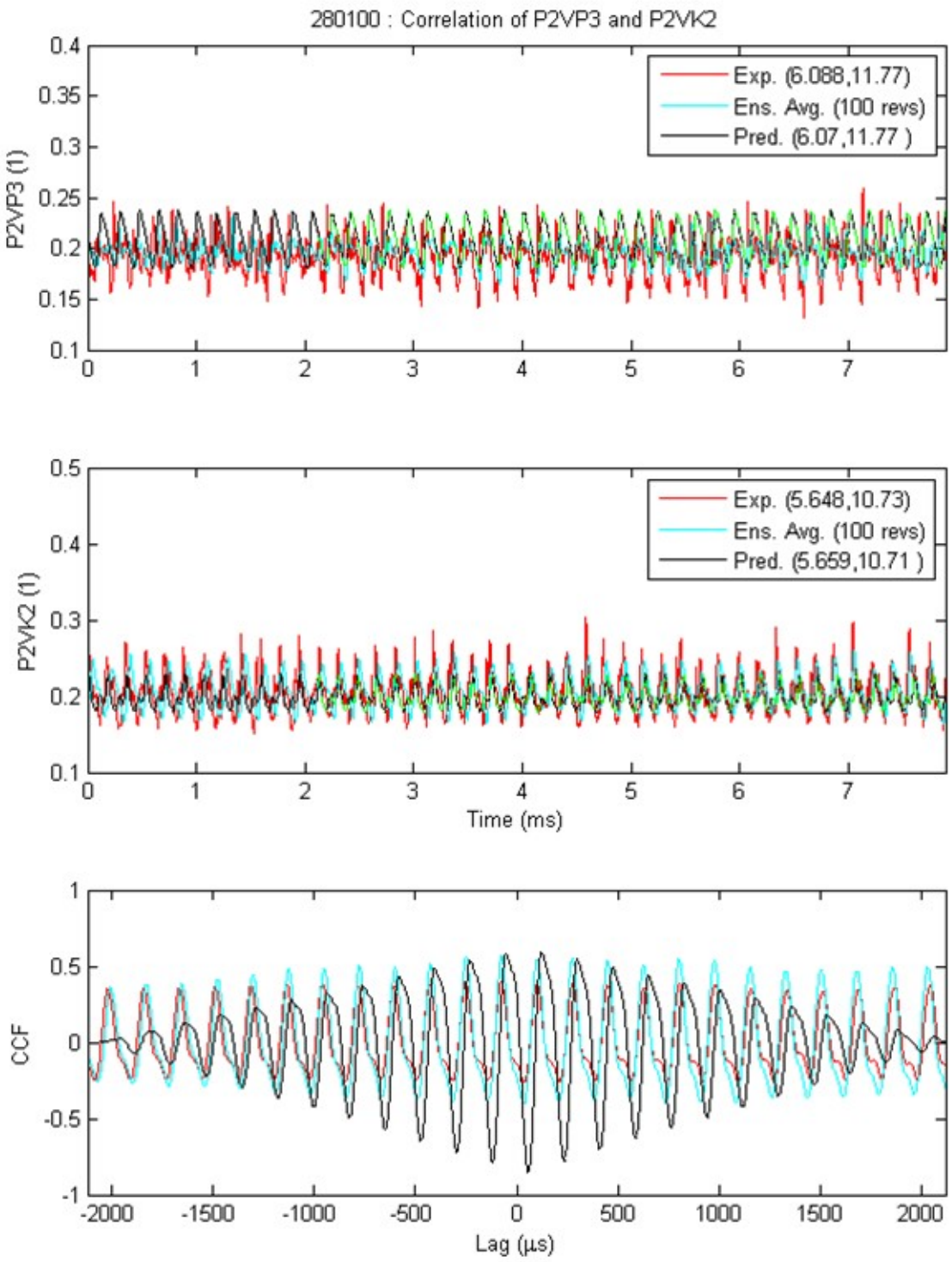

Figure 129: Pressure Traces of Reference Point P2VP3 (top) and P2VK2 (middle) and CCF vs Lag (bottom)

Despite the maximum CCF prediction and measurements not showing good absolute levels of agreement, the lags to maximum CCF of the prediction and experiment align well. The shock impact trajectories on the downstream vane pressure and suction sides are shown in

Figure 130 and Figure 131, respectively. For each span in which sensors were located, one sensor was chosen as the reference sensor and the lag to maximum CCF are plotted relative to that sensor. The reference sensor is easily identified as the location in which both the measured and predicted lag is zero. Recall, that a lag value greater than zero indicated that the unsteadiness occurred at that location prior to the occurrence at the reference location, and vice versa. Also, when comparing experimental and predicted lags, the time lags are plotted in microseconds. To compare the timing of the unsteadiness of any two points relative to one another, note that the unsteadiness first occurred at the location having the larger lag value.

The shock trajectories were accurately predicted on most of the spans measured on the pressure side of the downstream vane. The predictions and experimental measurements capture the shock moving from the trailing edge of the airfoil to the leading edge of the pressure side. This behavior can also be seen in Figure 107 as the shock from the trailing edge of the blade is dragged across the pressure side of the downstream vane, from the trailing edge to the leading edge. One can also see in Figure 107 that this shock reflects off the pressure side of the downstream vane and impacts the adjacent vane on the suction side, near mid-chord. The unsteady pressure on the suction side travels both up- and downstream from the point of impact. This shock trajectory is also shown in Figure 131. Although the measured and predicted trajectories do not align as well as the comparisons made on the pressure side, both exhibit a similar trend.

Generally, the reflected shock first impacts the suction side between mid-chord and three-quarters chord and progresses up- and downstream from that point. One reason for the shock trajectory on the suction side being more difficult to predict may be that the impact on the suction side is a reflection of an incident shock, which involves more interaction flow physics (e.g. shock/shock and shock/shear-layer interactions) than simply an incident shock impacting the pressure side. In addition, the smaller time scales at which the shock is traveling across the surface make it more difficult for the predictions to match the experiment more accurately. This indicates that the reflected shock impact is sometimes near normal to the suction side of the vane.

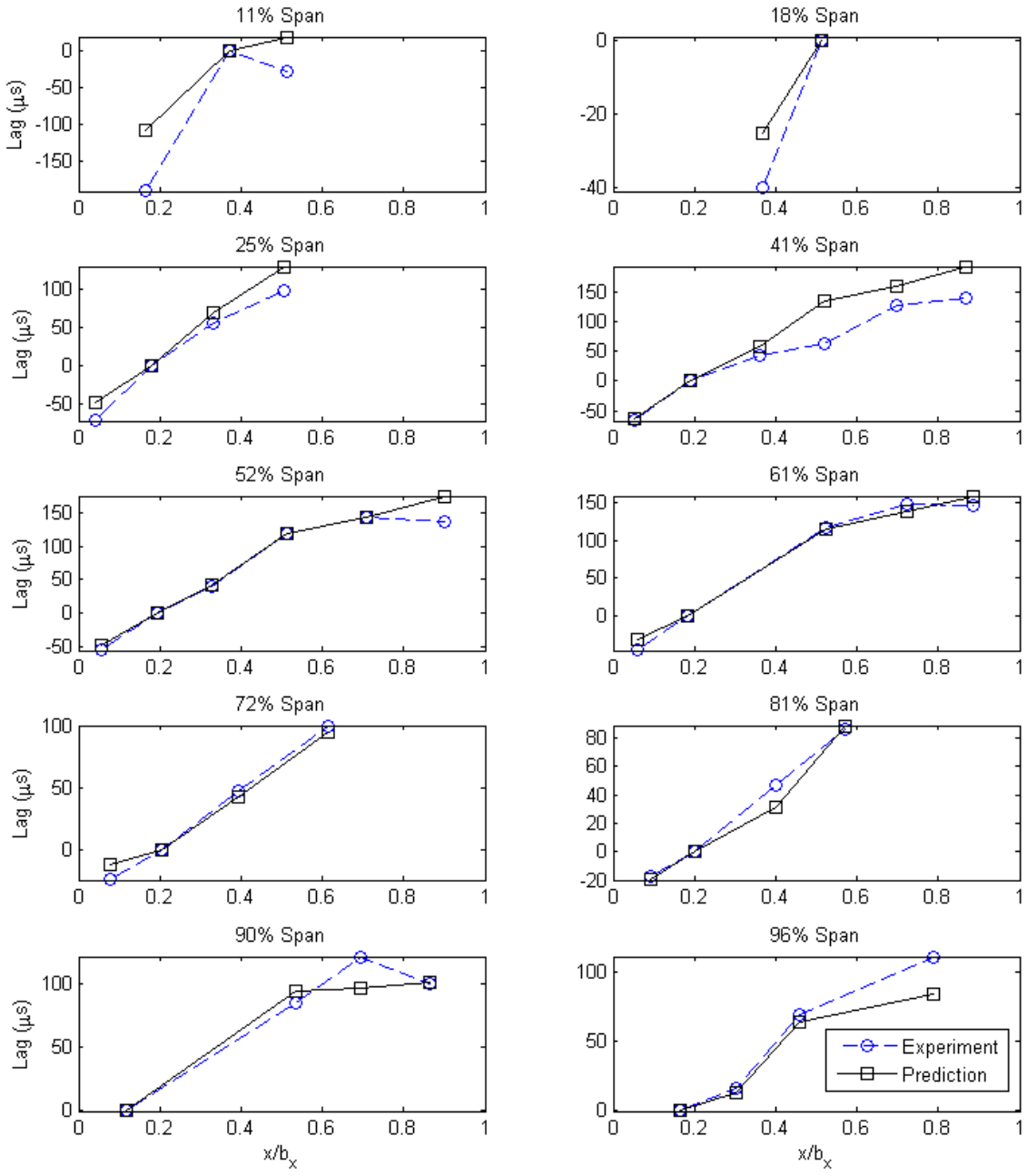

Figure 130: Shock Impact Trajectories on the Pressure Side of the Downstream Vane

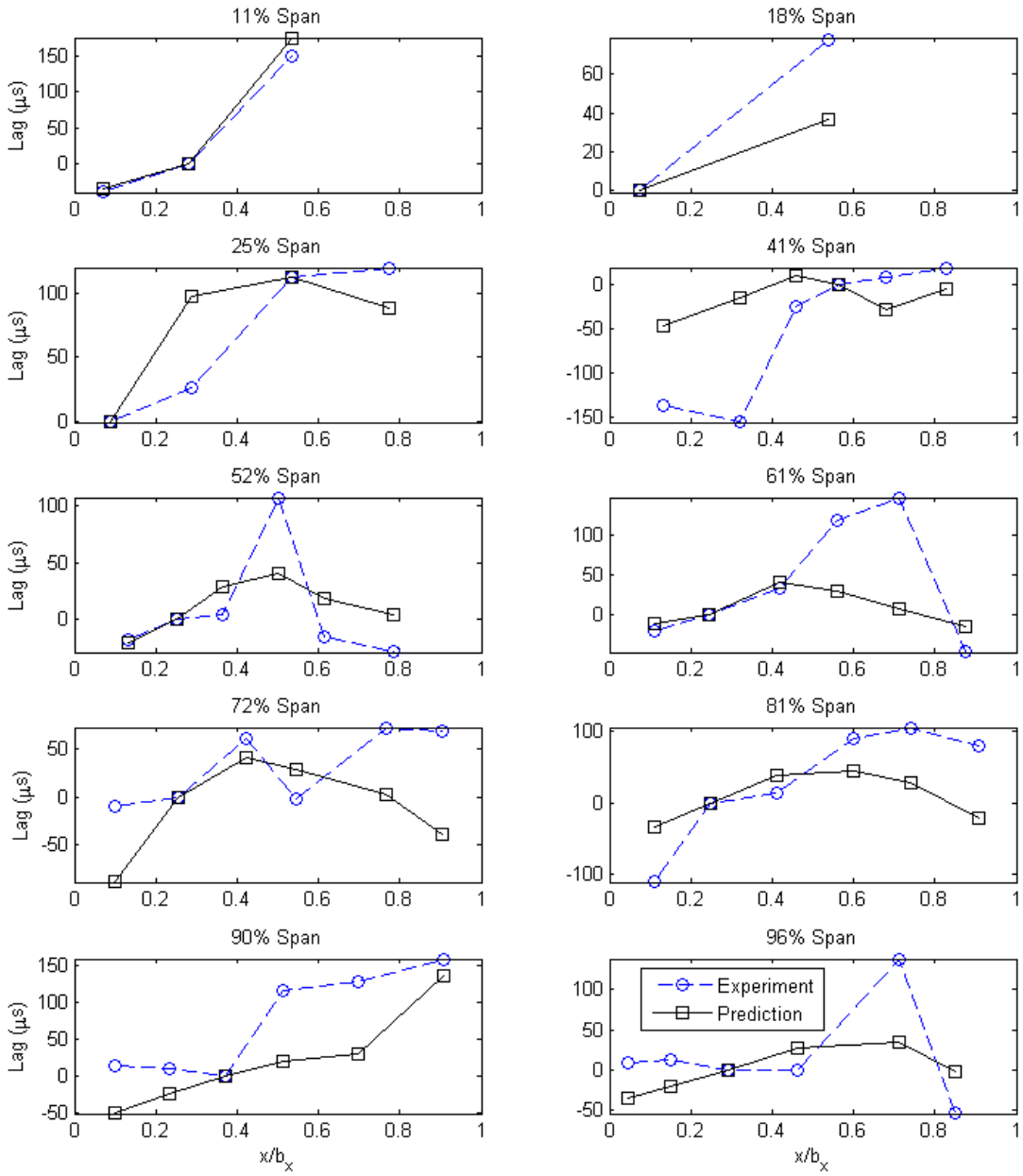

Figure 131: Shock Impact Trajectories on the Suction Side of the Downstream Vane

The shock trajectories can be visualized on the entire pressure and suction side surfaces as a whole, rather than on a per-span basis. Shock trajectory contours of the pressure and suction sides are shown in Figure 132 and Figure 133, respectively. The time lag contours were generated by referencing the predicted and measured time lag at each sensor location to a reference sensor for each side, and interpolating the data on to the grid coordinates of the airfoil. The reference sensor for each side is labeled in the figures. The interpolation is made in between sensors, therefore the lag contours are bounded by sensor coverage on each side of the airfoil. Recall that when comparing time lag values between two points, the point corresponding to the larger time lag experienced the impact of the unsteady event first.

The pressure side predicted and measured lag contours, shown in Figure 132, are in close agreement. Both predicted and measured contours indicate that the incident shock is traveling from the trailing edge to the leading edge of the pressure side at nearly identical timing. There are some areas in which the predicted and measured contours do not match, particularly near the root at mid-chord. This was also indicated in Figure 130 at the 11 and 18 percent span regions.

The suction side predicted and measured contours (Figure 133) do not match in magnitude as well as the pressure side comparison, but do show a similar trend of shock trajectory. This result is not surprising, especially in light of the span-wise shock trajectories on the suction side shown in Figure 131. Once again, as indicated by the larger lag values, the reflected shock impacts near mid-chord of the suction side and the unsteadiness travels up- and downstream toward the leading and trailing edges. The measured contours contained an island of very large lag values, as indicated by the red island in the middle of the suction side surface. This is due to the three sensors in the region—P2VN4, P2VQ4, and P2VQ5 from leading edge to trailing edge—measuring phase-shifted time lag relative to the neighbors sensors. Therefore, the signals measured by these three sensors were further analyzed.

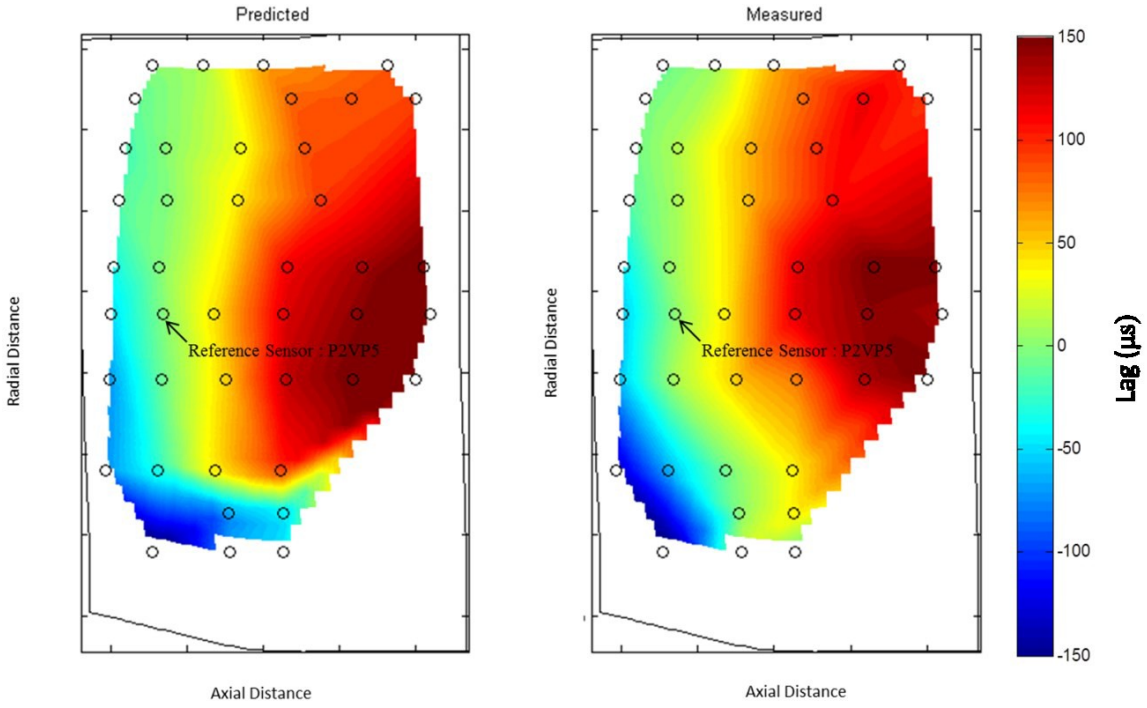

Figure 132: Shock Trajectory Contours on the Pressure Side of the Downstream Vane

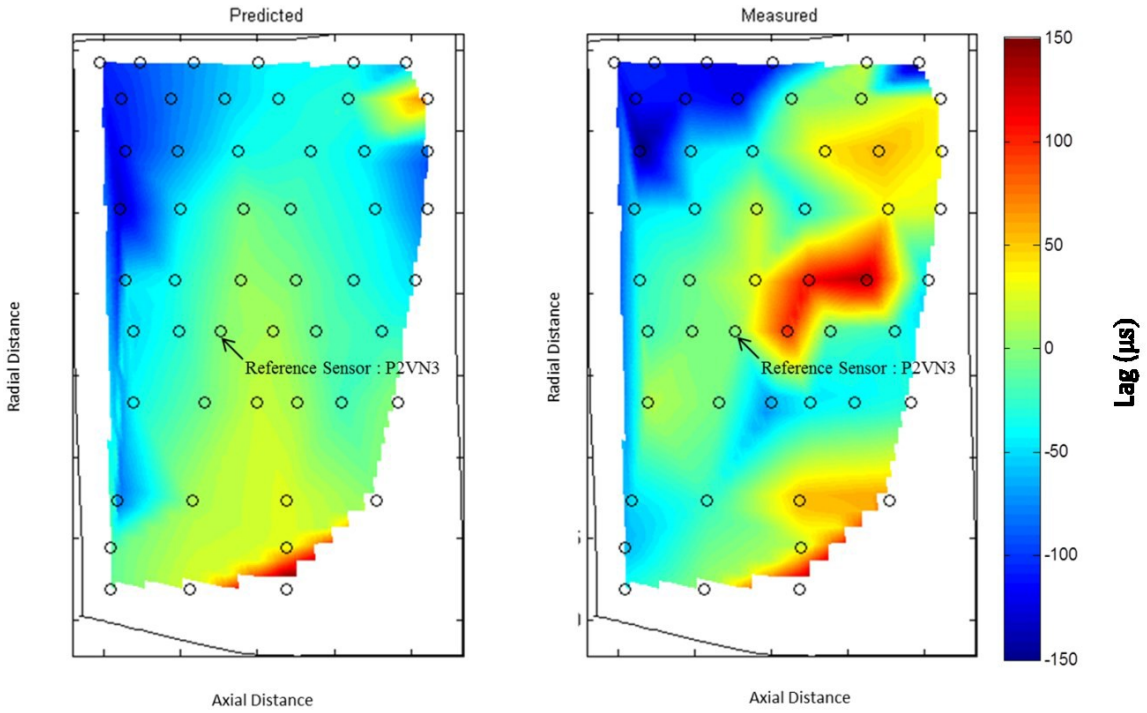

Figure 133: Shock Trajectory Contours on the Suction Side of the Downstream Vane

The static pressure traces and DFT magnitudes of sensors P2VN4, P2VQ4, and P2VQ5 are shown in Figure 134 through Figure 136, respectively. As previously explained, the magnitude shift in the static pressure traces corresponds to the differences in predicted and measured loading on the downstream vane. The ensemble averaged DFT magnitude of each of these sensors reveals that the unsteadiness at these locations consists of higher frequencies than the rest of the downstream vane. The DFT magnitudes of the downstream vane previously discussed—Figure 117 through Figure 122—are typical representations of the unsteadiness levels in which the fundamental frequency (5.84 kHz) of the vane is dominant, followed by the first (11.68 kHz) and second (17.52 kHz) harmonic. However, the signals measured by P2VN4, P2VQ4, and P2VQ5 indicate that the first, second, and third (23.36 kHz) harmonics of the vane have a stronger influence on the unsteadiness. The first and second harmonics have roughly the same magnitude as the fundamental frequency in the ensemble averaged data of sensor P2VN4. The magnitudes of the numerical analysis were significantly different, predicting a magnitude of the fundamental frequency much greater than the harmonics. The DFT analysis of the ensemble average data for sensor P2VQ4 (Figure 135) indicates that the first through third harmonics have a greater magnitude than the fundamental frequency. The predicted magnitudes differed significantly from the ensemble average, predicting that the fundamental frequency had over twice the magnitude of the first harmonic, and the second and third harmonic magnitudes were not predicted to have a significant response. The predicted and measured ensemble averaged DFT magnitudes of sensor P2VQ5 (Figure 136) have a similar trend regarding the most and least significant frequencies: the fundamental magnitude was the largest, followed by the first and second harmonics. However, the ensemble averaged data indicated the magnitudes of the first and second harmonics were significantly larger than those predicted.

The DFT analysis of P2VN4, P2VQ4, and P2VQ5 indicates that the unsteadiness measured by these sensors differs from the predicted data and the measured ensemble data from nearby sensors. That region of the vane was being impacted by a higher frequency signal that is not present in the prediction. This is the most likely cause of the inconsistency in the time lag span-wise graphs (Figure 131) and contour plot (Figure 133) of the suction side of the downstream vane.

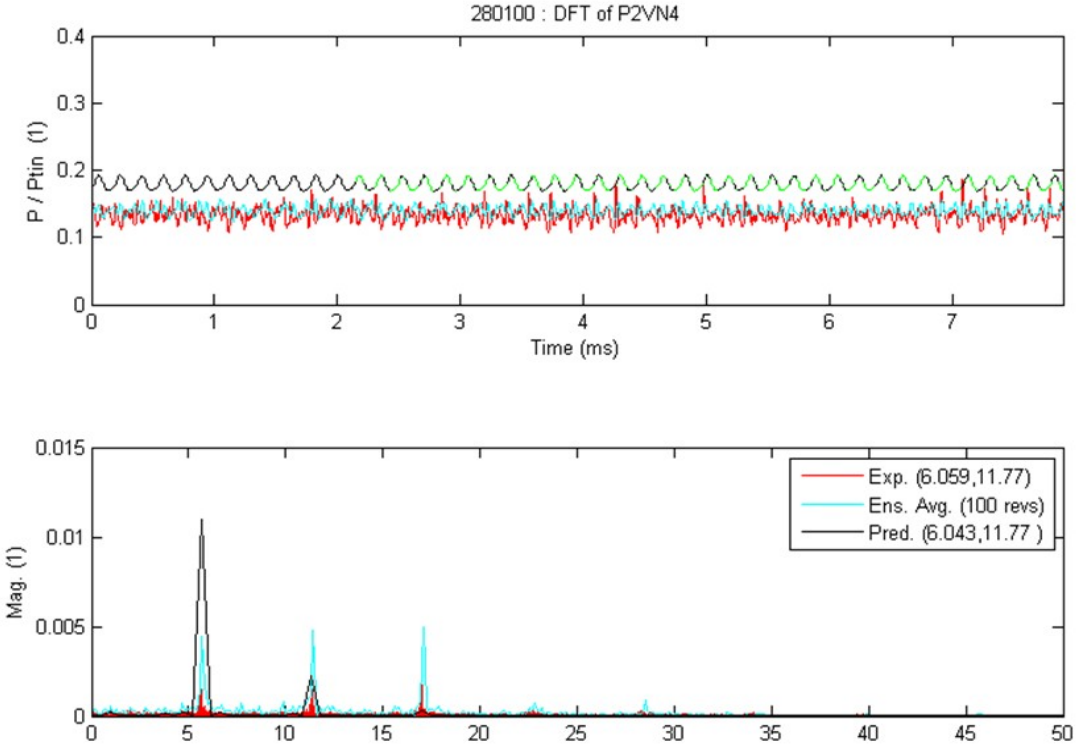

Figure 134: Experimental and Predicted DFT of P2VN4 (Downstream Vane SS, 52.2% Span, 50.2% Axial Chord)

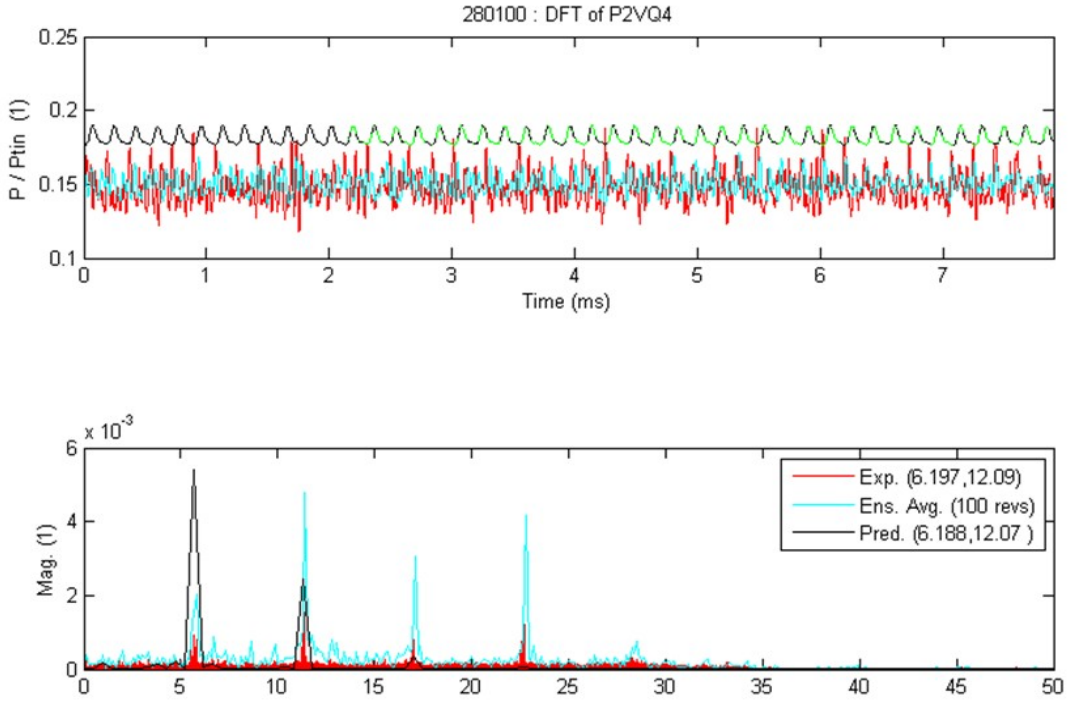

Figure 135: Experimental and Predicted DFT of P2VQ4 (Downstream Vane SS, 60.5% Span, 55.9% Axial Chord)

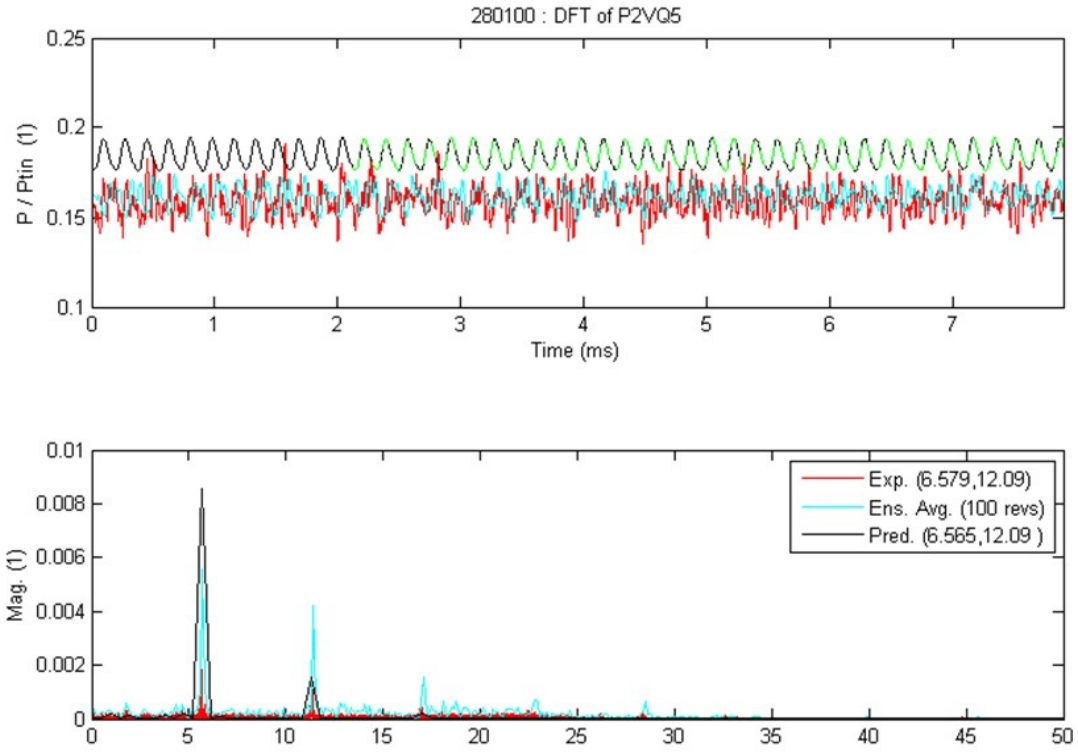

Figure 136: Experimental and Predicted DFT of P2VQ5 (Downstream Vane SS, 60.5% Span, 71.2% Axial Chord)

Finally, the time lag to maximum CCF of the pressure side of the downstream vane and the suction side of the blade aft of the throat were compared to determine how accurately the return of the reflected shock was captured in the numerical analysis. The reference sensor used on the pressure side of the downstream vane was P2VP5. The predicted and measured static pressure traces and time lags of the reference sensor to sensors on the suction side of the blade, including PRZA14, PRWX14, PRTT15, PRQQ16, and PRMM15, are shown in Figure 137 through Figure 141, respectively. Each of these sensors are labeled in Figure 108 and listed in Table 12 and Table 13 for reference. The predicted and measured time lags with respect to the reference sensor have a high degree of correlation, particularly for the sensors PRQQ16 (Figure 140) and PRMM15 (Figure 141) located at higher spans. The predicted time lag at maximum CCF for these two sensors is nearly identical to the measured lag. The predicted lags for sensors PRZA14 (Figure 137) and PRTT15 (Figure 139) are slightly more positive than the measured values, which indicates that the shock measured in the experiment took a slightly longer time to impact the blade than calculated in the CFD simulation. On the other hand, the opposite was true for sensor PRWX14 (Figure 138), in which the measured lag was greater than the predicted lag. However, these time differences in the latter three sensors are relatively small. As a whole, the reflected shock return from the downstream vane to the suction side of the blade is captured very well in the numerical analysis.

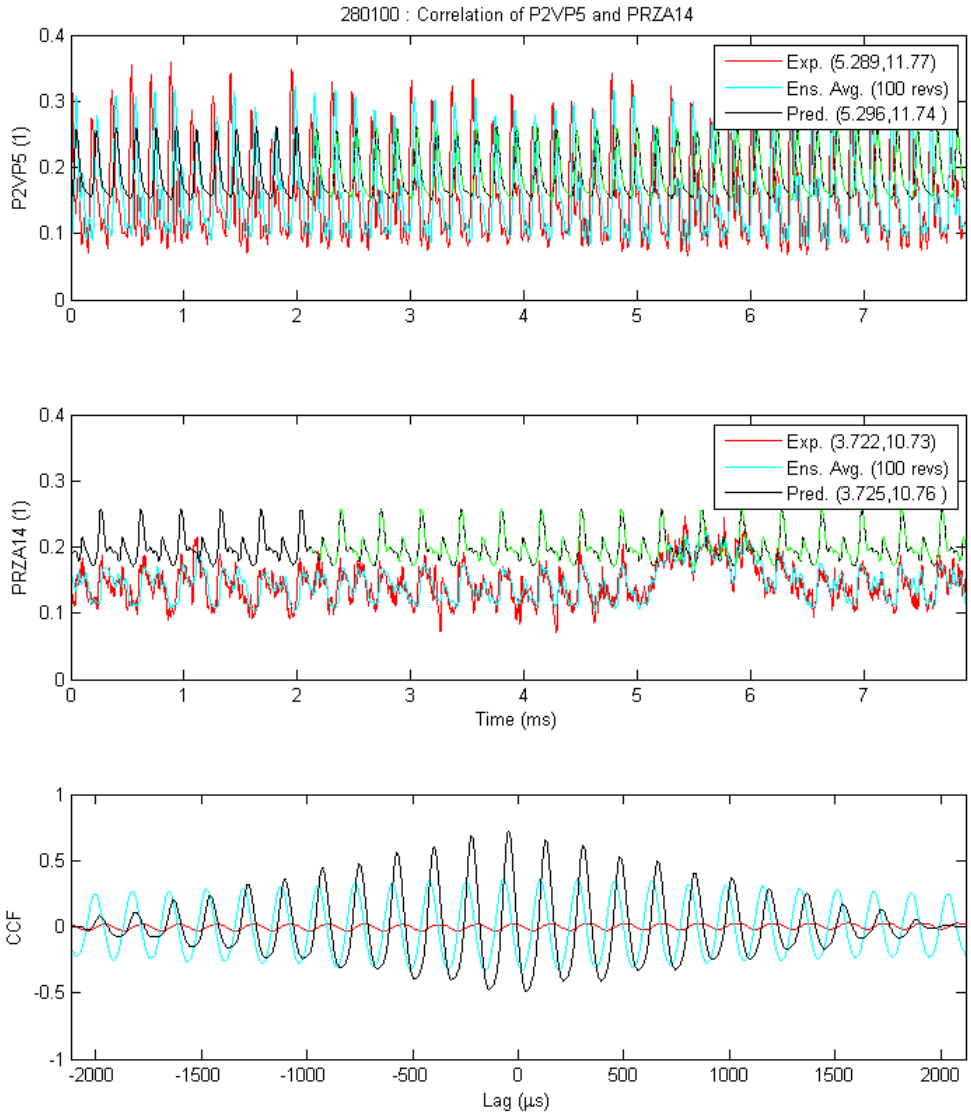

Figure 137: Pressure Traces of Reference Point P2VP5 (top) and PRZA14 (middle) and CCF vs Lag (bottom)

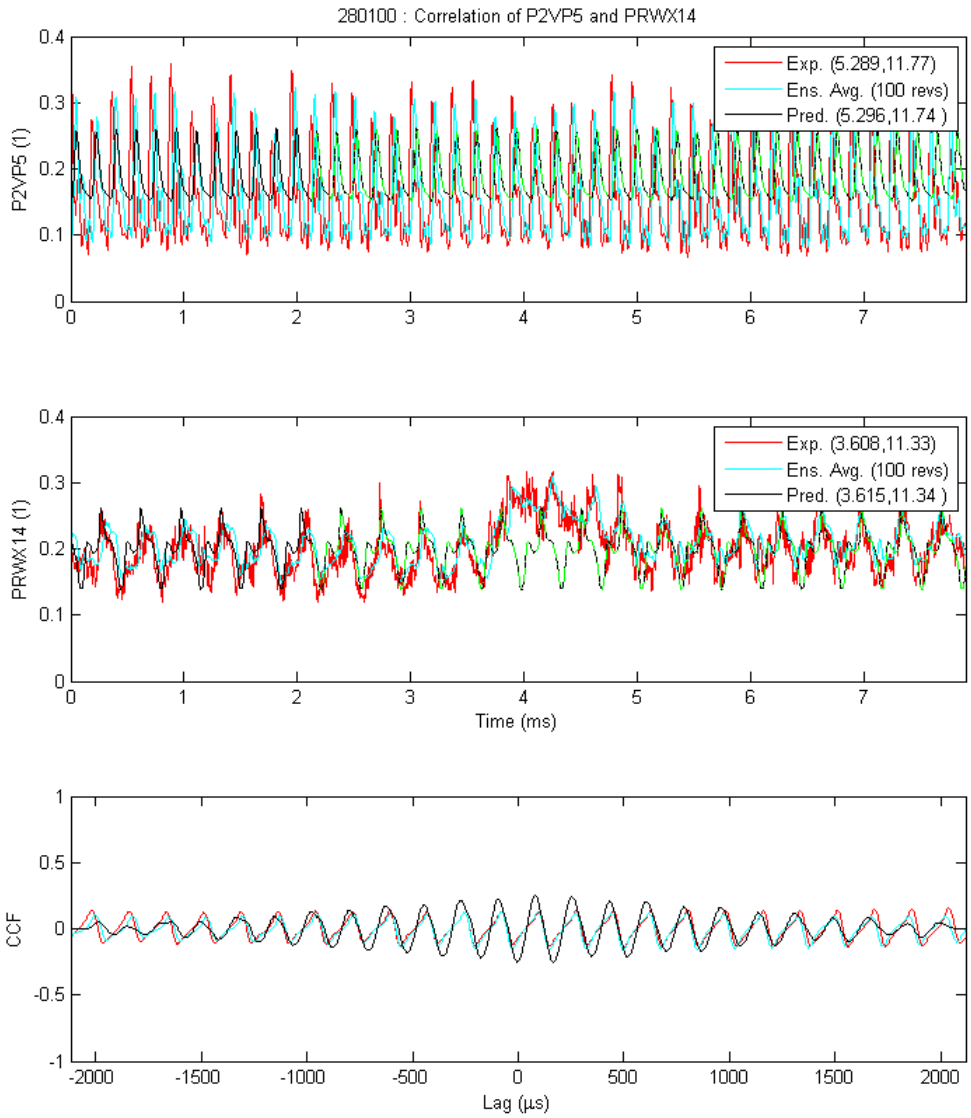

Figure 138: Pressure Traces of Reference Point P2VP5 (top) and PRWX14 (middle) and CCF vs Lag (bottom)

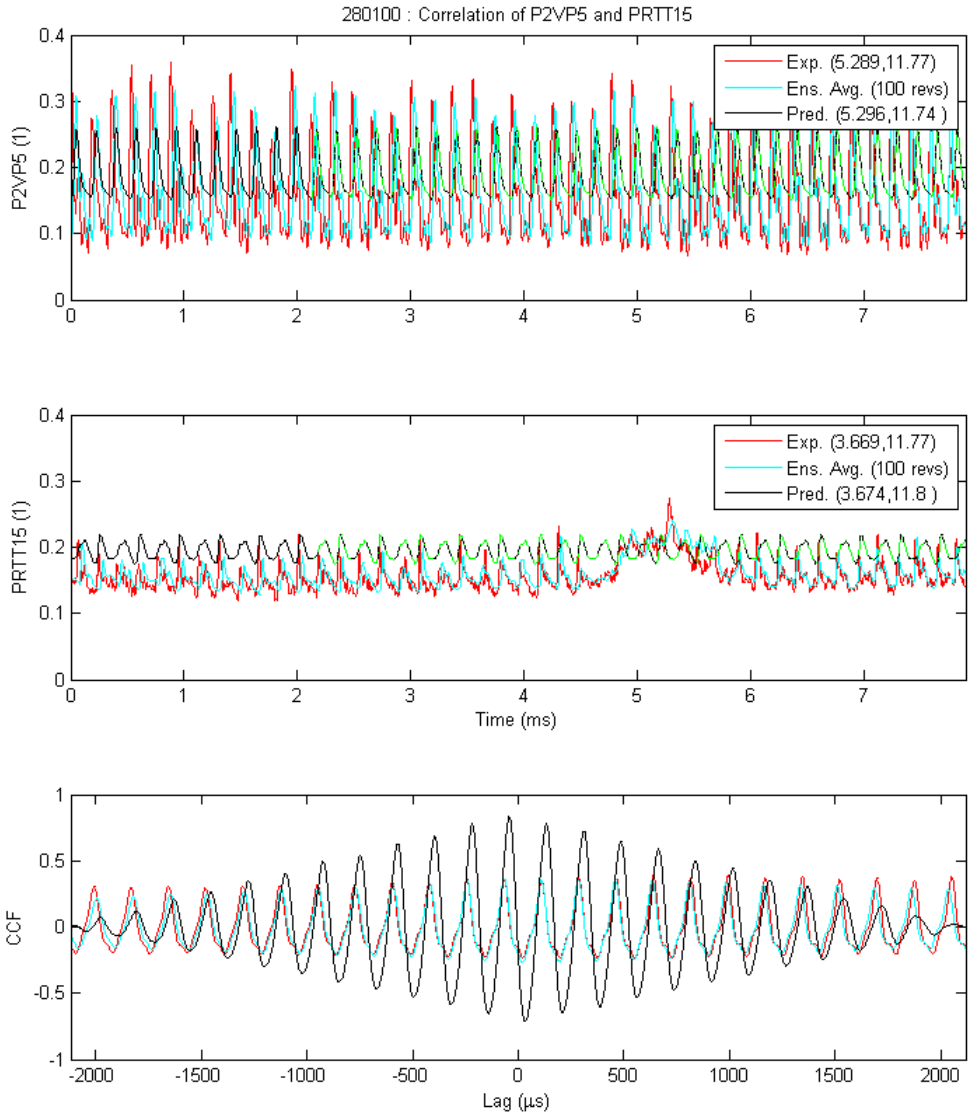

Figure 139: Pressure Traces of Reference Point P2VP5 (top) and PRTT15 (middle) and CCF vs Lag (bottom)

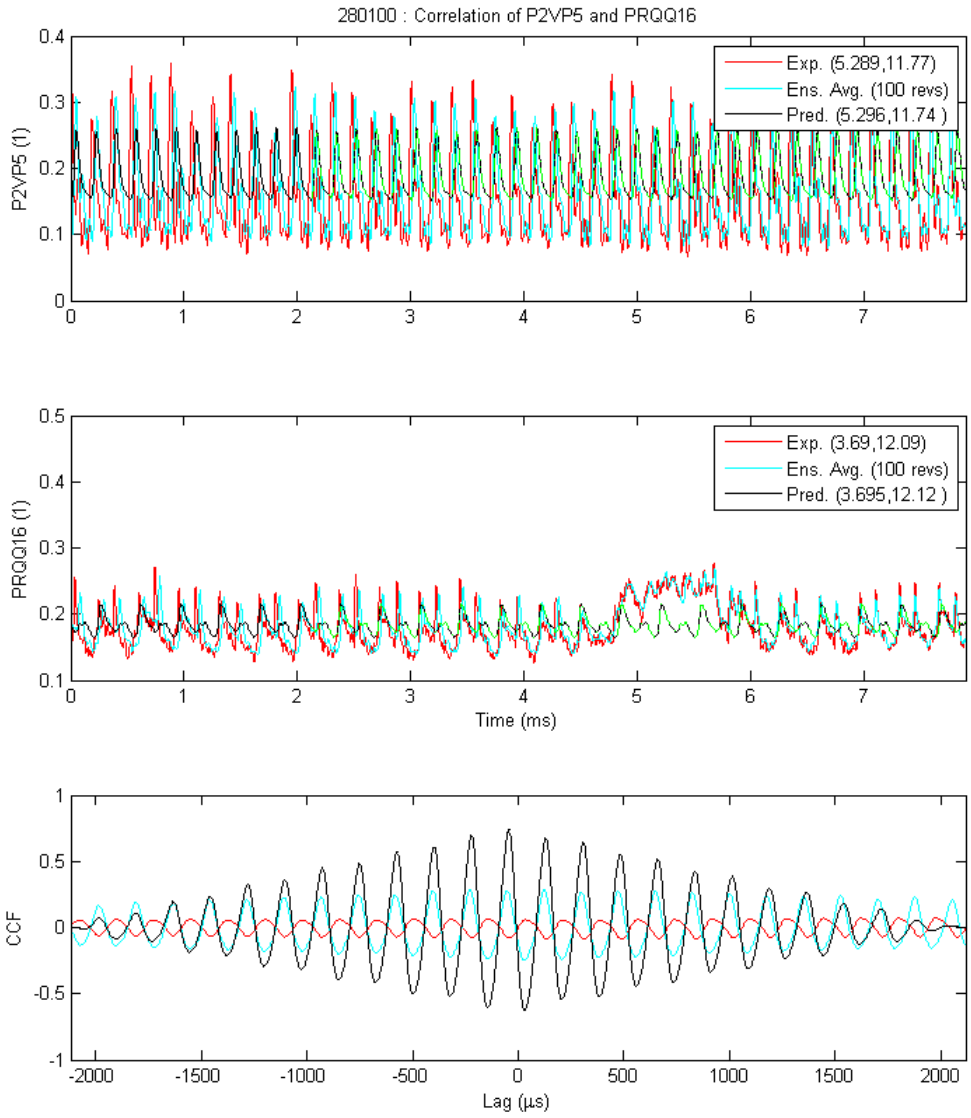

Figure 140: Pressure Traces of Reference Point P2VP5 (top) and PRQQ16 (middle) and CCF vs Lag (bottom)

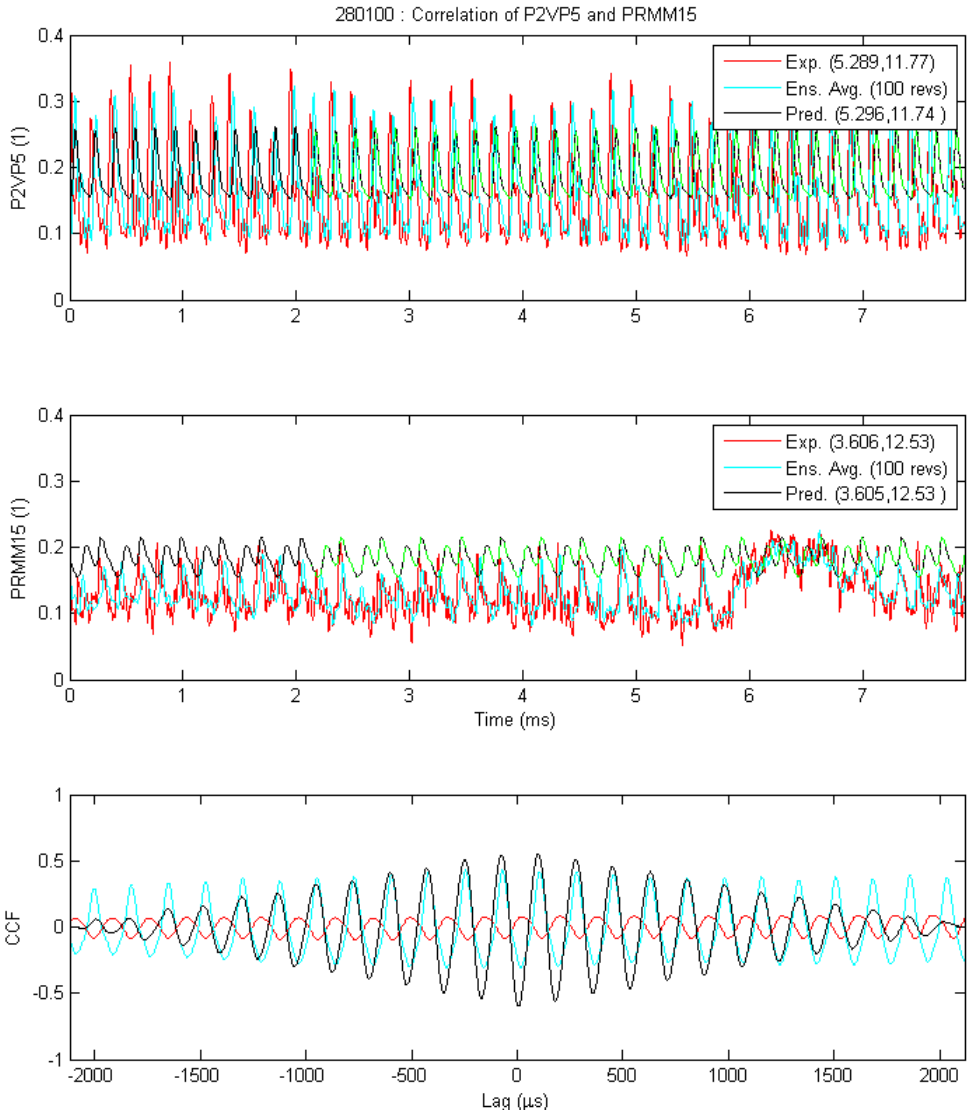

Figure 141: Pressure Traces of Reference Point P2VP5 (top) and PRMM15 (middle) and CCF vs Lag (bottom)

Summary

The stage-and-one-half HIT Research Turbine was tested in the Turbine Research Facility. The measurements from this experiment were compared to numerical analysis, the details of which were described in the previous chapter. Experimentally obtained time-averaged and time-accurate pressure data was compared and contrasted to the numerical predictions. The time-averaged pressure distributions included all three airfoil rows. The peak-to-peak pressures observed in the experiment were greater than those that were predicted in all three airfoil rows. Also, the surface pressures on the downstream vane were under predicted due to a difference in the predicted and experimental pressure loss in the first stage. However, the loading on the first stage was predicted quite accurately. The agreement of the predicted and measured pressure distributions on the suction side of the blade up- and downstream of the shock indicated that the target rotor speed and pressure ratio were achieved during the experiment, respectively.

The time-accurate comparisons between ensemble averaged experimental signals and the numerical analysis focused mostly on the suction side of the blade downstream of the throat and the pressure and suction sides of the downstream vane. The measurements and predictions both indicated that the majority of the unsteadiness in this region was driven at 46E (5.84 kHz). Recall that 46E is the first harmonic of the vane passing frequency, and the fundamental frequency of the blade passing. The shock interaction physics was described graphically using results from the numerical analysis (Figure 107). Trajectories of the shock—measured by the time lag to the maximum CCF—from the numerical analysis and experimental data confirmed the shock movement on the pressure and suction sides of the downstream vane (as shown in Figure 130 and Figure 131, respectively). Although the predicted and measured data do not match quantitatively in some respects, in general similar trends were observed. The majority of the discrepancy between the predicted and measured data is attributed to the additional unsteadiness present in the experimental facility that is not modeled in the simulations. For example, the lag to max cross-correlations coefficient was less accurately predicted on the suction side of the vane. Two major differences between the pressure and suction side shock movements were noted. First, the shock impacting the suction side is a reflection of the incident shock impacting the pressure side of a neighboring vane. Second, the time scale of the shock movement across the suction side surface was much smaller due to a near normal impact of the shock reflected from the neighboring vane pressure side.

The predicted and measured time lag between the pressure side of the downstream vane and the suction side of the blade were compared as a measure of how accurately the return of the reflected shock from the downstream vane to the suction side of the blade was captured in the simulations. The predicted and measured time lag matched extremely well and this indicated that the numerical analysis accurately tracked the reflected shock between the airfoil rows.

CHAPTER VII

CONCLUSIONS AND RECOMMENDATIONS

Conclusion

A rigorous study of the flowfield in a stage-and-a-half transonic turbine with a downstream vane consistent with contra-rotation was conducted. The rigor and fidelity of the experimental tests and numerical analysis methods were built through two- and three-dimensional steady-state comparisons, leading to three-dimensional time-accurate comparisons. Experimental pressure data was compared to numerical predictions at each step. The flow solver used for all comparisons was Code Leo—a second order accurate code in time and space that implements a Reynolds-Averaged Navier-Stokes method with the two-equation Wilcox 1998 k-ω turbulence model for numerical closure.

First, the two-dimensional geometries of the blade midspan and quarter-tip were analyzed by modeling each of the geometries in a time-averaged simulation. The experimental data was obtained from a linear cascade facility, in which the two middle passages of each blade pack contained static pressure measurements. Pressure distributions and wake loss profiles for multiple exit Mach and Reynolds numbers and angles of attack were obtained and compared to predictions with matching similarity parameters. The analysis showed similar trends and compared very well to the experimental data. Both geometries maintained consistent pressure loadings as the Reynolds number was allowed to vary, and this is a desirable trait for turbine airfoils as it indicates stable performance over a range of engine conditions. The loading on the suction side trailing edge increased and neared the limit loading as the exit Mach number was increased. Also, varying the inlet air angle had an effect only on the forward half of the airfoil on the suction side. While additional work can be done to improve the wake predictions and measurement techniques, the simulations and measurements matched reasonably well. The effect on the pressure distribution of the blade of varying the incidence angle and exit Mach number was used during the post-test analysis of stage- and-one-half experiment to determine whether or not the target rotor speed and turbine pressure ratio were achieved.

The inlet guide vane of the stage-and-one-half turbine was tested in isolation as an annular cascade in the Turbine Research Facility prior to testing as a complete turbine. The experimental results were compared to both cooled and uncooled time-averaged numerical simulations of the first vane. The boundary conditions for the simulations were provided by the facility measurements up- and downstream of the vane row. The operation of the blowdown facility was optimized for the HIT Research Turbine during the initial tests as well. The predicted and measured surface pressure data matched very well. The flow field exiting the vane was well characterized prior to the stage-and-one- half experiment. The three-dimensional, steady aerodynamics were sufficiently captured by the CFD simulation. Also, higher fluctuations were measured near the endwalls relative to the midspan, and increased toward the trailing edge. This is evidence of secondary flows on the airfoil surface.

Finally, the full stage-and-a-half turbine was tested in the Turbine Research Facility. Multiple experimental tests with the same boundary conditions were necessary in order to obtain all measurements from sensors on the rotating hardware due to slip ring limitations. The experimental data was compared to time-accurate simulations modeling the first vane, blade,

and downstream vane. In order to create a model that sufficiently captured the flow physics, a rigorous numerical study was conducted that assessed the grid, iterative, periodic, temporal, and geometric convergences. Consequently, the numerical model used in the comparison to measured data was a 3/23rd sector of the wheel, comprised of over 15 million nodes. The steady simulation was run for 8,000 iterations prior to being used at the initial condition for the time-accurate simulation. The time-accurate simulations were run with 400 time-steps per cycle (i.e., one vane passing) and were executed for 15 complete cycles to establish periodicity before two additional cycles for post-processing were computed.

The numerically predicted time-averaged and time-accurate pressure variations were compared against experimental data, with a primary focus of the study being the unsteady interaction of the blade and downstream vane. The predicted and measured time-averaged data of the first stage of the turbine matched particularly well. The agreement of the predicted and measured pressure distributions on the suction side of the blade up- and downstream of the shock indicated that the target rotor speed and pressure ratio were achieved during the experiment, respectively. Time-accurate pressure traces and DFT magnitudes were found to be in good agreement. Both the measured and predicted data indicated that the majority of the unsteadiness on the suction side of the blade downstream of the throat and the downstream vane occurred at 46E (a predicted frequency of 5.84 kHz), and the remaining areas of the blade were dominated by 23E (a predicted frequency of 2.92 kHz). Time lags to the maximum correlation coefficient (CCF) computed from two-point space/time correlations were used to track the shock movement along the pressure and suction sides of the downstream vane. The predicted and measured lags at maximum CCF on the pressure side matched very closely. The data indicated that the shock trajectory on the pressure side began at the trailing edge and moved toward the leading edge. Although the lags on the suction side did not match as well as the pressure side lags, both the experiment and numerical analysis exhibited similar trends. The shock impacted near the mid- to three-quarter-chord region and then the unsteadiness traveled up- and downstream on the airfoil surface. A major source of discrepancies between measurements and simulations was the additional inherent unsteadiness and noise measured in the facility that was not modeled in the predictions.

Recommendations for Future Work

There are several additional studies that one can perform with the HIT Research Turbine. A few can be performed without the need to either collect additional data or execute additional numerical analysis. The heavily instrumented Research Turbine has enabled the collection of sufficient experimental data for many studies.

It has been noted several times throughout this study that there is additional inherent unsteadiness and noise that was measured in the facility that was not modeled in the simulations. A valuable contribution to future research on this and related topics would be an effort to improve the experimental measurement capability and data processing, as well as to create a more representative numerical model.

The present study focused on the unsteady interaction between the blade and the downstream vane. Within this context, but not investigated in this thesis, one could inspect the endwall sensors on the inner and outer diameter flowpaths between the downstream vane passage. The intent would be to track the shock movement in the vane passage on the endwalls.

The interaction between the first vane and blade could also be investigated. Although this type of interaction has been studied more often with numerical analysis and tests in experimental facilities, there is value in such a study, particularly with a heavily instrumented rotor.

In the present study, the surface pressures were the primary focus for the measure of unsteadiness. However, as previously mentioned, the HIT Research Turbine is equipped with dual-sided heat flux gages and has a rainbow cooling scheme in order to obtain heat transfer data. The effects of the unsteady interaction between both vanes and the rotating blade on the time-resolved heat flux would be a worthwhile study.

Finally, several off-design studies could be conducted. For example, it would be useful to determine the effect of the pressure ratio and wheel speed on the blade and downstream vane interaction.

REFERENCES

[1] Clark, J. P., Koch, P. J., Ooten, M. K., Johnson, J. J., Dagg, J., McQuilling, M. W., Huber, F., and Johnson, P. D., 2009, “Design of Turbine Components to Answer Research Questions in Unsteady Aerodynamics and Heat Transfer,” AFRL Report No. AFRL-RZ-WP-TR-2009-2180, WPAFB, OH.

[2] Clark, J. P., Koch, P. J., Ooten, M. K., Johnson, J. J., Anthony, R. J., Lemaire, R. P., Kennedy, S. W., White, A. L., Finnegan, J. M., Kobelak, M. D., Johnson, P. D., Huber, F., Downs, J., and Hendershot, J., 2010, “The High Impact Technologies Research Turbine, Build 1,” AFRL Report No. AFRL-RZ-WP-TR-2010-2262, WPAFB, OH.

[3] Clark, J. P., Aggarwala, A. S., Velonis, M. A., Magge, S. S., and Price, F. R., 2002, “Using CFD to Reduce Resonant Stresses on a Single-Stage, High-Pressure Turbine Blade,” ASME Paper No.GT2002-30320.

[4] Puterbaugh, S. L. and Copenhaver, W. W., 1994, "Flow Field Unsteadiness in the Tip Region of a Transonic Compressor Rotor," in Unsteady Flows in Aeropropulsion, ed. Ng, W., Fant, D., and Povinelli, L., ASME AD-Vol. 40, pp. 77-86, November.

[5] Dunn, M. G. and Haldeman, C. W., Jr., 1995, "Phase-Resolved Surface Pressure and Heat Transfer Measurements on the Blade of a Two-Stage Turbine," ASME Journal of Fluids Engineering, Vol. 117, pp. 653-658.

[6] Ifeachor, E. C. and Jervis, B. W., 1996, Digital Signal Processing, Addison-Wesley, New York.

[7] Clark, J. P., and Grover, E. A., 2007, “Assessing Convergence in Predictions of Periodic-Unsteady Flowfields,” ASME Journal of Turbomachinery, Vol. 129, pp. 740-749.

[8] Kemp, N. H. and Sears, W. R., “Aerodynamic Interference Between Moving Blade Rows,” Journal of Aero. Science, Vol. 20, No. 9, September 1953, pp. 585-597

[9] Kemp, N. H. and Sears, W. R., “The Unsteady Forces Due to Viscous Wakes in Turbomachines,” Journal of Aero. Science, Vol. 22, No. 7, July 1955, pp. 478-483

[10] Ashworth, D. A., LaGraff, J. E., Schultz, D. L., Grindrod, K. J., “Unsteady Aerodynamic and Heat Transfer Processes in a Transonic Turbine Stage,” Journal of Engineering for Gas Turbines and Power, Vol. 107, Oct. 1985, pp. 1022-1030.

[11] Guenette, G. R., Epstein, A. H., Giles, M. B., Haimes, R., Norton, R. J. G., “Fully Scaled Transonic Turbine Rotor Heat Transfer Measurements,” Journal of Turbomachinery, Vol. 111, Jan. 1989, pp. 1-7.

[12] Dring, R. P., Joslyn, H. D., Hardin, L. W., and Wagner, J. H., 1982, “Turbine Rotor-Stator Interaction , ASME Journal of Engineering for Power,” Vol. 104, pp. 729-742.

[13] Dunn, M. G. and Haldeman, C. W., Jr., 1995, “Phase-Resolved Surface Pressure and Heat-Transfer Measurements on the Blade of a Two-Stage Turbine,” ASME Journal of Fluids Engineering, Vol. 117, pp. 653-658.

[14] Adamczyk, J. J., 2000, “Aerodynamic Analysis of Multi-Stage Turbomachinery Flows in Support of Aerodynamic Design,” ASME Journal of Turbomachinery, Vol. 122, pp. 189-217.

[15] Ni, R.H., 1999, “Advanced Modeling Techniques for New Commercial Engines,” XIV ISOABE Conference, Florence, Italy, 5-10 September.

[16] Ni, R. H., 1982, “A Multiple-Grid Scheme for Solving the Euler Equations,” AIAA Journal, Vol. 20, No. 11, pp. 1565-1571.

[17] Ni, R. H. and Bogoian, J. C., 1989, “Prediction of 3-D Multistage Turbine Flow Field Using a Multiple-Grid Euler Solver,” AIAA Paper No. 89-0203.

[18] Rai, M. M., 1987, “Navier-Stokes Simulations of Rotor-Stator Interaction Using Patched and Overlaid Grids,” AIAA Journal of Propulsion and Power, Vol. 3, pp. 387-396.

[19] Rai, M. M., June 1987, “Unsteady Three-Dimensional Navier-Stokes Simulations of Turbine Rotor-Stator Interaction,” AIAA Paper 87-2058.

[20] Giles, M. B., 1990, “Stator/Rotor Interaction in a Transonic Turbine,” AIAA Journal of Propulsion and Power, Vol. 6, pp. 621-627.

[21] Dunn, M. G., Bennett, W. A., Delaney, R. A., and Rao, K. V., 1992, “Investigation of Unsteady Flow Through a Transonic Turbine Stage: Data/Prediction Comparison for Time-Averaged and Phase-Resolved Pressure Data,” Journal of Turbomachinery, Vol. 114, pp. 91-99.

[22] Rao, K. V., Delaney, R.A., and Dunn, M.G., 1994, “Vane-Blade Interaction in a Transonic Turbine, Part 1: Aerodynamics,” ASME Journal of Propulsion and Power, Vol. 10, No. 3, pp. 305-311.

[23] Sharma, O. P., Pickett, G.F., and Ni, R.H., 1992, “Assessment of Unsteady Flows in Turbines,” ASME Journal of Turbomachinery, Vol. 114, pp. 79-90.

[24] Klir, G.J., St. Clair, U.H., and Yuan, B., 1997, Fuzzy Set Theory: Foundations and Applications, Prentice Hall PTR, Upper Saddle River, NJ.

[25] Clark, J.P. and Yuan, B., 1998, “Using Fuzzy Logic to Detect Turbulent/Non- Turbulent Interfaces in an Intermittent Flow,” Intelligent Automation and Control, Vol. 6, pp. 113-118, TSI Press, Albuquerque, NM

[26] Davis, R. L., Yao, J., Clark, J. P., Stetson, G., Alonso, J. J., Jameson, A., Haldeman, C. W., Dunn, M. G., 2004, “Unsteady Interaction Between a Transonic Turbine Stage and Downstream Components,” International Journal of Turbomachinery, pp. 495- 506.

[27] Ni, R. H., Humber, W., Fan, G., Johnson, P. D., Downs, J., Clark, J. P., and Koch, P. J., 2011, “Conjugate Heat Transfer Analysis of a Film-Cooled Turbine Vane,” ASME Paper No. GT2011-45920.

[28] Casey, M. V., 1994, “Computational Methods for Preliminary Design and Geometry Definition in Turbomachinery,” in Turbomachinery Design Using CFD, AGARD Lecture Series 195, pp. 1-1:1-22.

[29] Dorney, D. J. and Davis, R. L., 1992, "Navier-Stokes Analysis of Turbine Blade Heat Transfer and Performance," ASME Journal of Turbomachinery, Vol. 114, pp. 795-806.

[30] Praisner, T. J. and Clark, J. P., 2007, “Predicting Transition in Turbomachinery, Part I – A Review and New Model Development,” ASME Journal of Turbomachinery, Vol. 129, pp. 1-13.

[31] Davis, R. L. and Dannenhoffer, J. D., III, 2008, “A Detached-Eddy Simulation Procedure Targeted for Design,” AIAA Journal of Propulsion and Power, Vol. 126, pp. 1287-1294.

[32] Wilcox, D. C., 2006, Turbulence Modeling for CFD, 3rd Edition, DCW Industries, La Cañada, CA.

[33] Vanderplaats, G. N., 1984, Numerical Optimization Techniques for Engineering Design: With Applications, McGraw-Hill, New York.

[34] Anthony, R. J. and Clark, J. P., 2013, “A Review of the AFRL Turbine Research Facility,” ASME Paper No. GT2013-94741.

[35] Shapiro, A. H., “The Dynamics and Thermodynamics of Compressible Fluid Flow,” (2 vols.), Ronald, New York, 1953.

[36] Johnson, J. J., King, P. I., Clark, J. P., Anthony, R. J., Koch, P. J., Ooten, M. K., Finnegan, J., Kobelak, M., Johnson, P. D., and Huber, F., " Three-Dimensional Viscous CFD Predictions of Vane-Only Configuration of a Full-Scale Experimental Turbine Rig," Proceedings of the 46th AIAA/ASME/SAE/AASE Joint Propulsion Conference, Nashville TN, 25-28 July 2010, Paper AIAA 2010-7027.

[37] Anthony, R. J., Clark, J. P., Kennedy, S. W., Finnegan, J. M., Johnson, P. D., Hendershot, J., Downs, J., 2011, “Flexible Non-Instrusive Heat Flux Instrumentation on the AFRL Research Turbine,” ASME Paper No. GT2011-46853.

[38] Anthony, R. J., Clark, J. P., Finnegan, J. M., Johnson, P. D., 2012, “Modifications and Upgrades to the AFRL Turbine Research Facility,” ASME Paper No. GT2012- 70084.

[39] Polanka, M. D., Clark, J. P., White, A. L., Meininger, M., Praisner, T. J., 2013, “Turbine Tip and Shroud Heat Transfer and Loading, Part B: Comparisons Between Prediction and Experiment Including Unsteady Effects,” ASME Paper No. GT2003- 38916.

[40] Ni, R. H., Humber, W., Ni, M., Fan, G., 2012, “Conjugate Heat Transfer Analysis and Large Scale Unsteady Analysis Capabilities for Turbine Durability Design,” AFRL Report No. AFRL-RQ-WP-TR-2012-0189, WPAFB, OH.

[41] Roache, P. J., “Quantification of Uncertainty in Computational Fluid Dynamics,” Annual: Review of Fluid Mechanics, Annual Reviews, Inc., Palo Alto, CA, 1997, pp. 126-160.

[42] AIAA, “Guide for the Verification and Validation of Computational Fluid Dynamics Simulations,” AIAA G-077-1998, 1998.

[43] Sonntag, R. E., Borgnakke, C., and Van Wylen, G. J., 2003, Fundamentals of Thermodynamics Sixth Addition, John Wiley & Sons, New York.